EXPERIMENTAL AND COMPUTATIONAL STUDIES OF LOW-DIMENSIONAL FUNCTIONAL MATERIALS

by

JAMES CUMBY

A thesis submitted to
The University of Birmingham
for the degree of
DOCTOR OF PHILOSOPHY

School of Chemistry
College of Engineering and Physical Sciences
University of Birmingham
June 2014

ABSTRACT

This thesis describes the synthesis, characterisation and density functional theory investigation of a range of MX_2O_4 compounds related to Schafarzikite, $FeSb_2O_4$. Chemical substitution of the M cation has been performed to yield $Mn_xCo_{1-x}Sb_2O_4$, which is characterised both structurally and magnetically. Additionally, the synthesis and magnetic behaviour of the mineral Trippkeite ($CuAs_2O_4$) has been investigated.

Density functional theory calculations have been performed for a wide range of MX_2O_4 compounds, both to investigate structural behaviour at high pressure, and also to rationalise the experimentally observed magnetic order. In addition, the technique has been used to predict the magnetic groundstate of $CuAs_2O_4$, before an experimental validation.

The structurally-related compounds Versiliaite and Apuanite have been synthesised for the first time, and characterised both structurally and magnetically. Their relation to the Schafarzikite structure is discussed, as are the differences in magnetic ordering.

ACKNOWLEDGEMENTS

Firstly, I would like to thank Prof. Colin Greaves for all the expert guidance, support and enthusiasm throughout this project. It has been a real pleasure to work with you, and you have inspired me to continue asking questions and pushing the boundaries. I would like to thank you for all of your patience and support, particularly when faced with a mountain of incomprehensible symbols and terminology! Although it can generate a lot of drivel, I hope I've convinced you of the merits of DFT.

To Dr. David Quigley, I would like to thank you for guiding me through the complex world of codes, compiling and calculations, and for your willingness to hack Fortran where needed. It has been a steep learning curve, but I am very grateful to you for answering my (often simple) questions, and also going above and beyond to solve more complex issues.

I would also like to thank Prof. Frank Berry, not only for long discussions about Mössbauer spectroscopy, but also your dogged determination in collecting and fitting complex spectra. Your enthusiasm in discussing all other aspects of the project has also been invaluable.

Thanks must go to the Greaves group who have come and gone; the many hours of Schafarzikite-based discussions and company on various trips has made the past few years a lot of fun, as well as benefiting my research enormously. I would also like to thank everyone else on Floor 5 for all the fun and games, in particular to Dr. Jackie Deans for her patience and willingness to wrestle the TGA into line.

I would also like to thank instrument scientists and technicians I have met, particularly Dr. Winfried Kockelmann for his help on GEM. I am also grateful to Advantage West Midlands, the EPSRC, the University of Birmingham and BlueBEAR for funding and equipment.

Finally, I would like to thank my wife, family and friends for all their support. Lucy, you have had to put up with long chemistry-based ramblings and my frequent gazing into empty space, which you have approached with great patience. For this I am truly grateful. I hope that the mention of 'intimate grinding' in my lab book will continue to make you smile!

Contents

List of Abbreviations

1D	One-Dimensional.
2D	Two-Dimensional.
3D	Three-Dimensional.
AC	Alternating Current.
AFM	Antiferromagnetic.
BFGS	Broyden-Fletcher-Goldfarb-Shanno.
BV	Basis Vector.
BVS	Bond Valence Sum.
BZ	Brillouin Zone.
CMR	Colossal Magnetoresistance.
CW	Constant Wavelength.
DAC	Diamond Anvil Cell.
DC	Direct Current.
DFT	Density Functional Theory.
DOS	Density of States.
DTA	Differential Thermal Analysis.
E_{XC}	Exchange-Correlation Functional.
ELF	Electron Localisation Function.
esd	Estimated Standard Deviation.
FC	Field-Cooled.
FM	Ferromagnetic.
GB	Grain-Boundary.
GEM	General Materials Diffractometer.
GGA	Generalised Gradient Approximation.
GSAS	General Structural Analysis System.
HI	High-Intensity.
HR	High-Resolution.
HRPT	High Resolution Powder Diffractometer for Thermal Neutrons.
HS	High Spin.
ILL	Institut Laue-Langevin.
IR	Irreducible Representation.
JT	Jahn-Teller.

LAPW Linearised Augmented Planewave.
LDA Local Density Approximation.
LP Lone Pair.
MD March-Dollase.
MPMS Materials Properties Measurement System.
NPD Neutron Powder Diffraction.
PBE Perdew, Burke and Ernzerhof.
PDOS Partial Density of States.
PSD Position Sensitive Detector.
PSI Paul Scherrer Institute.
PSP Pseudopotential.
PTFE Polytetrafluoroethylene: $(\text{---}CF_2-CF_2\text{---})_n$.
PVDF Polyvinylidene fluoride: $(\text{---}CH_2-CF_2\text{---})_n$.
RMS Root Mean Squared.
RT Room Temperature.
SCXRD Single Crystal X-ray Diffraction.
SOC Spin-Orbit Coupling.
SQUID Superconducting Quantum Interference Device.
TEM Transmission Electron Microscopy.
TG Thermal Gravimetry.
TGA Thermal Gravimetric Analysis.
TM Transition Metal.
TOF Time of Flight.
XRF X-ray Fluorescence.
XRPD X-ray Powder Diffraction.
ZFC Zero-Field Cooled.

CHAPTER 1
INTRODUCTION

Functional materials are those which possess useful properties (such as magnetism, piezoelectricity or ionic conductivity) in addition to their structural behaviour (*i.e.* load-bearing abilities). These additional properties have been used to create almost every 'technological' advance after the 19^{th} century, from the silicon chips in computers, through sonar and medical ultrasound, to the batteries used to power missions to Mars. In fact, without functional materials it would be impossible to generate electricity, and therefore few of the associated advances would exist. Hopefully then, it is clear why functional materials are important to society. Arguably more important, however, is the development of new functional materials for next generation technologies. One particularly active area of interest is the development of 'multi-functional' or 'multi-ferroic' materials, which combine two or more functional properties into one material, such as ferroelectric and ferromagnetic effects. Such materials would allow simplification and miniaturisation of existing technologies (such as magnetic data storage) but may also lead to the development of new, unknown technologies for the future. Another area of study is low-dimensional materials (those showing noticeably different atomic structures in different crystallographic directions) and the development of functional properties inherently dependent on the orientation of a given crystal. This research project has been concerned with the investigation of possible functional effects (particularly magnetism) within a series of compounds derived from low-dimensional mineral structures, the functional properties of which have been largely unexplored.

1.1 Functional Materials from Minerals

The use of known mineral structures as a basis for the development of new materials has many advantages; not only are there a huge array of structural possibilities, but minerals also generally represent thermodynamically stable structures, allowing for relatively easy lab synthesis. In addition (and perhaps more importantly for chemists) many mineral structures can be recreated with a range of cations and anions, giving an extra handle to 'tune' functional properties. A prime example of this is Perovskite ($CaTiO_3$, or more generally ABO_3) which has been extensively studied and cation-substituted, generating a range of new functional materials such as (ferroelectric) $BaTiO_3$,[1] $La_xSr_{1-x}MnO_3$ (which shows colossal magnetoresistance (CMR) behaviour[2]) and the structurally-related high-temperature superconductor $YBa_2Cu_3O_7$.[3] ABO_3-related structures abound in the literature, and continue to provide a large avenue of investigation. Other minerals have also served as a starting point, however, such as Spinel, $MgAl_2O_4$ (AB_2X_4). Many materials adopt this structure, including other well-known minerals such as Magnetite, Fe_3O_4, which displays charge ordering below the Verwey transition at 123 K.[4] Synthetic approaches have led to the development of alternative cathodes for Li-ion batteries ($LiMn_2O_4$[5]) and the investigation of thermoelectric properties for chalcogenide spinels, X = S or Se (see *e.g.* [6] for review).

A number of minerals have received interest as low-dimensional structures, often with regards to magnetic properties. Hollandite ($Ba_xMn_8O_{16}$ or $A_xB_8O_{16}$, $1 \leq x \leq 2$) is one such material that exhibits a one-dimensional (1D) structure consisting of double Mn-O octahedral chains, arranged around channels containing the (often disordered) A cation (figure 1.1). This mineral has been studied for its magnetic and electronic properties[7] but has also received interest as a potential Li-ion conductor[8] and as a means to encapsulate nuclear waste materials.[9] Rutile (TiO_2) is another well known structure also demonstrating a crystal structure unique along one crystallographic direction; here chains of edge-sharing [MO_6] octahedra are aligned along this (c) direction, joined together by corner linking (figure 1.2). A wide range of compositions are known to form with this structure, and have been investigated for a range of interesting properties including metal-insulator transitions (VO_2[10]), transparent optical properties (MgF_2[11]) and

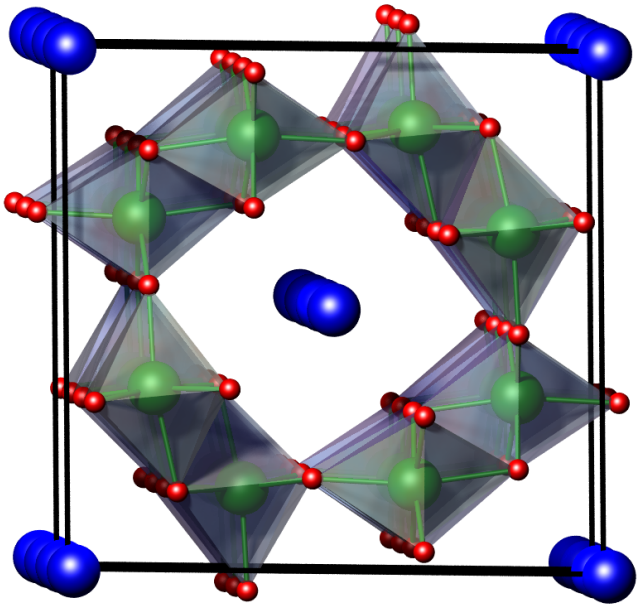

Figure 1.1 – Hollandite ($A_xB_8O_{16}$) structure viewed approximately along [010] direction. A - blue spheres, B - green spheres, O - red spheres.

catalytic properties for use in gas-sensing (SnO_2).[12] Another low-dimensional mineral closely related to this work is Kusachite, $CuBi_2O_4$; this material exhibits 'chains' of stacked [CuO_4] square-planar units, separated by bismuth linkages. This mineral has also been extensively studied, particularly with regard to its magnetic behaviour as a model spin-$\frac{1}{2}$ 1D system,[13] and the effect of atomic substitution.[14]

The structures discussed above represent a tiny fraction of those in existence; as of 2003, an estimated 4051 valid mineral species were known.[15] Although many share the same (or similar) atomic structure, a wide range of compounds are still available as starting points for chemical investigation.

1.2 Schafarzikite, $FeSb_2O_4$

The basis of much of the work in this project is the mineral Schafarzikite, $Fe^{2+}Sb_2^{3+}O_4$. Found in few locations around the world, this tetragonal mineral (spacegroup $P4_2/mbc$,[16] a = 8.61574 (9) Å and c = 5.92069(8) Å[17]) is structurally related to Minium, $Pb^{4+}Pb_2^{2+}O_4$, used as a red pigment throughout history.[18] In many respects, this MX_2O_4 structure is intermediate between that

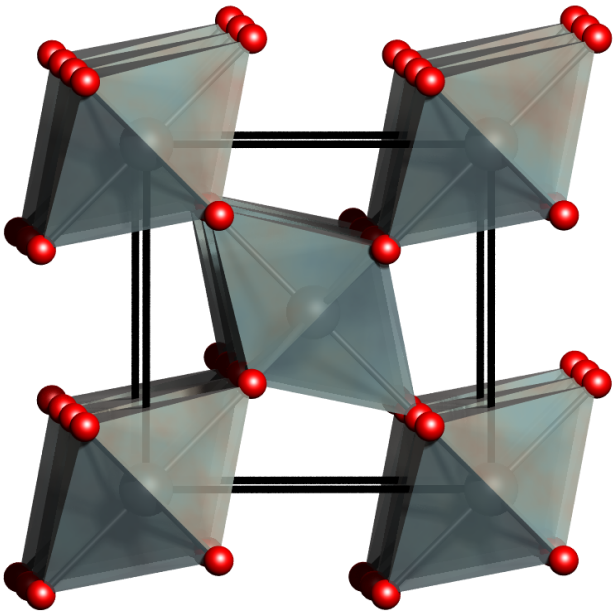

Figure 1.2 – Rutile (AX_2) structure viewed approximately along [001] direction. A - grey polyhedra, X - red spheres.

of Rutile and Kusachite; it consists of infinite chains of edge-sharing [MO_6] octahedra aligned along the *c*-axis direction (as in TiO_2) but these are separated from each other by O−X−O bridges (similar to $CuBi_2O_4$). This separation of the octahedral chains causes a significantly larger M−M separation within the *ab* plane (6.1 Å) *cf.* along the chains (3.0 Å), suggesting essentially 1D interactions between M cations.

The Sb cations adopt a trigonal pyramidal coordination to oxygen, however, they can also be described as occupying a distorted tetrahedral site, formed by the three oxygen atoms and the Sb lone pair (LP) of electrons; these LPs are oriented along (110) directions, and occupy the 'channels' formed within the structure (figure 1.3).

A wide range of possible atomic substitutions on both the M and X cation sites have been reported, primarily for M as a first-row transition metal (TM) (table 1.1). Notably, no Schafarzikite-like structures are reported for X = Bi^{3+}. Additionally, a range of mixed-cation systems have been reported. For the M site, mixed Fe/Co,[19] Mn/V[20] and Mg/Ni[21] compositions have all been reported at various doping levels, as well as the non-magnetic $Sn_{0.5}Pb_{0.5}Pb_2O_4$.[22] Mixed X-site cations are also possible, with details reported of mixing Sb and Pb in $MnSb_2O_4$,[23] $CoSb_2O_4$[24] and $FeSb_2O_4$;[17] in the first two cases this substitution was not purely confined to

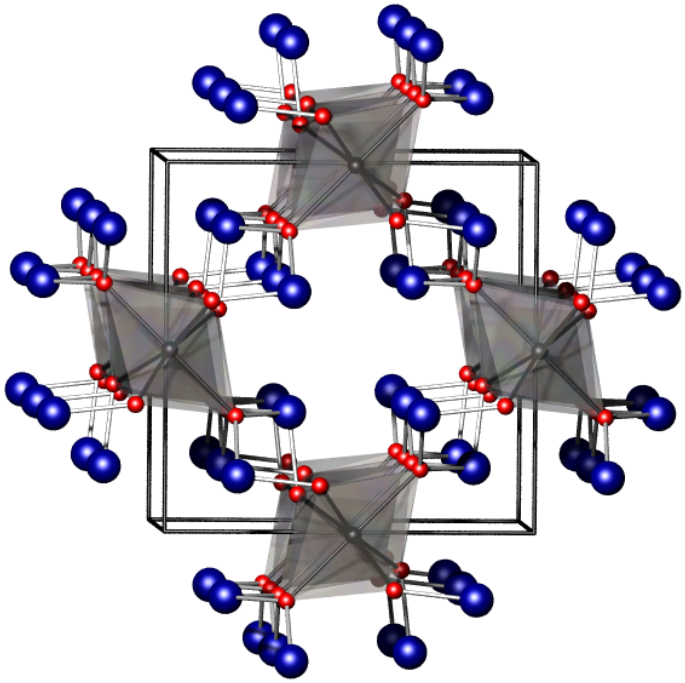

(a)

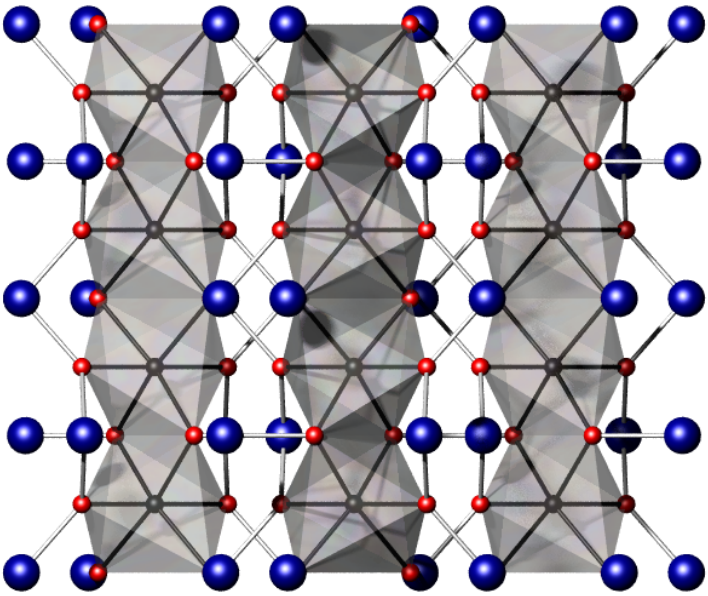

(b)

Figure 1.3 – Schafarzikite (MX_2O_4) structure viewed (a) approximately along (001) and (b) along (100) directions (two unit cells shown). M - grey octahedra, X - blue spheres, O - red spheres (X LPs not shown).

Table 1.1 – Reports of MX_2O_4 compositions adopting a Schafarzikite-like structure (mixed cation compositions are not shown).

	X cation			
M cation	As^{3+}	Sn^{2+}	Sb^{3+}	Pb^{2+}
Mg	-	-	25	-
Ti	-	26	-	-
Mn	-	-	27	*
Fe	-	-	16	-
Co	-	-	24	-
Ni	28	-	29	-
Cu	30	-	31	-
Zn	†	-	32	-
Sn	-	-	-	33
Pt	-	-	-	34‡
Pb	-	-	-	35

* Forms with a different low-dimensional structure, of 'zig-zag' octahedral chains.[36]

† Adopts a layered $NaAsO_2$-like structure but suggested to have a high-temperature Schafarzikite structure polymorph.[37]

‡ Adopts an orthorhombic Schafarzikite-like structure, similar to Pb_3O_4 at low temperature.

the X site, instead forming Sb^{5+} on the octahedral site.

1.2.1 MX_2O_4 Magnetic Properties

The low-dimensional nature of the Schafarzikite structure makes it particularly interesting with regards to magnetic behaviour. Due to the significant focus of this project on magnetic properties of this and other materials, previously reported magnetic behaviour will briefly be discussed.

Within each MX_2O_4 unit cell are four formula units, with symmetry equivalent M positions (in the tetragonal $P4_2/mbc$ structure) at S_1 $(0, \frac{1}{2}, \frac{1}{4})$, S_2 $(0, \frac{1}{2}, \frac{3}{4})$, S_3 $(\frac{1}{2}, 0, \frac{1}{4})$, and S_4 $(\frac{1}{2}, 0, \frac{3}{4})$.

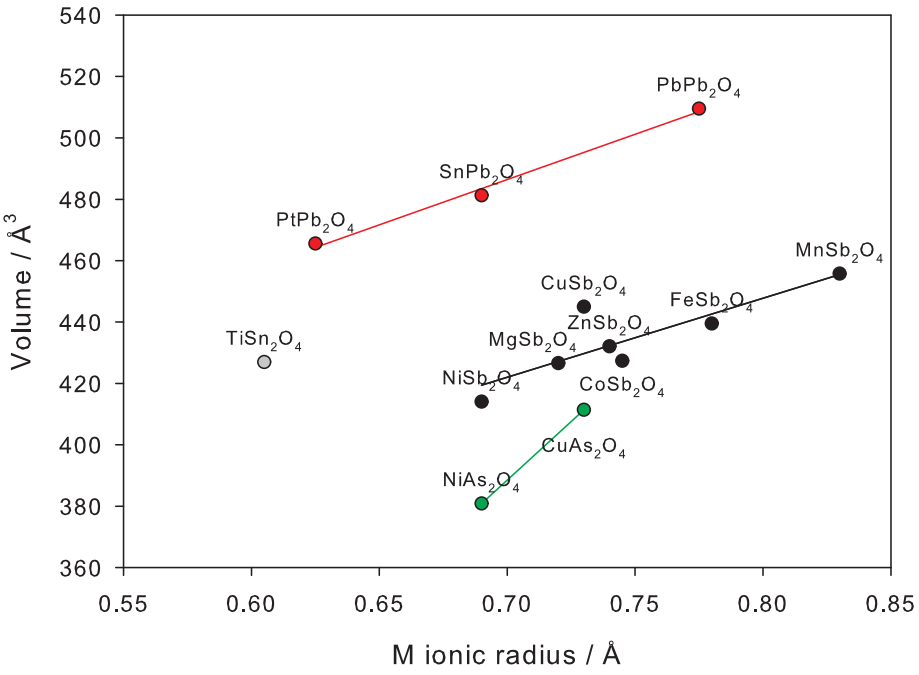

Figure 1.4 – Trends in MX_2O_4 unit cell volume with M ionic radius.

By considering possible orientations of magnetic moments on each of these sites, four possible magnetic structures (without forming a magnetic supercell) are possible. These are labelled (from symmetry arguments[38]) as:

$$\begin{aligned} \mathrm{A} &= +S_1 - S_2 + S_3 - S_4, \\ \mathrm{C} &= +S_1 + S_2 - S_3 - S_4, \\ \mathrm{G} &= +S_1 - S_2 - S_3 + S_4, \\ \mathrm{FM} &= +S_1 + S_2 + S_3 + S_4, \end{aligned} \tag{1.1}$$

and are shown graphically in figure 1.5. Although the magnetic moments are shown aligned along c, they could adopt a range of orientations. More generally, these structures can be described as a combination of ferromagnetic (FM) or antiferromagnetic (AFM) interactions occurring both along the octahedral chains, and between nearest-neighbour chains in the ab plane. Experimentally, A- and C-type magnetic structures are observed for most TM–containing com-

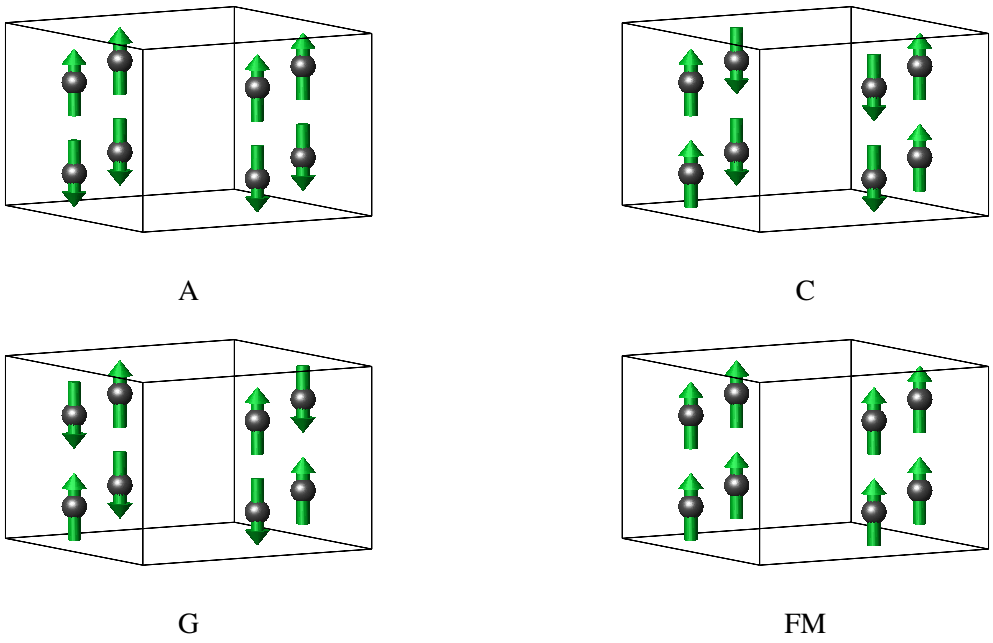

Figure 1.5 – Possible (colinear) MX_2O_4 magnetic structures, viewed approximately along (110) (only M cations shown).

positions, with a change from A-type to C-type on crossing the periodic table (table 1.2). The exception here is $CuSb_2O_4$; this has very recently been reported to behave as non-interacting 1D Heisenberg-like chains, with a possible long-range AFM structure below 1.8 K.[31]

The onset of AFM ordering in the reported MX_2O_4 compounds generally occurs in the range 40–80 K, with the highest temperature reported for $CoSb_2O_4$ (79 K[24]). The change in magnetic groundstate on crossing the TM period can be broadly attributed to the filling of the high spin (HS) *d*-orbitals (particularly the t_{2g} set) and the resulting effect on the magnetic interactions.

Table 1.2 – Reported magnetic structures for MX_2O_4.

		M cation				
		Mn	Fe	Co	Ni	Cu
X cation	Sb^{3+}	A[29]	A[39]	C[24]	C[29]	Isolated Chains[31]
	As^{3+}	-	-	-	Unknown	Unknown
	Pb^{2+}	G[40]	-	-	-	-

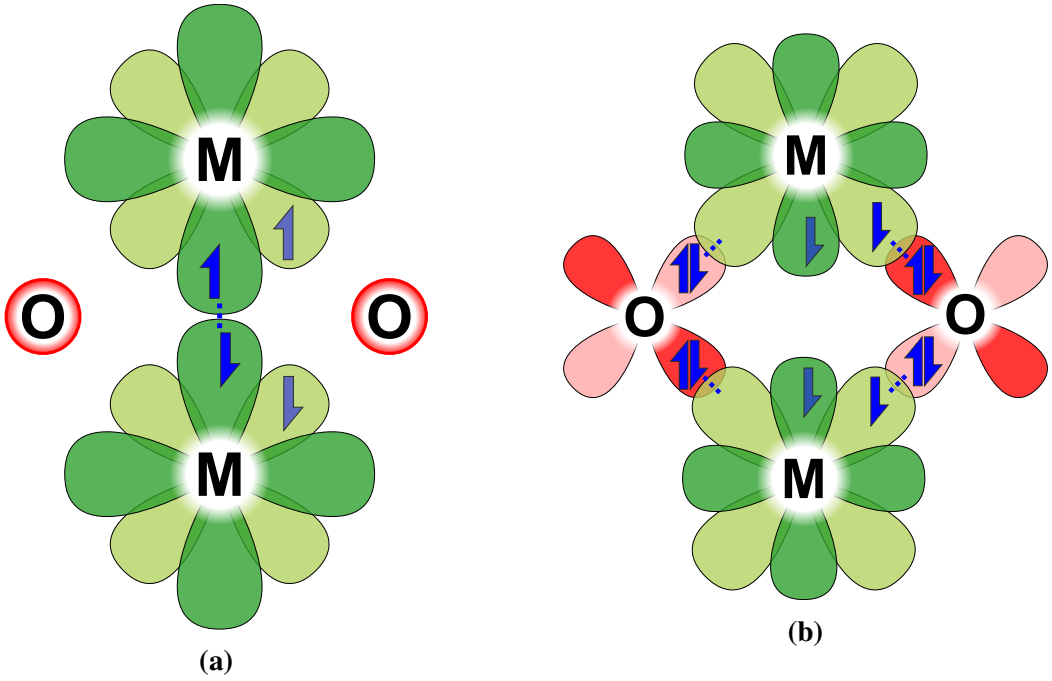

Figure 1.6 – Competing exchange interactions between edge-sharing octahedra; (a) M−M direct-exchange and (b) 90° M−O−M superexchange.

Within materials of this type a number of competing exchange interactions can occur, either directly between M cations ('direct' exchange) or via an intermediate ion, typically oxygen. This anion-mediated 'superexchange' can occur over a range of angles, giving rise to either a FM or AFM exchange on increasing the angle from 90° to 180°.[41]

Along the octahedral chains there is a competition between direct M−M exchange and 90° superexchange via oxygen, which gives rise to a competition between AFM and FM coupling, respectively (figure 1.6). For Mn and Fe the direct-exchange dominates, while for Co and Ni the greater number of t_{2g} electrons prevents effective M−M interactions, resulting in the observed FM chains.

1.3 Apuanite, $Fe_{20}Sb_{16}O_{48}S_4$ and Versiliaite, $Fe_{12}Sb_{12}O_{32}S_2$

Structurally related to Schafarzikite, Apuanite and Versiliaite are rarer still, originating from the Buca della Vena mine in the Apuan Alps (Italy).[42] Both are related to $FeSb_2O_4$ by the partial substitution of Fe^{3+} onto the X (*i.e.* Sb) site, with a corresponding insertion of S between the resulting pairs of tetrahedral iron, into the structural channel. Correspondingly, some of the oc-

tahedral Fe^{2+} is oxidised to Fe^{3+}, to give the formal compositions $[Fe^{2+}_4Fe^{3+}_8][Fe^{3+}_8Sb^{3+}_{16}]O_{48}S_4$ (Apuanite, figure 1.7) and $[Fe^{2+}_4Fe^{3+}_4][Fe^{3+}_4Sb^{3+}_{12}]O_{32}S_2$ (Versiliaite, figure 1.8). The substituted Fe−S−Fe 'linkages' between octahedral chains are ordered along the *c*-axis, giving rise to a periodicity of 3*c* and 2*c* compared to Schafarzikite, respectively.[43] The spacing of the sulfur links maintains the tetragonal $(P4_2/mbc)$ symmetry in Apuanite, but gives rise to an orthorhombic $(Pbam)$ symmetry for Versiliaite.

1.4 Project Aims

The data presented in table 1.1 show that although a wide range of MX_2O_4 compositions are known, there are still a wide range of compositions to be studied, particularly with regards to mixed-cation species on both the M and X sites. As such, the primary aim of this project was to explore the structural and magnetic properties of new compositions adopting the Schafarzikite structure. Additionally, a number of phases have been reported with regards to atomic structure, but show little or no investigation of any functional properties they possess. These properties were explored not only through experiment, but also with the aid of theoretical results; a particular aspect of this was to rationalise the magnetic interactions within the MX_2O_4 series, in order to suggest potential compositions worthy of experimental investigation.

The closely related Apuanite and Versiliaite phases have not been successfully synthesised before, nor are any physical properties reported. These phases were thus to be explored experimentally, to investigate if they could be successful synthesised, and also to report any properties thereof.

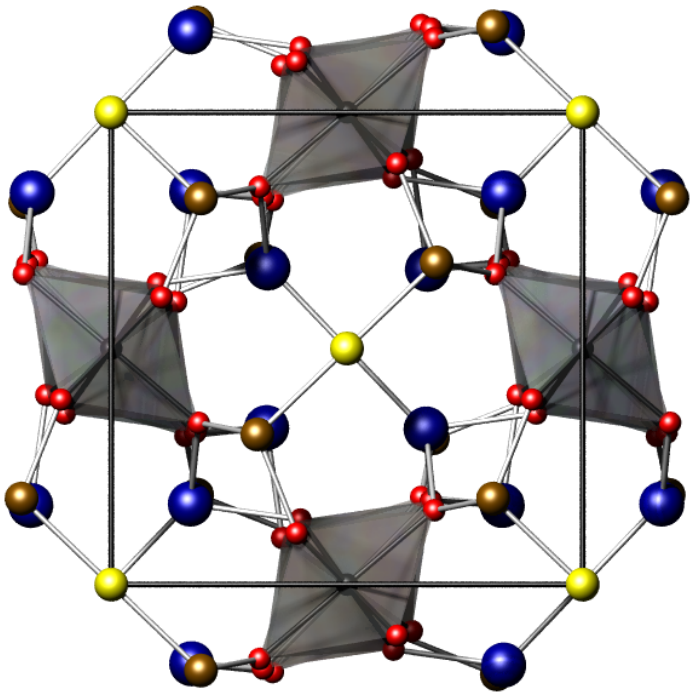

(a)

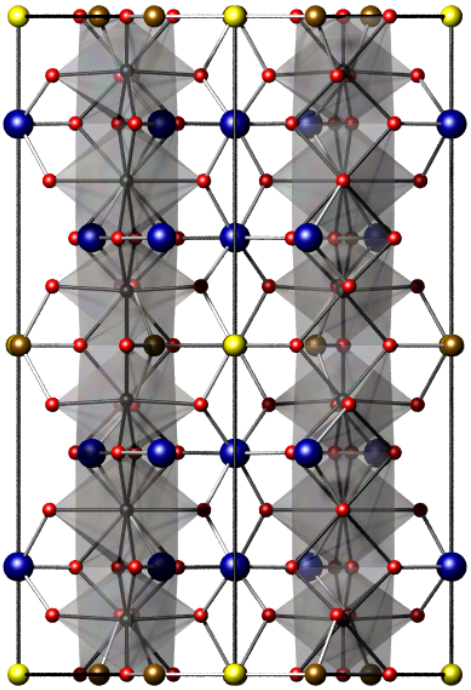

(b)

Figure 1.7 – Apuanite structure viewed along (a) [001] and (b) [110]. ^{VI}Fe - grey polyhedra, $^{IV}Fe^{3+}$ - brown spheres, Sb - blue spheres, O - red spheres, S - yellow spheres.

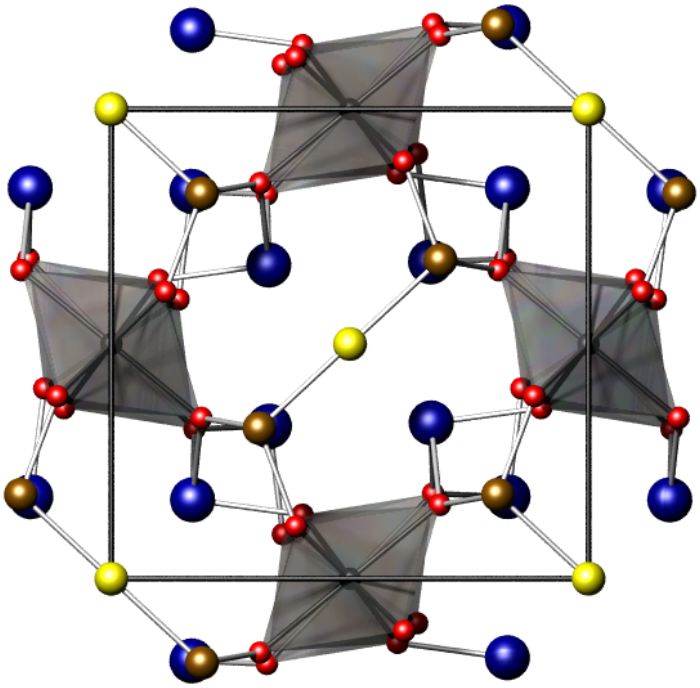

(a)

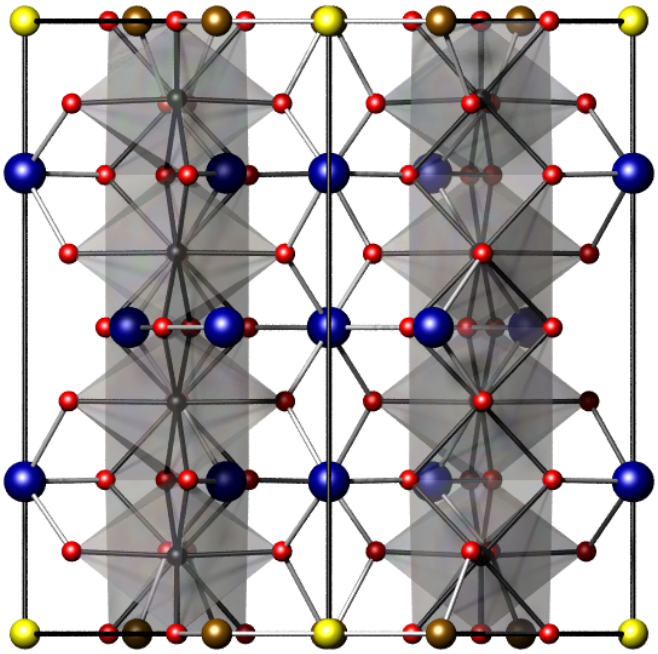

(b)

Figure 1.8 – Versiliaite structure viewed along (a) [001] and (b) [110]. ^{VI}Fe - grey polyhedra, $^{IV}Fe^{3+}$ - brown spheres, Sb - blue spheres, O - red spheres, S - yellow spheres.

References

[1] A. von Hippel, R. G. Breckenridge, F. G. Chesley and L. Tisza, *Industrial & Engineering Chemistry*, 1946, **38**, 1097–1109.

[2] J. Van Santen and G. Jonker, *Physica*, 1950, **16**, 599–600.

[3] M. Wu, J. Ashburn, C. Torng, P. Hor, R. Meng, L. Gao, Z. Huang, Y. Wang and C. Chu, *Physical Review Letters*, 1987, **58**, 908–910.

[4] E. J. W. Verwey, *Nature*, 1939, **144**, 327–328.

[5] B. L. Ellis, K. T. Lee and L. F. Nazar, *Chemistry of Materials*, 2010, **22**, 691–714.

[6] G. J. Snyder, T. Caillat and J.-P. Fleurial, *Materials Research Innovations*, 2001, **5**, 67–73.

[7] S. Ishiwata, J. W. G. Bos, Q. Huang and R. J. Cava, *Journal of Physics: Condensed Matter*, 2006, **18**, 3745–3752.

[8] S. Barbato, *Electrochimica Acta*, 2001, **46**, 2767–2776.

[9] A. Leinekugel-le Cocq, P. Deniard, S. Jobic, R. Cerny, F. Bart and H. Emerich, *Journal of Solid State Chemistry*, 2006, **179**, 3196–3208.

[10] F. Morin, *Physical Review Letters*, 1959, **3**, 34–36.

[11] K. Ramesh Babu, C. Bheema Lingam, S. Auluck, S. P. Tewari and G. Vaitheeswaran, *Journal of Solid State Chemistry*, 2011, **184**, 343–350.

[12] G. T. Ang, G. H. Toh, M. Z. A. Bakar, A. Z. Abdullah and M. R. Othman, *Process Safety and Environmental Protection*, 2011, **89**, 186–192.

[13] O. Janson and H. Rosner, *Physica C: Superconductivity*, 2007, **460-462**, 458–459.

[14] N. Bettahar, P. Conflant and F. Abraham, *Journal of Alloys and Compounds*, 1992, **188**, 211–214.

[15] L. Horváth, *Minstats*, 2003, 20.

[16] R. Fischer and F. Pertlik, *Tschermaks Mineralogische und Petrographische Mitteilungen*, 1975, **22**, 236–241.

[17] M. J. Whitaker, R. D. Bayliss, F. J. Berry and C. Greaves, *Journal of Materials Chemistry*, 2011, **21**, 14523–14529.

[18] R. E. Dinnebier, S. Carlson, M. Hanfland and M. Jansen, *American Mineralogist*, 2003, **88**, 996–1002.

[19] B. P. de Laune, *Low Dimensional Sytructures of some Mixed Metal Oxides Containing Antimony: Synthesis and Characterisation*, PhD thesis, School of Chemistry, The University of Birmingham, 2013.

[20] H. Abe, K. Yoshii and H. Kitazawa, *Physica status solidi (a)*, 2002, **189**, 429–432.

[21] B. Y. Brach, N. V. Chezhina and Y. V. Shapoval, *Inorganic Materials*, 1989, **25**, 601.

[22] J. P. Vigouroux, E. Husson, G. Calvarin and N. Q. Dao, *Spectrochimica Acta Part A: Molecular Spectroscopy*, 1982, **38**, 393–398.

[23] A. M. Abakumov, M. G. Rozova, E. V. Antipov, J. Hadermann, G. V. Tendeloo, M. V. Lobanov, M. Greenblatt, M. Croft, E. V. Tsiper, A. Llobet, K. A. Lokshin and Y. Zhao, *Chemistry of Materials*, 2005, **17**, 1123–1134.

[24] B. P. de Laune and C. Greaves, *Journal of Solid State Chemistry*, 2012, **187**, 225–230.

[25] C. Giroux-Maraine and G. Perez, *Revue de Chimie minérale*, 1975, **12**, 427–432.

[26] N. Kumada, Y. Yonesaki, T. Takei, N. Kinomura and S. Wada, *Materials Research Bulletin*, 2009, **44**, 1298–1300.

[27] H. Fjellvåg and A. Kjekshus, *Acta Chemica Scandinavica Series A-Physical and Inorganic Chemistry*, 1985, **39**, 389–395.

[28] H. T. Witteveen, *Solid State Communications*, 1971, **9**, 1313–1315.

[29] J. R. Gavarri and A. W. Hewat, *Journal of Solid State Chemistry*, 1983, **49**, 14–19.

[30] F. Pertlik, *Tschermaks Mineralogische und Petrographische Mitteilungen*, 1975, **22**, 211–217.

[31] M. T. Atanasova, A. M. Strydom, C. J. H. Schutte, L. C. Prinsloo and W. W. Focke, *Journal of Materials Science*, 2014, **49**, 3497–3510.

[32] E. Gutiérrez Puebla, E. Gutiérrez Rios, A. Monge and I. Rasines, *Acta Crystallographica Section B*, 1982, **38**, 2020–2022.

[33] J. R. Gavarri, J. P. Vigouroux, G. Calvarin and A. W. Hewat, *Journal of Solid State Chemistry*, 1981, **36**, 81–90.

[34] N. Bettahar, P. Conflant, F. Abraham and D. Thomas, *Journal of Solid State Chemistry*, 1987, **67**, 85–90.

[35] M. K. Fayek and J. Leciejewicz, *Zeitschrift für Anorganische und Allgemeine Chemie*, 1965, **336**, 104–109.

[36] A. Teichert and H. Müller-Buschbaum, *Zeitschrift für Anorganische und Allgemeine Chemie*, 1991, **598**, 319–325.

[37] S. Ghose, P. Sengupta and E. Schlemper, *American Mineralogist*, 1987, **72**, 629–632.

[38] E. O. Wollan and W. C. Koehler, *Physical Review*, 1955, **100**, 545–563.

[39] J. A. Gonzalo, D. E. Cox and G. Shirane, *Physical Review*, 1966, **147**, 415–418.

[40] S. A. J. Kimber and J. P. Attfield, *Journal of Materials Chemistry*, 2007, **17**, 4885–4888.

[41] J. Goodenough, *Magnetism and the Chemical Bond*, Interscience Publishers, 1963.

[42] S. M. Marcello Mellini and P. Orlandi, *American Mineralogist*, 1979, **64**, 1230–1234.

[43] M. Mellini and S. Merlino, *American Mineralogist*, 1979, **64**, 1235–1242.

CHAPTER 2
EXPERIMENTAL TECHNIQUES

2.1 Solid State Synthesis

A number of synthetic methods have been used during this project, in all cases starting from a stoichiometric mixture of metal oxide and metal sulphide powders, in order to give the required chemical composition. Reagents were dried before use, either under dynamic vacuum (approximately 10^{-6} mbar) at 150 °C, or at 350 °C in air, depending on reagent stability to oxidation/decomposition.

2.1.1 Ceramic Method

The ceramic method has been used for the majority of synthetic procedures throughout this work. This procedure relies on the use of high temperature to cause significant atomic diffusion within an intimately ground mixture of reagent powders to produce a new phase. Depending on the peak temperature used and the heating/cooling rates, both thermodynamically and kinetically stable compounds can be reached. In this study, temperatures in the range 300 °C to 800 °C have been used during reactions. These relatively low temperatures for solid state reactions have been employed due to the low melting points of Sb_2O_3 (656 °C) and Sb_2S_3 (550 °C).[1] For Versiliaite- and Apuanite-like phases (chapter 7) it was also necessary to cool reactions slowly (6 °C hr^{-1}) to achieve maximum purity of the resulting phase. Sb_2O_3 also poses problems during reactions due to low-temperature oxidation (either 463 °C or 575 °C for

the polymorphs Valentinite or Senarmontite, respectively[2]) combined with excessive volatility (beginning at 450 °C and 502 °C, respectively[3]). To prevent potential loss of Sb_2O_3 during heating, reactions were therefore performed within sealed quartz glass ampoules, which were evacuated to approximately 5×10^{-6} mbar pressure. This reduction in oxygen partial pressure also served to prevent oxidation-products from forming (for both Sb^{3+} and Fe^{2+}). In many cases, samples were placed inside alumina (Al_2O_3) crucibles within the quartz tubes, to avoid reaction between Sb_2O_3 and the silica. Where necessary, re-grinding and re-heating of the reaction mixture was sometimes used to encourage further reaction, due to reactions occurring at particle interfaces.

2.1.2 Hydrothermal Method

The hydrothermal method offers an alternative, low temperature synthesis route, particularly suitable for reactions where reagents have very different melting points which would make them less suitable for the ceramic method. It consists of heating water to above its boiling point in a sealed container in order to dissolve the reaction mixture, thus allowing atomic rearrangement and formation of the desired product. By varying temperature and/or any added mineralising agents (such as KCl) it is possible to promote precipitation of this resulting compound, thus encouraging further reaction to occur. Reactions in this project have all used pure water as a solvent, heating to temperatures of approximately 200 °C in a Parr 4746 hydrothermal bomb.

2.2 Diffraction Techniques

Due to the periodic arrangement of atoms within a crystal, diffraction of radiation with a similar wavelength to the interatomic spacing ($\simeq$ 1 Å) from these atoms can give rise to constructive and destructive interference effects. Because of the huge number of regularly arranged atoms in even a small crystal, constructive interference is amplified for certain scattering angles (2θ). By describing the periodic arrangement of atoms in terms of equally-spaced planes (denoted by Miller indices $[hkl]$) it is possible to derive the 'Bragg' equation, relating the spacing between a

given set of planes (d) to the incident wavelength:

$$n\lambda = 2dsin\theta, \tag{2.1}$$

where n is any integer, normally taken as 1. By measuring the scattering angles at which constructive interference occurs, it is therefore possible to determine the corresponding d-spacings from equation 2.1. These d-spacings can then be assigned to individual $[hkl]$ indices in a procedure known as indexing, which in this work has been performed using the software DICVOL.[4] Geometrically, these planes can be used to determine the size and shape of the crystallographic unit cell, while the intensities (or absences) of individual peaks give details of the atomic positions and symmetry within the structure. For this reason, diffraction is a widely used technique for materials characterisation. In single-crystal diffraction high-intensity points occur as a two-dimensional (2D) array, related to the orientation of a crystal relative to the incident beam. In a polycrystalline sample, however, the random arrangement of crystallites causes these points to merge into diffraction 'cones', effectively as a superposition of many single-crystal patterns. For this reason, powder diffraction patterns are normally presented as a 1D 'slice' taken radially across these cones, and plotted as a graph of diffracted intensity *vs.* either scattering angle (2θ) or d-spacing. Further details regarding diffraction methods can be found in the literature.[5] In this project two types of radiation have been used to give complementary information, X-ray powder diffraction (XRPD) and neutron powder diffraction (NPD), which are discussed below.

2.2.1 X-ray Powder Diffraction

Incident X-rays interact with the electrons in a material, and are thus scattered more strongly by heavier atoms. They are readily produced by bombarding a metal anode with electrons, accelerated using high voltages (usually 30–40 kV). These electrons ionise core (1s) electrons within the metal; the resulting holes are then filled by a higher energy electron, resulting in the production of an X-ray. The K_α transition (1 s$\leftarrow$2 p) is most intense, and therefore most commonly used for diffraction experiments. Due to spin-orbit coupling (SOC) within the 2p orbital, the

Table 2.1 – Chacteristic X-ray wavelengths (Å) for different sources.

Target	$K_{\alpha 1}$	$K_{\alpha 2}$	$K_{\overline{\alpha}}{}^{\dagger}$
Co	1.7890	1.7929	1.7903
Cu	1.5406	1.5444	1.5419

† $\overline{\alpha}$ is the intensity-weighted average of $\alpha 1$ and $\alpha 2$.

K_{α} transition actually occurs as a doublet of different X-ray wavelengths, $K_{\alpha 1}$ and $K_{\alpha 2}$. In this study, both copper and cobalt anodes have been used for analysis, to address the high fluorescence exhibited by iron-containing samples when using a copper source. This fluorescence is observed as a high diffraction background, not seen with a cobalt source. Wavelengths of the respective sources are given in table 2.1.

Data were collected using either a Bruker AXS D8 diffractometer operating in transmission (Debye-Scherrer) geometry, or a Bruker AXS D2 diffractometer operating in reflection (Bragg-Brentano) geometry. The D8 instrument used a germanium crystal monochromator to achieve pure $Cu_{K_{\alpha 1}}$ incident radiation, while the D2 used mixed $Co_{K_{\alpha 1,2}}$ (filtered using an iron foil) for analysis. In both cases, a solid-state 'Lynxeye' position sensitive detector (PSD) was used to measure diffracted intensity over the desired 2θ range.

Because heavier atoms (*i.e.* those with more electrons) scatter X-rays more strongly, XRPD patterns are dominated by heavier elements, *e.g.* Sb^{3+}. For this reason, information regarding lighter elements (such as oxygen) in the presence of these heavier elements can be less reliable. The diffuse nature of the electron cloud surrounding an atom also gives rise to a reduced scattering intensity with increasing scattering angle (2θ) due to partial destructive interference occuring within a given atom.[5] This gives rise to an atomic form-factor, f_j, which occurs as a function of $\frac{\sin\theta}{\lambda}$ (abbreviated as (s)) and is proportional to the atomic number, Z.

The intensity I_{hkl} of a given diffraction peak is directly related to the atomic structure *via*

the structure amplitude, $\mathbf{F}_{hkl}$:

$$I_{hkl} \propto |\mathbf{F}_{hkl}|^2.$$

The proportionality allows for other contributing factors to the intensity, such as an overall scale factor for the pattern, multiplicity of the reflection (*i.e.* $(h00)$ and $(\bar{h}00)$ will contribute to the same peak), Lorentz factor (related to the geometry of diffraction) and polarisation factors (due to the polarisation of incident and diffracted X-rays). In addition, sample absorption and *hkl*-dependent preferred orientation (due to non-isotropic crystallites) may affect the intensity of a given peak. Throughout this work, XRPD data have been corrected for absorption using the software ABSORB,[6] thus removing the need for absorption correction during data analysis. Preferred orientation has been observed for many samples; its implementation is discussed in section 2.3.

The structure amplitude itself for a given reflection is calculated from the crystallographic structure:

$$\mathbf{F}_{hkl} = \sum_j g_j t_j(s) f_j(s)(\cos\delta_j + i\sin\delta_j), \tag{2.2}$$

where

$$\delta_j = 2\pi(hx_j + ky_j + lz_j)$$

and the sum j is over the fractional positions $(x,\ y,\ z)$ of all atoms in the unit cell. g_j is the population factor for atom j (1 for a fully occupied site), $t_j(s)$ describes the reduction in scattering due to the atomic displacement, and $f_j(s)$ is the scattering factor for atom j.[7] Atomic displacement $t_j(s)$ relates to the root mean squared (RMS) displacement $\left(\overline{u}_j^2\right)$ of atom j in Å^2 from its equilibrium position, due to either thermal motion, or crystalline disorder. This displacement can occur either isotropically (displacement occurs spherically around the atomic position),

$$t_j(s) = \exp\left(-U_j \frac{\sin^2\theta}{\lambda^2}\right) \tag{2.3}$$

where $U_j = \left(\overline{u}_j^2\right)$, or anisotropically:

$$t_j(s) = \exp\left(-2\pi^2\left[u_{11}h^2a^{*2} + u_{22}k^2b^{*2} + u_{33}l^2c^{*2} + u_{12}hka^*b^* + u_{13}hla^*c^* + u_{23}klb^*c^*\right]\right), \tag{2.4}$$

where a^*, b^* and c^* are reciprocal lattice vectors. Throughout this study, isotropic displacement parameters have been used during analysis, except for occasions where atoms showed significant anisotropic displacements.

2.2.2 Neutron Powder Diffraction

Unlike X-rays, neutrons interact predominantly with the atomic nucleus (via the strong nuclear force) and so do not show a reduction in scattering with (s), due to the effectively point-sized atomic core. Additionally, the scattering strength of atoms (denoted by scattering length b_j, rather than f_j) is independent of atomic number, occurring almost randomly throughout the periodic table. For this reason, NPD can give complementary information to XRPD, particularly in samples containing both heavy and light elements, and can also distinguish between atoms with similar atomic number. In this study, average scattering lengths (which take into account isotopic abundance and nuclear spin) have been used throughout.[8]

Another important aspect of NPD is that neutrons possess spin $(\frac{1}{2})$ and thus a magnetic moment ($\gamma = -9.649 \times 10^{-27}$ JT^{-1}). This means that they can interact with the magnetic moment of unpaired electrons, giving rise to additional scattering effects. NPD is therefore the main technique for determining magnetically ordered structures, as it gives information of both the ordering and orientation of atomic spins. Because this magnetic scattering occurs from the very diffuse unpaired electrons of an atom, a magnetic form factor (f_j) must be used to describe the scattering, similar to that seen for X-rays. Because the scattering occurs only from unpaired valence electrons, however, the form factor is dependent on ionic charge, and also shows greater decrease with increasing (s), as demonstrated for Mn^{2+} in figure 2.1. This form factor appears in the definition of the magnetic scattering length (p), analogous to the nuclear scattering length

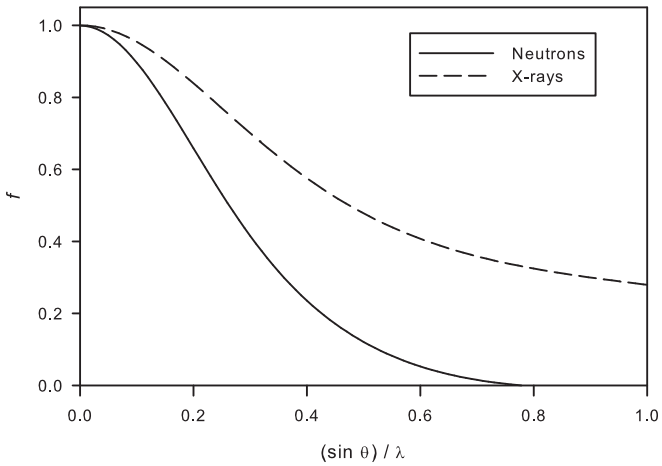

Figure 2.1 – The magnetic neutron form factor for Mn^{2+} compared with the corresponding (normalised) X-ray form factor.

b_j:[9]

$$p_j = \left(\frac{e^2\gamma}{2m_e c^2}\right) gJf_j,$$

where e and m_e are the electon charge and mass, respectively, γ is the neutron magnetic moment, c is the speed of light, g is the Landé splitting factor and J is the spin-orbit quantum number. For a spin-only magnetic moment, gJ reduces to $2S$, twice the total spin quantum number.

As mentioned above, the strength of the interaction between an incident neutron and a magnetic moment also depends on the orientation of the moment, and is related by $\mathbf{q}$, the magnetic interaction vector:

$$\mathbf{q} = \hat{\mathbf{Q}} \times \left(\hat{\mu} \times \hat{\mathbf{Q}}\right) = \hat{\mu} - \left(\hat{\mathbf{Q}} \cdot \hat{\mu}\right) \hat{\mathbf{Q}},$$

where $\hat{\mathbf{Q}}$ is the unit scattering vector and $\hat{\mu}$ is a unit vector representing the magnetic moment. The scattering vector ($\mathbf{Q}$) is defined as the vector difference between incident and scattered neutron wavevectors, and lies perpendicular to the diffraction plane $[hkl]$ when the Bragg condition is satisfied. This magnetic interaction can hence be related to the angle (α) between the magnetic moment and the scattering vector;

$$|q| = \sin\alpha.$$

In order to show scattering, a magnetic moment must therefore have a component perpendicular to **Q**, or alternatively within the diffraction plane (hkl), for diffraction to occur.

For paramagnetic materials no long range ordering of magnetic moments occurs, resulting in incoherent scattering of neutrons from the sample (which contributes to the background of a NPD pattern). In magnetically ordered materials, however, coherent scattering occurs, the resulting amplitude of which can be described by a magnetic structure amplitude, as for XRPD. For NPD, the total structure amplitude is a linear combination of nuclear and magnetic structure factors (2.5).

$$\mathbf{F}_{hkl} = \sum_j b_j g_j t_j(s)(\cos\delta_j + i\sin\delta_j) + \sum_j p_j \mathbf{q}_j g_j t_j(s)(\cos\delta_j + i\sin\delta_j) \tag{2.5}$$

2.2.3 Neutron Generation

Neutrons can be generated via a number of methods, the most common being either the fission of heavy elements (such as enriched ^{235}U) or spallation from a metal target (*e.g.* W) that is bombarded with high-energy protons. In this project, both techniques have been applied, using the high-resolution D2B diffractometer at the Institut Laue-Langevin (ILL) (fission source), the general materials diffractometer (GEM) at ISIS (spallation source), or the high resolution powder diffractometer for thermal neutrons (HRPT) beamline at the Paul Scherrer Institute (PSI) (spallation). In each case, the neutrons generated are moderated after production, to produce neutrons of the appropriate energy range for diffraction experiments.

D2B provides a constant wavelength (CW) neutron source, using the (335) lattice planes of a germanium monochromator crystal to achieve a wavelength of 1.594 Å.[10] This gives diffraction patterns similar to those seen from XRPD. Samples were contained in 8 mm vanadium cans, and diffracted intensity measured over the range 5°–165° using a movable bank of one-hundred and twenty eight, 300 mm long ^{3}He detectors. These PSD detectors can be operated in either high-intensity (HI) or high-resolution (HR) modes, the latter achieved by sampling data from the central third of each detector tube. HR mode produces sharper diffraction peaks with less

peak-asymmetry, but at the expense of reduced peak intensity. In most cases in this work, HR data have been used for analysis. Liquid-He temperatures were achieved using a He cryostat.

GEM provides a time of flight (TOF) neutron beam, producing a range of neutron wavelengths in pulses at 50 Hz. In this method, diffracted intensity is measured relative to the time-of-flight of diffracted neutrons $(\propto 1/\lambda)$ rather than diffraction angle (2θ). The instrument uses 6 'banks' of fixed detectors (7270 elements in total) to measure an effective scattering angle range of 1.1° to 169.3°.[11] This corresponds to a measured d-spacing range of 0.3 Å (for bank 6) to 30 Å (bank 1). Samples were contained in V cans of varying diameter (depending on sample volume), while cryogenic temperatures were achieved using a He cryostat.

PSI is a spallation neutron source (from a Pb target) yet is configured to provide CW neutrons. This unique setup provides a highly intense source of monochromatic neutrons. Like D2B, the HRPT instrument uses a Ge monochromator to select the desired monochromatic wavelength; for this work, $\lambda = 1.494$ Å or 1.886 Å were both utilised. Samples were contained in 8 mm V cans, while diffracted intensity was measured by a 1600-wire PSD, capable of measuring $0° < 2\theta < 160°$. Low temperature measurements were achieved using a He cryostat.

2.3 Rietveld Refinement

The Rietveld method is a full-pattern refinement technique, used to adjust a model structure based upon observed powder diffraction data.[12] In this study it has been implemented using the General Structural Analysis System (GSAS) software, with the EXPGUI graphical interface.[13,14] The method uses a least-squares approach to reduce the difference between observed and calculated patterns, by minimising the residual, S_y;

$$S_y = \sum_i w_i \left(y_{i,obs} - y_{i,calc}\right)^2, \tag{2.6}$$

where w_i is a weighting factor $(= 1/y_{i,obs})$ for each point i, and $y_{i,obs}$ and $y_{i,calc}$ are the observed and calculated intensities of point i, respectively. At each point i, the intensity is calculated from

$$y_{i,calc} = s \sum_{hkl} p_{hkl} L_\theta P_\theta A_\theta T_{hkl} |\mathbf{F}_{hkl}|^2 \phi (2\theta_i - 2\theta_{hkl}) + y_{i,bg}, \tag{2.7}$$

where s is an overall scale factor for the pattern, and the sum is over all peaks (hkl) contributing to the point. The peak multiplicity p_{hkl}, Lorentz factor L_θ, polarisation factor P_θ and absorption factor A_θ have been discussed in section 2.2.1. Preferred orientation (T_{hkl}) occurs due to non-random packing of crystallites due to sample morphology, *i.e.* plate-like or needle-like crystals. The result is an over- (or under-) expression of certain peaks, depending on (hkl). GSAS employs two possible methods of modelling preferred orientation; the March-Dollase (MD) method or a spherical-harmonic function.[15,16] The MD method adjusts peak intensity according to a given set of reflections, specified through knowledge of the crystallite shape. For instance, a tetragonal unit cell can show over- or under-expression of $(00l)$ peaks. The spherical-harmonic model is more effective for complex orientation effects, for which the MD model is less suitable; it involves a variable number of harmonic terms to account for sample orientation. In this work, both methods have been used, depending on the significance of the preferred orientation observed.

$\phi (2\theta_i - 2\theta_{hkl})$ is a peak broadening function to accommodate for broadening due to both instrument and sample effects. Throughout this work, this has been adopted as a pseudo-Voigt function (convolution of Gaussian and Lorentzian functions) using GSAS profile functions type 2 or 4. The exception to this is TOF data, where a convolution of an Ikeda-Carpenter function with a pseudo-Voigt has been used (GSAS TOF profile type 2). The background contribution to a point is accounted for as $y_{i,bg}$. The background function itself is modelled across the entire pattern as a polynomial function; in this work, either a 'shifted Chebyschev' function or a cosine Fourier series (with varying numbers of terms) have been used within GSAS (types 1 and 2, respectively). The number of terms used has been varied to provide a good fit to the observed background, usually around 15 terms.

Associated with the least-squares refinement are a number of statistical parameters, related to the quality of fit. In (2.10), N is the number of observed data points, while P is the number of parameters and C the number of constraints. In addition to a visual inspection of the difference $y_{i,obs} - y_{i,calc}$, the value of χ^2 arguably best reflects the goodness-of-fit, with $\chi^2 = 1$ being a statistically perfect fit.

$$R_p = \frac{\sum_i |y_{i,obs} - y_{i,calc}|}{\sum_i y_{i,calc}} \tag{2.8}$$

$$R_{wp} = \left(\frac{\sum_i [y_{i,obs} - y_{i,calc}]^2}{\sum_i w_i [y_{i,obs}]^2} \right)^{\frac{1}{2}} \tag{2.9}$$

$$R_{exp} = \left(\frac{N - P + C}{\sum_i w_i y_{i,obs}^2} \right)^{\frac{1}{2}} \tag{2.10}$$

$$\chi^2 = \left(\frac{R_{wp}}{R_{exp}} \right)^2 \tag{2.11}$$

The Rietveld method allows estimated standard deviations (esds) to be readily calculated for refined parameters. Throughout this work, such errors are reported to the *one* esd level. Where plots of variables are shown without associated error bars, the estimated deviation is less than the symbol size used.

2.3.1 Magnetic Refinement

A number of methods exist for refining magnetic structures from NPD data. Within GSAS, a phase can be set to provide both magnetic and nuclear reflections, or magnetic peaks only. Throughout this work, magnetic models have been inserted as a separate (magnetic-only) phase, of $P1$ or $P\bar{1}$ symmetry, constrained to match the nuclear phase unit cell size/atomic positions. This method allows for maximum flexibility of the magnetic structure (in particular the alignment of magnetic moments) and avoids restrictions due to symmetry. This method must be applied with care, however, to ensure a sensible magnetic structure. To aid this, representational analysis has been used to suggest potential structures based on symmetry arguments from the (paramagnetic) parent phase, as implemented using the SARAh software suite.[17] While this method would suggest that the true nuclear symmetry for many of the compounds studied is

lower than that of the paramagnetic phase, this change in nuclear symmetry has not been observed in diffraction data, presumably due to insufficient resolution.

2.4 Magnetic Susceptibility

Magnetic susceptibility measurements provide details of magnetic structure change under applied field and/or temperature variations, and are complementary to the data collected from NPD. Measurements in this work were performed using a Quantum Design materials properties measurement system (MPMS)-XL, which uses a superconducting quantum interference device (SQUID) to detect small changes in magnetic field around the sample, outputting a proportional voltage. The instrument can be operated in both direct current (DC) and alternating current (AC) modes, which give complementary information. DC susceptibility uses a static magnetic field and an oscillating sample to measure the sample moment, while AC susceptibility uses an oscillating magnetic field and static sample.

For DC susceptibility measurements, the sample ($\simeq$ 50 mg powder) was contained in a gelatin capsule, surrounded by polytetrafluoroethylene (PTFE) tape to suppress sample movement. Samples were centred within the SQUID coils using an applied field (normally 500 Oe) at room temperature before commencing measurements. Most experiments involved measuring susceptibility on heating, first under zero-field cooled (ZFC) conditions, and then under field-cooled (FC) conditions (cooling without and with an applied field H, respectively). Measurements were normally performed using 'sweep' conditions, whereby temperature was increased at a constant rate (5 K min^{-1}) and susceptibility was measured at set intervals, typically 5 K steps. On occasion, it was necessary to use 'settle' conditions, where the temperature is stabilised at given temperature intervals before measuring susceptibility. This provides more accurate temperature information, *e.g.* for transition temperature determination. In all FC measurements, the applied field on cooling was the same magnitude as the measuring field (100 or 500 Oe). Where applicable, hysteresis measurements (applied fields of $-48000 \leq H \leq 48000$ Oe) were performed following ZFC conditions.

2.5 Impedance Spectroscopy

Impedance spectroscopy is a technique to measure electronic and ionic conductivity within a sample. The method involves applying an AC voltage across the sample under test, and measuring the resulting current (due to either the motion of ions or electrons). This current follows the applied sinusoidal voltage but potentially with a phase shift, ϕ, due to capacitive or inductive effects. The impedance of the sample (Z) is defined as the ratio of applied voltage and resulting current, analogous to Ohm's law;

$$Z = \frac{E_t}{I_t} = \frac{E_0 \sin(\omega t)}{I_0 \sin(\omega t + \phi)} = Z_0 \frac{\sin \omega t}{\sin \omega t + \phi}, \tag{2.12}$$

where E_t and I_t are the voltage and current at time t, respectively, and E_0, I_0 and Z_0 are time-independent voltage, current and impedance. The radial frequency (ω) is related to the AC voltage frequency, f (in Hz) by $\omega = 2\pi f$.

In addition to representing impedance using Z and ϕ, it can also be expressed as a complex number,

$$Z(\omega) = Z_0(\cos\phi + i \sin\phi)$$

where $i = \sqrt{-1}$. For this reason, impedance data are most commonly shown in a Nyquist plot of imaginary impedance, $Z''\,(= Z_0 i \sin\phi)$ *vs.* real, $Z'\,(= Z_0 \cos\phi)$ (or alternatively, capacitive *vs.* resistive components). Note that by convention, this plot has a negative Z'' axis. By varying the applied frequency, f, a number of points can be obtained.

2.5.1 Data Analysis

The sample response with frequency can be described by an equivalent circuit of electrical components, the values of which can be fitted to the observed data. For an ideal resistor the impedance is constant with frequency and shows no phase-shift, hence a single point is observed at $(R, 0)$, where R is the resistance value. For a simple capacitor, the current lags behind the applied voltage by 90° $(\phi = -90)$, and shows points at $(0, Z'')$. The value of Z'' is frequency-

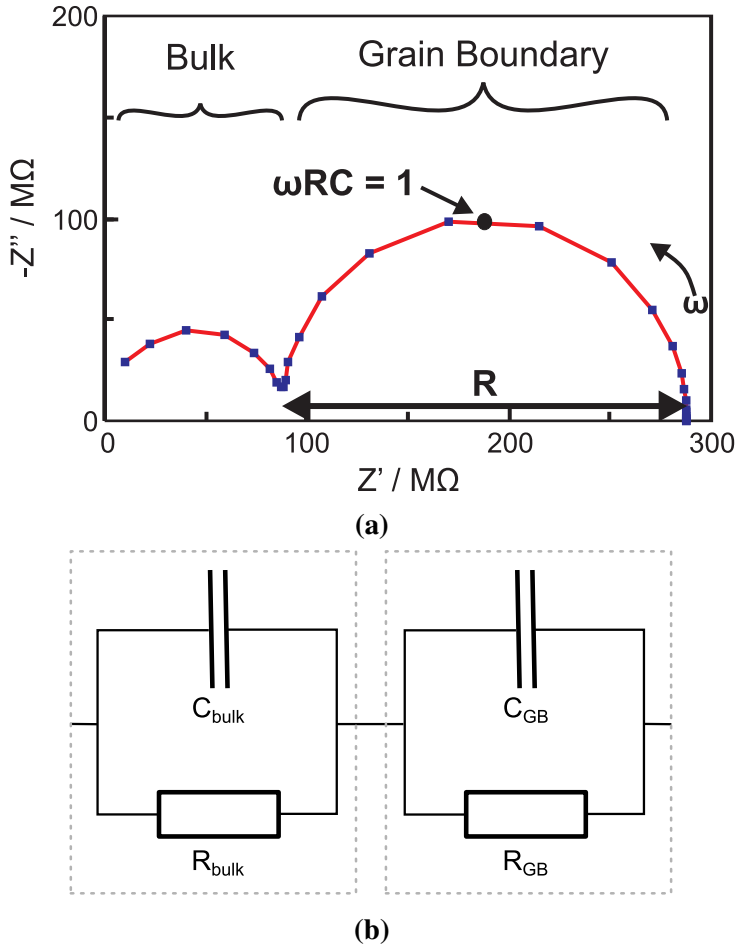

Figure 2.2 – Example impedance behaviour for a parallel RC circuit: (a) Nyquist plot and (b) corresponding circuit diagram.

dependent,

$$Z'' = \frac{1}{i\omega C},$$

where C is the capacitance. The electrical response of most compounds exhibits a semi-circular pattern in a Nyquist plot which corresponds to a parallel capacitor/resistor circuit. In real materials, however, different regions of the sample generally exhibit different response, resulting in multiple semi-circles (figure 2.2). For instance, bulk regions generally show capacitance of the order 10^{-12} F, while grain-boundary (GB) response is more usually 10^{-9} F. Often these semi-circles will overlap, making it difficult to distinguish between effects.

Using the bulk resistance of a sample it is possible to convert this value to a conductivity (σ), using knowledge of the sample shape and mass. By measuring impedance at a number of

temperatures, it is therefore possible to obtain an estimate of the thermal activation energy (E_a) for conductivity, using an Arrhenius-type relationship:

$$\ln \sigma = \frac{-E_a}{RT} + \ln \sigma_0$$

or

$$\log \sigma = \frac{-E_a}{2.303RT} + \log \sigma_0 \tag{2.13}$$

where R is the gas constant. For a semiconductor, this is equal to half the thermal bandgap, E_g.

In this work, AC impedance measurements have been performed using a Solartron SI 1260 impedance/gain-phase analyser within the frequency range 1 Hz–13 MHz. Portions of samples were pressed into pellets using an 8 mm die and an applied force of 1–3 tons. Pellets were sintered at similar temperatures to initial synthesis, having been sealed in evacuated silica ampoules where necessary to prevent oxidation. The circular faces of the pellet were coated with Ag-electrodag (Agar Scientific) and dried at 100 °C for at least 2 hr. Measurements were performed using a spring-loaded silver-wire contact system within a tube furnace, to enable measurements at a range of temperatures within the thermally stable region of the compound.

2.6 Mössbauer Spectroscopy

Mössbauer Spectroscopy is a technique involving the absorption of γ-rays by a sample, and depends on nuclear transitions. Knowledge of the energies of these transitions can give information about the local electronic structure around a nucleus including oxidation state, coordination number, bonding character and magnetic environment. The technique is only practical or possible for a limited number of elements; in this case ^{57}Fe has been studied. The spectra presented here were collected and interpreted by Professor Frank J. Berry.

The main principle for a Mössbauer experiment is that a γ-ray produced from the decay of an excited nucleus (such as $^{57}Fe^*$, produced by decay of ^{57}Co) will correspond in energy to a nuclear transition within an equivalent (Fe) nucleus only if the element has the same atomic environment. Differences in environment between source and sample give rise to different

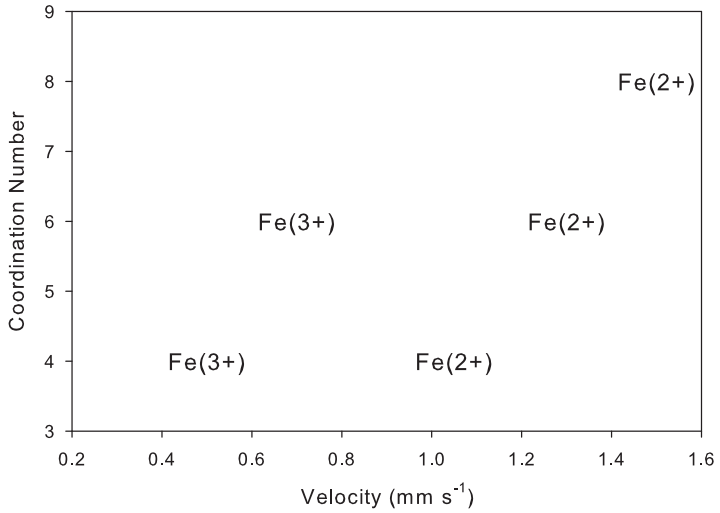

Figure 2.3 – Chemical isomer shifts in iron-containing compounds (modified from [5]).

transition energies, characterised by a number of parameters, described below. Absorption at these energies is achieved by varying the wavelength of the incident γ-ray through the Doppler effect, by oscillating the radiation source. The resulting spectra show absorption *vs.* source velocity, and occur as a pattern of absorption peaks.

The main variation of a peak along the velocity scale relates to the chemical isomer shift, δ, and occurs due to the interaction between nuclear and electronic charges. For this reason, it can be related to both oxidation state and coordination number of an element (see figure 2.3).

Peak splitting occurs due to two effects: quadrupole splitting and magnetic (hyperfine) splitting. Quadrupole splitting occurs for nuclei with $I > \frac{1}{2}$ due to the interaction between the non-spherical nuclear charge and any surrounding electric fields (such as those generated by surrounding ligands). For Fe, this gives rise to a doublet (centred around δ) with a splitting magnitude (Δ) related to the local symmetry and bonding interactions. Magnetic (hyperfine) splitting occurs for nuclei with $I > 0$, whereby a local magnetic field causes additional splitting of nuclear states. For Fe, this gives rise to six separate absorption peaks of varying intensities, again centred around δ.

Data in this work were collected using a ^{57}Co γ-source, operated in constant acceleration mode. Velocities are reported relative to Fe at room temperature.

2.7 Thermal Analysis

A combination of thermal gravimetry (TG) and differential thermal analysis (DTA) have been used in this work to study sample behaviour on heating under flowing gas, specifically phase and/or composition changes. TG involves measuring the mass change during a heating/cooling cycle, giving information about decomposition of the sample or reaction with the gas stream. Both N_2 and O_2 gas environments have been used in this work, to give complementary information. DTA is the measure of temperature difference between the sample and an inert reference material (in this case Al_2O_3) both heated in the same environment. A difference in temperature (due to different heat content) between sample and reference occurs at 'thermal events', such as melting or phase transitions within the structure. Further information can be obtained from the sign of the temperature difference, indicating either an endothermic $(T_{\text{sample}} < T_{\text{ref}})$ or exothermic $(T_{\text{sample}} > T_{\text{ref}})$ transition.

A software-controlled Netzsch STA449 F1 'Jupiter' thermogravimetric analyser was used for all measurements reported, using powder samples ($\simeq$ 50 mg) and a heating/cooling rate of 10 K min^{-1}. A correction for buoyancy was made using an empty sample holder and appropriate gas stream.

References

[1] D. Lide (Ed.), *Handbook of Chemistry and Physics Special Student Edition 73rd Edition*, CRC Press, 1993.

[2] S. E. Golunski, T. G. Nevell and M. I. Pope, *Thermochimica Acta*, 1981, **51**, 153–168.

[3] R. G. Orman and D. Holland, *Journal of Solid State Chemistry*, 2007, **180**, 2587–2596.

[4] A. Boultif and D. Louër, *Journal of Applied Crystallography*, 2004, **37**, 724–731.

[5] A. R. West, *Basic Solid State Chemistry*, Wiley, 2008.

[6] C. Greaves, *ABSORB software*, University of Birmingham.

[7] V. Pecharsky and P. Zavalij, *Fundamentals of Powder Diffraction and Structural Characterization of Materials, Second Edition*, Springer, 2009.

[8] V. F. Sears, *Neutron News*, 1992, **3**, 26–37.

[9] E. H. Kisi and C. J. Howard, *Applications of Neutron Powder Diffraction (Oxford Series on Neutron Scattering in Condensed Matter)*, Oxford University Press, USA, 2008.

[10] *The Yellow Book (Guide to Neutron Research Facilities)*, Institut Laue-Langevin, 2008.

[11] *GEM-General Materials Diffraction Key Facts*, Internet Publication, 2013, http://www.isis.stfc.ac.uk/instruments/gem/gem2467.html.

[12] H. M. Rietveld, *Journal of Applied Crystallography*, 1969, **2**, 65–71.

[13] A. C. Larson and R. B. von Dreele, *Los Alamos National Laboratory Report*, 1994, **LAUR 86-748**, 1.

[14] B. H. Toby, *Journal of Applied Crystallography*, 2001, **34**, 210–213.

[15] W. A. Dollase, *Journal of Applied Crystallography*, 1986, **19**, 267–272.

[16] R. B. Von Dreele, *Journal of Applied Crystallography*, 1997, **30**, 517–525.

[17] A. S. Wills, *Physica B: Condensed Matter*, 2000, **276–278**, 680–681.

CHAPTER 3
COMPUTATIONAL METHODS

A number of methods exist for modelling electronic and nuclear structures within crystalline solids, each with different benefits. In this study the main focus of calculations has been to determine the electronic structure of materials, particularly with regards to magnetic behaviour. As such, methods based around fundamental quantum mechanics (particularly the Schrödinger Equation, (3.1)) are required to produce accurate and reliable results. These methods are termed *ab initio*. A number of techniques exist to solve these problems, but here density functional theory (DFT) has been used, as it provides a good balance between accuracy and computational time (expense). Other computational methods have also been used to supplement the DFT results, and will be discussed below.

3.1 Density Functional Theory

3.1.1 Fundamental Quantum Mechanics

The starting point for all *ab initio* methods is the many-body wavefunction (Ψ) as determined from the Schrödinger equation, given here in its time-independent form;[1]

$$\hat{H}\Psi = E\Psi, \tag{3.1}$$

where $\hat{H}$ is the Hamiltonian for a system of interacting electrons (e) and nuclei (N), and E is the energy of the system. The Hamiltonian contains contributions from the kinetic $(\hat{T})$ and

potential $(\hat{V})$ energy terms for electrons, nuclei and the interactions between them,

$$\hat{H} = \hat{T}_N + \hat{T}_e + \hat{V}_{N-N} + \hat{V}_{N-e} + \hat{V}_{e-e}.$$

Knowledge of Ψ would theoretically enable calculation of any property of a system, but (3.1) is not directly soluble for more than two particles (*i.e.* a H atom) due to the complicated many-body terms $\hat{V}_{N-N}$, $\hat{V}_{N-e}$ and $\hat{V}_{e-e}$. One simplification is to introduce the Born-Oppenheimer approximation (assuming that the substantially heavier nuclei are static in relation to the electrons)[2] which removes the need to calculate $\hat{T}_N$ and $\hat{V}_{N-N}$, although this does not remove the complicated electron-electron interaction term, $\hat{V}_{e-e}$. Using atomic units $\hbar$, m_e, e, $4\pi/\varepsilon_0 = 1$ leads to the fundamental electronic Hamiltonian (excluding external electronic and magnetic fields):

$$\hat{H} = \hat{T}_e + \hat{V}_{N-e} + \hat{V}_{e-e} + E_N \tag{3.2}$$

where E_N represents the (constant) nuclear-nuclear interaction energy, as well as any other (non-electronic) terms that contribute to the total energy. The electron kinetic energy operator $\hat{T}_e$ is

$$\hat{T}_e = \sum_i -\frac{1}{2}\nabla_i^2,$$

$\hat{V}_{N-e}$ is the nuclear potential acting on the electrons

$$\hat{V}_{N-e} = \sum_{i,I} \frac{V_I}{|\mathbf{r}_i - \mathbf{R}_I|},$$

and $\hat{V}_{e-e}$ is the electron-electron interaction,

$$\hat{V}_{e-e} = \frac{1}{2}\sum_{i\neq j} \frac{1}{|\mathbf{r}_i - \mathbf{r}_j|}.$$

Sums are over electrons (denoted by lowercase subscripts) and nuclei (uppercase), while $\mathbf{r}$ and $\mathbf{R}$ denote electronic and nuclear positions, respectively.

The groundstate wavefunction Ψ_0 will be the lowest energy state, and can (in principle) be

determined by minimising E in (3.1) subject to the constraints on the wavefunction (such as being antisymmetric for an electron). This leads to the 'variational principle', whereby a trial wavefunction will give an energy higher or equal to the groundstate energy. This is used in most electronic structure calculations as the basis of an iterative procedure towards finding the electronic groundstate.

3.1.2 Density Functional Theory Foundations

Although methods exist to solve (3.1) through various approximations, most fail for problems with large numbers of atoms due to the number of parameters involved: each electron must be described by four degrees of freedom (x, y, z and spin), leading to more parameters (and corresponding interactions) than can be handled by even the most powerful computers for real chemical systems. By re-expressing the problem in terms of the electron density (which can be evaluated as a three-dimensional (3D) function) the number of parameters is greatly reduced, enabling calculation for larger systems. The foundations of DFT are two surprisingly simple theorems, first proved by Hohenberg and Kohn:[3]

Theorem 1. *For any system of interacting electrons in an external (nuclear) potential* $V_{\text{ext}}(\mathbf{r})$*, the potential* $V_{\text{ext}}(\mathbf{r})$ *is determined uniquely, except for a constant, by the ground state particle density* $n_0(\mathbf{r})$*.*

Theorem 2. *A universal functional for the energy* $E[n]$ *in terms of the density* $n(\mathbf{r})$ *can be defined, valid for any external potential* $V_{\text{ext}}(\mathbf{r})$*. For any particular* $V_{\text{ext}}(\mathbf{r})$*, the exact ground state energy of the system is the global minimum value of this functional.*

It is now helpful to re-express the previous Hamiltonian (3.2) as

$$\hat{H} = \sum_i -\frac{1}{2}\nabla_i^2 + \sum_i V_{\text{ext}}(\mathbf{r}_i) + \frac{1}{2}\sum_{i\neq j}\frac{1}{|\mathbf{r}_i - \mathbf{r}_j|}, \tag{3.3}$$

where $V_{\text{ext}}(\mathbf{r})$ now includes the nuclei-electron and nuclear-nuclear potential energy terms. From theorem 1 it follows that knowledge of the electron density $n(\mathbf{r})$ gives rise to V_{ext}, and

would therefore allow determination of Ψ (from solution of (3.1)). Theorem 2 is similar to the 'variational principle', and leads to the conclusion that if the exact density functional ($F_{\mathrm{HK}}[n]$) were known, minimising the energy $E[n_0]$ in terms of variations in the electron density $n(\mathbf{r})$ would lead to the groundstate energy and density. Mathematically, the functional can be expressed as

$$\begin{aligned} E[n] &= T_e[n] + E_{e-e}[n] + E_{N-e}[n] \\ &\equiv F_{\mathrm{HK}}[n] + E_{N-e}[n]. \end{aligned} \tag{3.4}$$

The density functional ($F_{\mathrm{HK}}[n]$) does not depend on the nuclear potential, and therefore only relates to the electron density of a system.

While elegant, the previous theorems provide no solution to the many-body problem, as the Hamiltonian (3.3) and density functional ($F_{\mathrm{HK}}[n]$) still require solution of the problematic electron-electron interactions. The breakthrough[4] for practical applications of DFT was to assume that the groundstate density of the original (interacting) system of electrons could be equal to that of a fictitious, non-interacting system of single electron wavefunctions. The Hamiltonian for this non-interacting system is greatly simplified compared to (3.3), allowing the exact solution of the groundstate density and (independent) wavefunctions. The complicated many-body terms relating to electron correlations (*i.e.* relationships between electron motions) and electron exchange (effectively the Pauli exclusion principle) are incorporated into the exchange-correlation functional (E_{XC}), and separated out from the (easily soluble) independent terms;

$$E = T_s[n] + E_{N-e}[n] + E_{\mathrm{Hartree}}[n] + E_{\mathrm{XC}}. \tag{3.5}$$

$T_s[n]$ represents the kinetic energy of the non-interacting electron system, while E_{Hartree} is the energy of the coloumbic interaction of the electron with the mean-field produced by all other electrons.

If E_{XC} were known exactly, the groundstate energy and density for the original interacting

system could be found by solving (3.5) for the non-interacting system, due to the identical densities. Unfortunately E_{XC} can only be approximated, but in practice quite simple approximations accurately reproduce experimental results for many systems.

3.1.3 Exchange-Correlation Functionals

As mentioned in section 3.1.2, while DFT does *in principle* provide an exact solution to (3.1), in reality E_{XC} is unknown, and must be approximated. The simplest approximation is the local density approximation (LDA), where the electron exchange and correlation at a given point are taken to be equal to that of a homogeneous electron gas of identical density. The form of this functional is known and, because of the dependence only on $n(\mathrm{r})$, can be calculated with relative ease for a given density. Although surprisingly simple, the LDA can give results very close to experimental values for many materials, due to an effective cancellation of errors from the exchange and correlation terms.[5] It is particularly effective for compounds with smoothly-varying electron density, such as many metals. Results for less electronically-homogeneous materials can be less accurate, often showing decreased bond lengths within a material, and therefore reduced lattice parameters in solids.[6] In addition, relative energies of different phases are often incorrect, particularly for magnetic materials. In this study, preliminary calculations found that for $FeSb_2O_4$, use of the LDA caused lattice parameters to be significantly underestimated by *ca.* 7 %, which was deemed unacceptable.

An improvement on the LDA is the generalised gradient approximation (GGA) whereby exchange and correlation at a given point are dependent not only on the electron density at that point, but also on the density gradient. This is more time-consuming to compute, but is much better suited to materials with rapidly varying charge density.[5] Generally, GGA approximations give more accurate results than the LDA, particularly in terms of relative energies of different phases. Unlike the LDA, however, the GGA can be formulated in a number of different mathematical forms. In this work, the formulation of Perdew, Burke and Ernzerhof (PBE)[7] has been used throughout, as a balance of accuracy and computational expense. One notable feature of the GGA is that it often results in under-binding of atoms in solids, resulting in a slight increase

in lattice parameters.[5]

Beyond the GGA approach, it is also possible to include higher-order terms in the expansion of the density, most often the kinetic energy density: these methods are termed 'meta-GGA'. While these methods generally produce more accurate results than GGAs, the improvement in accuracy often requires a significant increase in computational expense.

The methods described above form the first three 'rungs' on the 'Jacob's Ladder' of DFT, initially introduced by Perdew and Schmidt.[8] They are all local (or semi-local) in nature, referring to (an expansion of) the density at a given point, $n(\mathrm{r})$. More accurate methods involve the inclusion of non-local properties, present in exact definitions of exchange and correlation. Most notable amongst these approaches are hybrid functionals. These methods combine a (variable) proportion of exact exchange with either GGA or LDA functionals; a number of different implementations exist, depending on the proportion of exact exchange and the type of explicit density functional. These functionals are generally parameterised by comparison with experimental results or more expensive calculations. These methods can provide accurate results for materials showing complex electronic behaviour (such as strong electron correlations) for which other functionals fail to reproduce experimental results. Correspondingly, however, these methods are computationally more expensive. In this work, due to a limited range of existing experimental results, parameterised functionals have not been investigated.

Orbital-Dependent Functionals

Materials exhibiting strongly interacting or highly localised electrons (often found in transition metal oxides) often pose a challenge for standard DFT functionals (such as LDA and GGA); the high correlations in these materials are not well modelled. A well known example of this is the underestimation of bandgaps by DFT. For example, in simple oxides such as CoO, DFT often predicts a metallic groundstate, but it is in fact semiconducting with a band gap of 2.4 eV.[1,9,10] One solution to treat these highly correlated systems is to include a Hubbard-like 'U' term for the significantly correlated electrons (*i.e.* *d*-orbitals) which effectively shifts the energies of these (*d*-) bands relative to the untreated orbitals.[1,11] The value of U is typically fitted to

experimental results, and takes values of the order of 5 eV. This 'DFT+U' approach has been investigated for certain cases during this project, but only where standard DFT functionals significantly fail to reproduce experimental properties (such as predicting a metallic groundstate for a semi-conductor). This is due to the lack of experimental data for fitting purposes. It is possible to determine U purely theoretically from a linear response approach;[12] this method has been attempted for $FeSb_2O_4$ and $CuAs_2O_4$ during this work, but proved unsuccessful due to the significant computational resources required.

3.2 Practical DFT Methods

Section 3.1 gave an introduction to the foundations of DFT, but gave no details about the practical solution of real problems. A number of different approaches (basis sets) can be used to solve calculations, each with their own advantages and capabilities. If applied correctly, the different methods should produce the same results, but require different computational effort. The most significant difference between methods is how the wavefunctions, density and potential are defined; they can be described either in terms of (periodic) planewaves, or as combinations of localised (atomic-like) orbital functions. Throughout this project planewave methods have been used, as they are particularly suited to treating periodic solids.

3.2.1 Planewaves and Brillouin Zone Sampling

In a solid, the regular arrangement of atoms means that the potential felt by electrons is periodic, and therefore so is the electron density. Because the wavefunction is related to the density ($n(\mathbf{r}) = |\Psi(\mathbf{r})|^2$) the magnitude of the wavefunction must also be periodic, consistent with the lattice vectors $\mathbf{R}_L$. Ψ is a complex quantity, however, and therefore can possess an arbitrary phase; the total wave vector is denoted $\mathbf{k}$. The combination of these periodic and aperiodic components is shown graphically in figure 3.1, and can be described by a Bloch function

$$\Psi_{\mathbf{k}}(\mathbf{r}+\mathbf{R}_L) = e^{i\mathbf{k}\cdot\mathbf{r}}\Psi_{\mathbf{k}}(\mathbf{r}), \tag{3.6}$$

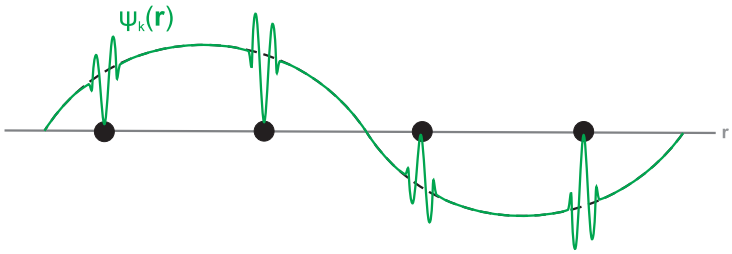

Figure 3.1 – One-dimensional schematic of a Bloch wavefunction (green) where the wavefunction is modulated by **k** (black dashed line).

that is, the wavefunction at position **r** within an 'adjacent' unit cell $(+\mathbf{R}_L)$ is the same as the wavefunction at position **r** within the original unit cell, multiplied by a phase factor $e^{i\mathbf{k}\cdot\mathbf{r}}$.

The periodic component of Ψ can be expressed as a sum of planewaves of various frequencies, each with a separate complex coefficient $c_{\mathbf{G}}$; higher frequency components model rapid oscillations of the wavefunction, such as near to nuclei (figure 3.1). Because of the periodicity with the lattice, these planewaves are described in terms of multiples of the reciprocal lattice vectors, **G**:

$$\Psi_{\mathbf{k}}(\mathbf{r}) = e^{i\mathbf{k}\cdot\mathbf{r}} \sum_{\mathbf{G}} c_{\mathbf{G}}(\mathbf{k}) e^{i\mathbf{G}\cdot\mathbf{r}}.$$

In the 'ideal' calculation, the sum over **G** should be to infinite values, to model even the slightest oscillation in the Kohn-Sham wavefunctions. In reality, however, $c_{\mathbf{G}} \to 0$ for large values of **G**, therefore the sum may be truncated at an appropriate value, denoted $\mathrm{E}_{\mathrm{cut}}$. Because of the variational nature of the computations, increasing the value of $\mathrm{E}_{\mathrm{cut}}$ can only reduce the computed groundstate energy, giving a more converged calculation. This reduction behaves roughly exponentially, however, so an appropriate value of $\mathrm{E}_{\mathrm{cut}}$ can be chosen by comparing the change in energy on increasing the number of planewaves. Energy differences between properties of interest (such as the different magnetic structures) converge much quicker than total energies, and are therefore used to set convergence criteria (to reduce computational expense). Throughout this work, a convergence accuracy of $\leq 1\%$ of the energy differences investigated has been used.

During calculations, the electron density is calculated as an integral over the occupied electronic bands within the first Brillouin zone (BZ). In reality, this integral can be approximated as

a finite summation over **k**, the points within this zone. Although **k** can take any value, the situation can be greatly simplified by use of the unit cell symmetry, by finding equivalent **k** values. This 'sampling' of the BZ can be performed in a number of ways, but in this study has been performed using a regularly spaced grid of points, as devised by Monkhorst and Pack.[13] The spacing of the grid used during calculations has been determined by comparison of groundstate energies with that of a densely-sampled calculation, to ensure convergence. Note that in some situations (such as band structure calculations) it is desirable to calculate values at specific, high-symmetry k-points, in order to obtain properties of waves along certain crystallographic directions.

3.2.2 Pseudopotentials

In order to model a complex crystal structure using a planewave basis set, it would be necessary to sum up to incredibly high values of **G** in order to model the rapid oscillations of the wavefunction close to the nucleus (figure 3.1). This is impossible in practice, and so it is necessary to introduce the idea of a pseudopotential (PSP) in order to reduce the number of planewaves required. In essence, a PSP replaces the inert 'core' potential from both the nucleus and the strongly bound core electrons with a single 'effective' potential. Outside a core radius (r_{cut}) the potential felt by the valence electrons is identical to the all-electron case, but within the core region the valence wavefunction is much smoother than for a calculation including core electrons (figure 3.2). These smoother wavefunctions require less planewaves to calculate, while still modelling the problem correctly.

A number of different approaches exist for generating and describing pseudopotentials, see for instance [1] for details. Ultrasoft pseudopotentials have been used throughout this work, due to their combination of transferability, 'softness' (the number of planewaves required to describe them) and accuracy. Most work involving PSPs and planewaves has been performed using the CASTEP code,[15] using versions 5.5–6.1. The PSP definitions used have been the 'on-the-fly' pseudopotentials generated within the CASTEP code[16] at run-time using the default definitions unless otherwise specified.

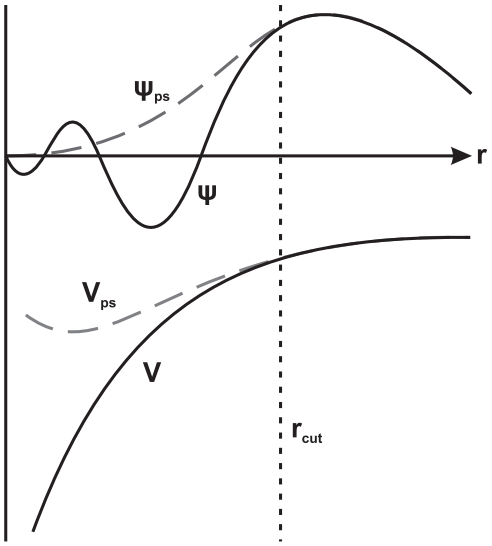

Figure 3.2 – Schematic showing the all-electron (solid line) wavefunction and core potential, and the replacement pseudopotential and corresponding wavefunction (dashed lines). Modified from [14].

3.3 Structural Analysis

Often there is a need to compare atomic structures in such a way that the comparison is independent of things such as cation size and unit cell symmetry. A number of methods exist for this purpose, some of which are described below.

3.3.1 Bond Angle Variance

Bond angle variance (σ^2) is a simple measure of the angular distortion around a central cation in a polyhedral coordination environment, and can be defined[17] as;

$$\sigma^2 = \frac{\sum_{i=1}^{m}(\phi_i - \phi_0)^2}{m-1} \tag{3.7}$$

where ϕ_i is the ith bond angle, ϕ_0 is the ideal bond angle (*i.e.* 90 ° for an octahedron) and m is the number of faces of the polyhedron $\times\frac{3}{2}$ (*i.e.* the number of bond angles). A smaller value for σ^2 indicates less angular distortion.

3.3.2 Distortion Index

The distortion index D is a measure of the deviation from the average bond length for a polyhedron, defined as[18]

$$D = \frac{1}{n}\sum_{i=1}^{n}\frac{|l_i - l_{av}|}{l_{av}}, \tag{3.8}$$

where l_i is the ith bond length and l_{av} is the average bond length.

3.3.3 Quadratic Elongation

The quadratic elongation $\langle\lambda\rangle$ gives a measure of the elongation of a polyhedron, independent of its volume. It is defined[17] as

$$\langle\lambda\rangle = \frac{1}{n}\sum_{i=1}^{n}\left(\frac{l_i}{l_0}\right)^2, \tag{3.9}$$

where n is the number of bonds, l_i is the length of bond i and l_0 is the bond length in a regular polyhedron of the same volume. A value of 1 represents a completely regular polyhedron, while deviations indicate distortion.

3.3.4 Bond Valence Sum

The bond valence sum (BVS) method is a means of estimating the effective valence of an atom within a crystal structure, based around the observed bond lengths.[19] The valence V of a given atom i is defined as the sum of individual valences to neighbouring atoms, i:

$$V_i = \sum_j \exp\left(\frac{r_0 - r_{ij}}{B}\right), \tag{3.10}$$

where r_0 are (tabulated) characteristic bond lengths between atoms i and j (table 3.1), r_{ij} are the experimentally determined bond lengths and B is an empirical constant, 0.37 Å for most compounds.

Table 3.1 – Tabulated r_0 values for species used throughout this work.

Cation, i	Anion, j	
	O^{2-}	S^{2-}
Fe^{2+}	1.734	2.125
Fe^{3+}	1.759	2.149
Mn^{2+}	1.790	2.22
Co^{2+}	1.692	1.94

3.3.5 Octahedral Twist Angle

Relating to the Schafarzikite structure, the octahedral twist angle as defined in this work is the torsion angle created between the $M(z=\frac{1}{4})-O1_{eq}(z=0)$ and $M(z=\frac{3}{4})-O1_{eq}(z=\frac{1}{2})$ bonds. It gives a measure of the buckling between adjacent octahedra along the structural chains.

3.3.6 Electron Localisation Function

Although not strictly structural, the electron localisation function (ELF) is a useful method for examining electronic structure, in addition to examining the basic charge density. In this study, it has particularly been used for visualising electron LPs on ions such as Sb^{3+}, the details of which often cannot be seen from the basic electron density due to their low intensity and diffuse nature. The ELF takes values $0 \leq \text{ELF} \leq 1$, and gives a measure of the degree of electron localisation (1 being maximally localised). Details of the method and its basis can be found in *e.g.* [20], [21] and [22]. In this work, the ELF has been generated using CASTEP, and displayed using the software VESTA.[23]

3.4 Magnetic Coupling Calculations

Heisenberg J-coupling parameters can be used to describe the strength of magnetic interactions between ions, following from the description of a simple Heisenberg model. During this work, they have been used to rationalise the strength of magnetic interactions both within and between

the octahedral chains of the MSb_2O_4 structure. These interactions can be calculated from the relative energies of the four different magnetic ordering modes (A, C, G and FM) which have been obtained through DFT calculations.

The basis of the Heisenberg magnetic model is the interaction energy between two magnetic ions, defined as

$$U_{ij} = -J_{ij}\mathbf{S}_i \cdot \mathbf{S}_j, \tag{3.11}$$

where U_{ij} is the energy contribution to the total energy from the interaction, $\mathbf{S}_i$ and $\mathbf{S}_j$ are the spins on atoms i and j, and J_{ij} is the coupling constant between them; a factor of $1/\hbar^2$ has been included in J_{ij} for simplicity. If a FM exchange is defined as positive J, a parallel alignment of $\mathbf{S}_i$ and $\mathbf{S}_j$ will give a reduction in the total energy of the system (negative U_{ij}). For a more complex system, the total interaction energy will be the sum of each individual interaction:

$$U = -\frac{1}{2}\sum_{j\neq i} J_{ij}\mathbf{S}_i \cdot \mathbf{S}_j \tag{3.12}$$

where the factor $\frac{1}{2}$ is to prevent double-counting. Throughout this work, calculations have been simplified by assuming an ideal moment on each ion, *e.g.* assuming that Mn^{2+} is d^5, and therefore $S = \frac{1}{2}$. This may be a potential source of error, however, as the magnetic moment calculated per ion from DFT results is not necessarily constant within a unit cell, or of the ideal value. For all results reported the difference between calculated and ideal spin per cell is negligible, therefore errors should be minimal.

The MSb_2O_4 unit cell contains four formula units. The coupling between ions can be described by three J values:

- The nearest-neighbour *intra*-chain coupling along c (either by direct exchange between cations or 90° superexchange) which shall be labelled J_1.
- The nearest-neighbour *inter*-chain coupling within a given *ab* plane, through M−O−Sb−−O−M linkages, labelled J_2.
- The diagonal *inter*-chain interaction (*i.e.* between cations in adjacent *ab* planes) labelled

J_3.

Each of these J values actually represents a number of different interaction pathways (*i.e.* direct- and super-exchange along the octahedral chains) but this method will not separate them. Within a given cell, there are four J_1 couplings (figure 3.3a) eight J_2 couplings (figure 3.3b) and sixteen J_3 couplings (figure 3.3c).

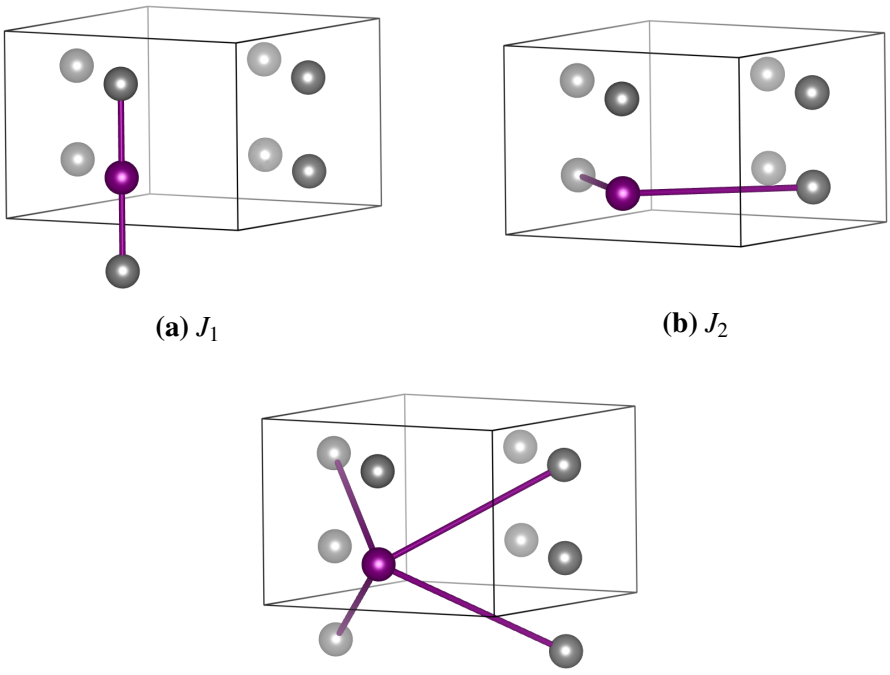

(a) J_1 **(b)** J_2

(c) J_3

Figure 3.3 – Magnetic coupling pathways within the MSb_2O_4 structure. (a) intra-chain J_1 interaction, (b) inter-chain, intra-plane J_2 interaction and (c) inter-chain, inter-plane interaction. Structure viewed approximately along (110); only magnetic cations shown.

From these definitions, the energy of each magnetic state can be related to the sign of each Heisenberg interaction, depending on the sign of J for a given structure:

$$\begin{aligned}
\text{FM:} \quad & E_{tot} = E_0 - 8SJ_1 - 16SJ_2 - 32SJ_3 \\
\text{A:} \quad & E_{tot} = E_0 + 8SJ_1 - 16SJ_2 + 32SJ_3 \\
\text{C:} \quad & E_{tot} = E_0 - 8SJ_1 + 16SJ_2 + 32SJ_3 \\
\text{G:} \quad & E_{tot} = E_0 + 8SJ_1 + 16SJ_2 - 32SJ_3
\end{aligned} \tag{3.13}$$

where E_0 is taken as the total energy ignoring any magnetic coupling. This system of equations can be related to the energies of the individual magnetic structures for a given system

$$\begin{pmatrix} 1 & -8S & -16S & -32S \\ 1 & +8S & -16S & +32S \\ 1 & -8S & +16S & +32S \\ 1 & +8S & +16S & -32S \end{pmatrix} \cdot \begin{pmatrix} E_0 \\ J_1 \\ J_2 \\ J_3 \end{pmatrix} = \begin{pmatrix} E_{FM} \\ E_A \\ E_C \\ E_G \end{pmatrix}, \tag{3.14}$$

which can then be solved through inversion to find values for J and E_0.

References

[1] R. M. Martin, *Electronic Structure: Basic Theory and Practical Methods (Vol 1)*, Cambridge University Press, 2004.

[2] M. Born and R. Oppenheimer, *Annalen der Physik*, 1927, **389**, 457–484.

[3] P. Hohenberg and W. Kohn, *Physical Review*, 1964, **136**, B864–B871.

[4] W. Kohn and L. J. Sham, *Physical Review*, 1965, **140**, A1133–A1138.

[5] C. Fiolhais, F. Nogueira and M. Marques (Ed.), *A Primer in Density Functional Theory (Lecture Notes in Physics)*, Springer, 2003.

[6] P. Fulde, *Electron Correlations in Molecules and Solids (Springer Series in Solid-State Sciences)*, Springer, 1995.

[7] J. P. Perdew, K. Burke and M. Ernzerhof, *Physical Review Letters*, 1996, **77**, 3865–3868.

[8] J. P. Perdew and K. Schmidt, AIP Conference Proceedings, 2001, p. 1.

[9] T. Leung, C. Chan and B. Harmon, *Physical Review B*, 1991, **44**, 2923–2927.

[10] K. Terakura, T. Oguchi, A. R. Williams and J. Kübler, *Physical Review B*, 1984, **30**, 4734–4747.

[11] V. I. Anisimov, F. Aryasetiawan and A. I. Lichtenstein, *Journal of Physics: Condensed Matter*, 1997, **9**, 767–808.

[12] M. Cococcioni and S. de Gironcoli, *Physical Review B*, 2005, **71**, 1–16.

[13] H. J. Monkhorst and J. D. Pack, *Physical Review B*, 1976, **13**, 5188–5192.

[14] D. J. Singh, *Planewaves, Pseudopotentials, and the LAPW Method*, Springer, 1994.

[15] S. J. Clark, M. D. Segall, C. J. Pickard, P. J. Hasnip, M. I. J. Probert, K. Refson and M. C. Payne, *Zeitschrift fuer Kristallographie*, 2005, **220**, 567–570.

[16] C. J. Pickard, *On-the-fly pseudopotential generation in CASTEP*, University of St. Andrews technical report, 2006.

[17] K. Robinson, G. V. Gibbs and P. H. Ribbe, *Science*, 1971, **172**, 567–570.

[18] W. H. Baur, *Acta Crystallographica Section B Structural Crystallography and Crystal Chemistry*, 1974, **30**, 1195–1215.

[19] I. D. Brown and D. Altermatt, *Acta Crystallographica Section B Structural Crystallography and Crystal Chemistry*, 1985, **41**, 244–247.

[20] P. Fuentealba, E. Chamorro and J. C. Santos, in *Theoretical Aspects of Chemical Reactivity*, A. Toro-Labbé (Ed.), Elsevier B.V., 2007, ch. Understanding and Using the Electron Localization function, pp. 57–85.

[21] P. Fuentealba, D. Guerra and A. Savin, in *Chemical Reactivity Theory: A Density Functional View*, P. K. Chattaraj (Ed.), CRC Press, 2008, ch. An Introduction to the Electron Localization Function, pp. 281–292.

[22] A. D. Becke and K. E. Edgecombe, *Journal of Chemical Physics*, 1990, **92**, 5397–5403.

[23] K. Momma and F. Izumi, *Journal of Applied Crystallography*, 2008, **41**, 653–658.

Chapter 4
Density Functional Theory Study of Magnetism in MSb_2O_4 Compounds

4.1 Background

As discussed in section 1.2.1, a wide range of magnetic MSb_2O_4 compounds have been reported, with Néel temperatures of a similar magnitude (table 4.1). The interactions between M cations within a single octahedral chain can readily be rationalised as a competition between M−M direct-exchange and M−O−M 90° superexchange, resulting in a change from A- to C-type magnetic order on crossing the TM series. Due to the 3D ordering within these compounds, however, the interactions *between* magnetic chains cannot be negligible. This is particularly true for $NiSb_2O_4$ where the ordering temperature is not easily explained due to the 90° superexchange; this should be quite weak given the ionic nature of the Ni−O bonds and the angle involved.[1–3] The interactions occurring between adjacent chains are not easily rationalised, however. As such, there is very little theoretical study of magnetism (or indeed any other properties) within compounds of this type. Exceptions to this are the recent report of $CuSb_2O_4$[4] which compares DFT-computed phonon frequencies to experimental values, and $TiSn_2O_4$, which was examined for use as a potential photo-catalyst for water splitting.[5]

$FeSb_2O_4$ has been studied at high pressures experimentally[15] and found to undergo a series of phase transitions; the first (at 3.2 GPa $< P <$ 4.1 GPa) is a second-order transition to a monoclinic unit cell ($P2_1/c$, a = 5.7792(4) Å, b = 8.3134(9) Å, c = 8.455(1) Å, β = 91.88(1)°)

Table 4.1 – Reported Néel temperatures for magnetic MSb_2O_4 compounds.

M cation	Reference	T_N / K	θ / K
Mn	6	60(5)	-
	7	55(2)	-190(20)
Fe	8	45	-
	9	45(6)	-
	10	42	-
	11	41.8(1)*	-
	12	46(1)†	-
Co	13	79	3(1)
Ni	14	46(3)	-98(5)
		45.0(1)*	-
	1	47.0(5)	-40(1)
	6	46(2)	-
Cu	4	1.8	-

* Obtained from heat capacity measurements.

† Obtained from Mössbauer spectroscopy

showing a distorted $FeSb_2O_4$-like structure. The second ($6.4\ \text{GPa} < P < 7.4\ \text{GPa}$) is a first-order transition back to tetragonal symmetry ($P4_2/m$, a = 7.8498(4) Å, c = 5.7452 Å) forming a structure with channels in two dimensions, and significantly different bonding around Sb. $NiSb_2O_4$ has also been studied at moderate pressure (0.36 GPa) but at low temperature; the most relevant result here is the formation of a small G-type magnetic component from the NPD results, in addition to the C-type observed at ambient pressure.[16]

While the lack of experimental data for MX_2O_4 compounds could pose problems for fitting theoretical parameters to experimental results, it is obviously attractive as an avenue for investigation. This chapter explores the results of electronic structure calculations on a range of compositions, particularly with regards to magnetic behaviour.

4.2 Methodology

4.2.1 CASTEP Calculations

Calculations of magnetic structure have been performed for a range of MSb_2O_4 structures, for M = Mn, Fe, Co, Ni and Cu. In each case, the four possible magnetic ordering modes (A, C, G and FM) have been calculated for each structure. The calculations presented here were performed using the CASTEP code[17] (versions 5.5–6.1) with default on-the-fly pseudopotentials. Convergence of parameters was checked relative to energy differences between different magnetic states; in all cases parameters were chosen to be accurate to within 1 % of the mean energy difference observed. For all compounds studied, a Monkhorst-Pack k-point grid of $3 \times 3 \times 4$ was found to be fully converged. The planewave cutoff values used for each structure are given in table 4.2. Gaussian smearing of occupied states (0.2 eV width) was used to aid convergence, as were additional empty bands to the default settings. The number of additional bands were chosen as the minimum necessary to aid convergence. All other parameters were defaults of the code, unless where explicitly mentioned.

In many cases, magnetic calculations proved difficult (if not impossible) to converge, mainly due to crossing between different spin states during the self-consistent loop. Where possible,

Table 4.2 – CASTEP planewave cutoff values for MSb_2O_4.

M	E_{cut} / eV
Mn	750
Fe	1000
Co	700
Ni	750
Cu	1050

the calculations were constrained to remain in the intended magnetic structure by fixing the total and absolute magnetic moments for a certain number of iterations (using the CASTEP keywords `spin_fix` and `geom_spin_fix`). This method has not always been successful for AFM structures however, as all AFM models (nominally) have the same total and absolute moments per unit cell. For this reason, a number of calculations could not be converged, particularly for $FeSb_2O_4$ and $CoSb_2O_4$. Convergence of the self-consistent iteration procedure was achieved using either the 'Broyden' or 'Pulay' density mixing algorithms;[18] Pulay mixing was used in situations where Broyden mixing failed to converge. The results obtained from each method are comparable within the convergence criteria adopted.

In almost all calculations, optimisation of both unit cell parameters and atomic positions has been obtained using the Broyden-Fletcher-Goldfarb-Shanno (BFGS) method[19] for the magnetic state in question. This ensures self-consistency within the DFT results. Where applicable, self consistent energy results have also been obtained using experimental geometries, for comparison.

4.3 Structural Parameters

The unit cell parameters obtained from geometry optimisations using default PSPs and starting from the experimental structural models (with the exception of $CuSb_2O_4$, which was generated from a 'scaled' $CuAs_2O_4$ model) are shown in figures 4.1 and 4.2; also shown are the corre-

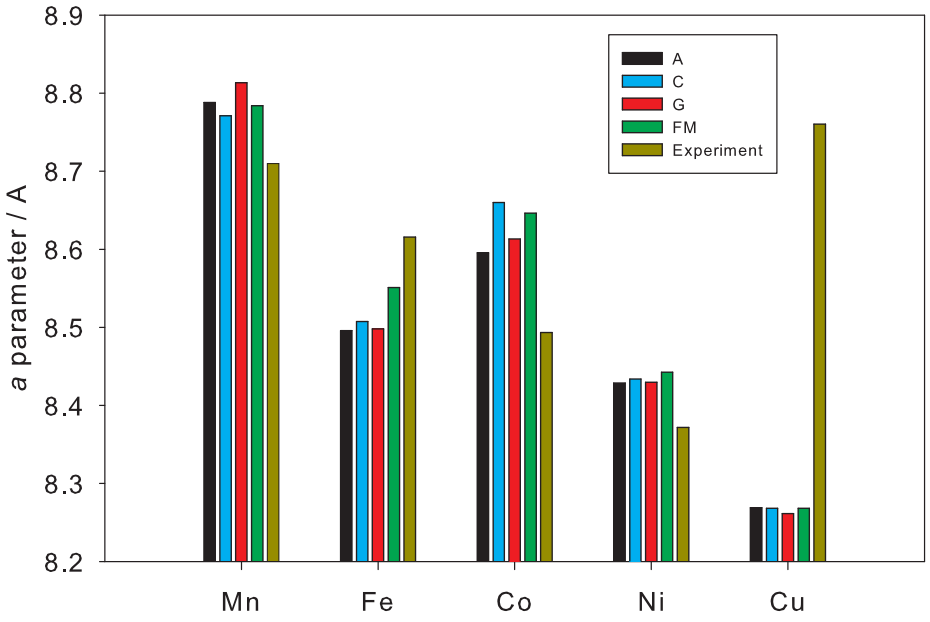

Figure 4.1 – Calculated and experimental *a* parameter for M = Mn, Fe, Co, Ni and Cu.[4,6–8,13]

sponding (300 K) experimental parameters. For Mn, Co and Ni, the *a* parameter is slightly over-estimated compared to experiment, within 2 % of the experimental result. This is as expected for a GGA functional, however, which are well known to over-estimate bond-lengths.[20] $FeSb_2O_4$ and $CuSb_2O_4$ both show underestimation of the *a* parameter, however, by quite a considerable amount (5.7 % for Cu). The *c* parameters for all systems are overestimated as expected; generally within 3.5 % of experimental results, although $NiSb_2O_4$ is over-estimated by 4.6 %. These results would suggest incorrect modelling of the $FeSb_2O_4$ and $CuSb_2O_4$ structures, although it is unclear whether this is due to the PBE functional employed, or other parameters (such as the pseudopotentials) specific to these systems. Testing of alternative functionals or pseudopotentials was beyond the scope of this project, however, this could prove to be useful further work.

It is interesting to note that the different magnetic ordering modes give rise to quite different unit cell parameters for each system. The trend observed is that A and G modes adopt similar unit cell sizes, while C and FM also form similar structures, particularly for the *c* parameter. This could be related primarily to the magnetic ordering along the octahedral chains; A and G both adopt AFM order between adjacent octahedra, while C and FM show FM alignment. The

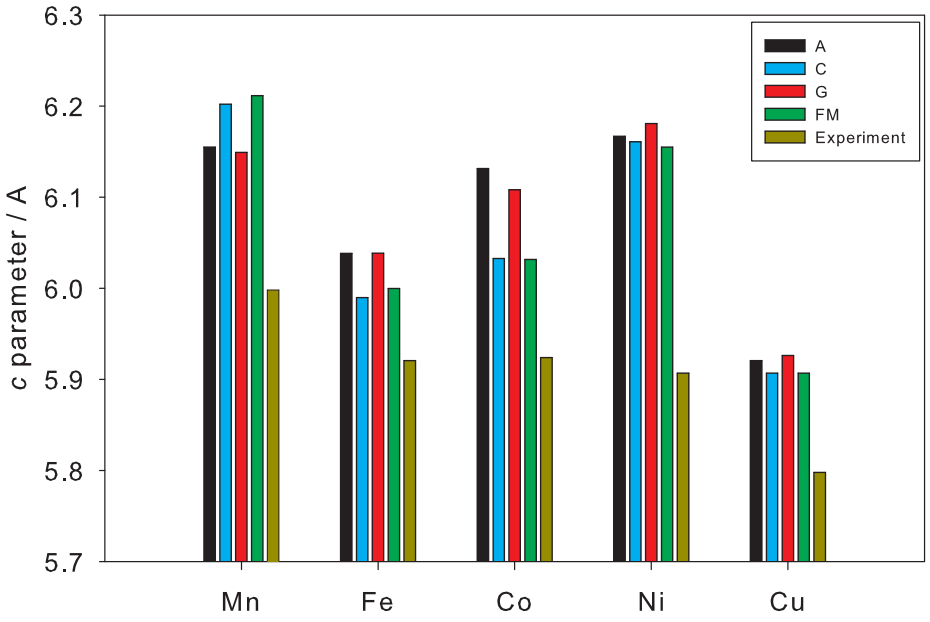

Figure 4.2 – Calculated and experimental *c* parameter for M = Mn, Fe, Co, Ni and Cu.

relationship between these pairs across the M cation range can also be examined; for Mn, A- and G-modes give longer *a* and shorter *c* than C- and FM-modes, while the opposite is true for M = Fe, Co, Ni and Cu. This relates to the groundstate magnetic ordering (section 4.4) where Mn is predicted to be A-type, Fe, Co and Ni are C-type and Cu is FM.

4.4 Electronic Configuration

4.4.1 Magnetic Ordering

By calculating the enthalpies for each of the collinear magnetic structures (A, C, G and FM) it is possible to determine the predicted magnetic groundstate, assuming a magnetic structure commensurate with the nuclear unit cell. It is important to note that the enthalpy differences involved are a small fraction of the total calculated enthalpies: for this reason, the magnetic enthalpy data presented here are given relative to the FM state ($E_{state} - E_{FM}$).

The calculated enthalpies relative to the FM enthalpy are given in table 4.3 for each of the MSb_2O_4 compositions. From these results, it is clear that DFT predicts an A-type magnetic groundstate in $MnSb_2O_4$, C-type in $FeSb_2O_4$, $CoSb_2O_4$ and $NiSb_2O_4$, and FM (although

Table 4.3 – CASTEP predicted magnetic enthalpies for M = Mn, Fe, Co, Ni and Cu (0 GPa).

		Mn	Fe	Co	Ni	Cu
	A	-0.212	0.249	0.351	-0.101	0.153
$E_{state} - E_{FM}$ / eV per cell	C	-0.108	-0.039	-0.039	-0.109	0.008
	G	-0.133	0.287	0.418	0.039	0.159
E_{FM} / eV per cell		-14167.4	-14844.3	-15476.5	-16564.7	-17801.3
Predicted groundstate		A	C	C	C	FM
Experimental groundstate		A	A	C	C	-

closely contested by C-type) for $CuSb_2O_4$. The general trend on traversing the TM series is to change from A-type to C-type, and then finally to FM. These results compare very favourably with the experimentally determined groundstates (by NPD): $MnSb_2O_4$ shows A-type ordering,[7] while $CoSb_2O_4$ and $NiSb_2O_4$ both order with a C-mode.[13,14] The exceptions are $FeSb_2O_4$ and $CuSb_2O_4$, which are discussed below. It is important to note that the calculations reproduce the change from A- to C-type on crossing the first row TMs, although the change between the two occurs at the wrong point in the series.

For $CuSb_2O_4$, a very recent report[4] has found that the magnetic response is essentially due to isolated (non-interacting) 1D Heisenberg chains of edge-sharing octahedra. No evidence has been observed for a FM response, but some (potentially AFM) long range order has been observed below 1.8 K; a NPD study would be required to determine the nature of this ordering. Relating this to the FM groundstate predicted here, it is important to note that the calculations performed would not allow for the formation of a disordered magnetic state due to the imposed symmetry and single (not multiple) unit cell definition. The low enthalpy of the C-type structure relative to FM in $CuSb_2O_4$ could provide an indication of a potential long-range AFM order at 1.8 K, but this is by no means conclusive. Reference must also be made to the predicted FM groundstate for $CuAs_2O_4$ (chapter 5) using the same pseudopotential set, which has been proved correct experimentally. Like those results, however, calculations for $CuSb_2O_4$ give rise

to anomalously large magnetic moments (7 μ_B per Cu^{2+}) suggesting the presence of ghost states due to the Cu pseudopotential. For this reason, $CuSb_2O_4$ is not considered further within the following results; see chapter 5 for further discussion regarding the Cu pseudopotential.

The discrepancy between predicted and measured groundstate for $FeSb_2O_4$ is more difficult to rationalise; additional work has been carried out to examine this, and is discussed in more detail in section 4.5. Experimentally, $FeSb_2O_4$ shows a relatively complex magnetic groundstate which may contribute to the disagreement; although A-type ordering dominates, weak C- and G-type ordering have also been observed.[21]

For both $FeSb_2O_4$ and $CuSb_2O_4$, the geometry optimised structures show deviations from the experimental models, and also the general trend across the TM series (section 4.3). For this reason, self-consistent calculations for each of the magnetic structures within the experimental geometry were performed. In both cases there was no change in the predicted groundstate, or any significant change in the relative enthalpies of each of the magnetic states.

4.4.2 Electronic Structure

Plots of both bandstructure and partial density of states (PDOS) for $MnSb_2O_4$ (figure 4.3), $FeSb_2O_4$ (A- and C-type magnetism, 4.6 and 4.7), $CoSb_2O_4$ (4.8) and $NiSb_2O_4$ (4.4) reveal more information about the 0 GPa electronic structure. Here, the PDOS represents the density of states (DOS) decomposed by both atom type and angular momentum l for all atoms within the unit cell, while the bandstructure is constructed from a path between high-symmetry points in the Brillouin zone for the primitive tetragonal unit cell.[22] DOS and PDOS plots were produced using the OptaDOS code[23,24] with adaptive broadening.[25]

$MnSb_2O_4$

In $MnSb_2O_4$, DFT predicts semi-conducting behaviour as expected, with a mixture of Mn d and O p states dominating the valence band. One of the d states (at $\simeq$ -7.7 eV) gives a very sharp feature in the PDOS, while others are broader; this indicates different degrees of bonding (and delocalisation) between the d orbitals and the surrounding oxygen p orbitals. Given the

distortion of the octahedra and orbital overlap along the chains, this sharp feature most likely corresponds to the d_{yz} orbital. Coupling of *d*-orbitals with those in adjacent octahedra may also contribute to the broad nature of the other *d*-states. The conduction band consists mainly of Sb *p*-states, mixed with Sb *s* states. The actual density of these states is quite low at this energy, however; the unoccupied Mn states show greater DOS at higher energy (figure 4.5). From this bandstructure, the bandgap would be concluded to be indirect (Γ $(0,\ 0,\ 0) \leftarrow M$ $(\frac{1}{2},\ \frac{1}{2},\ 0)$), however, calculations using alternative magnetic structures (within the A-type optimised geometry) would suggest a direct ($\Gamma \leftarrow \Gamma$) bandgap (appendix A.3.1). Comparison between the different geometry optimisations revealed only very minor deviations in the band energies.

$NiSb_2O_4$

$NiSb_2O_4$ is also predicted to be a semiconductor (figure 4.4) with many similar features in the bandstructure as seen in $MnSb_2O_4$; the Ni *d* and O *p* states dominate the valence band, while the Sb *p* states are most significant in the conduction band. In $NiSb_2O_4$, however, the Ni *d* states are less disperse and show many sharper features, indicating less effective bonding with surrounding atoms. This is consistent with the smaller size of Ni *cf.* Mn (ionic radii of 0.69 Å *vs.* 0.83 Å).[26] For $NiSb_2O_4$, the lowest energy points in the conduction band occur at *X* $(0,\ \frac{1}{2},\ 0)$ and Γ, however, there is also a minimum between *M* and Γ, at approximately $(\frac{1}{4},\ \frac{1}{4},\ 0)$. As for the other structures investigated, the conduction band is higher in energy at points *Z* $(0,\ 0,\ \frac{1}{2})$, *R* $(0,\ \frac{1}{2},\ \frac{1}{2})$ and *A* $(\frac{1}{2},\ \frac{1}{2},\ \frac{1}{2})$ compared to *X*, *M* and Γ within the Brillouin zone.

$FeSb_2O_4$

For $FeSb_2O_4$ (figures 4.6 and 4.7) DFT predicts a metallic behaviour for both A- and C-type magnetic structures, with a significant DOS at E_f. For the A-mode, this metallic behaviour is predicted across the entire Brillouin zone, while for C-type it is only predicted for the Σ $(\alpha,\ \alpha,\ 0)$ points. This behaviour is erroneous ($FeSb_2O_4$ is experimentally found to be a semiconductor[27]) and reflects significant self-interaction errors present for this composition. Interestingly, the PDOS plots for $FeSb_2O_4$ show significant asymmetry between the up- and down-spin channels. Because the PDOS plots are decomposed onto all M cations within the

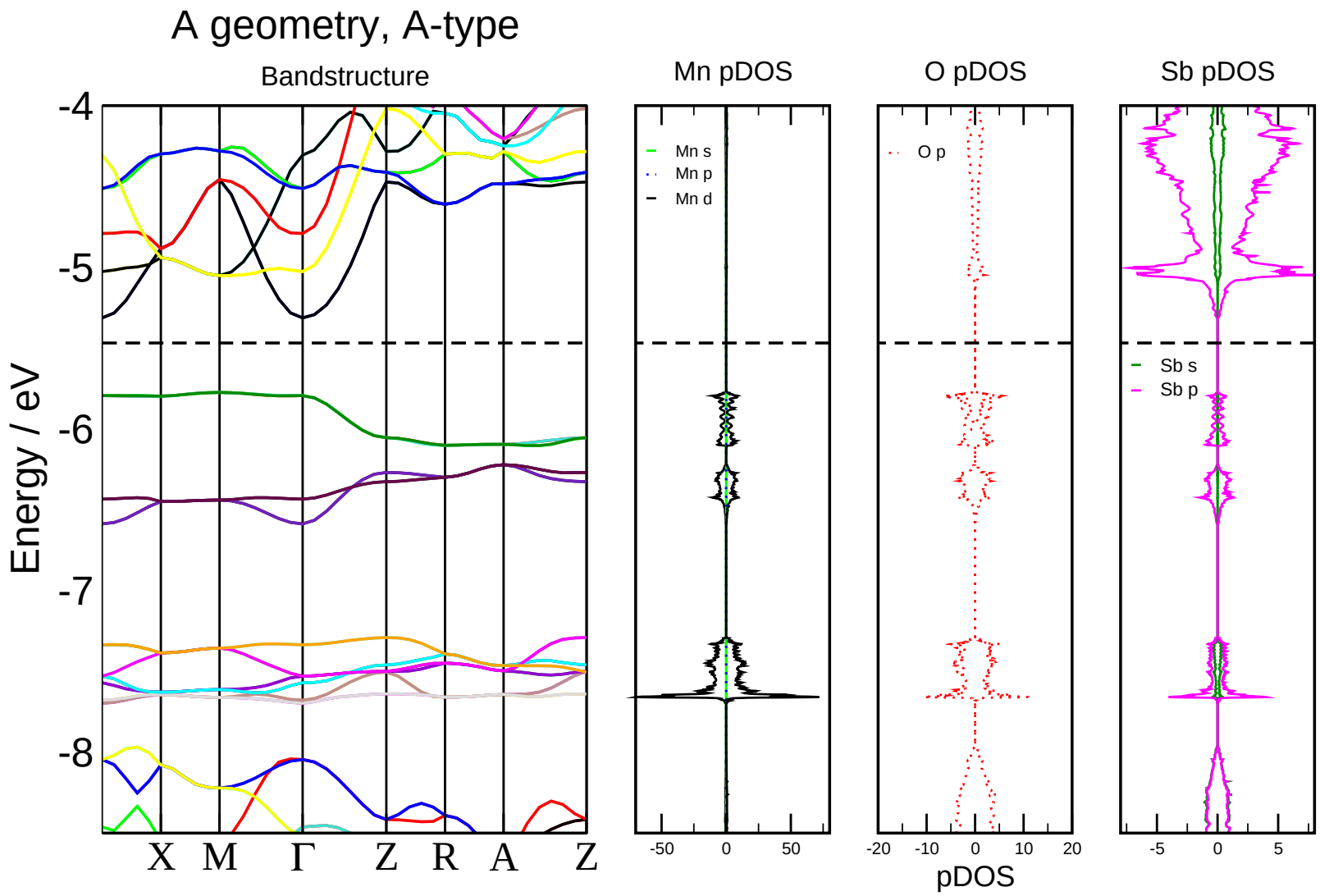

Figure 4.3 – Selected region from $MnSb_2O_4$ bandstructure and corresponding species-decomposed PDOS. Black dashed line-E_f.

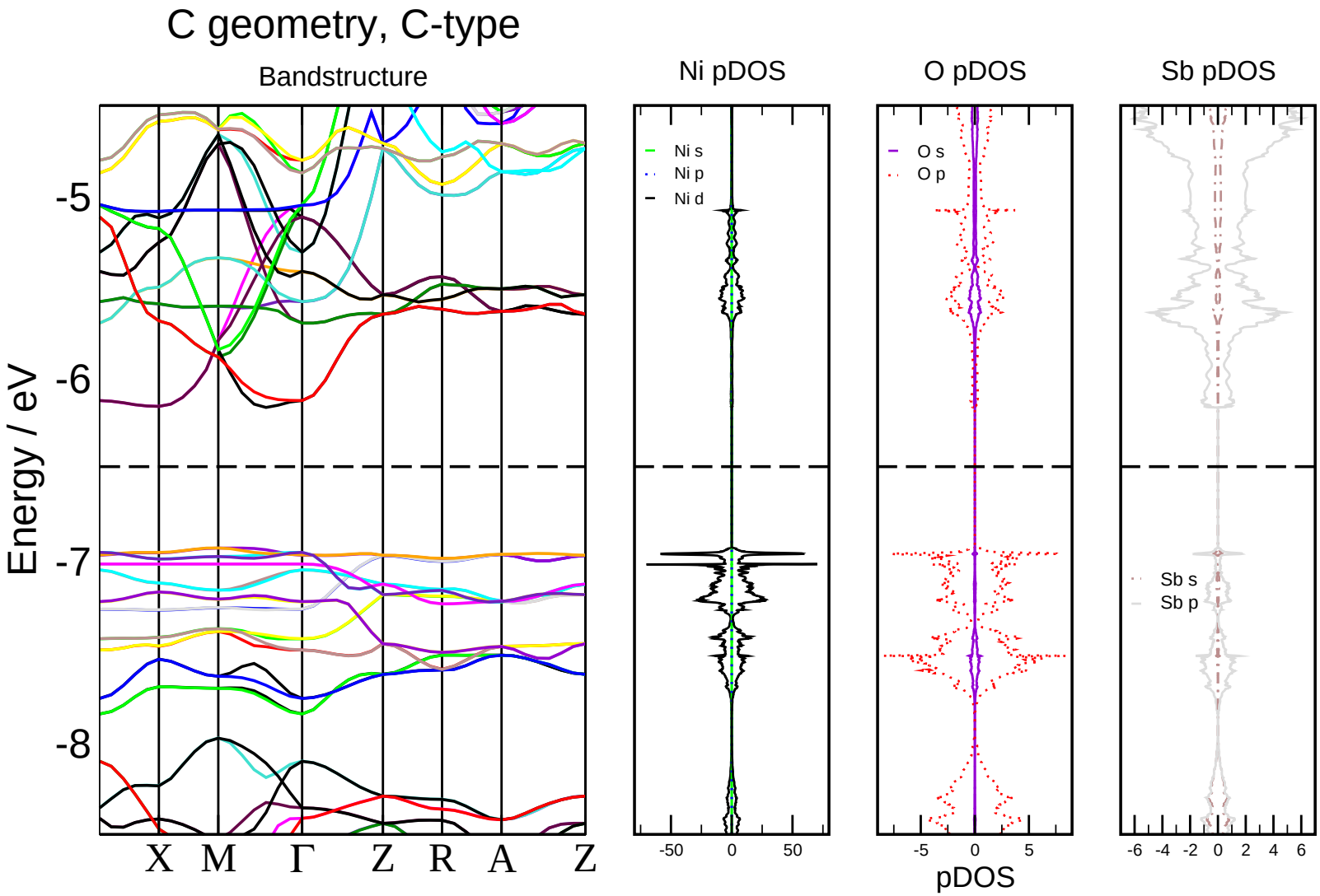

Figure 4.4 – Selected region from bandstructure and corresponding species-decomposed PDOS for C-type magnetism in $NiSb_2O_4$. Black dashed line-E_f.

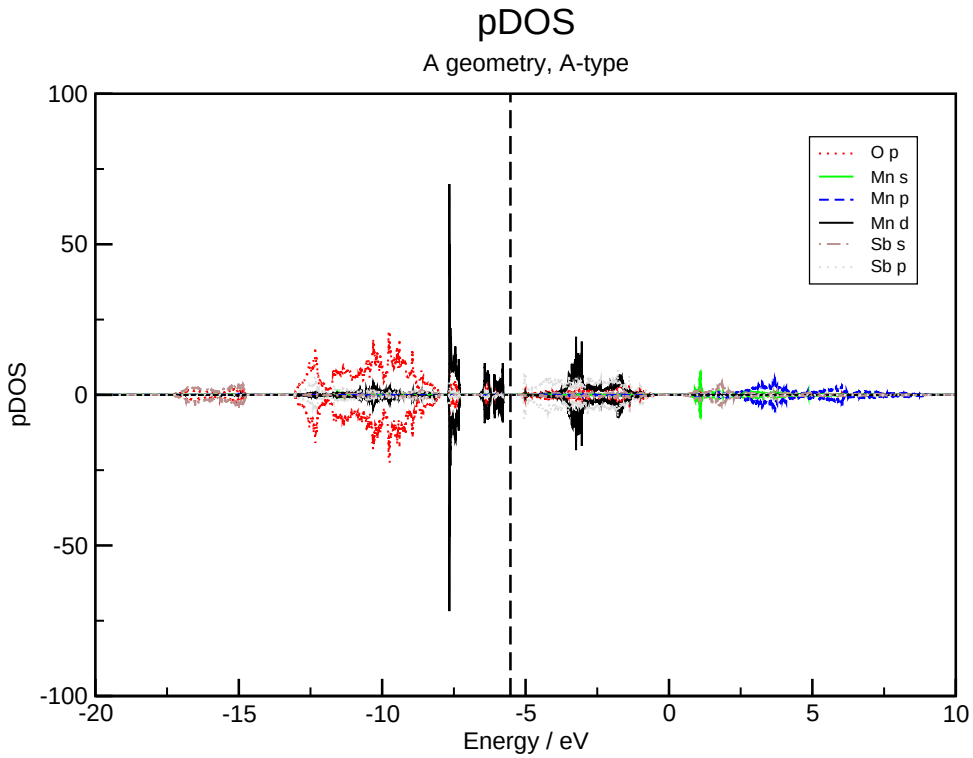

Figure 4.5 – Larger section of $MnSb_2O_4$ PDOS.

unit cell, the up- and down-spin densities should be identical due to the AFM arrangement overall. The cause of this asymmetry is unknown, but may possibly be due to numerical noise (all the asymmetric features occur as very sharp bands).

$CoSb_2O_4$

Like $FeSb_2O_4$, $CoSb_2O_4$ is also predicted to be metallic by DFT (figure 4.8) although with a small DOS at the Fermi level. Like the other structures, a difference in band energy is seen between the $\Sigma\ (\alpha,\ \alpha,\ 0)$ and $S\ (\alpha,\ \alpha,\ \frac{1}{2})$ points in the BZ, particularly around E_f. In addition, however, $CoSb_2O_4$ also shows a definite 'splitting' of bands on going from S to Σ; for some bands the loss of a $c*$ (reciprocal lattice vector) component of the electron momentum is unfavourable, while for others it causes a reduction in energy. This indicates a distinct difference for electrons propagating along the c-axis, to perpendicular to it, consistent with effectively 1D chains.

The PDOS for Co, O and Sb show very similar shapes around E_f, suggesting a significant interaction between their respective orbitals, consistent with the (delocalised) metallic behaviour

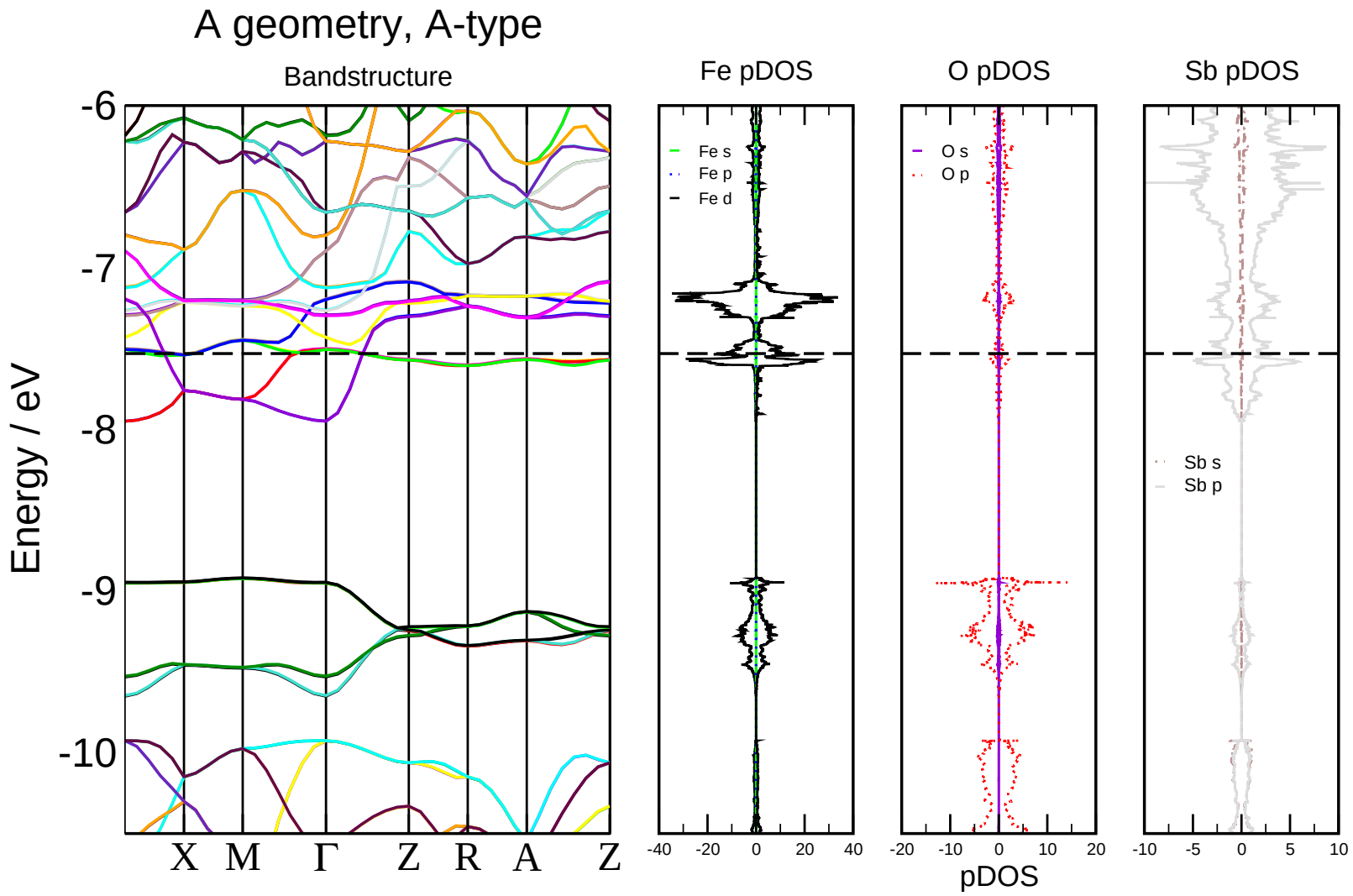

Figure 4.6 – Selected region from bandstructure and corresponding species-decomposed PDOS for A-type magnetism in $FeSb_2O_4$. Black dashed line-E_f.

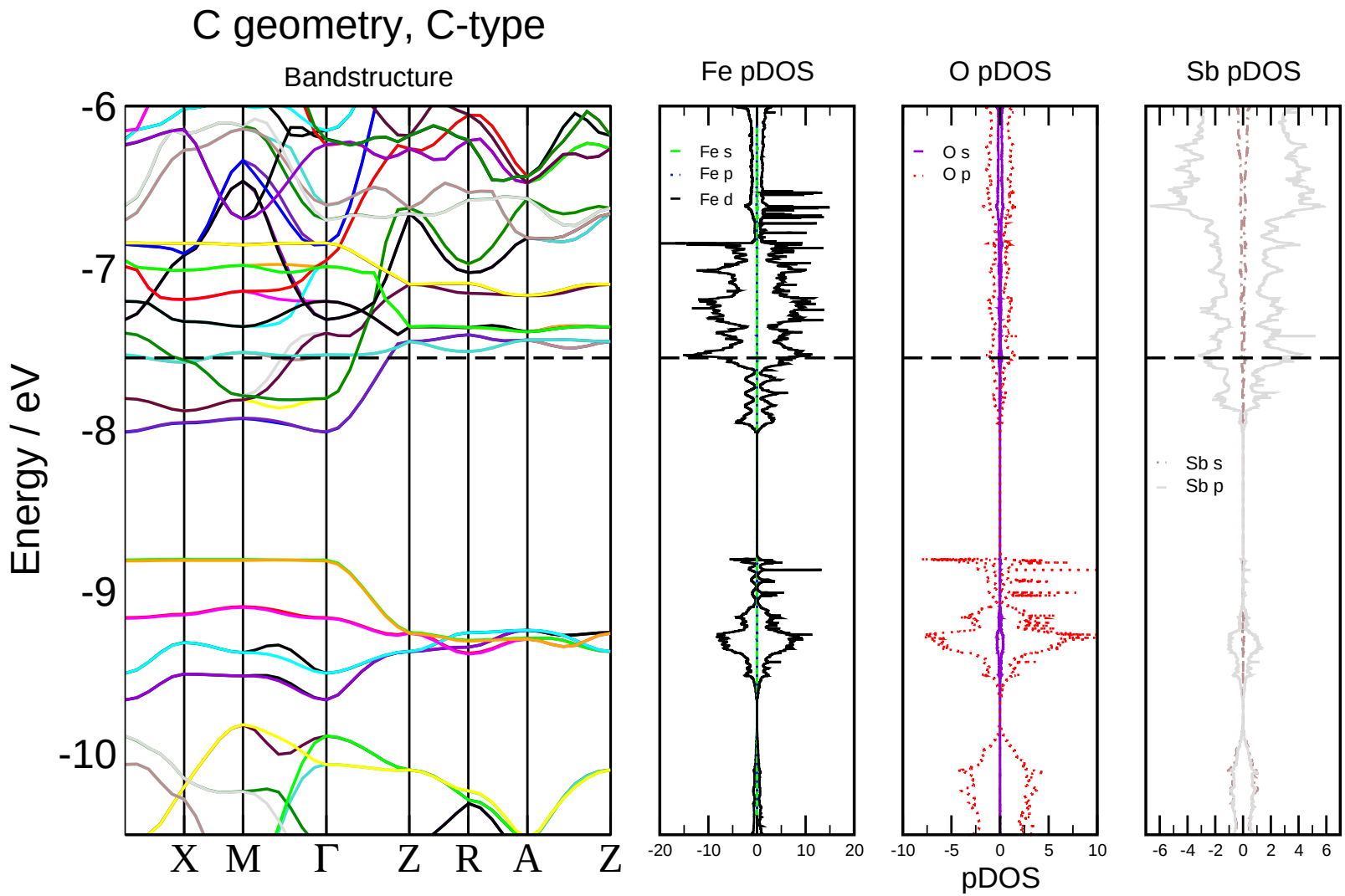

Figure 4.7 – Selected region from bandstructure and corresponding species-decomposed PDOS for C-type magnetism in $FeSb_2O_4$. Black dashed line-E_f.

predicted. Experimentally, $CoSb_2O_4$ is also found to be semiconducting,[28] again suggesting that this composition is strongly affected by an underestimation of the bandgap.

4.5 Extended Calculations for MSb_2O_4

Following the calculation of metallic structures for both $FeSb_2O_4$ and $CoSb_2O_4$ (as well as the incorrect magnetic groundstate predicted for $FeSb_2O_4$) it was necessary to consider alternative calculation methods, to investigate the effect of an improved level of theory on the calculated properties. Due to the over-delocalisation seen for the *d*-electrons and potentially high correlations for the TM cations, the GGA+U approach was adopted.

4.5.1 GGA+U for $FeSb_2O_4$ and $CoSb_2O_4$

As no previous work exists regarding the optimal value of a Hubbard U parameter for the TM *d* electrons within these systems and the computational requirements needed to calculate it (*i.e.* through a linear response method) proved too large, a range of values $(0 \leq U \leq 10 \text{ eV})$ were tested for both $FeSb_2O_4$ and $CoSb_2O_4$. In both cases, the parameter was applied to the TM *d* electrons and geometry optimisation performed.

$CoSb_2O_4$

The variation of the enthalpies of the different magnetic states relative to the FM enthalpy are shown in figure 4.9, as well as the overall FM enthalpy (grey line). The general trend is that as U increases, the enthalpy difference between the states decreases (the overall enthalpy also increases). For the values of U tested, the C-type magnetic structure remains the groundstate for all points, except for $U = 1$ eV and $U = 10$ eV. At both values, the A-type magnetic structure becomes favourable; at $U = 1$ eV the difference is significant, while at 10 eV the difference between magnetic states is approaching the convergence limits. The cause of the variation at 1 eV is unknown, but seems to lie off of the main trend.

Under applied U, the *a* parameter increases almost linearly from 8.62 Å to 8.84 Å (average over magnetic structures) thus moving away from the experimental value (8.49 Å). The *c* pa-

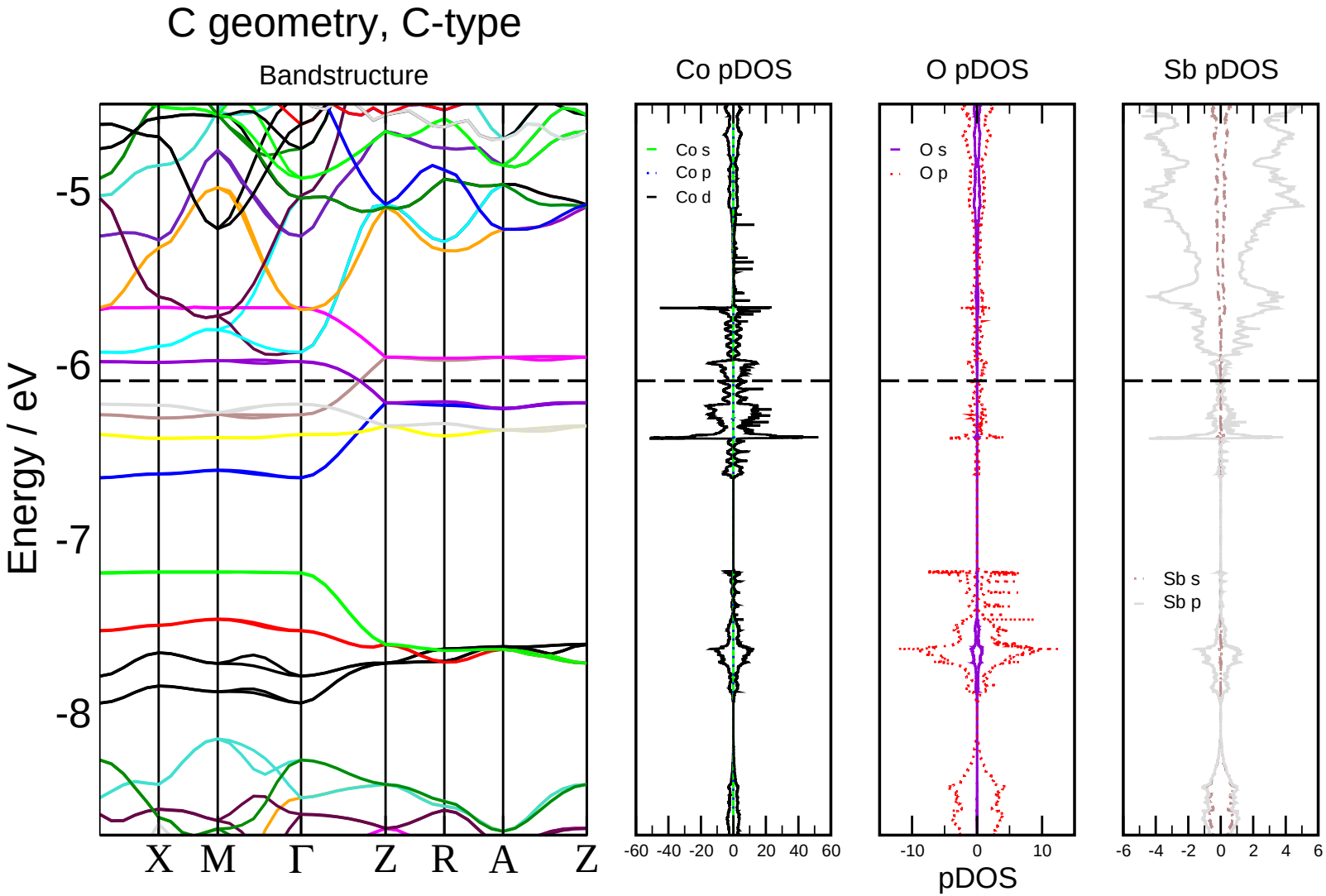

Figure 4.8 – Selected region from bandstructure and corresponding species-decomposed PDOS for C-type magnetism in $CoSb_2O_4$. Black dashed line-E_f.

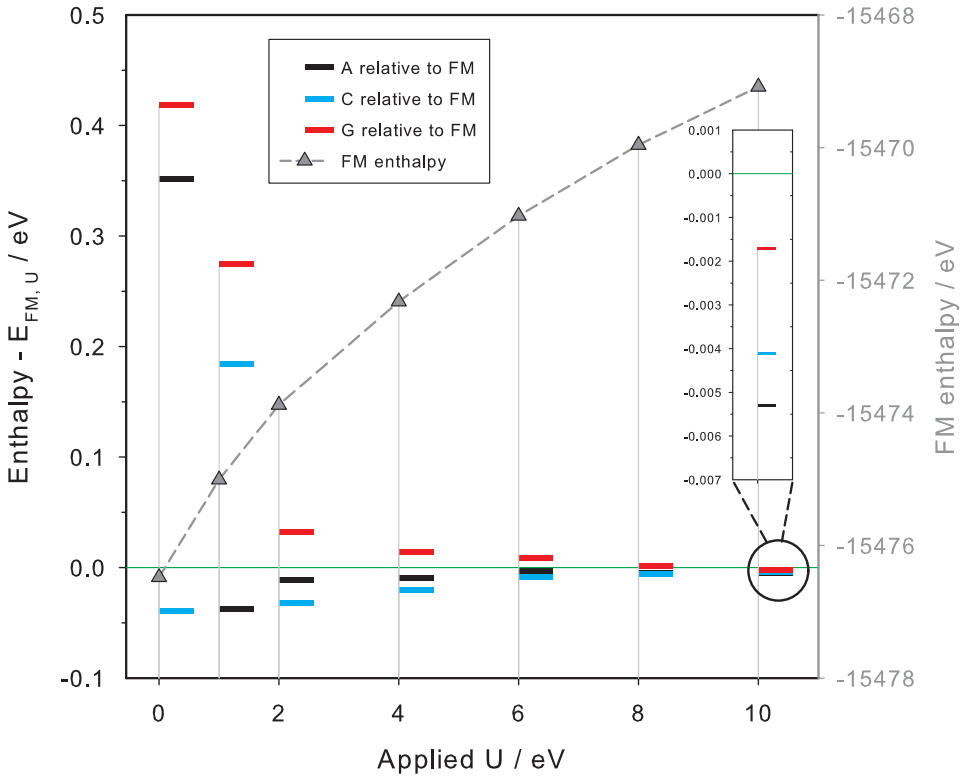

Figure 4.9 – Variation of enthalpy relative to FM enthalpy with applied Hubbard U parameter in $CoSb_2O_4$.

rameter shows no obvious trend, showing a maximum deviation of 0.03 Å over the applied U range.

Although not revealing all of the fine details of the bandstructure, examining the DOS produced from the $3 \times 3 \times 4$ k-point grid does give an indication of the effect of the applied U on the electronic structure. For all values of U investigated, the DOS shows the opening of a band-gap, more consistent with experimental observations. Further work (with greater computational resources) would be required to compute an *ab initio* value of U for use in further calculations.

$FeSb_2O_4$

For $FeSb_2O_4$, it proved impossible to converge most of the AFM calculations for 1 eV $\leq U <$ 6 eV, as shown in figure 4.10. From the available data, the enthalpy behaviour with U is similar to that seen for $CoSb_2O_4$, with an increase in E_{FM}, and a reduction in the enthalpy differences between states. For most calculations the C mode remains lowest in enthalpy, but for $U \geq 8$ eV, A-type becomes favourable. The value of U required to reproduce the experimental groundstate is much higher than that commonly seen for other octahedral-Fe materials, where it generally lies in the range 4 eV $< U <$ 7 eV.[29–31] This could reflect very strong electron correlations in this material (compared to other compounds) or may indicate that additional physics is required, such as spin-orbit coupling. For $U = 4$ eV the G-mode seems particularly low in enthalpy compared to the trend; the cause of this is unclear, but the difficulty in converging calculations for this Hubbard parameter may question the reliability of this value.

Examining the DOS from the coarse BZ sampling (particularly from the complete FM results) reveals that for $U = 1$ eV the system remains metallic, but for $U \geq 4$ eV a band gap is opened, consistent with the experimental results. Between these values, the plots suggest a half-metallic nature with a gap opening in the up-spin bands. This could explain the difficulty in converging AFM solutions in this region, as large energy changes resulting from small occupation shifts (*i.e.* 'charge-sloshing') are likely to be problematic.

On increasing U, the a parameter increases approximately linearly, matching the experimental value at $U \simeq 2$ eV. The c parameter also increases for $U < 4$ eV, before remaining constant

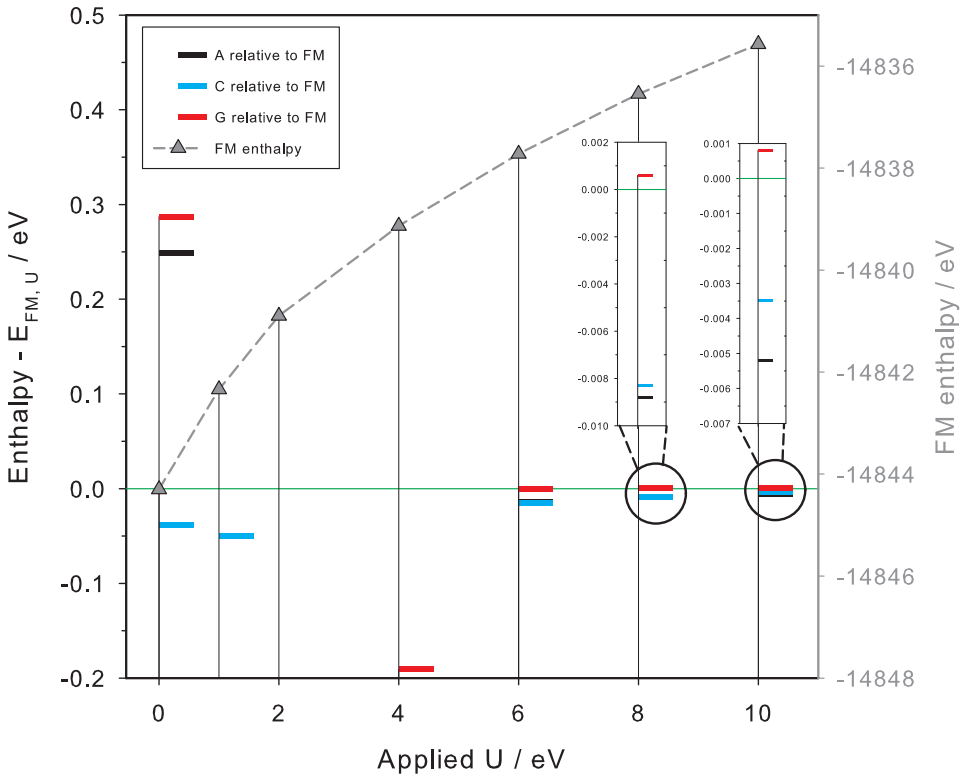

Figure 4.10 – Variation of enthalpy relative to FM enthalpy with applied Hubbard U parameter in $FeSb_2O_4$.

at *ca.* 6.25 Å. This leads to a greater discrepancy in *c* compared with experiment using PBE+U calculations.

Due to the (incorrect) metallic groundstate observed for $FeSb_2O_4$ and $CoSb_2O_4$ and the lack of experimental data to determine an accurate value of U, these compositions are omitted from further structural and magnetic analyses. An extended study of these compositions using more advanced DFT functionals would be required to draw any accurate conclusions.

4.6 0 GPa Structure

The structural deviations seen between experimental results and the average calculated structures are similar for both M cations; values are given in table 4.4. Both calculations show a slightly contracted $M-O2_{ax}$ bond compared to experiment, and an overestimated $M-O1_{eq}$ bond. The net result is that the octahedral volume is over-estimated compared to experiment, as is the quadratic elongation. While the elongation is increased, however, the octahedral distortion index is actually less from DFT. This apparent disagreement occurs due to changes in the O−M−O bond angles; the bond angle variance is much larger than expected from experiment. The results suggest that it is more favourable to angularly distort the octahedra than to cause significantly different bond lengths. Another point regarding the $[MO_6]$ coordination is that the $M-O1_{eq}-M$ bond angle is overestimated compared with experiment for all M; this is the significant contribution to the overestimate in the *c* parameter. The Sb−O bond lengths are overestimated from DFT compared with experiment as expected for the PBE functional used, and do not show any significant deviations across the M cation range.

4.7 Structure changes under applied pressure

Calculations were performed for each of the MSb_2O_4 systems to examine the effect of hydrostatic pressure (up to 15 GPa) on both the structure and magnetic order; the large empty 'channels' within the unit cell are interesting regarding compressibility under high-pressure, and have previously shown interesting results in the structurally related Pb_3O_4.[32] Structural

Table 4.4 – Selected bond data for (0 GPa) CASTEP geometry optimisations and experimental results in MSb_2O_4 for M = Mn and Ni.

	$MnSb_2O_4$		$NiSb_2O_4$	
	Expt.[7]	DFT†	Expt.[6]	DFT†
$M-O1_{eq}$ / Å	2.115	2.143	2.051	2.077
$M-O2_{ax}$ / Å	2.205	2.196	2.084	2.074
Distortion Index	0.0186	0.0109	0.0070	0.0006
Octahedral Volume / $Å^3$	12.98	13.21	11.52	11.67
Quadratic Elongation	1.0096	1.0125	1.0097	1.0148
$[MO_6]$ bond angle variance / °	31.53	61.23	34.17	64.58
$Sb-O1_{eq}$ / Å	1.808	2.001	1.925	2.008
$Sb-O2_{ax}$ / Å	2.028	2.063	1.999	2.054
$\angle M-O2_{ax}-Sb$ / °	121.3	118.4	117.8	117.2
$\angle M-O1_{eq}-M$ / °	90.3	92.2	92.1	95.9
Octahedral Twist / °	18.5	21.4	18.9	21.0

† DFT results shown are the average of A, C, G and FM magnetic geometry optimisations

transformations are discussed in this section, while magnetic response is reported in section 4.8.

4.7.1 $MnSb_2O_4$

Under applied pressure, the unit cell of $MnSb_2O_4$ contracts as expected, as shown in figure 4.11. The contraction in *a* is greater than *c*, consistent with the difference in atomic packing in these directions (the spaces making up the 'channel' occur in the *ab* plane). The compression in *c* is relatively linear with pressure, although the difference between the A / G and C / FM structures increases at higher pressure. The *a* parameter shows slightly different behaviour, however, with the greatest contraction occurring in the 2–6 GPa range, the rate of compression then reducing at higher pressures. This is directly reflected in the $Mn-O2_{ax}$ bond length (figure 4.12), which has a dominant effect on the *a* parameter. A similar contraction is seen in the $Mn-O1_{eq}$ bond length, although to a much lesser degree. This change in Mn−O bonds is directly correlated with the change in magnetic behaviour seen in $MnSb_2O_4$ over the same pressure range (section 4.8.1). As the $Mn-O2_{ax}$ bond length decreases, the $Sb-O2_{ax}$ bond increases very slightly, but not enough to compensate ($\simeq -0.15$ Å *cf.* $\simeq +0.017$ Å). The $Sb-O1_{eq}$ bond does extend quite significantly, however (figure 4.13). The net result is that $\angle$ $Mn-O2_{ax}-Sb$ actually *decreases* under pressure, even though $O2_{ax}$ is moving closer to Mn. This significant change in the Sb coordination is connected with the distortion of the Sb LP of electrons, which occupy the channels within the structure. At low pressure there is enough space for the LPs to point directly at each other, but as the unit cell is compressed they experience greater repulsion, and must distort to relieve strain. This can be observed in the ELF (figure 4.14) which shows the LPs rotating away from each other at high pressure. Very little distortion occurs in the *z* direction, except a slight expansion of each lone pair (figure 4.15). The change in $Sb-O1_{eq}$ and $Sb-O2_{ax}$ bond lengths enables this distortion to occur.

The change in *c* under pressure is almost directly related to the change in $Mn-O1_{eq}-Mn$ bond angle (figure 4.16) which shows a steady decrease with pressure. The exception is the 2–6 GPa pressure range, where a slight increase in angle serves to counteract the decrease in

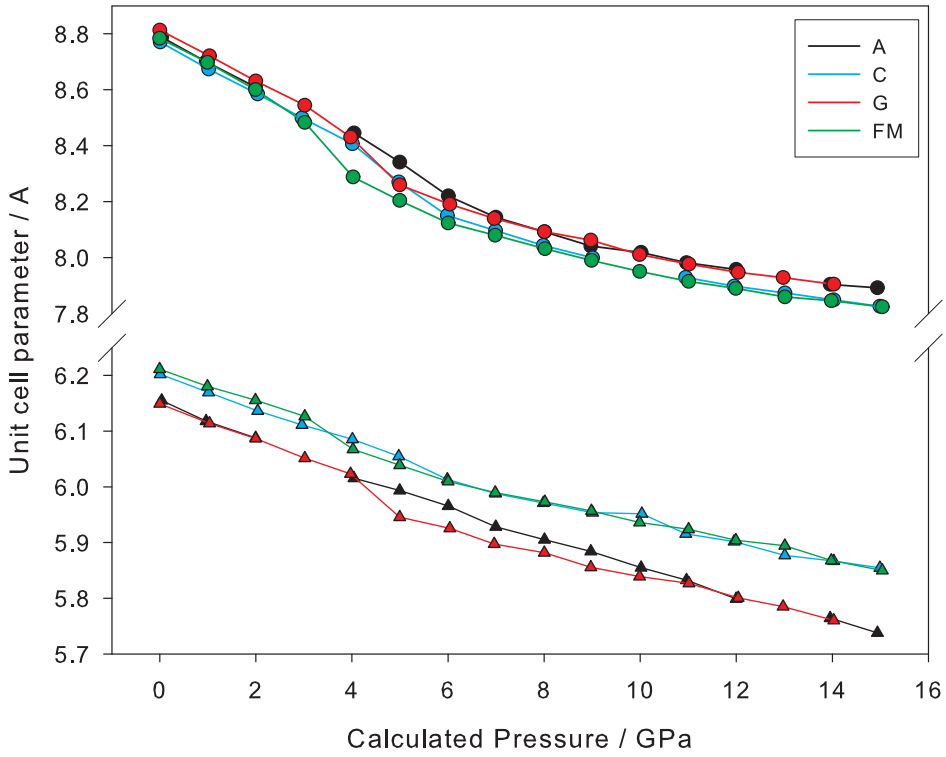

Figure 4.11 – Change in *a* and *c* unit cell parameters under applied pressure in $MnSb_2O_4$; *a*-circles, *c*-triangles.

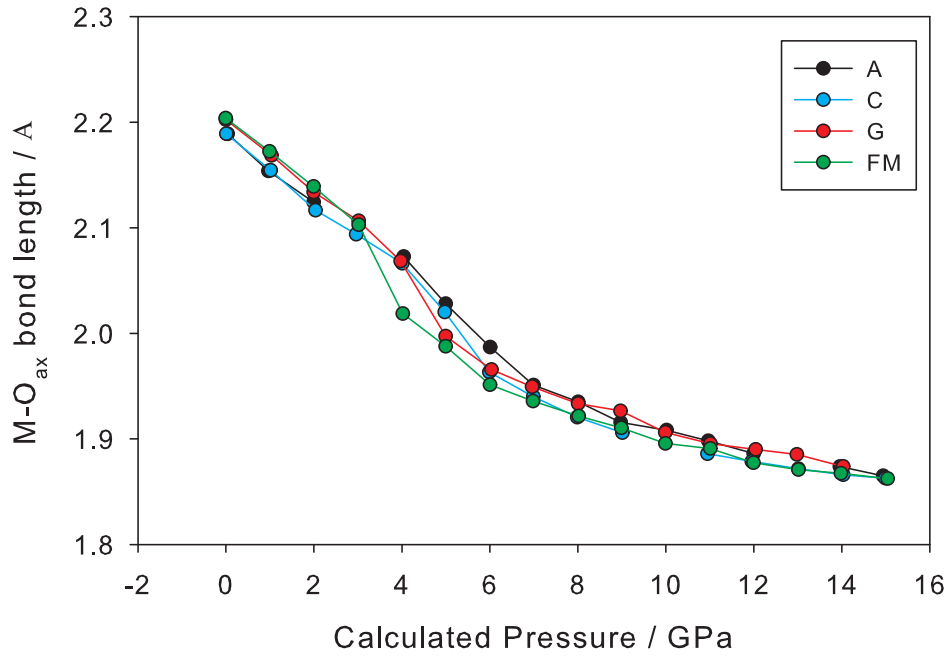

Figure 4.12 – Change in Mn−$O2_{ax}$ bond length under applied pressure in $MnSb_2O_4$.

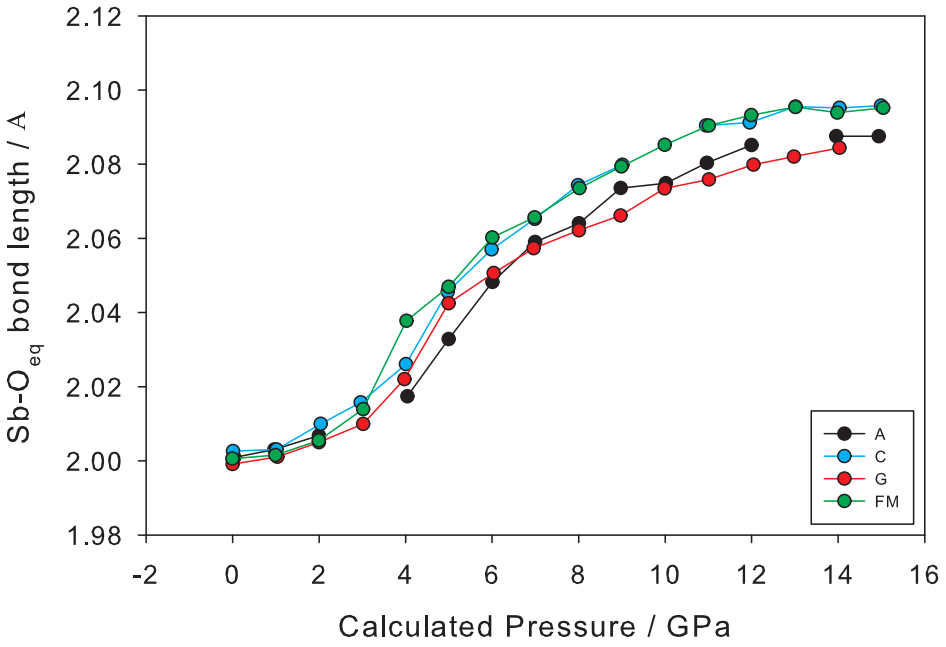

Figure 4.13 – Change in Sb−O1$_{eq}$ bond length under applied pressure in $MnSb_2O_4$.

M−O1$_{eq}$ bond length over the same range, resulting in a gradual *c* contraction.

One interesting change that occurs under pressure is observed in the [MnO_6] octahedral distortion index (figure 4.17). This distortion decreases under small applied pressure, but then increases rapidly above 2 GPa. The exact cause of this is unclear, but represents a combination of the previously mentioned structural changes. This pressure also corresponds to the point at which the A–type magnetic order is most stable (section 4.8.1) which would suggest that the two effects are related.

4.7.2 $NiSb_2O_4$

The variation of unit cell parameters with pressure is shown in figure 4.18. Both *a* and *c* contract with pressure, but in slightly different manners; whereas *a* decreases most at lower pressure with the compressibility decreasing with *P*, *c* shows greatest compressibility at high pressure. The net result is that unit cell volume decreases almost linearly. Throughout this pressure range, the Ni−O2$_{ax}$ bond decreases in length almost linearly, while the Ni−O1$_{eq}$ length slightly mirrors the change in *c*, but is approximately linear. The shapes of the *a* and *c* curves are more closely

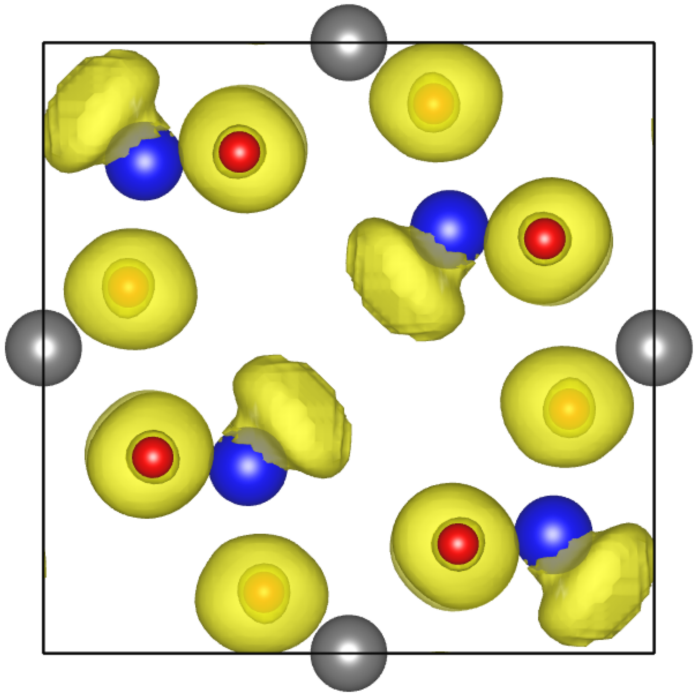

(a)

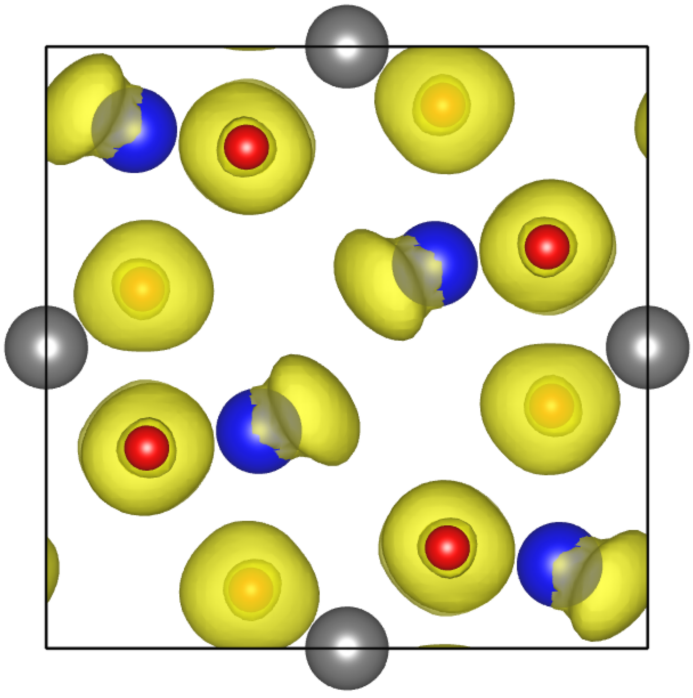

(b)

Figure 4.14 – ELF for $MnSb_2O_4$ (0.005 surface level) showing Sb lone pair structure at (a) 0 GPa and (b) 15 GPa, viewed along [001] (only $z = 0.25$–0.75 shown); Mn - grey spheres, Sb - blue spheres, O - red spheres.

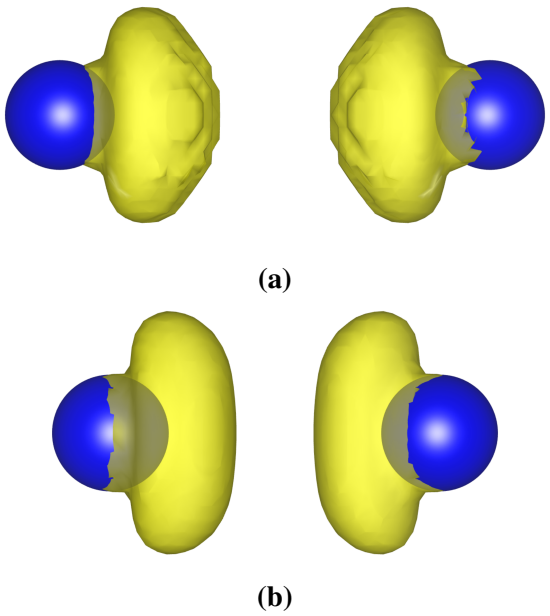

Figure 4.15 – ELF for $MnSb_2O_4$ (0.005 surface level) showing Sb lone pair structure at (a) 0 GPa and (b) 15 GPa, viewed along [110].

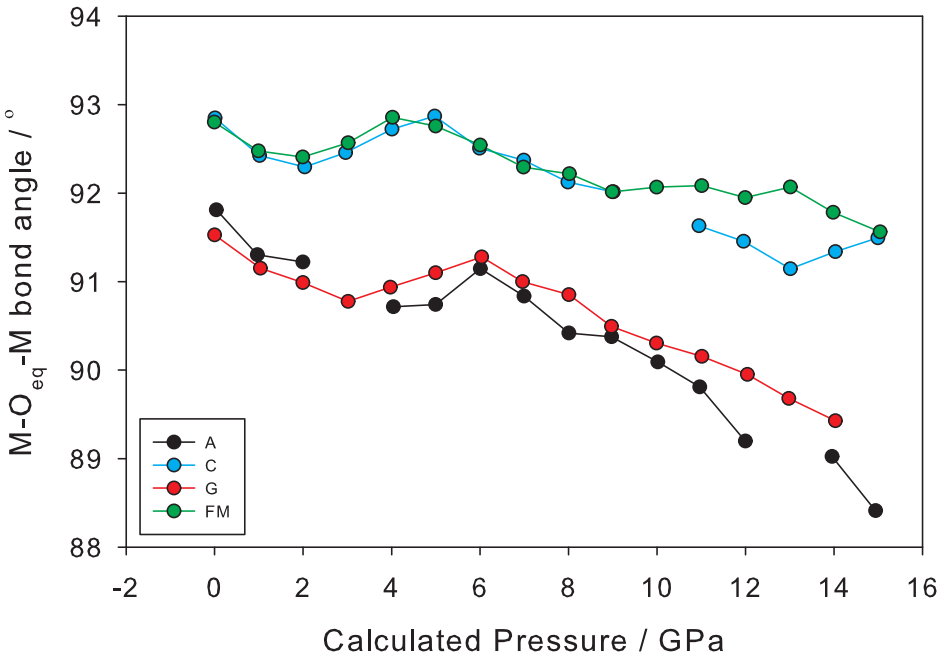

Figure 4.16 – Change in Mn−O1$_{eq}$−Mn bond angle under applied pressure in $MnSb_2O_4$.

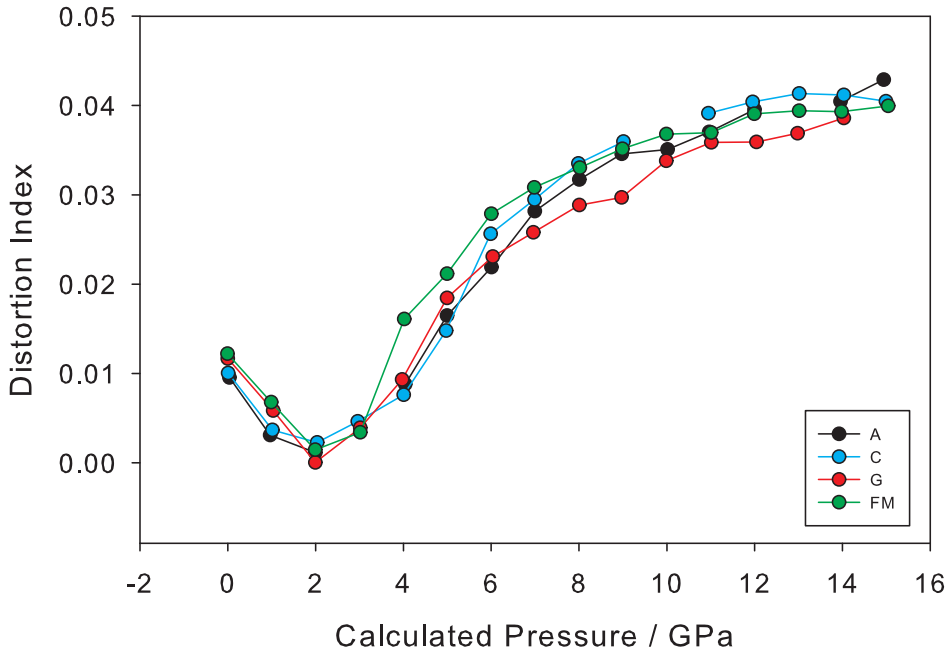

Figure 4.17 – Change in [MnO_6] octahedral distortion under applied pressure in $MnSb_2O_4$.

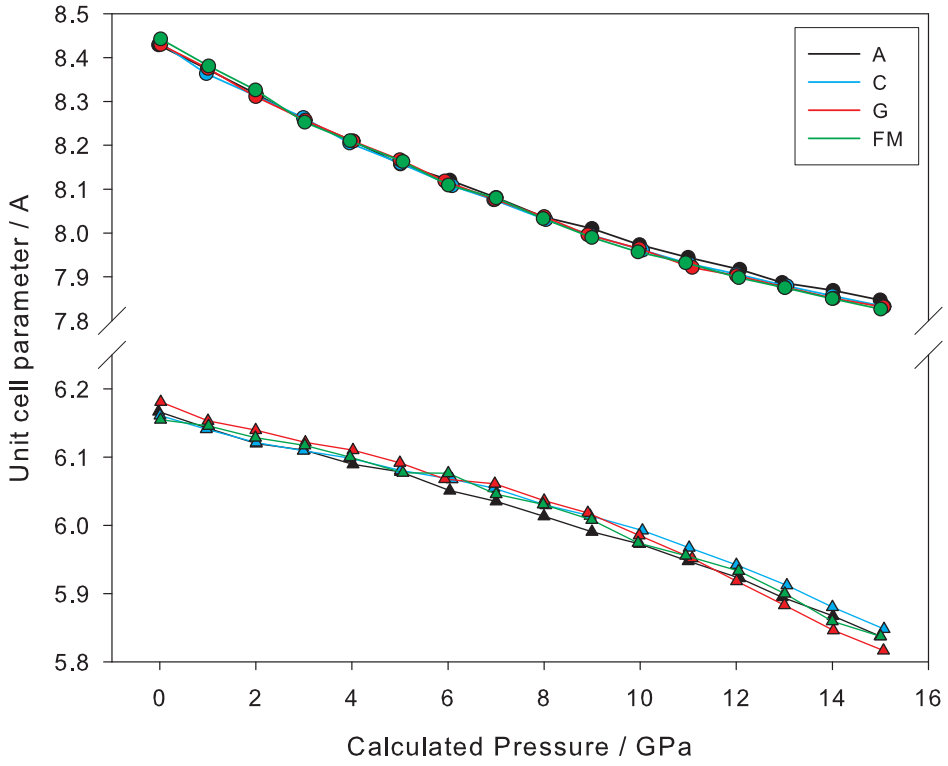

Figure 4.18 – Change in *a* and *c* unit cell parameters in $NiSb_2O_4$ under applied pressure. *a*-circles; *c*-triangles.

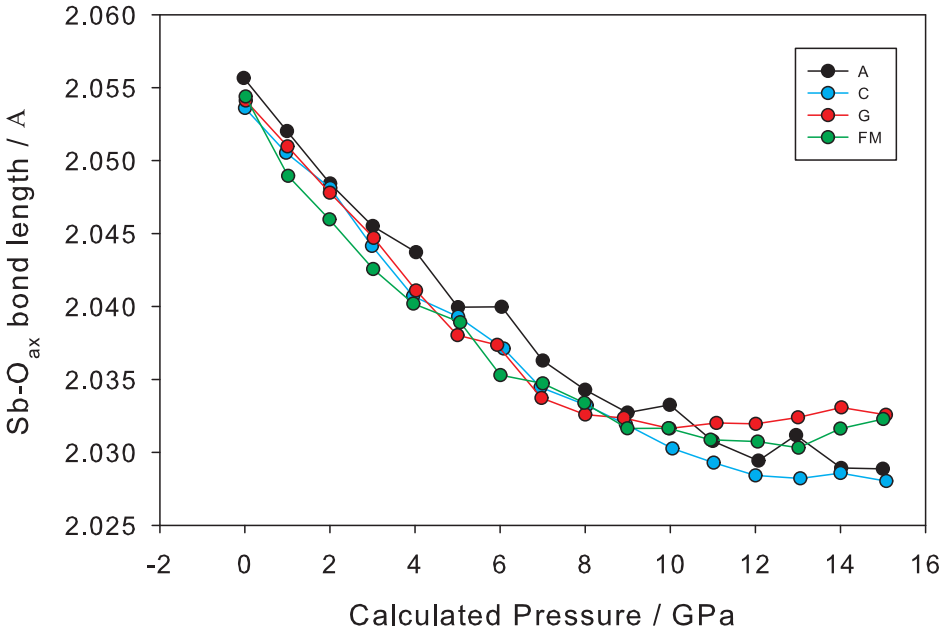

Figure 4.19 – Change in Sb−O2$_{ax}$ bond length under applied pressure in $NiSb_2O_4$.

correlated with the Sb−O2$_{ax}$ bondlength (figure 4.19) and Ni−O1$_{eq}$−Ni bond angle (figure 4.20), respectively. As the Sb−O2$_{ax}$ bond length decreases with pressure, the Sb−O1$_{eq}$ bond increases almost linearly to compensate, consistent with an increased distortion around Sb to accommodate the LP within the reduced unit cell volume. The decrease in Ni−O1$_{eq}$−Ni bond angle under pressure allows for adjacent octahedra to move closer together, but in addition an increase in octahedral twist angle is observed (figure 4.21). This twisting provides a mechanism to accommodate the unit cell contraction, while allowing for the change in coordination around the Sb cation.

In addition, the quadratic elongation of the Ni octahedra is seen to increase rapidly at low pressure, but levelling off at higher pressures (figure 4.22). This elongation of the octahedra goes against the overall contraction in the *ab* plane, but overall the octahedral volume still decreases linearly with pressure. This change in the effective crystal field around Ni on increasing pressure could be related to the observed change in magnetic groundstate (section 4.8.2).

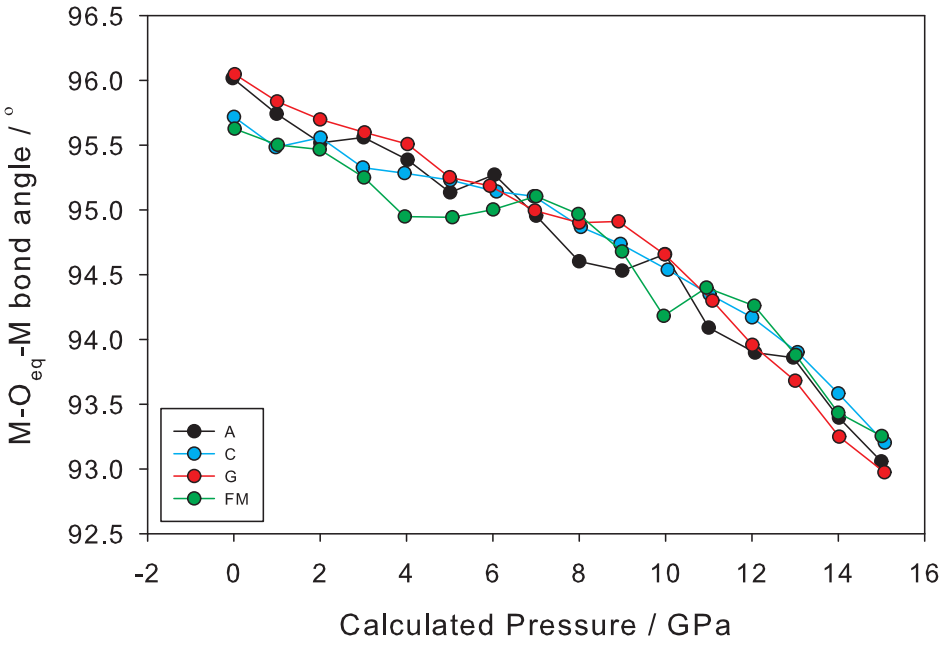

Figure 4.20 – Change in Ni−O1$_{eq}$−Ni bond angle under applied pressure in $NiSb_2O_4$.

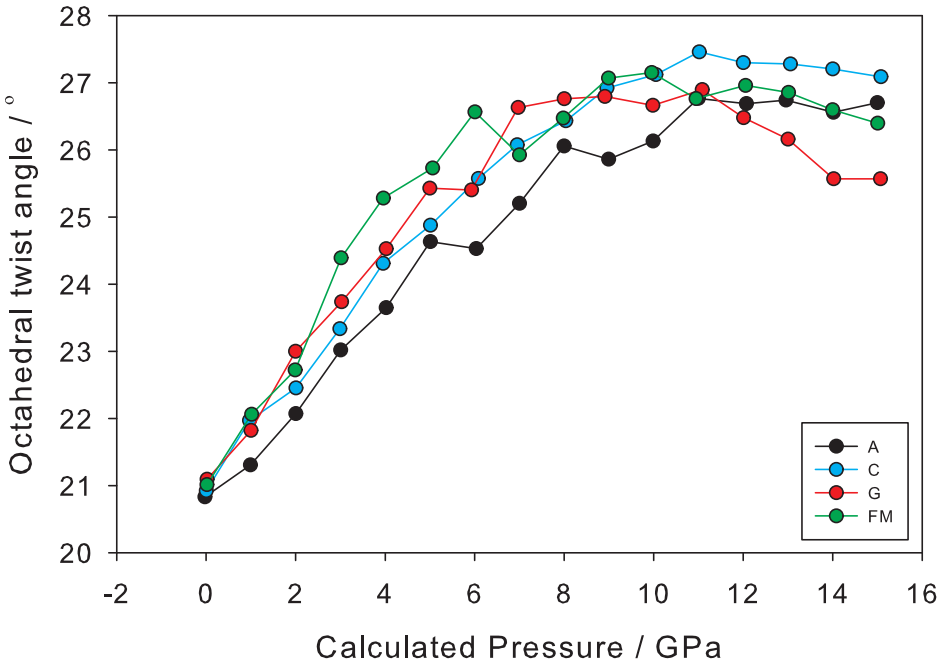

Figure 4.21 – Change in octahedral twist under applied pressure in $NiSb_2O_4$.

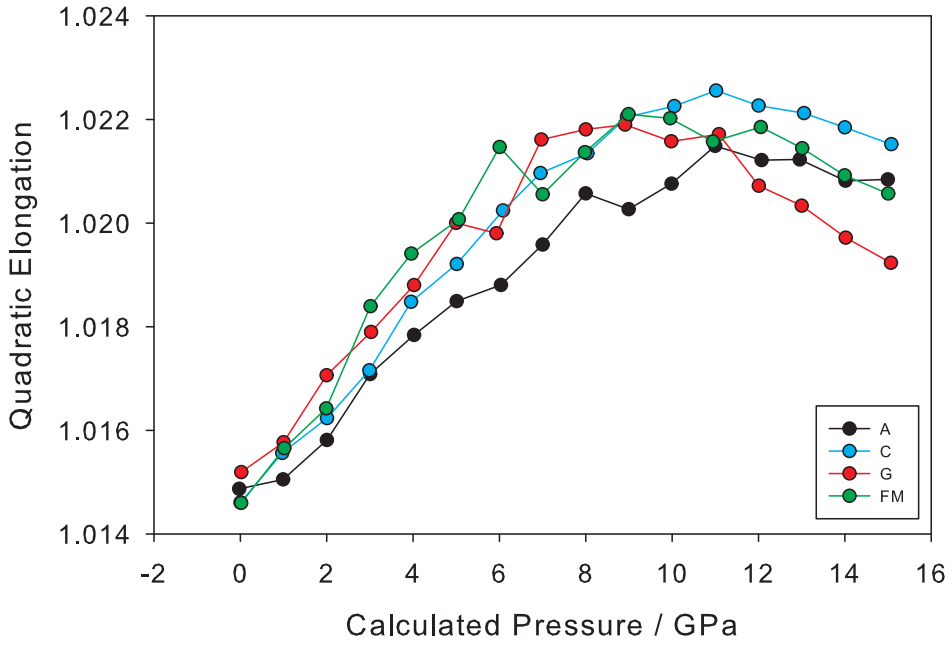

Figure 4.22 – Change in [NiO_6] octahedral quadratic elongation under applied pressure in $NiSb_2O_4$.

4.8 Variation of Magnetism Under Applied Pressure

In many materials, changes occur in the magnetic behaviour under applied pressure due to variations in the interactions between magnetic ions. For this reason, the stabilities of the different magnetic ordering modes in the MSb_2O_4 series were investigated. The pressure range investigated could be applied using physical methods (such as using a diamond anvil cell (DAC)) or through 'chemical' pressure (*i.e.* ionic substitution within the structure to produce an overall change in unit cell size or strain).

Under applied pressure, the total enthalpy for each state increases almost linearly (see for example figure 4.23), the enthalpy change due to pressure being much more than the enthalpy differences between magnetic states. While the reported enthalpy differences are highly dependent on the FM enthalpy obtained, the results can be checked for anomalies by plotting enthalpy relative to a linear fit to the FM data (figure 4.24). For all systems studied, the variation in total enthalpy relative to the regression curve show a similar shape.

The variation of enthalpy (relative to the FM enthalpy) with pressure for M = Mn and Ni are

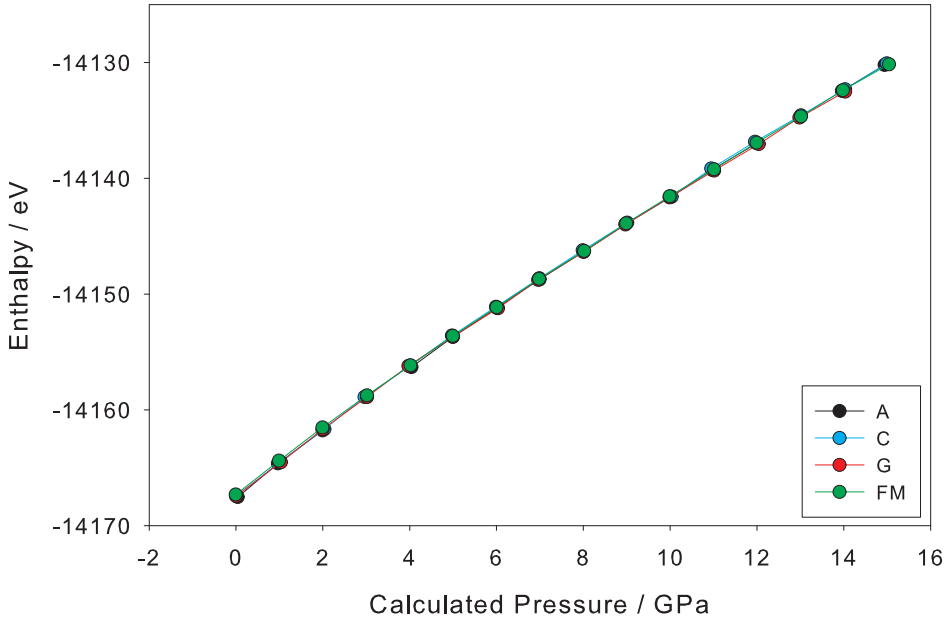

Figure 4.23 – Change in calculated total enthalpy for $MnSb_2O_4$ under applied pressure.

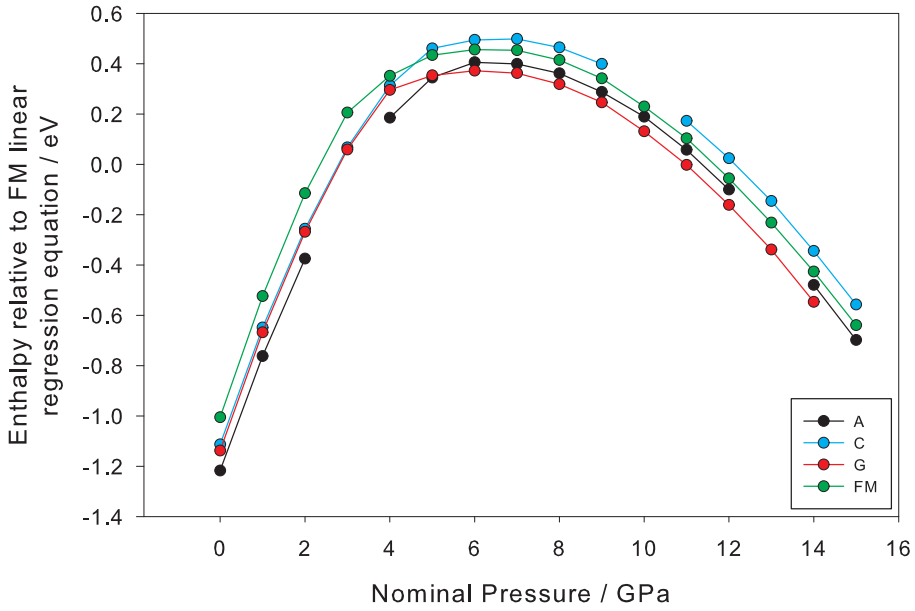

Figure 4.24 – Plot of enthalpy difference relative to least-squares linear fit to FM total enthalpy data ($E_{state} - E_{fit}$) for $MnSb_2O_4$.

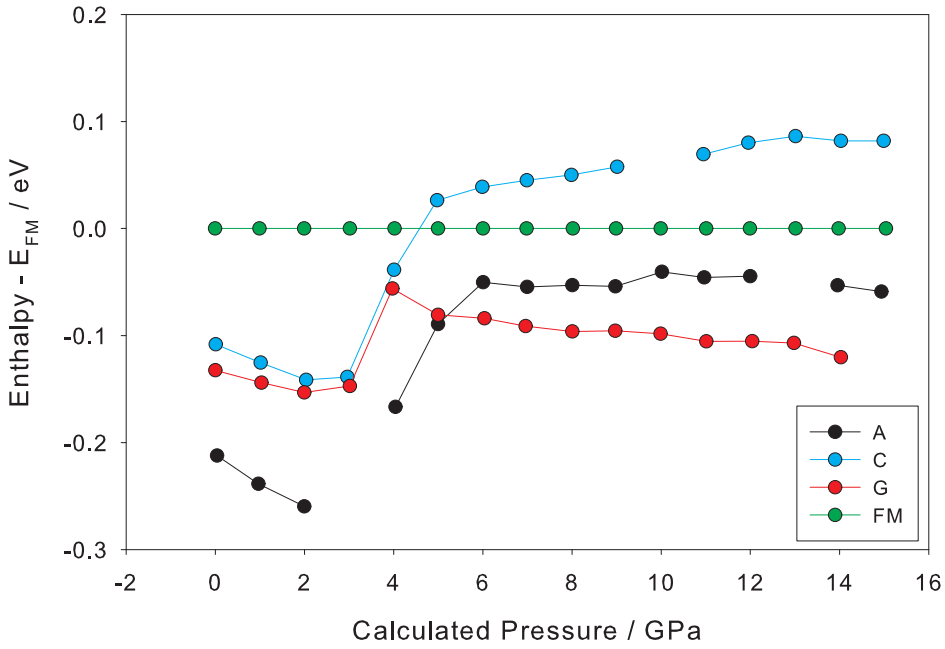

Figure 4.25 – Variation of enthalpy relative to FM state under applied pressure in $MnSb_2O_4$.

shown in figures 4.25 and 4.28, respectively, and are discussed below.

4.8.1 $MnSb_2O_4$

$MnSb_2O_4$ (figure 4.25) shows very interesting behaviour under pressure; above 5 GPa, the A-mode ceases to be the lowest enthalpy magnetic structure, and the G-type becomes most stable. This occurs due to the slightly different curvatures of the enthalpy with respect to pressure, as can be seen in figure 4.24. This change in ordering is somewhat reflected in experimental results, where a significant G-type order has been observed previously.[7] It is also strongly correlated to both the calculated octahedral twist angle (figure 4.26) and quadratic elongation (figure 4.27), where the G-mode shows a sudden change in the same pressure region. What is unclear, however, is whether the change in octahedral coordination promotes the change in magnetic groundstate, or whether the G-type structure is favourable due to the contracted unit cell, and the geometry-optimised structure only further minimises the overall enthalpy. Relating the effect to experimental data, it is clear that different sample preparation methods could lead to different residual strains which may cause changes in the octahedral coordination, resulting in the observed G-mode. Further work at high pressure could help to rationalise this effect more

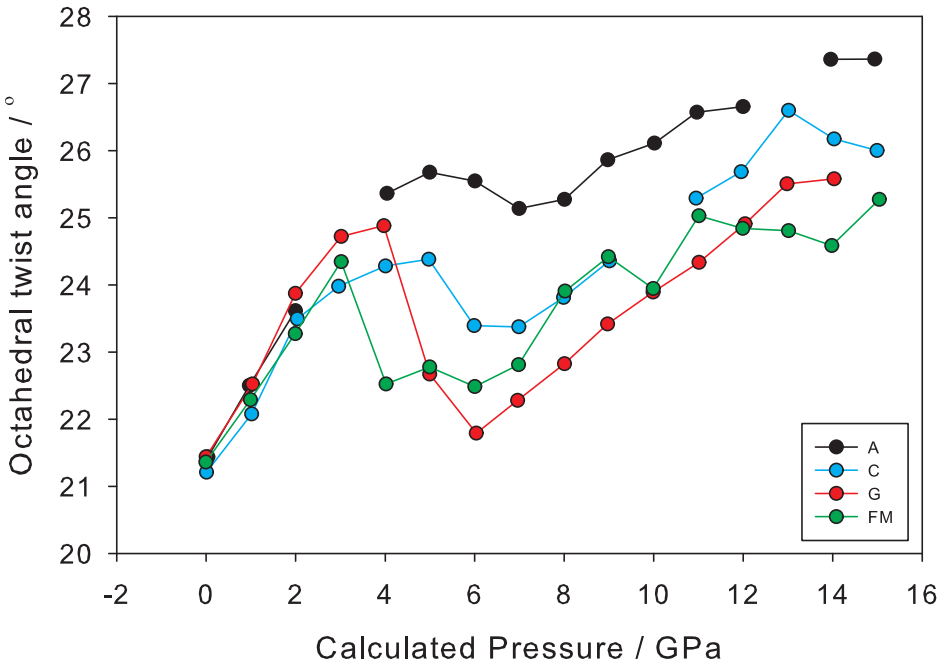

Figure 4.26 – Variation of octahedral twist angle under applied pressure in $MnSb_2O_4$.

precisely.

4.8.2 $NiSb_2O_4$

The enthalpy differences between magnetic states in $NiSb_2O_4$ (figure 4.28) is less than in the other systems studied, and also shows different ordering behaviour; whereas other systems show pairing of the A / G and C / FM modes (as seen in the structural parameters) this is not seen in $NiSb_2O_4$. Instead, a C-type groundstate is predicted, but only marginally below an A-state. Indeed, a transition between the two states is predicted above 10 GPa. This is inconsistent with experimental reports, where a weak G-component is observed at 4 GPa.[16] Both results do suggest a development of AFM ordering along the octahedral chains with pressure, the difference being in *inter*-chain ordering. Calculations involving non-collinear ordering may be necessary to reproduce the experimental results, however, due to the extra interactions involved.

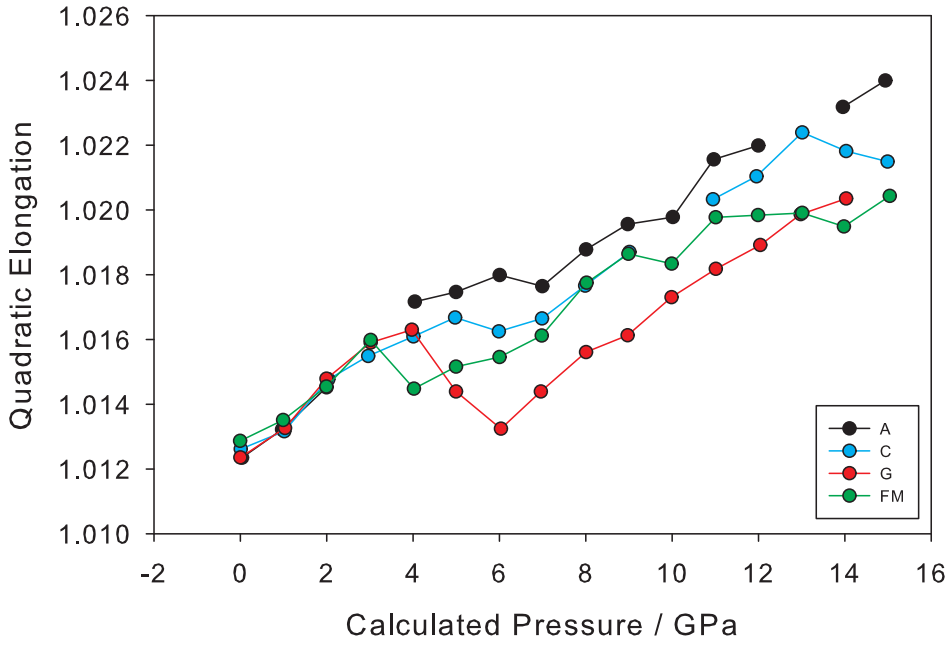

Figure 4.27 – Variation of [MnO_6] quadratic elongation under applied pressure in $MnSb_2O_4$.

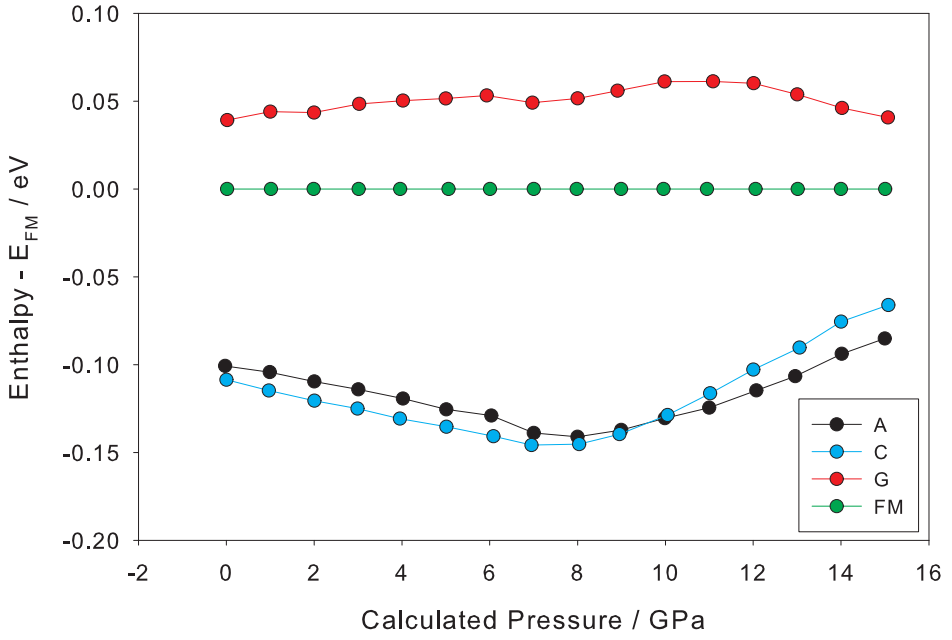

Figure 4.28 – Variation of Enthalpy relative to FM state under applied pressure in $NiSb_2O_4$.

4.9 Magnetic Coupling Parameters

Using the method described in section 3.4, Heisenberg coupling constants between the magnetic cations were calculated for each of the MSb_2O_4 systems. Calculated total energies were used for the calculations (with a correction applied to account for the finite basis set[33]) and were obtained for each magnetic order, within each of the geometry-optimised structures. The reported values (table 4.5) are an average of the four geometry-optimisation results; although the different structures gave slightly different values, they were all of a similar magnitude and sign. In addition, the energy of each of the magnetic structures within the experimental unit cell were also calculated for comparison. Calculating total energies in this way avoids problems due to variable unit cell size, although the deviations are small.

From these values, it is clear that J_1 is the dominant interaction in most cases, often by a considerable amount. This is not unexpected given the close proximity of the cations along the chains, compared with the longer-range interactions J_2 and J_3. The large value of J_1 directly correlates with the magnetic groundstate predicted; a negative J_1 will give rise to either A- or G-type magnetism, while a positive J_1 will lead to C or FM.

The J_1 coupling can be rationalised as a combination of direct exchange between adjacent M cations along the chains, and 90° superexchange occurring via the M−O−M pathway. The latter $d_{x^2-y^2} - O_{2p}|O_{2p} - d_{x^2-y^2}$ interaction is predicted by Goodenough-Kanamori rules[34] to be FM, while the direct interaction (primarily $d_{xy} - d_{xy}$) would be expected to be AFM for two HS d^5 cations (such as Mn^{2+}). Greater occupancy of the t_{2g} orbitals would be expected to decrease the strength of the direct-exchange interaction (assuming localised electrons), negating it completely for $NiSb_2O_4$. This change in direct-exchange strength due to filling of the t_{2g} on crossing the TM series is directly reflected in the change in J_1, from negative for Mn (dominant direct-exchange) to positive for Ni (dominant super-exchange).

The value of J_1 calculated for $NiSb_2O_4$ is much less than expected, smaller in magnitude than J_3. This shows a much weaker interaction consistent with a dominant superexchange, however, the experimental ordering temperature (47.0(5) K[1]) is of a similar value to both $MnSb_2O_4$ and $FeSb_2O_4$ (55 K[7] and 46 K,[10] respectively). The overall ordering temperature will be related

Table 4.5 – Calculated J-coupling values for MSb_2O_4 from both average geometry-optimised structures (Opt.), and experimental geometries (Expt).

	$MnSb_2O_4$		$NiSb_2O_4$	
	Opt.	Expt.	Opt.	Expt.
E_0 (eV)	-14167.498	-14163.103	-16564.781	-16563.618
J_1 (meV)	-2.92	-5.11	1.51	2.31
J_2 (meV)	-0.17	-0.18	0.49	0.52
J_3 (meV)	-0.56	-0.43	-1.93	-1.95
J_1/K_b (K)	-33.9	-59.2	17.5	26.8
J_2/K_b (K)	-2.0	-2.1	5.7	6.0
J_3/K_b (K)	-6.5	-5.0	-22.4	-22.7

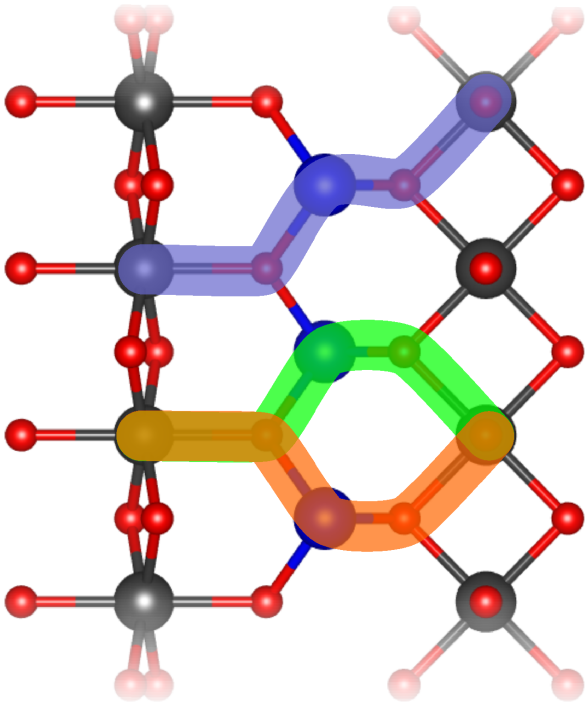

Figure 4.29 – J_2 (highlighted orange and green) and J_3 (highlighted blue) exchange pathways *via* O−Sb−O linkages within MSb_2O_4, viewed approximately along [110].

to all of the interactions present, however, so the ordering will not depend solely on J_1; the similar magnitudes of J_1 and J_3 may result in an enhanced effect, rather than cancellation between them. Similar calculations for $NiAs_2O_4$ (known to order experimentally at 53.5(5) K[1]) give equally small coupling values (2.1 meV, 0.7 meV and -1.9 meV for J_1, J_2, and J_3 respectively) suggesting that the low values are inherently related to the presence of Ni within the structure.

The J_2 and J_3 values are generally smaller than J_1, but serve to differentiate between A / FM or G / C ordering, depending on whether the overall interaction between chains is positive or negative, respectively. Somewhat surprisingly, J_3 has a larger magnitude than J_2 for all systems; based purely on interaction distance, J_3 should be weaker. The atomic interaction pathway is actually very similar for both J_2 and J_3, however, occurring primarily through the O−Sb−O chain linkages (d_{z^2} − O−Sb−O − $d_{x^2-y^2}$, figure 4.29). The origin of the weaker interaction for

J_2 *cf.* J_3 could be related to a conflict between the two similar J_2 pathways (highlighted orange and green) resulting in a reduced interaction overall; for J_3, such a conflict does not exist.

The J_2 interaction is of a similar strength for Mn and Ni, although the sign is closely correlated with the observed change from A-type to C-type on crossing the TM series; for $MnSb_2O_4$ it is negative, while for $NiSb_2O_4$ it is positive. Overall, J_2 is opposed to the predicted groundstate; for A-type (where the inter-chain alignment in the *ab* plane is parallel) J_2 is negative, while for C-type (where adjacent chains are aligned AFM) J_2 is positive. J_3 is negative for both compounds, suggesting a strong tendency towards C- or G-type structures. The A-type observed for $MnSb_2O_4$ can be rationalised due to the relatively strong negative J_2 exchange.

4.10 Conclusions

This chapter has presented results of DFT calculations on a range of MSb_2O_4 compounds (M = Fe, Mn, Co, Ni and Cu) and predicted both structural and magnetic response under applied pressure. Using the PBE functional, optimised lattice parameters are within 6% of experimental results; $FeSb_2O_4$ and $CuSb_2O_4$ both show a contraction of the a parameter in contrast to the over-estimate expected. DFT results show less variance in M−O bond lengths compared to experimental results, at the expense of greater angular distortion within the octahedral chains. Although overestimated compared to experiment, the Sb−O bonds show little interesting variation between compounds.

Study of the magnetic ordering within MSb_2O_4 reveals a change in groundstate similar to that observed experimentally, from A-type for $MnSb_2O_4$ to C-type for $NiSb_2O_4$. $FeSb_2O_4$ shows anomalous behaviour, with DFT predicting a C-type structure, while A-type is observed experimentally. This (and the associated metallic groundstate) can be corrected using an abnormally high Hubbard on-site repulsion term $(U = 8\ eV)$ compared to other reports, indicating complex magnetic behaviour and strong electron correlations. DFT also predicts an incorrect metallic groundstate for $CoSb_2O_4$, although for $1\ eV \leq U \leq 10\ eV$ the correct semiconducting behaviour is obtained.

All compounds show valence bands dominated by a mixture of M d-orbitals and O p-

orbitals, while the valence band corresponds mainly to Sb *p*-orbitals, with a greater DOS at higher energies corresponding to unoccupied M *d*-orbitals. Under applied pressure, $MnSb_2O_4$ and $NiSb_2O_4$ both show changes in magnetic groundstate, to G- and A-type, respectively.

Under applied pressure all systems show a contraction in both *a* and *c*, although more significant in *a*. This is related both to changes in octahedral coordination (particularly the $M-O2_{ax}$ bonds and $M-O1_{eq}-M$ angle) and changes in the Sb trigonal pyramid environment, in order to accommodate the Sb LP within the contracted structure.

Calculations of Heisenberg *J*-coupling parameters from the magnetic state energies have found that the J_1 (intra-chain) interaction is dominant for $MnSb_2O_4$, and dictates the magnetic groundstate. For $NiSb_2O_4$, the J_3 (inter-chain, inter-plane) interaction is dominant, consistent with the absence of a direct Ni−Ni interaction. The J_3 interaction has been found to be more significant for magnetic ordering than the J_2 (inter-plane) interaction for both compounds, and has been rationalised due to competing pathways within the J_2 description, not seen for J_3. The competition between these interactions is critically dependent on the Sb−O coordination, and so could explain the change in magnetic structures observed under pressure.

References

[1] H. T. Witteveen, *Solid State Communications*, 1971, **9**, 1313–1315.

[2] J. Goodenough, *Magnetism and the Chemical Bond*, Interscience Publishers, 1963.

[3] J. R. Gavarri, R. Chater and J. Ziółkowski, *Journal of Solid State Chemistry*, 1988, **73**, 305–316.

[4] M. T. Atanasova, A. M. Strydom, C. J. H. Schutte, L. C. Prinsloo and W. W. Focke, *Journal of Materials Science*, 2014, **49**, 3497–3510.

[5] C. R. A. Catlow, Z. X. Guo, M. Miskufova, S. A. Shevlin, A. G. H. Smith, A. A. Sokol, A. Walsh, D. J. Wilson and S. M. Woodley, *Philosophical Transactions of the Royal Society A: Mathematical, Physical and Engineering Sciences*, 2010, **368**, 3379–3456.

[6] J. R. Gavarri and A. W. Hewat, *Journal of Solid State Chemistry*, 1983, **49**, 14–19.

[7] H. Fjellvåg and A. Kjekshus, *Acta Chemica Scandinavica Series A-Physical and Inorganic Chemistry*, 1985, **39**, 389–395.

[8] M. J. Whitaker, R. D. Bayliss, F. J. Berry and C. Greaves, *Journal of Materials Chemistry*, 2011, **21**, 14523–14529.

[9] R. Chater, J. R. Gavarri and A. Hewat, *Journal of Solid State Chemistry*, 1985, **60**, 78–86.

[10] G. Gorodetsky, M. Sayar and S. Shtrikman, *Materials Research Bulletin*, 1970, **5**, 253–255.

[11] R. Chater, K. Chhor, J. R. Gavarri and C. Pommier, *Materials Research Bulletin*, 1986, **21**, 703–708.

[12] F. Varret, P. Imbert, A. Gerard and F. Hartmann-Boutron, *Solid State Communications*, 1968, **6**, 889–892.

[13] B. P. de Laune and C. Greaves, *Journal of Solid State Chemistry*, 2012, **187**, 225–230.

[14] R. Chater, K. Chhor, J. R. Gavarri and C. Pommier, *Materials Research Bulletin*, 1985, **20**, 1427–1434.

[15] B. Hinrichsen, R. E. Dinnebier, P. Rajiv, M. Hanfland, A. Grzechnik and M. Jansen, *Journal of Physics: Condensed Matter*, 2006, **18**, S1021–S1037.

[16] R. Chater, J. R. Gavarri and A. W. Hewat, *Journal of Solid State Chemistry*, 1987, **67**, 98–103.

[17] S. J. Clark, M. D. Segall, C. J. Pickard, P. J. Hasnip, M. I. J. Probert, K. Refson and M. C. Payne, *Zeitschrift fuer Kristallographie*, 2005, **220**, 567–570.

[18] G. Kresse, *Physical Review B*, 1996, **54**, 11169–11186.

[19] B. G. Pfrommer, M. Cote, S. G. Louie and M. L. Cohen, *Journal of Computational Physics*, 1997, **131**, 233–240.

[20] F. Tran, R. Laskowski, P. Blaha and K. Schwarz, *Physical Review B*, 2007, **75**, 115131.

[21] J. A. Gonzalo, D. E. Cox and G. Shirane, *Physical Review*, 1966, **147**, 415–418.

[22] M. Lax, *Symmetry Principles in Solid State and Molecular Physics*, John Wiley & Sons Inc, 1974.

[23] R. J. Nicholls, A. J. Morris, C. J. Pickard and J. R. Yates, *Journal of Physics: Conference Series*, 2012, **371**, 012062.

[24] A. J. Morris, R. J. Nicholls, C. J. Pickard and J. R. Yates, *The OptaDOS code*, in preparation.

[25] J. Yates, X. Wang, D. Vanderbilt and I. Souza, *Physical Review B*, 2007, **75**, 195121.

[26] R. D. Shannon, *Acta Crystallographica Section A*, 1976, **32**, 751–767.

[27] M. J. Whitaker, *Synthesis and Characterisation of Chemically Modified Schafarzikite and Pyrochlore minerals*, PhD thesis, School of Chemistry, The University of Birmingham, 2013.

[28] B. P. de Laune, *Impedance spectroscopy of $CoSb_2O_4$*, Private Communication.

[29] H.-C. Wu, S.-H. Li and S.-W. Lin, *International Journal of Photoenergy*, 2012, **2012**, 1–6.

[30] M. S. Senn, I. Loa, J. P. Wright and J. P. Attfield, *Physical Review B*, 2012, **85**, 125119.

[31] Y. G. Yu, H. Hsu, M. Cococcioni and R. M. Wentzcovitch, *Earth and Planetary Science Letters*, 2012, **331-332**, 1–7.

[32] R. E. Dinnebier, S. Carlson, M. Hanfland and M. Jansen, *American Mineralogist*, 2003, **88**, 996–1002.

[33] G. P. Francis and M. C. Payne, *Journal of Physics: Condensed Matter*, 1990, **2**, 4395–4404.

[34] J. B. Goodenough, *Physical Review*, 1960, **117**, 1442–1451.

Chapter 5
Magnetic and Structural Characterisation of $CuAs_2O_4$

5.1 Background

The mineral Trippkeite ($CuAs_2O_4$) was first investigated by Zemann[1] and was found to adopt the Schafarzikite structure-type ($P4_2/mbc$, a = 8.59(4) Å and c = 5.56(5) Å). Later, a synthetic sample was prepared by Pertlik[2] from CuO and As_2O_3 under hydrothermal conditions in concentrated acetic acid (200 °C) with an almost identical structure. Compared with $FeSb_2O_4$, the structure shows significantly more elongation in the [MO_6] octahedra (quadratic elongation of 1.0325 *cf.* 1.0107[3]) and a correspondingly large *a*/*c* ratio of 1.54 *cf.* 1.46 (figure 5.1). Despite this, the average M−O bond length is similar (2.12 Å *cf.* 2.13 Å in $FeSb_2O_4$). The unit cell volume is one of the smallest for any MX_2O_4 composition, however, only being surpassed by $NiAs_2O_4$; this is due to the size of the As cation. The average M−X bond length is only 1.80 Å in $CuAs_2O_4$, compared with 1.98 Å in $FeSb_2O_4$. $CuAs_2O_4$ also shows one of the smallest octahedral 'twist' angles (14.1°) of any of the MX_2O_4 compositions, only found to be less in $TiSn_2O_4$.[4]

The recently reported $CuSb_2O_4$[5] adopts a slightly different tetragonal crystal structure to $CuAs_2O_4$ ($P4_2bc$) with a = 8.76033(5) Å and c = 5.79786(4) Å. Here, the Cu octahedra are significantly distorted, showing three distinct M−O bond lengths, rather than two as in $CuAs_2O_4$. The compound has been characterised magnetically as a system of isolated (1D) Heisenberg-

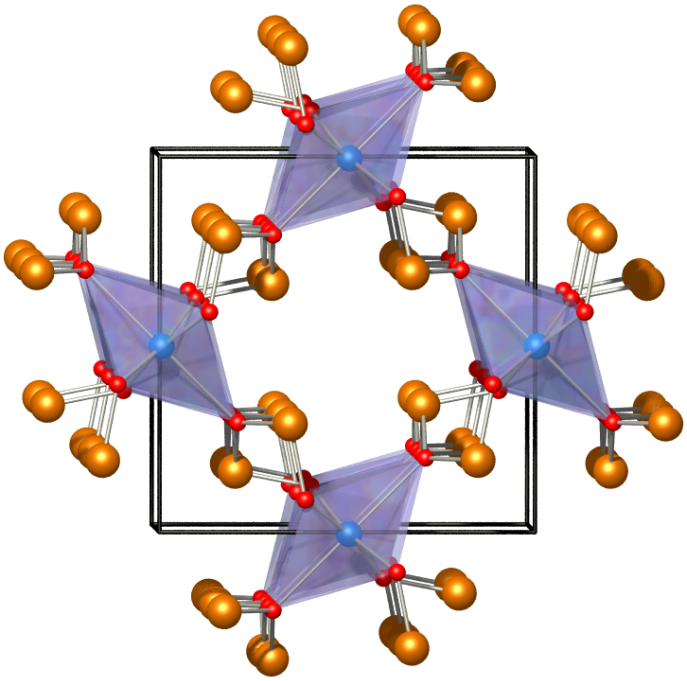

Figure 5.1 – $CuAs_2O_4$ structure viewed along [001]. Cu-purple octahedra, As-orange spheres, O-red spheres.

like chains, showing a broad reduction in susceptibility at *ca.* 10 K, and non-Curie-Weiss behaviour above this temperature. Development of long-range AFM order has been suggested below 1.8 K from both heat capacity and susceptibility measurements, however, the nature of this is currently undetermined.

This chapter reports the successful prediction using DFT of a FM groundstate in $CuAs_2O_4$ (the first reported FM state in any MX_2O_4 system) and the subsequent synthesis and magnetic characterisation of this compound. Also reported are the electronic properties of the material, and attempts to produce mixed Cu oxidation states within the octahedral chains.

5.2 Synthesis and Computational Method

$CuAs_2O_4$ was synthesised by a hydrothermal method, heating a mixture of CuO ($>$ 99 %, Aldrich) and As_2O_3 ($>$ 99 %, Aldrich) in 9 cm^3 of de-ionised water at 180 °C for 48 hours. This gave an approximate saturated vapour pressure of 1 MPa, although the desired product can form over a wide temperature/pressure range, potentially even under atmospheric reflux.[2]

XRPD data were collected on the D8 diffractometer, while NPD patterns were recorded on the GEM diffractometer at ISIS. GEM data were collected at a range of temperatures using 8 mm diameter vanadium cans. All data were refined with GSAS and EXPGUI.[6,7] The diffraction background was modelled using a shifted Chebyschev function, and peak shapes were modelled using GSAS profile type 2. TOF-dependent absorption for NPD data was modelled using a single (linear) term constrained to be equal for all histograms. Preferred orientation was found to be necessary, and was applied using the MD function for the [001] planes; it was constrained to be equal for both magnetic and nuclear phases, and all histograms.

Calculations were performed using CASTEP; planewave and k-point convergence was precise to 0.5 meV per unit cell. This necessitated a planewave cut-off energy of 1050 eV and a Brillouin zone sampling of $3 \times 3 \times 4$ k-points. Self-consistent geometry optimisations of both unit cell volume and atomic positions were performed for A, C, G and FM magnetic structures. In some cases, it was necessary to constrain the total and/or absolute magnetic moments for a large (≤ 300) number of self-consistent iterations, in order to converge to the desired magnetic structure.

5.3 Magnetic Groundstate Prediction

DFT calculations were initially performed for $CuAs_2O_4$ based on the reported (room temperature (RT)) structure of Pertlik.[2] Using the PBE functional and the default CASTEP PSP definitions, theoretical unit cell parameters were all within 4 % of experimental results, and atomic positions show a maximum RMS deviation of 0.013 (fractional coordinates) from the initial structure. Unit cell parameters and selected structural details are given in table 5.1. As is typical for a GGA such as PBE, the c-axis is overestimated compared to the experimental value. Unexpectedly, however, the a-parameter is underestimated. This is primarily due to a reduction in the $Cu-O2_{ax}$ bond lengths compared to experiment, which act along the [110] and $[\bar{1}10]$ directions, directly influencing a. Although the $Cu-O1_{eq}$ bonds are overestimated as expected, there is a net decrease in octahedral volume compared with experiment. Overall, the theoretical results show a reduction in quadratic elongation compared to experiment, $\langle\lambda\rangle = 1.01$ *cf.* 1.03.

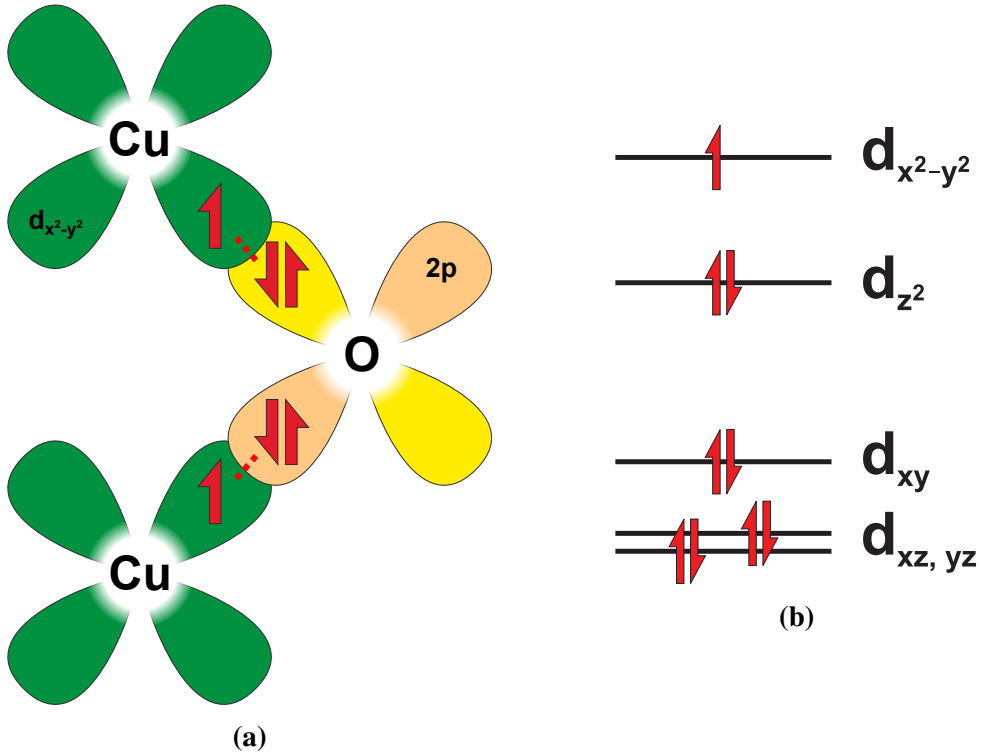

Figure 5.2 – (a) Schematic showing the 90° super-exchange interaction between edge-shared $[CuO_6]$ octahedra viewed approximately along [110]; (b) schematic showing crystal field levels for Jahn-Teller distorted Cu^{2+}.

The cause of the reduced $Cu-O2_{ax}$ bond lengths is unclear, but indicates a preference for a reduced Jahn-Teller (JT) elongation in the theoretical case. It is also worth noting that the calculations show less octahedral twisting along the edge sharing chains than experimental results. These two factors show that DFT predicts a more regular octahedral arrangement.

From these calculations, the minimum enthalpy state is FM (values given in table 5.2). The fact that the FM- and C-magnetic structures lie considerably lower in enthalpy than A- and G- shows a definite preference within the structure for ferromagnetic spin alignments along the octahedral chains. This can be explained through a dominant 90° $Cu-O-Cu$ superexchange occurring along the edge-sharing octahedral chains. Goodenough-Kanamori rules[8] predict a FM interaction for Cu^{2+} (d^9), in order to maximise orbital overlap between the partially occupied $d_{x^2-y^2}$ orbitals on Cu and the O_{2p} orbitals (figure 5.2a). Here direct exchange between the copper cations (which would predict AFM coupling) does not occur because of the filled t_{2g} orbitals (figure 5.2b).

Table 5.1 – Unit cell parameters and selected structural parameters for CASTEP geometry optimisations and experimental results.

	CASTEP Default PSPs				CASTEP Modified PSPs				Pertlik (300 K)[2]	NPD (300 K)	NPD (1.8 K)
	A	C	G	FM	A	C	G	FM			
a / Å	8.242	8.254	8.252	8.250	9.151	9.090	9.160	9.073	8.592(4)	8.5942(3)	8.5573(2)
c / Å	5.751	5.694	5.747	5.689	5.662	5.635	5.665	5.633	5.573(4)	5.5456(2)	5.5485(1)
$Cu-O2_{ax}$ / Å	2.123	2.109	2.133	2.108	2.807	2.753	2.817	2.739	2.472	2.4652(1)	2.42976(6)
$Cu-O1_{eq}$ / Å	1.986	1.992	1.983	1.989	1.941	1.951	1.940	1.952	1.945	1.92752(5)	1.94011(4)
Quadratic Elongation	1.005	1.005	1.006	1.004	1.071	1.064	1.072	1.062	1.033	1.034	1.029
$As-O2_{ax}$ / Å	1.887	1.886	1.887	1.887	1.842	1.842	1.841	1.843	1.815	1.80790(5)	1.81955(5)
$As-O1_{eq}$ / Å	1.781	1.775	1.782	1.775	1.801	1.801	1.801	1.800	1.765	1.77000(7)	1.76375(6)
$\angle$ $As-O2_{ax}-As$ / °	126.17	124.61	125.93	124.69	127.07	125.56	127.34	125.37	127.25	126.630(2)	126.131(2)
$\angle$ $Cu-O1_{eq}-Cu$ / °	92.75	91.24	92.84	91.33	93.63	92.46	93.78	92.34	91.50	91.989(3)	91.285(3)
Octahedral Twist / °	9.21	10.69	9.81	10.25	10.37	14.56	9.92	14.73	14.14	13.45	13.76

Table 5.2 – Calculated enthalpies for geometry-optimised structures.

Structure	Difference from groundstate (FM) / eV per cell
A	+0.307
C	+0.018
G	+0.317

The lower enthalpy of FM *cf.* C depends inherently on the inter-chain interactions, and can be related to the filling of the d_{z^2} orbital for JT-elongated Cu^{2+}. Because this $Cu_{d_{z^2}}-O2_p-Sb_p-O1_p-Cu_{d_{x^2-y^2}}$ pathway occurs through the filled d_{z^2} orbitals, it would be expected that the superexchange mechanism is disrupted completely. The explanation of FM *vs* C is unclear from a simple superexchange argument, but may reflect the competition between J_2 and J_3 coupling pathways (section 4.9).

5.3.1 Further Investigations

Following these calculations, experimental synthesis and characterisation of $CuAs_2O_4$ was carried out, which proved that the compound does exhibit a FM groundstate, ordering magnetically at T_c= 8.0 K (see section 5.4.2). Further analysis of the theoretical results indicated some inconsistencies, however.

Firstly, the predicted magnetic moment per Cu ion was found to be much higher than that expected for d^9 Cu^{2+}. Values obtained were 6.9 μ_B via Mulliken analysis (the projection of charge density onto atomic-like orbitals) or 7.2 μ_B through (*absolute moment per unit cell*)/4 (*i.e.* assuming that the total moment originates only from Cu). The large value was also confirmed by a Bader analysis method[9] (7.9 μ_B per Cu) which partitions charge (and spin) density according to minima in the charge density between atoms. The value expected for Cu^{2+} should be $\simeq 1\,\mu_B$, given that the calculations show charges on Cu as expected (+1.45 *e* and +1.61 *e* from Mulliken and Bader methods, respectively). From CASTEP's Mulliken analysis, the origin of this effect is due to a strange partitioning of electrons on the Cu; $[3d]^{6.1}[4s]^{0.4}[4p]^{3.0}$. This shows that the calculation has promoted three $3d$ electrons into the $4p$ orbitals: the electronic

states of the other atoms in the unit cell are as expected (As^{3+}, O^{2-}). This behaviour can be seen from the PDOS plot, figure 5.3. Here, the up- and down-spin *d* states are well separated in energy ($\simeq 10\,\text{eV}$), as are the *p* states. The up-spin Cu *p* electrons lie lower in energy than the down-spin *d* states, however, giving rise to a large (up-spin) *p* occupation, and the large overall moment. These *p* states are very narrow, indicating their largely localised nature, although it would be expected for them to lie higher in energy than the *s* states. For reference, the input files from these calculations are included in appendix A.1.

The second major inconsistency discovered from the DFT results was that $CuAs_2O_4$ is predicted to be metallic (see figures 5.3 and 5.4) with the Fermi level cutting across bands throughout the entire first Brillouin zone, particularly the *d* states. From experiment, $CuAs_2O_4$ was found to be an insulator (section 5.4.4). Because DFT is well known to underestimate band-gaps for highly correlated systems (see section 3.1.3) it was decided to investigate the effect of an additional Hubbard U term for Cu *d* electrons.

Values of U up to 10 eV were applied to the copper *d* electrons, the results of which are shown in figure 5.5. Addition of a U term increases the overall enthalpy of the system, but also causes significant changes in the relative stabilities of each magnetic state. For all non-zero values of U investigated, the FM state ceases to be most stable, instead predicting A-type groundstates (although equal in enthalpy to G for U = 8 eV). For U = 4 eV, the C-mode is predicted to be considerably (4.7 eV) lower in enthalpy than FM, although this is a slightly questionable comparison (see below). In all cases, the correction for on-site repulsion does not change the predicted magnetic moment, still remaining $\simeq 6.9\,\mu_B$. The origin of this continues to be the low energy *p*-states, as seen from DOS plots.

While not affecting the magnetic moment, the addition of a U term does change the density of states around the Fermi level. For $U < 4$ eV the system remains metallic, while above this value, the downwards shift in *d* electron energies causes them to drop below the Fermi energy. This results in the opening of a band-gap, which widens with increasing U. The exception to this is at 4 eV, where the C-mode alone remains metallic; this could be the origin of the vast energy differences observed.

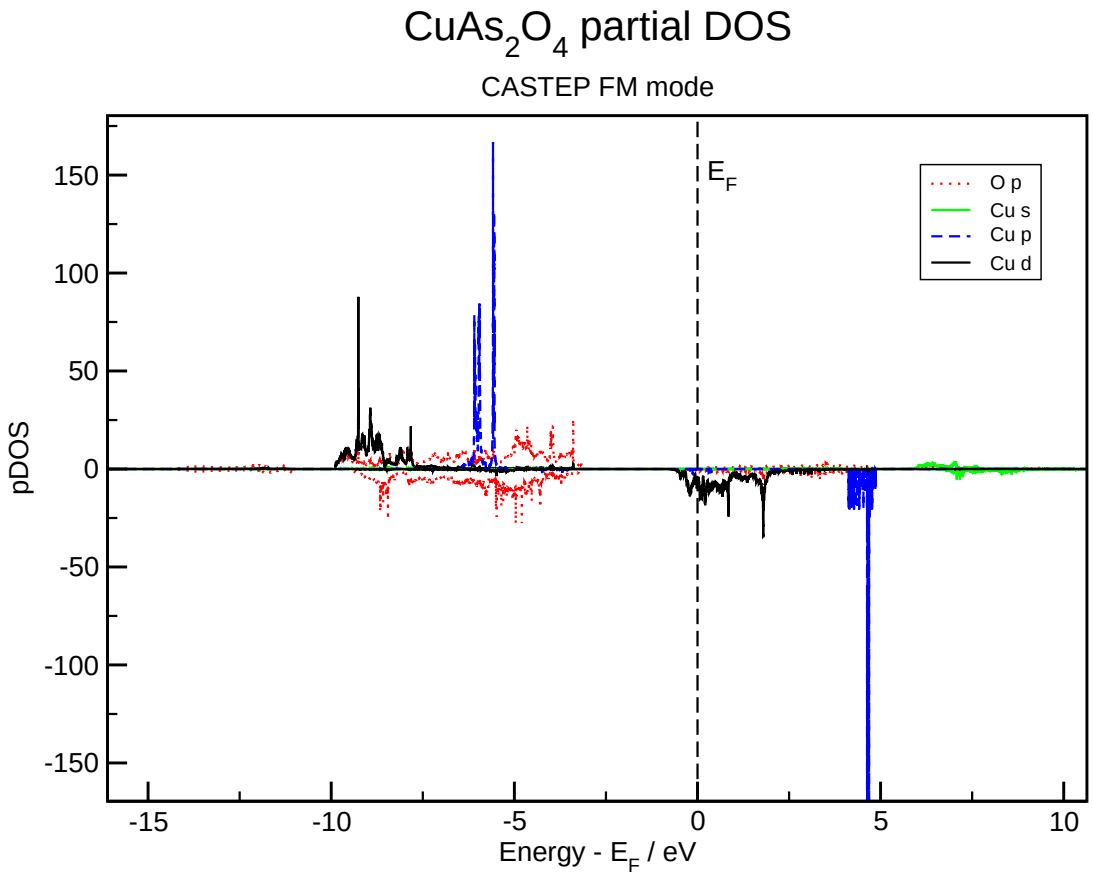

Figure 5.3 – Section of PDOS for $CuAs_2O_4$ showing occupation of Cu *s* (green), *p* (dashed blue) and *d* (black) states, as well as O *p* states (dotted red). Up- and down-spin electronic states are reported as positive and negative pDOS, respectively, while the Fermi energy (E_F)) is shifted to 0 eV.

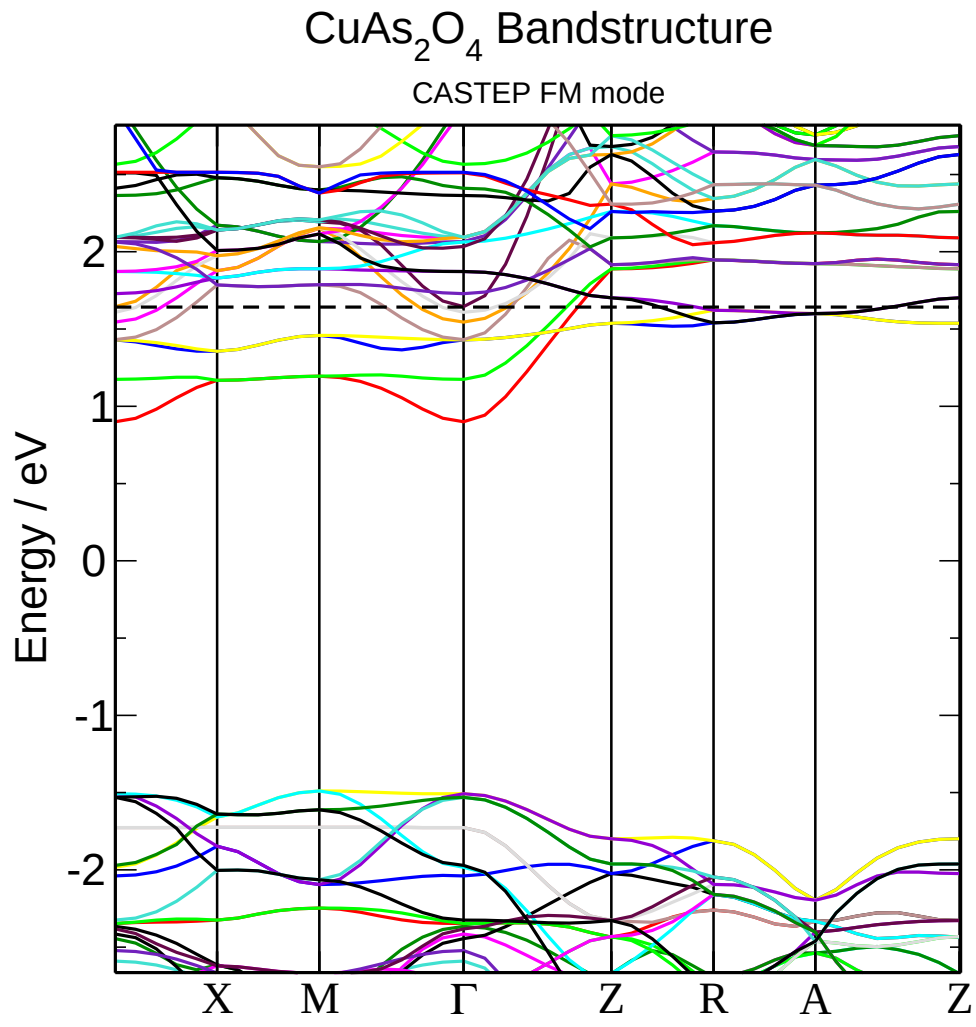

Figure 5.4 – Section of bandstructure for FM $CuAs_2O_4$. Fermi level is shown as a dashed black line, while the *x*-axis denotes a path through high-symmetry points in reciprocal space.

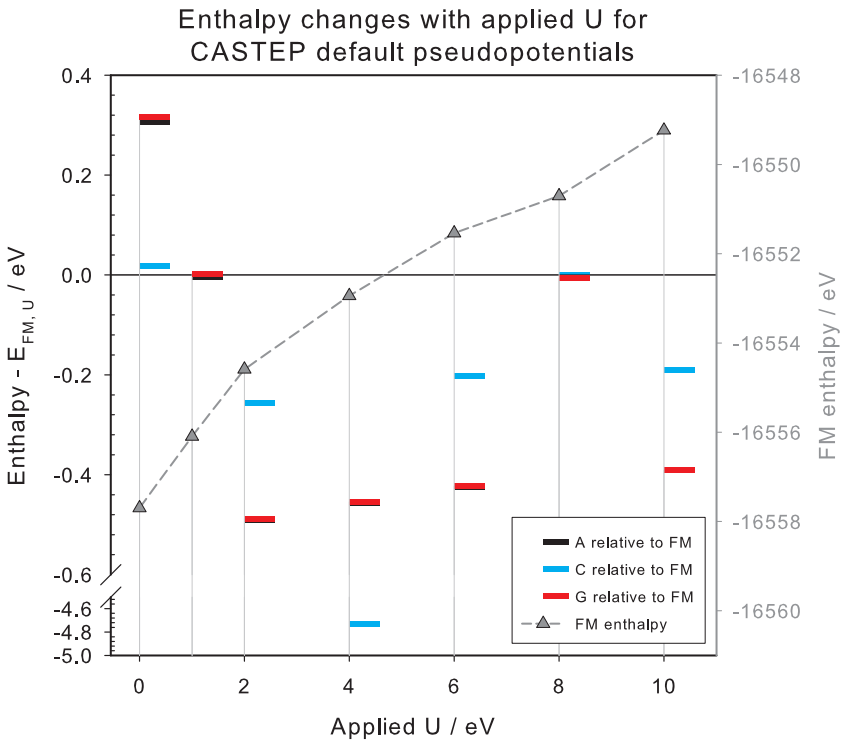

Figure 5.5 – Change in enthalpy for $CuAs_2O_4$ with increasing U applied to Cu *d* electrons. Graph shows enthalpies of A, C and G states relative to FM (boxes) as well as total FM enthalpy (triangles).

Increasing the U term promotes an increase in *a*-parameter in a loosely linear fashion. For $U \leq 10$ eV, however, the experimental lattice parameter is not reached. The *c*-axis shows a more complicated behaviour with U, however. For A- and G-type calculations, *c* decreases to a minimum at U = 2 eV (although still remains +0.15 Å *cf.* experiment) and then increases with further increases in U. The C- and FM-modes show a less regular behaviour, generally increasing with U.

The dramatic change in groundstate magnetic structure following addition of a U parameter (and the deviation away from experimental magnetic and structural results) indicates that the addition of a self-interaction correction does not have the intended effect; while it correctly modifies the metallic behaviour above U = 4 eV, the change in magnetic groundstate is inconsistent with experimental data. For this reason, other possible causes of the erroneous moments have been investigated.

5.3.2 Modified Pseudopotentials

The results obtained using the default CASTEP pseudopotential are unphysical, exhibiting a magnetic moment that disagrees with experiment (section 5.4.2). The presence of sharp *p* orbitals at lower energies than expected could indicate an incorrect pseudopotential definition, giving rise to 'ghost' bands (low energy states with an incorrect number of wavefunction nodes). For this reason, an alternative set of pseudopotential definitions (distributed separately with CASTEP, and supplied as defaults with the commercial CASTEP distribution) were investigated. These alternative definitions (see appendix A.2) differ mainly in terms of the energies at which projector functions are defined (see [10] for details). It was found necessary to use new definitions for all elements, in order to converge calculations correctly.

Geometry optimisations using the modified pseudopotentials change the groundstate structure significantly; now both the *a* and *c* parameters are overestimated compared to the Pertlik model, by as much as 6.6 % for the G-mode *a*-parameter (table 5.1). The *c* axis is modelled more effectively, however, with a maximum deviation of 1.6 % (again for G-type). Atomic positions are closer to experiment than the default pseudopotentials, with a maximum RMS fractional position deviation of 0.009. The main change in structure occurs for the Cu octahedra; with the new pseudopotentials, the $Cu-O1_{eq}$ and $Cu-O2_{ax}$ bond lengths are 1.95 Å and 2.78 Å respectively, compared with 1.99 Å and 2.12 Å previously. This dramatic increase in octahedral elongation (from $\langle\lambda\rangle = 1.005$ to 1.067) indicates a preference for greater JT distortion with the modified pseudopotentials. It also exhibits the more 'usual' overestimation of bonds *cf.* experiment. Other structural parameters remain relatively similar between PSP definitions, indicating that the Cu PSP is the main cause of the discrepancy.

In addition to changing the structure, these new pseudopotentials predict a different magnetic groundstate to the CASTEP defaults; here a G-type is favoured (table 5.3). The corresponding PDOS for the FM state is shown in figure 5.6. The new pseudopotential definitions produce a significantly different bandstructure to figure 5.3; the up- and down-spin *d* states are now much closer in energy, as are the *p* states. The *d* states now also lie lower in energy than the narrow *p* bands, resulting in orbital occupations closer to those expected ($[3d]^{9.4}[4s]^{0.5}[4p]^{0.4}$),

although still more occupied than expected. In addition, the modified pseudopotentials predict a moment of 0.5 μ_B per Cu (consistent with the Mulliken-predicted charge of $Cu^{0.67+}$). The calculations also now predict semiconducting behaviour for all magnetic structures, with the Cu *p* orbitals providing the major contribution to the conduction band. The fact that the *p* orbitals are still low enough in energy to show density of states near the Fermi level might indicate that the pseudopotential definition still shows *p*-like ghost states, although at a different energy to the original results. Further work would be required to test a range of pseudopotential definitions, to investigate the effect of changes on the electronic groundstate.

Table 5.3 – Calculated enthalpies for geometry-optimised structures using alternate CASTEP pseudopotentials.

Structure	Difference from FM-state / eV
A	-0.030
C	+0.005
G	-0.034

One thing to note in comparing figures 5.3 and 5.6 is that using the new pseudopotential definitions, the *d*-bands are now much broader, indicating increased bonding character. This could indicate an over-delocalisation of these *d* electrons, consistent with self-interaction. For this reason calculations were performed again using a Hubbard U parameter, as in section 5.3.1. For $U > 2$ eV it was not possible to converge calculations for all magnetic states using CASTEP, while for G–type it was not possible for $U \geq 1$ eV. From the limited data, it is not possible to say if an additional U contribution will change the predicted groundstate, or what effect it would have on the unit cell parameters.

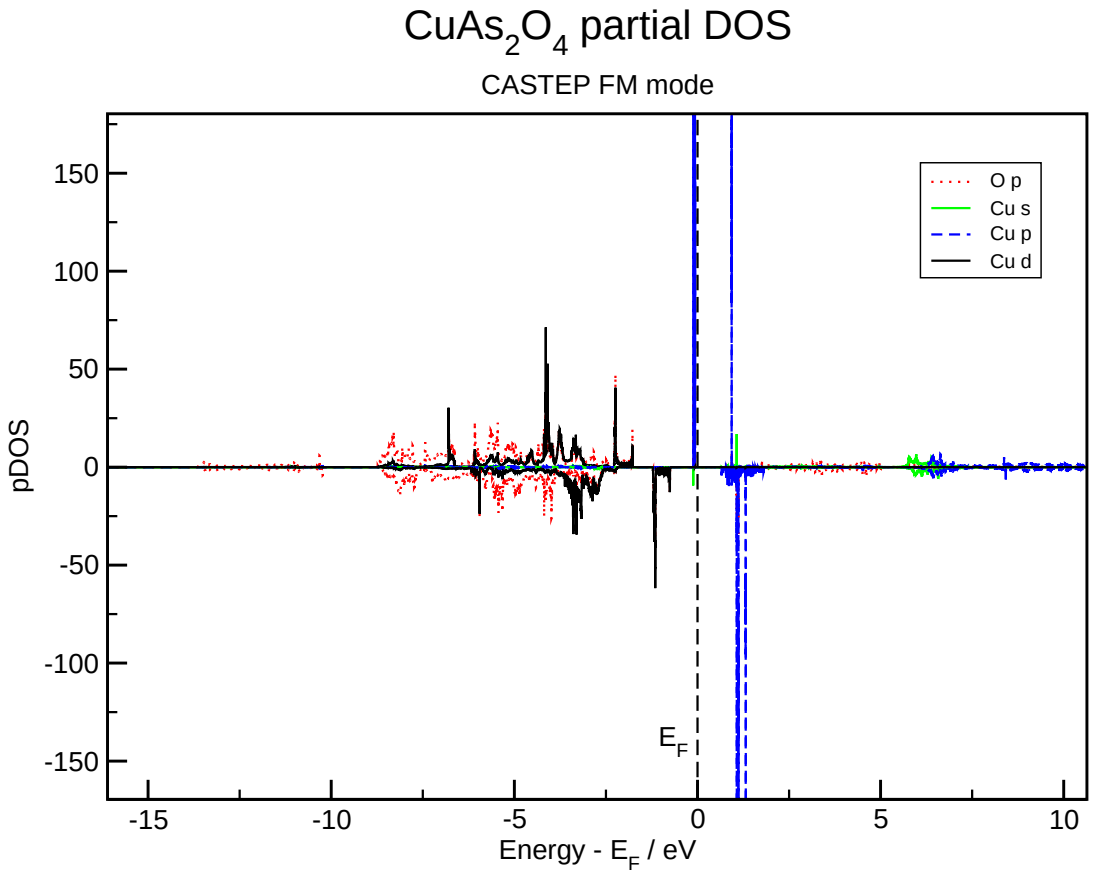

Figure 5.6 – Section of PDOS for $CuAs_2O_4$ with alternative pseudopotential definitions, showing Cu *s* (green), *p* (dashed blue) and *d* (black) states, as well as O *p* states (dotted red).

5.4 Experimental Characterisation

5.4.1 Nuclear Structure

Rietveld refinement of the structure from NPD data proceeded from the reported tetragonal model of Pertlik.[2] Refinement was performed using banks three (d = 0.8–7 Å) and six (d = 0.3–1.7 Å) of data simultaneously, in order to model the full useful d-spacing range while minimising the need for additional profile or background parameters. It was necessary to exclude the region 0.44–0.50 Å from the refinement of bank six due to a very small step function in the background, which was difficult to model correctly using the chosen background function. This exclusion improved the quality of fit, but more importantly made the calculated atomic temperature factors more stable during refinement. The results for the final 300 K NPD fit are shown in table 5.4 and figure 5.7. Structural parameters are consistent with the model of Pertlik, the only significant difference being the reduced c parameter. The cause of this difference is unclear, but could be due to included water from the hydrothermal synthesis (presumably greater for the reported structure, given the large c parameter).

On cooling from 300 K to 15 K, a number of structural changes occur. The structural results from 15 K NPD data are shown in table 5.4, while graphical fits are shown in figure 5.8. The most significant structural change is the *increase* in c-axis from 5.5456(2) Å to 5.5490(2) Å. This can be explained on account of the increase in the $Cu-O1_{eq}$ bond length, from 1.92752(5) Å to 1.93954(5) Å. Although $\angle\, Cu-O1_{eq}-Cu$ reduces slightly to compensate (from 91.989(3)° to 91.326(3)°) the net result is still an expansion along c. Conversely, the $Cu-O2_{ax}$ bond length decreases on cooling, from 2.46517(7) Å to 2.43014(8) Å. The combined effect of these two processes is to reduce the quadratic elongation of the CuO_6 octahedra, from 1.0337 to 1.0290, while causing only a slight reduction in octahedral volume (12.121 $Å^3$ to 12.098 $Å^3$). The contraction of the $Cu-O2_{ax}$ bond length is also a major contributor to the overall reduction of the a parameter, although this is slightly compensated by the increase in the $As-O2_{ax}$ bond-length (1.80790(6) Å to 1.81979(4) Å). Although the octahedra become less elongated on cooling, increased angular distortion occurs along the chains as a ‘twist’. At

Table 5.4 – Refined structure values for $CuAs_2O_4$ at 300 K, 15 K and 1.8 K.

		$CuAs_2O_4$		
		300 K	15 K	1.8 K
Cu, 4d	$100 \times U_{iso}$ (Å^2)	0.82(3)	0.18(2)	0.16(2)
As, 8h	$(x, y, 0)$	0.2014(1), 0.1622(1)	0.1993(1), 0.16159(9)	0.19939(10), 0.16163(9)
	$100 \times U_{iso}$ (Å^2)	1.09(3)	0.20(2)	0.21(2)
O1, 8h	$(x, y, 0)$	0.0965(1), 0.6223(1)	0.0978(1), 0.6246(1)	0.0978(1), 0.6247(1)
	$100 \times U_{iso}$ (Å^2)	0.79(3)	0.32(2)	0.31(2)
O2, 8g	$(x, y, \frac{1}{4})$	0.70283(9), 0.20282(9)	0.70080(8), 0.20079(8)	0.70078(7), 0.20077(7)
	$100 \times U_{iso}$ (Å^2)	1.52(3)	0.42(2)	0.41(2)
χ^2, R_{wp}, R_p		4.999, 0.0243, 0.0227	3.466, 0.0187, 0.0184	3.344, 0.0183, 0.0182
a / Å		8.5942(3)	8.5579(3)	8.5574(3)
c / Å		5.5456(2)	5.5490(2)	5.5487(2)

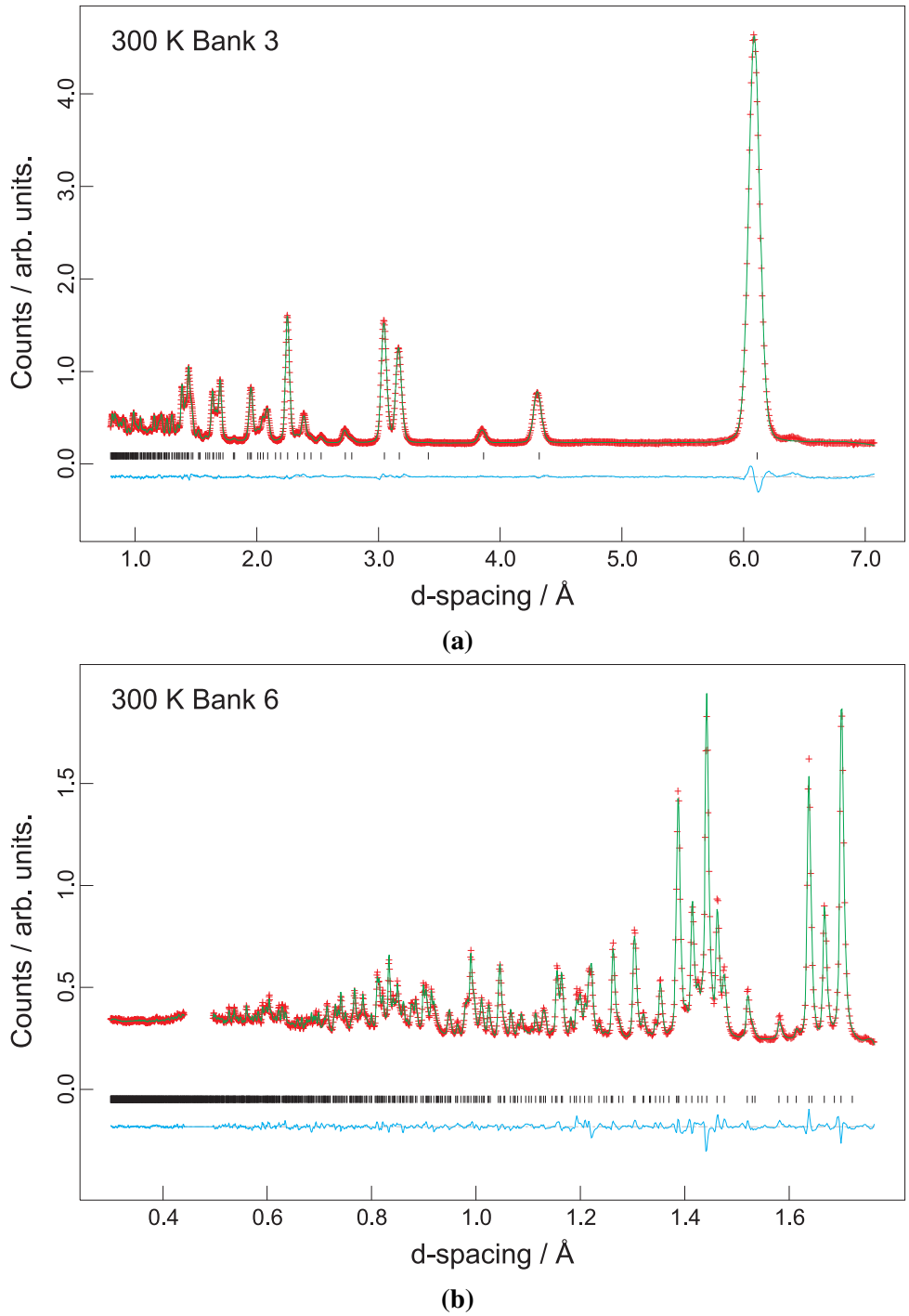

Figure 5.7 – Rietveld refinement of 300 K NPD data for $CuAs_2O_4$; (a) bank 3 (b) bank 6. Observed points–red crosses; calculated model–green curve; difference–blue curve. Tick marks show allowed peaks.

300 K, this angle is 13.448°, increasing to 13.744° at 15 K. This twisting provides a mechanism to accommodate the increase in length of the $Cu-O1_{eq}$ bonds, while still achieving an overall reduction in unit cell volume, from 409.6 $Å^3$ to 406.4 $Å^3$.

5.4.2 Magnetic Susceptibility and Structure

Magnetic susceptibility is shown in figure 5.9, and is characteristic of a ferromagnet. It is clear that there is no divergence between FC and ZFC data. The effective paramagnetic moment (obtained from a linear fit to the inverse susceptibility, figure 5.10) is $\simeq 1.93\,\mu_B$. This is slightly higher than the spin-only value ($\mu_{eff} = \sqrt{4S(S+1)} = 1.73\,\mu_B$) indicating a possible orbital contribution to the moment. The slight curvature in the paramagnetic region makes this fit somewhat questionable, however, and is indicative of non-Curie-Weiss behaviour, such as a temperature-dependent Curie constant. The value of θ (the Weiss constant) obtained from this plot is +16 K, consistent with a dominant ferromagnetic exchange. Figure 5.11 shows the corresponding ferromagnetic hysteresis at 4 K, indicating that $CuAs_2O_4$ exhibits a weak coercivity. By measuring the magnetic moment at high field, the saturated spin moment is obtained as 0.92 μ_B. This is very similar to the value of 1.0 μ_B expected for Cu^{2+}.

The magnetic neutron refinement at 1.8 K is shown in figure 5.12. Because of the relatively low magnetic moment for Cu^{2+} and the lack of additional peaks on cooling (due to ferromagnetism), the magnetic structure proved difficult to fit. The most significant intensity change on cooling occurred for the (110) peak, indicating moments aligned with a component in this plane. A model with moments aligned along $[100]$ gave a better fit than aligned along $[001]$. A combination of the two models (i.e. FM_{xz}) was found to be unstable, and achieved no improvement in fit. From these powder diffraction data, it is not possible to determine where within the *xy* plane the magnetic moments lie due to the tetragonal symmetry. Local magnetic moments obtained from the $[100]$ model are 0.91(6) μ_B, consistent with the saturated spin moment (0.92 μ_B) and the spin-only value expected for Cu^{2+}. Shorter NPD scans were also taken at a range of temperatures below the magnetic transition, and refined as for the 2 K data to obtain the variation of magnetic moment with temperature. Although the statistics for these data were

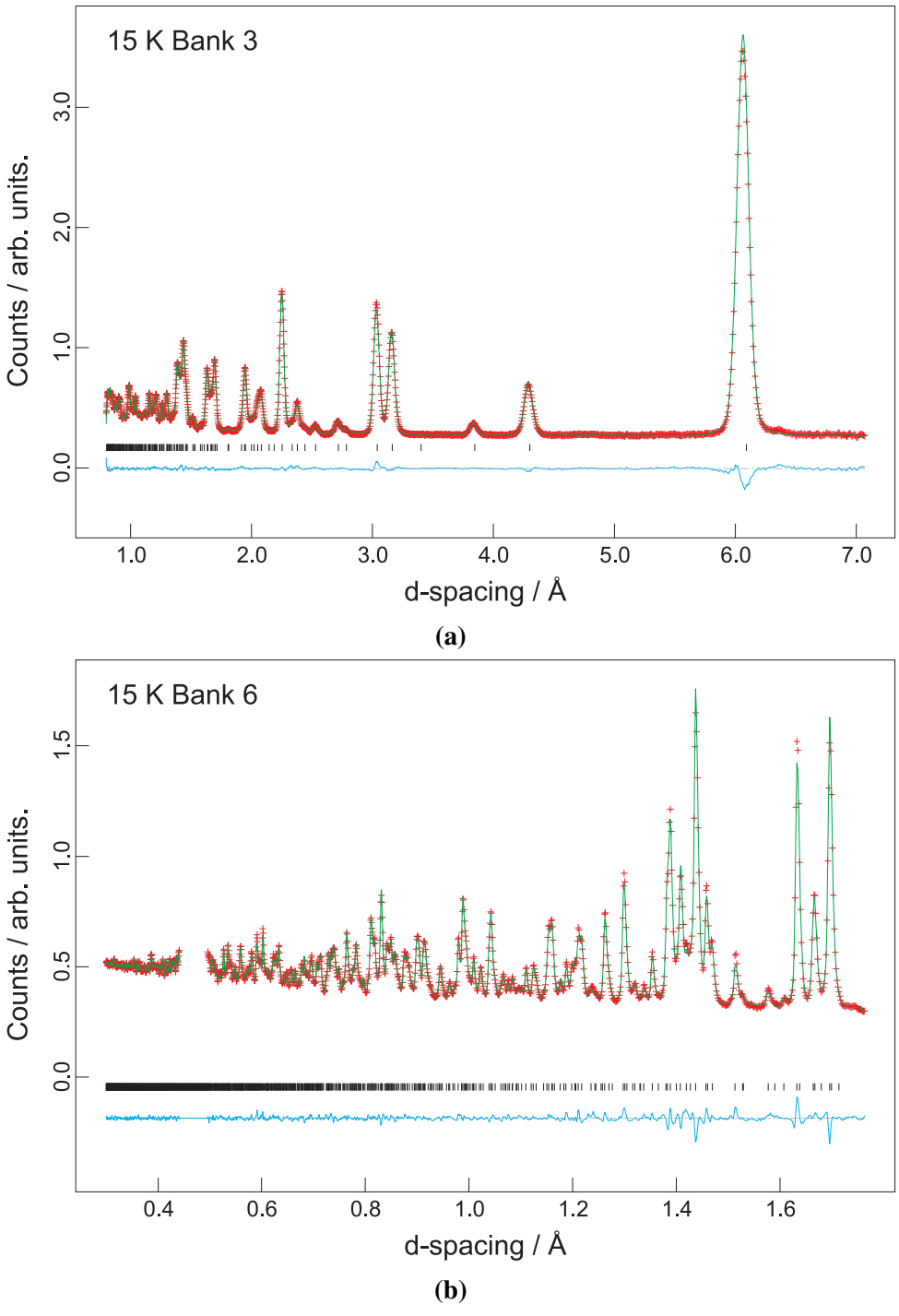

Figure 5.8 – Refinement of 15 K $CuAs_2O_4$ NPD data; (a) bank 3 (b) bank 6.

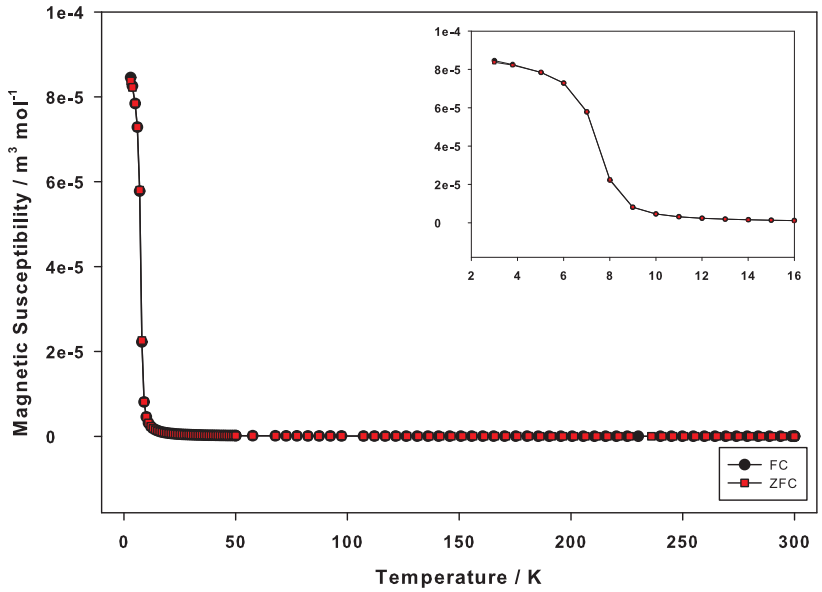

Figure 5.9 – Magnetic susceptibility for $CuAs_2O_4$; inset shows transition temperature. FC - black diamonds; ZFC - red squares.

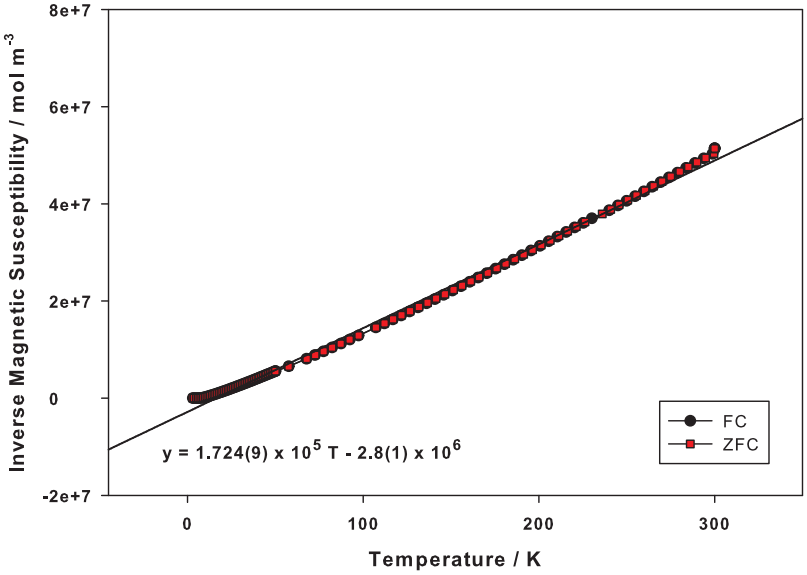

Figure 5.10 – Inverse magnetic susceptibility for $CuAs_2O_4$ with linear regression fit; FC - black diamonds; ZFC - red squares.

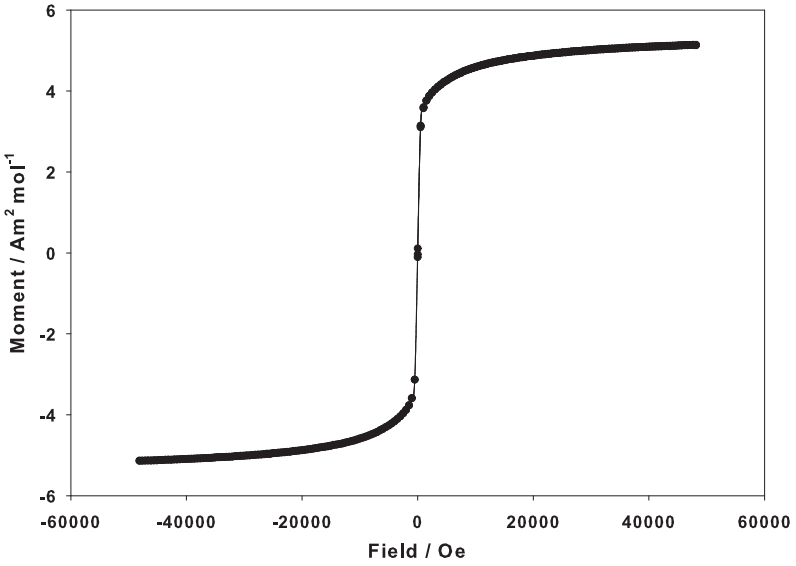

Figure 5.11 – 4 K hysteresis for $CuAs_2O_4$.

less reliable (corresponding to higher errors) they could be fitted with a Brillouin function, to extrapolate the transition temperature. This function can be expressed as

$$M = M_0 \left(1 - \frac{T}{T_c}\right)^{\beta}, \tag{5.1}$$

where M_0 is the '0 K' moment, T_c is the Curie temperature and β is an exponent connected with the transition behaviour. The data (figure 5.13) were fitted by varying all three parameters, and produce the results shown in table 5.5. Note that the errors quoted are based around the linear regression statistics; actual errors will be considerably larger due to the error in the data points.

The values of both M_0 and T_c are consistent with the other measurement techniques. The value of the critical exponent (β) is much lower than that observed in many materials ($\simeq 0.36$) [11] but is consistent with a low-dimensional structure, similar to the theoretical value for a 2-dimensional Ising model ($\beta = 0.125$). [12] It is also similar to that seen previously for $FeSb_2O_4$ (0.18 ± 0.05) [13] and $NiSb_2O_4$ ($\beta = 0.12 \pm 0.03$, [14] although this is also reported as 0.21 from

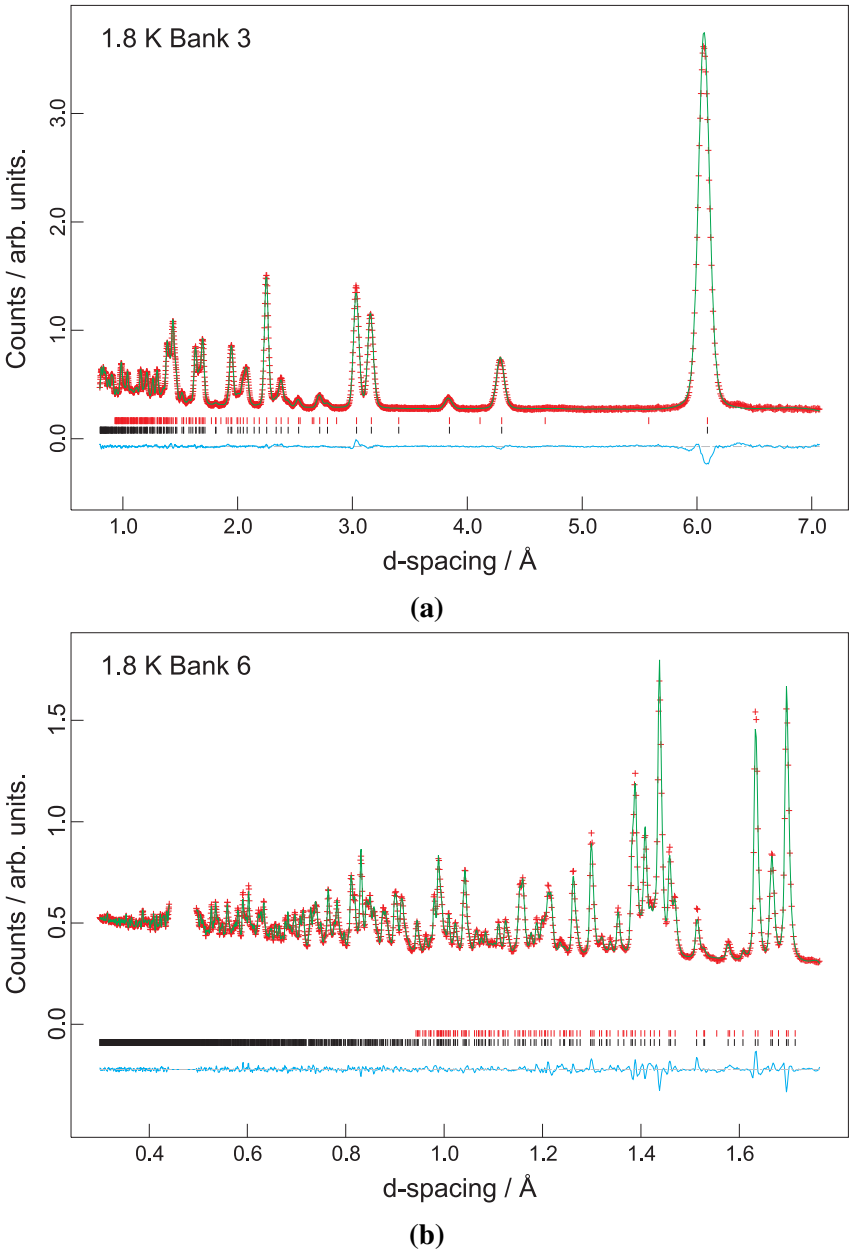

Figure 5.12 – Refinement of 1.8 K NPD data; (a) bank 3 (b) bank 6; Nuclear phase shown with black tick-marks, magnetic phase with red.

Table 5.5 – Calculated Brillouin function values for $CuAs_2O_4$.

Parameter	Value (Error estimate from regression fit)
M_0 / μ_B	0.96(4)
T_c / K	8.00002(8)
β	0.13(5)

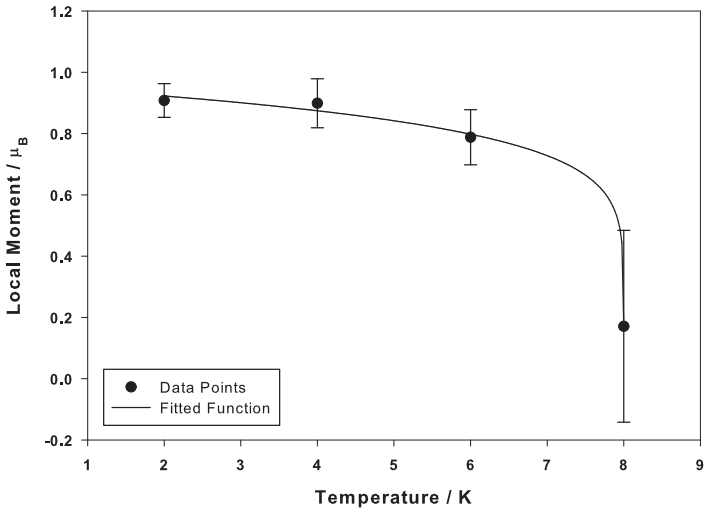

Figure 5.13 – Fit of $M = M_0 \left(1 - \frac{T}{T_c}\right)^{\beta}$ for experimental data points.

[15]). The value is somewhat lower than that observed for $MnSb_2O_4$ ($\beta = 0.36$[16] or 0.5 ± 1[14]).

On cooling from 15 K to 1.8 K, the structural changes observed are a continuation of those seen between 300 K and 15 K, although significantly smaller due to the smaller temperature range. Refined atomic positions and thermal parameters are given in table 5.4. As such, there is no evidence of a structural transition related to the occurrence of magnetic order. The magnetic model observed cannot be described using the parent (non-magnetic) spacegroup $(P4_2/mbc)$, instead requiring an orthorhombic magnetic (Shubnikov) group of $Pb'am'$ (55.358) with the axis transformation:

$$\begin{pmatrix} 0 & 1 & 0 \\ \bar{1} & 0 & 0 \\ 0 & 0 & 1 \end{pmatrix}.$$

Although the refined magnetic model is inconsistent with tetragonal symmetry, there is no observed peak splitting in the pattern to suggest a significant nuclear distortion. As such, the tetragonal nuclear model has been used to minimise the number of parameters required, and avoid 'over-fitting', while the magnetic structure has been modelled using a separate phase of $P1$ symmetry. The symmetry of the magnetic structure corresponds to a single irreducible representation (IR) (Γ_9, using Kovalev notation[17]), consistent with a single, second-order phase

transition (propagation vector $k = (0,\ 0,\ 0)$). Note that this IR can simultaneously give rise to a C_y magnetic mode in addition to the FM_x mode using a different combination of basis vectors, ψ (see appendix B.1). The combination of these two modes can occur without breaking symmetry arguments, and allows some freedom of the moments within the *ab* plane. No contribution from this antiferromagnetic moment has been observed experimentally using the techniques discussed, however.

5.4.3 Thermal Stability

Thermal gravimetric analysis (TGA) was performed for $CuAs_2O_4$ under flowing oxygen, at a heating rate of 10 °C min^{-1} up to a maximum of 1100 °C. The results are shown in figure 5.14. The sample loses a significant proportion of its mass above 430 °C, occurring over a very narrow temperature range. Due to the large mass loss and sample melting, it was not possible to determine the decomposition product(s) from XRPD. The mass change observed could correspond to loss of "AsO_2" per formula unit, but further information would be required to determine if this were the case.

5.4.4 Electronic Properties

$CuAs_2O_4$ was synthesised as a pale green solid, indicating absorption of light at both the low- and high-energy (*i.e.* red and blue) ends of the visible spectrum. A pelletised sample was made by pressing hydrothermally synthesised $CuAs_2O_4$ under 2 tons of force (8 mm die) and heating in air at 330 °C for 60 hours. This gave a pellet of 84.5 % theoretical maximum density and 1.53 mm thickness. Impedance spectroscopy of this pellet showed that it was an insulator, with an impedance beyond the maximum of the impedance analyser (100 Mω) at all temperatures measured (50 °C–330 °C).

5.5 Substituted Variants

A number of attempts were made to substitute atoms into $CuAs_2O_4$, with a view to producing mixed-valent Cu within the octahedral chains. This could potentially give rise to some very

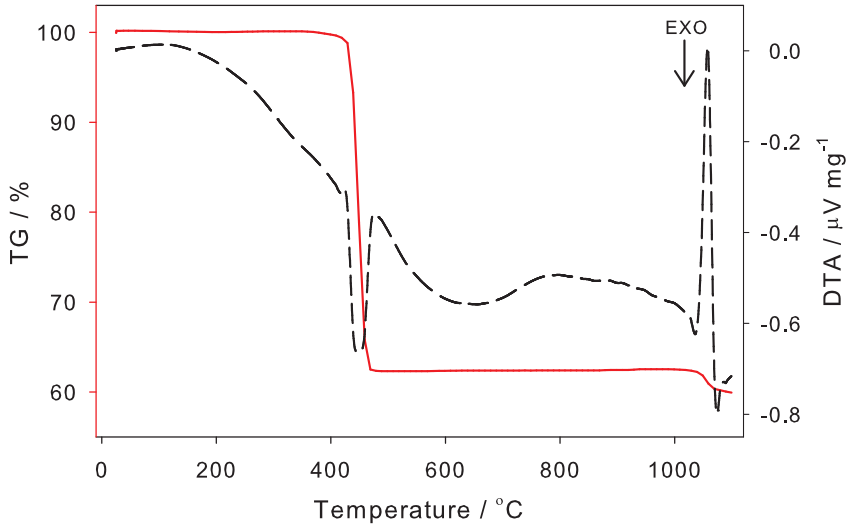

(a)

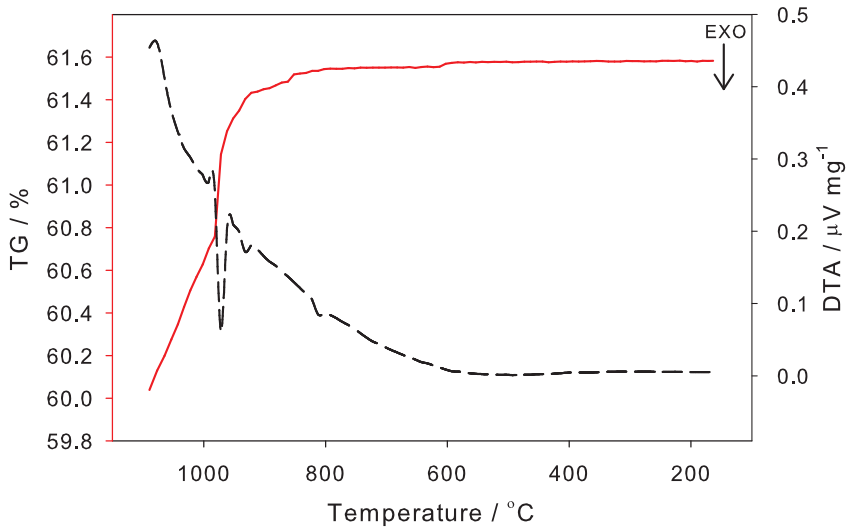

(b)

Figure 5.14 – TG (solid red line) and DTA (dashed black line) for $CuAs_2O_4$ on (a) heating and (b) cooling in O_2.

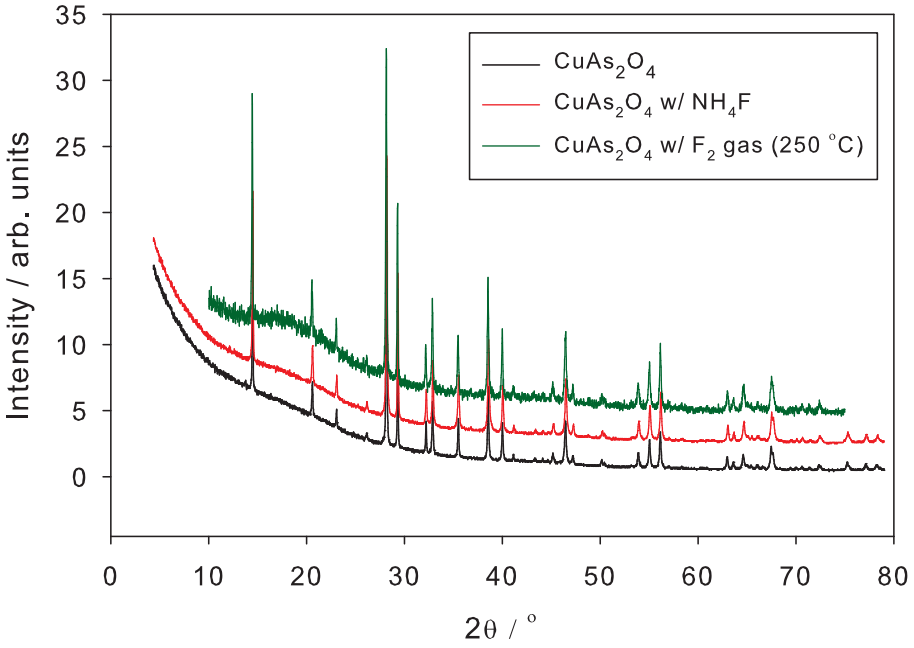

Figure 5.15 – XRPD patterns of $CuAs_2O_4$ and fluorination using NH_4F during synthesis (red) and fluorination after synthesis by heating in F_2 gas at 250 °C for 20 minutes (green).

interesting electronic and magnetic properties. The main method tested was the addition of fluorine within the structure, and was performed using a number of techniques. Direct reaction on pre-synthesised $CuAs_2O_4$ using F_2 gas and the milder fluorinating agent, polyvinylidene fluoride (PVDF) were used, as well as fluorination during initial synthesis using excess NH_4F or stoichiometric amounts of CuF_2. In many cases, the resulting products contained a mixture of Cu-O and Cu-F impurities such as CuF_2 or Cu_2O. Where impurities did not form, no significant change occurred in the XRPD patterns from the pure $CuAs_2O_4$ to conclude a change in the Cu oxidation state had occurred (see figure 5.15).

5.6 Conclusions

Preliminary DFT calculations predicted a FM groundstate in $CuAs_2O_4$, which has been proved correct experimentally. The theoretical results show anomalously large magnetic moments on Cu, connected with the copper pseudopotential employed and the presence of ghost states. Use of a modified pseudopotential reduced the moment, but changed the predicted groundstate to a

G-type structure; it is unclear whether the modified pseudopotential still contained ghost states. Inclusion of a Hubbard U term did not significantly alter the results using the original PSP, but prevented convergence for the modified PSP. Further work should involve a full study of other PSP definitions, as well as all-electron (*i.e.* linearised augmented planewave (LAPW)) methods to avoid PSPs entirely.

A synthetically prepared sample was found to order ferromagnetically below 8 K, with a magnetic moment (from NPD) of 0.96(4) μ_B. Fitting the evolution of this magnetic moment with temperature found a critical exponent $\beta = 0.13(5)$, typical of a low-dimensional system. On cooling through this transition, no significant strucural changes are observed, however negative thermal expansion of the *c*-parameter is seen between 300 K and 15 K.

Investigation of sample stability on heating in flowing O_2 found a dramatic mass loss at 430 °C, most likely due to loss of arsenic from the structure. Attempts to vary oxidation state of the Cu cations within the structure by substitution of oxygen with fluorine proved unsuccessful in creating a single, Schafarzikite-structured phase.

References

[1] J. Zemann, *Tschermaks Mineralogische und Petrographische Mitteilungen*, 1951, **2**, 417–423.

[2] F. Pertlik, *Tschermaks Mineralogische und Petrographische Mitteilungen*, 1975, **22**, 211–217.

[3] M. J. Whitaker, R. D. Bayliss, F. J. Berry and C. Greaves, *Journal of Materials Chemistry*, 2011, **21**, 14523–14529.

[4] N. Kumada, Y. Yonesaki, T. Takei, N. Kinomura and S. Wada, *Materials Research Bulletin*, 2009, **44**, 1298–1300.

[5] M. T. Atanasova, A. M. Strydom, C. J. H. Schutte, L. C. Prinsloo and W. W. Focke, *Journal of Materials Science*, 2014, **49**, 3497–3510.

[6] A. C. Larson and R. B. von Dreele, *Los Alamos National Laboratory Report*, 1994, **LAUR 86-748**, 1.

[7] B. H. Toby, *Journal of Applied Crystallography*, 2001, **34**, 210–213.

[8] J. Goodenough, *Magnetism and the Chemical Bond*, Interscience Publishers, 1963.

[9] W. Tang, E. Sanville and G. Henkelman, *Journal of Physics: Condensed Matter*, 2009, **21**, 084204.

[10] C. J. Pickard, *On-the-fly pseudopotential generation in CASTEP*, University of St. Andrews technical report, 2006.

[11] R. M. Suter and C. Hohenemser, *Journal of Applied Physics*, 1979, **50**, 1814–1816.

[12] R. Skomski, *Simple Models of Magnetism*, Oxford University Press, Oxford, 2008.

[13] R. Chater, J. R. Gavarri and A. Hewat, *Journal of Solid State Chemistry*, 1985, **60**, 78–86.

[14] J. R. Gavarri and A. W. Hewat, *Journal of Solid State Chemistry*, 1983, **49**, 14–19.

[15] R. Chater, K. Chhor, J. R. Gavarri and C. Pommier, *Materials Research Bulletin*, 1985, **20**, 1427–1434.

[16] H. Fjellvåg and A. Kjekshus, *Acta Chemica Scandinavica Series A-Physical and Inorganic Chemistry*, 1985, **39**, 389–395.

[17] O. V. Kovalev, *Representations of the Crystallographic Space Groups: Irreducible Representations, Induced Representations and Corepresentations*, Gordon and Breach, 1993.

Chapter 6
Magnetic and Structural Characterisation of $Mn_xCo_{1-x}Sb_2O_4$

6.1 Background

$MnSb_2O_4$ and $CoSb_2O_4$ are both known to adopt the Schafarzikite structure-type, although with slightly different unit cell sizes consistent with the different sized M cations (table 6.1). The atomic structures are very similar, with changes in M−O bonding reflecting the different cation sizes. There are quite different Sb−O bonding requirements, however, presumably to accommodate the larger Mn cation within the structure (the $CoSb_2O_4$ and $FeSb_2O_4$ structures are more similar in this respect). Mn represents the largest reported M cation to adopt this structure type (figure 1.4).

$MnSb_2O_4$ and $CoSb_2O_4$ order antiferromagnetically at low temperature, with T_N = 55 K and 79 K, respectively. The magnetic structures are completely different however; $MnSb_2O_4$ adopts A_x-type ordering, while $CoSb_2O_4$ shows C_z-type (μ = 4.52(13) μ_B and 3.73(2) μ_B, respectively). Additionally, for $MnSb_2O_4$ a weak G-type component has been observed in some reports but not others; the properties observed are closely related to sample preparation and quality.[1,4,5]

A number of previous reports of mixed-cation species exist, and have often focussed on $MnSb_2O_4$ as a starting point. $V_xMn_{1-x}Sb_2O_4$ was synthesised for $0 \leq x \leq 0.6$ and found (somewhat surprisingly) to retain the $x = 0$ lattice parameters for all compositions;[6] no other

Table 6.1 – Reported unit cell parameters and selected bonding characteristics for M = Mn and Co.

	$MnSb_2O_4$ [1]	$CoSb_2O_4$ [2]
a / Å	8.7097(6)	8.49340(9)
c / Å	5.9982(9)	5.92387(8)
M radius [3] / Å	0.83	0.75
Average M−O distance / Å	2.145	2.098
M quadratic elongation	1.0096	1.0105
Octahedral twist / °	18.5	19.4
Sb−$O1_{eq}$ distance $(\times 1)$ / Å	1.81(3)	1.936(2)
Sb−$O2_{ax}$ distance $(\times 2)$ / Å	2.03(2)	1.9903(9)

structural data are reported. The magnetic susceptibility for $x = 0$ is similar to previous reports (T_N = 60.5 K) however for $x > 0.1$ a FM response (seen as a deviation between FC and ZFC measurements below T_c) is observed. This is attributed to a ferrimagnetic ordering (AFM alignment of Mn^{2+} [d^5] and V^{2+} [d^3]) although this would necessitate a non-random distribution of Mn and V over the M sites, which is not discussed.

Mixing of Sb and Pb on the X site in $MnSb_2O_4$ was also attempted by Abakumov *et al.*,[7] in order to generate a mixed Mn^{2+}/Mn^{3+} octahedral species. Mn^{2+} proved resistant to oxidation, however, instead forming a range of $[Mn^{2+}_{1-x}Sb^{5+}_x][Sb^{3+}_{2-y}Pb^{2+}_y]O_4$ phases, for $0.05 \leq x = \frac{3}{2}y \leq 0.25$. For low x A-type ordering was observed as in the parent compound, however this was reduced at higher x due to the presence of non-magnetic Sb^{5+} within the chains; ordering of the highly charged Sb^{5+} was also reported. A similar study in $CoSb_2O_4$ found partial oxidation of Co^{2+}, but coupled with oxidation of Sb.[2] The magnetic order showed a change from C-type for $CoSb_2O_4$ to a combination of C- and G-type for $CoSb_{1.5}Pb_{0.5}O_4$.

For comparison, the formation of $FeSb_{2-y}Pb_yO_4$ $(0.2 \leq y \leq 0.7)$ formed mixed octahedral Fe^{2+} and Fe^{3+}, and produced a C-type magnetic structure for $y \neq 0$.[8] In both this compound and $Co_{0.25}Fe_{0.75}Sb_{2-y}Pb_yO_4$ $(0.25 \leq y \leq 0.75)$[9] the C-type magnetic structure is seen to change

orientation from C_x to C_z with increasing y (increasing M oxidation). The $Co_xFe_{1-x}Sb_2O_4$ series ($0 \leq x \leq 1$) has also been analysed, and shows a change from A_x- to C_z-type magnetic structures with increasing x, effectively as a superposition of the structures for the two end-members.[9]

$Mg_{1-x}Ni_xSb_2O_4$ have also been reported for $0.01 \leq x \leq 0.20$, and show orthorhombic distortions as seen in low-temperature Pb_3O_4.[10] The paramagnetic susceptibility increases with x as expected, but no other study of the magnetic or structural behaviour has been reported.

This chapter reports the synthesis and structural characterisation of $Mn_xCo_{1-x}Sb_2O_4$, as well as the magnetic characterisation of these compounds.

6.2 Synthesis and Experimental

$Mn_xCo_{1-x}Sb_2O_4$ samples (for $x = 0.2,\ 0.4,\ 0.5,\ 0.6,\ 0.8$) were synthesised by a solid state reaction between stoichiometric amounts of CoO (> 99 %, Aldrich), MnO (99 %, Aldrich) and Sb_2O_3 (> 99 %, Aldrich). Reagents were intimately ground and sealed in an evacuated quartz tube, heating to 700 °C for 36 hours before cooling within the furnace. Phase purity was checked using XRPD (D8 instrument). Reagents were dried either under dynamic vacuum at 150 °C (Sb_2O_3) or at 350 °C in air (CoO, MnO) prior to use. The samples produced ranged in colour from pale green ($MnSb_2O_4$ and $Mn_{0.8}Co_{0.2}Sb_2O_4$) to pale brown ($Mn_{0.2}Co_{0.8}Sb_2O_4$) after heat treatment.

NPD data were collected on the D2B diffractometer at ILL at a range of temperatures. Data were refined using GSAS and EXPGUI.[11,12] The background data were modelled using a shifted Chebyschev polynomial (GSAS type 1) with between 15 and 25 terms. Peak shapes were modelled using a pseudo-Voigt function. It was found to be necessary to include parameters to describe strain and particle-size broadening in order to give a good quality fit; these were implemented both with profile type 2 (stec, ptec and GP) and profile type 4 (Stephen's *hXXX* terms). Additionally, preferred orientation was necessary (using the MD method) and was constrained to be equal for both magnetic and nuclear phases (where appropriate).

Due to the different signs of the neutron scattering length for Mn and Co (-3.73(2) and

2.49(2) fm, respectively[13]) compositions of $Mn_xCo_{1-x}Sb_2O_4$ close to $x = 0.4$ give a very small total scattering from the magnetic cation (M) site (see table 6.2). This can lead to large uncertainties in refined parameters based on this site, particularly temperature factors. For this reason, for the $Mn_{0.4}Co_{0.6}Sb_2O_4$ data presented here it has been necessary to fix U_{iso} to a reasonable value based on that of $Mn_{0.6}Co_{0.4}Sb_2O_4$, in order to produce a stable refinement.

Table 6.2 – Total scattering length from M site for $Mn_xCo_{1-x}Sb_2O_4$.

x	M Scattering length / fm
0.2	1.246
0.4	0.002
0.5	-0.620
0.6	-1.242
0.8	-2.486

6.3 Structural Characterisation

6.3.1 Analysis by XRPD

Following synthesis, the compounds were initially studied through XRPD using the D8 instrument. The patterns could all be indexed as single-phase, $MnSb_2O_4$-like compounds (spacegroup $P4_2/mbc$) but showing a shift in peak positions consistent with an increase in lattice parameters on increasing x (see figure 6.1).

Rietveld refinement of these data were performed starting from a $CoSb_2O_4$ model[2] with fixed atomic fractions for the M cation site, due to the insensitivity of XRPD to the Mn / Co ratio. Isotropic temperature factors were also constrained to be equal for Mn / Co, as well as the oxygen positions (due to the low scattering of O *cf.* Sb). All refinements using profile function #2 showed a significant under-estimation of intensity for the (110), (220) and (002) peaks (see figure 6.2a or appendix C.1). This could be corrected (and χ^2 significantly improved)

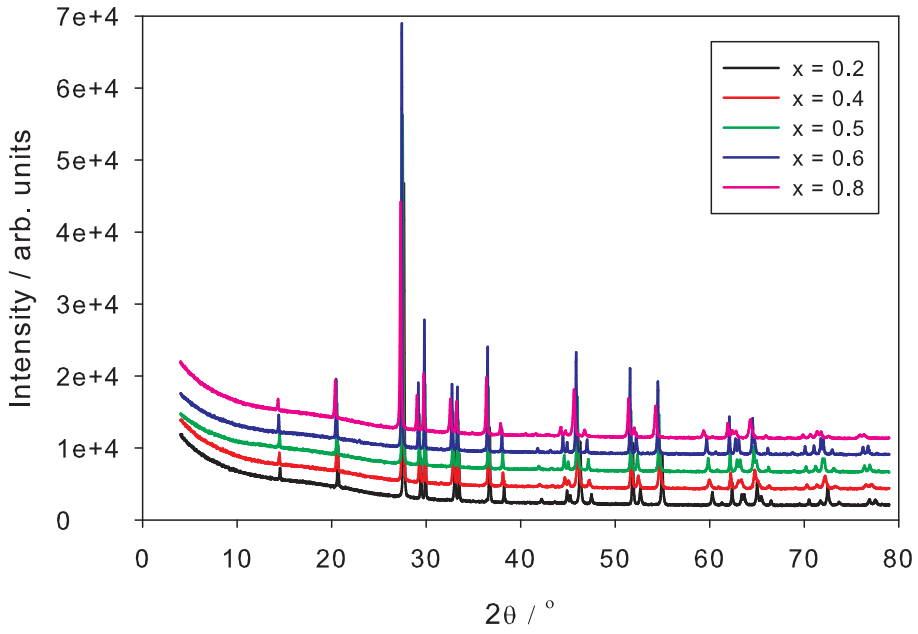

Figure 6.1 – Stacked XRPD plots for $Mn_xCo_{1-x}Sb_2O_4$ showing peak shift with increasing x.

by including anisotropic strain broadening (profile type 4) in the refinement, particularly the $H400$ Stephen's term (figure 6.2b). The cause of this strain is presumably due to an uneven distribution of the different sized Co^{2+} and Mn^{2+} cations within the structure (0.745 Å and 0.83 Å,[3] respectively). The η value within the Stephens model (corresponding to the Gaussian / Lorentzian ratio for the broadening) normally refined to 1 (and was subsequently fixed), indicating largely Lorentzian character. This is consistent with the large values observed for stec, which is a (simpler) model of anisotropic Lorentzian broadening.

An orthorhombic structural model ($Pbam$) improved the fit slightly from the $P4_2/mbc$ case (profile #2) but not as much as the inclusion of anisotropic strain. Although the $Pbam$ model does obtain slightly different a and b unit cell parameters with differences $> 3\sigma$, the differences are probably due to modelling of strain rather than a true orthorhombic structure. No ($h00$) peaks in the tetragonal model(s) show any sign of splitting, again refuting the orthorhombic hypothesis. That the orthorhombic model gives a lower χ^2 could be due to the increased number of variable parameters involved. In all of the above cases, the XRPD patterns showed significant preferred-orientation effects, which were modelled using the MD method. Data are tabulated in

tables 6.3 ($x = 0.2$), 6.4 ($x = 0.4$), 6.5 ($x = 0.5$), 6.6 ($x = 0.6$) and 6.7 ($x = 0.8$).

6.3.2 Analysis by NPD at 300 K

RT NPD data were refined starting from the appropriate models based on XRPD refined data. Due to the lower resolution of NPD *cf.* XRPD anisotropic peak broadening was not as problematic. Including it in the model (profile #4) did improve the overall fit, however, so it was included throughout all refinements. An example of this is shown graphically in figure 6.3 for $Mn_{0.2}Co_{0.8}Sb_2O_4$, where χ^2 is improved from 2.090 (R_{wp} = 0.048, 49 variables) to 1.981 (R_{wp} = 0.0467, 49 variables) by including Stephens' parameters.

The wavelength of the neutron source (which is inherently variable) was determined accurately by means of a simultaneous refinement of XRPD and NPD data collected for $Mn_{0.2}Co_{0.8}Sb_2O_4$. The value thus determined ($\lambda = 1.59309(5)$ Å) was then used for all further refinements.

On analysing the $x = 0.8$ dataset, a number of additional peaks were observed (particularly at 36.3° and 73.2° 2θ) in addition to a poor quality fit. These peaks could be indexed as a cubic unit cell ($Fm\bar{3}m$), corresponding to a small (0.01 wt%) MnO impurity which was included in further refinements (figure 6.4).

Refined room temperature atomic positions and statistical data are shown in table 6.8; graphical representations of the refinements can be seen in appendix C.1.2. From these data, a number of trends can be surmised. Firstly, the unit cell parameters change almost linearly with x, as can be seen from figure 6.5. This is consistent with the formation of a solid solution, the overall increase in volume being attributed to the larger ionic radius of Mn^{2+} *vs.* Co^{2+}. This is also seen from examining inter-atomic bond lengths (table 6.9). On increasing x, both M−O bond lengths increase almost linearly (figure 6.6) resulting in an overall octahedral expansion from 12.38 Å^3 to 13.11 Å^3. The slight deviation for $x = 0.5$ shows an increase in $M-O1_{eq}$ and a corresponding decrease for $M-O2_{ax}$ compared to the trend. The net result is that the octahedral volume does exhibit the correct trend for this point (figure 6.7). The deviation is also seen in the octahedral distortion index, where the value for $x = 0.5$ is lower than the neighbouring compositions (dis-

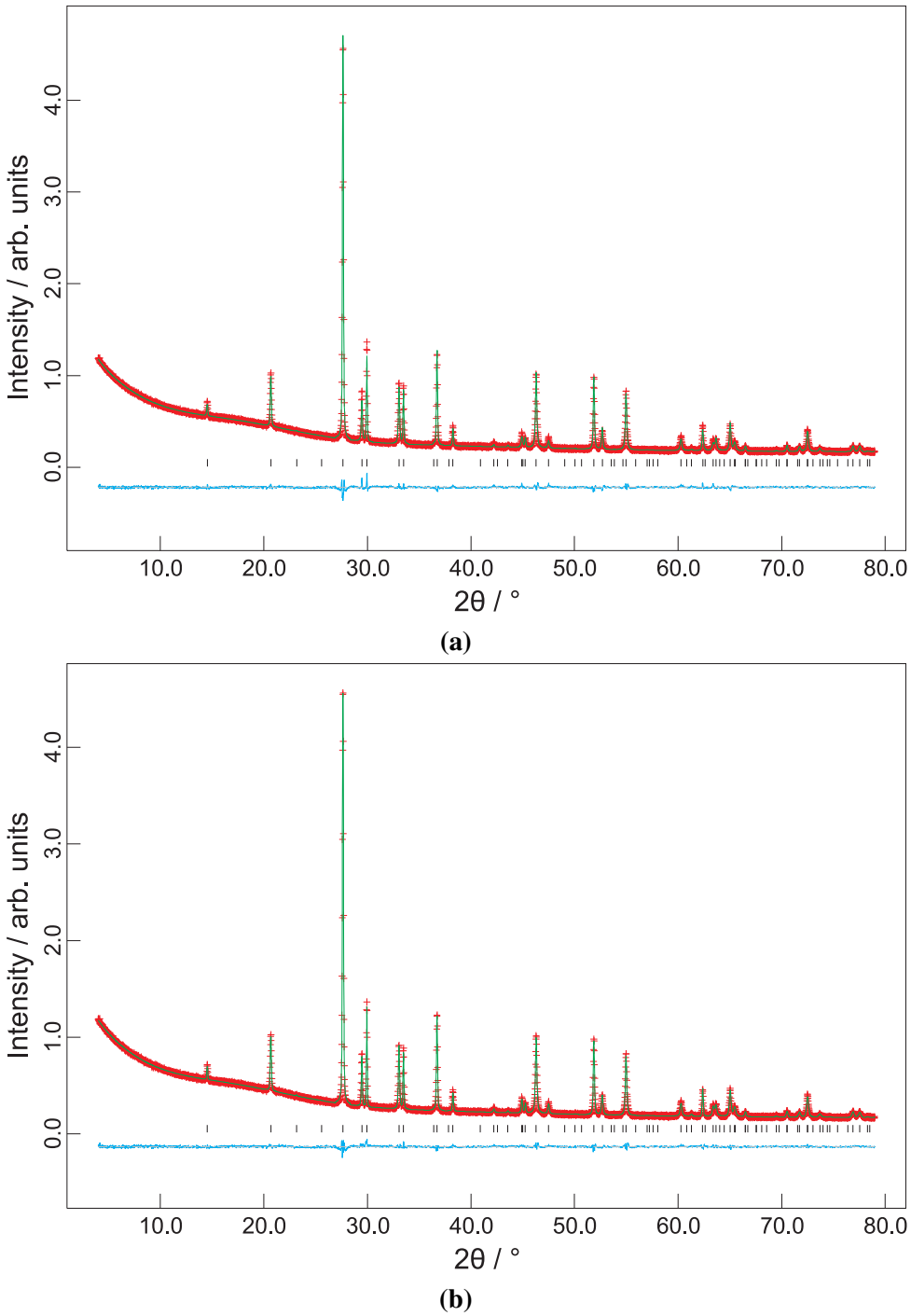

Figure 6.2 – Rietveld refinement for $Mn_{0.2}Co_{0.8}Sb_2O_4$ showing (a) underestimation of $(hh0)$ peaks using profile #2 and (b) correction using profile function #4. Observed data - red crosses; calculated - green line; difference (obs-calc) - cyan line.

Table 6.3 – XRPD-refined values for $Mn_{0.2}Co_{0.8}Sb_2O_4$.

		$P4_2/mbc$ model		*Pbam* model
		Profile #2	Profile #4	Profile #2
a / Å		8.5355(2)	8.5343(2)	8.5297(3)
b / Å		-	-	8.5416(3)
c / Å		5.9405(1)	5.9398(2)	5.9406(1)
Mn / Co (4d / 4f)	$(0,\ \frac{1}{2},\ \frac{1}{4})$ / $(0,\ \frac{1}{2},\ z)$	-	-	0.262(2)
	$100\times$ U_{iso} / Å^2	1.1(1)	1.4(1)	0.9(1)
Sb1 (8h / 4g)	$(x,\ y,\ 0)$	0.1769(3), 0.1652(3)	0.1763(3), 0.1650(2)	0.6723(8), 0.3344(6)
	$100\times$ U_{iso} / Å^2	1.58(5)	1.47(5)	1.0(2)
Sb2 (4h)	$(x,\ y,\ \frac{1}{2})$	-	-	0.3338(8), 0.3204(7)
	$100\times$ U_{iso} / Å^2	-	-	2.3(2)
$O1_{eq}$ (8h / 4g)	$(x,\ y,\ 0)$	0.089(1), 0.633(1)	0.096(1), 0.637(1)	0.583(3), 0.900(3)
	$100\times$ U_{iso} / Å^2	1.3(4)	0.6(3)	-0.4(3)
$O1_{eq}$ (4h)	$(x,\ y,\ \frac{1}{2})$	-	-	0.823(2), 0.401(3)
	$100\times$ U_{iso} / Å^2	-	-	-0.4(3)
$O2_{ax}$ (8g / 8i)	$(x,\ y,\ \frac{1}{4})$ / $(x,\ y,\ z)$	0.6886(8), 0.1886(8)	0.6831(8), 0.1830(8)	0.305(3), 0.820(3), 0.245(5)
	$100\times$ U_{iso} / Å^2	1.1(3)	2.0(3)	-0.4(3)
χ^2, No. of parameters		2.647, 35	2.105, 37	2.461, 43
R_{wp}, R_p		0.0265, 0.0183	0.0236, 0.0168	0.0255, 0.0179
$(00l)$ Preferred Orientation		0.869(2)	0.891(2)	0.865(2)
stec		-17.0(5)	-	-14.1(6)
ptec		0	1.2(1)	0
GP		0	0	10(10)
η		-	1	-
$S400$		-	0.155(4)	-
$S220$		-	-0.014(5)	-
$S202$		-	0.063(4)	-

Table 6.4 – XRPD-refined values for $Mn_{0.4}Co_{0.6}Sb_2O_4$.

		$P4_2/mbc$ model		*Pbam* model
		Profile #2	Profile #4	Profile #2
a / Å		8.5772(2)	8.5763(3)	8.5681(4)
b / Å		-	-	8.5864(4)
c / Å		5.9538(2)	5.9534(2)	5.9537(2)
Mn / Co (4d / 4f)	$(0,\ \frac{1}{2},\ \frac{1}{4})$ / $(0,\ \frac{1}{2},\ z)$	-	-	0.263(2)
	$100\times$ U_{iso} / Å^2	0.8(1)	1.17(9)	0.6(1)
Sb1 (8h / 4g)	$(x,\ y,\ 0)$	0.1783(3), 0.1655(2)	0.1771(3), 0.1659(2)	0.6749(9), 0.3333(6)
	$100\times$ U_{iso} / Å^2	1.19(5)	1.16(5)	0.5(2)
Sb2 (4h)	$(x,\ y,\ \frac{1}{2})$	-	-	0.3348(9), 0.3195(7)
	$100\times$ U_{iso} / Å^2	-	-	2.0(2)
$O1_{eq}$ (8h / 4g)	$(x,\ y,\ 0)$	0.091(1), 0.636(1)	0.096(1), 0.639(1)	0.579(3), 0.894(2)
	$100\times$ U_{iso} / Å^2	2.1(4)	0.8(3)	0.1(3)
$O1_{eq}$ (4h)	$(x,\ y,\ \frac{1}{2})$	-	-	0.826(2), 0.395(3)
	$100\times$ U_{iso} / Å^2	-	-	0.1(3)
$O2_{ax}$ (8g / 8i)	$(x,\ y,\ \frac{1}{4})$ / $(x,\ y,\ z)$	0.6889(8), 0.1889(8)	0.6818(7), 0.1818(7)	0.312(3), 0.813(3), 0.253(5)
	$100\times$ U_{iso} / Å^2	1.2(3)	1.5(3)	0.1(3)
χ^2, No. of parameters		2.377, 35	1.802, 40	2.171, 43
R_{wp}, R_p		0.0260, 0.0185	0.0226, 0.0168	0.0248, 0.0180
$(00l)$ Preferred Orientation		0.913(2)	0.921(2)	0.906(2)
stec		-28.3(6)	-	-23.0(7)
ptec		0	1.6(2)	0
GP		0	28.8(0)	0
η		-	0.68(1)	-
$S400$		-	0.356(7)	-
$S220$		-	0.035(9)	-
$S202$		-	0.115(8)	-

Table 6.5 – XRPD-refined values for $Mn_{0.5}Co_{0.5}Sb_2O_4$.

		$P4_2/mbc$ model		*Pbam* model
		Profile #2	Profile #4	Profile #2
a / Å		8.6036(1)	8.6019(2)	8.5972(2)
b / Å		-	-	8.6102(2)
c / Å		5.96481(8)	5.9636(2)	5.96478(8)
Mn / Co (4d / 4f)	$(0,\ \frac{1}{2},\ \frac{1}{4})$ / $(0,\ \frac{1}{2},\ z)$	-	-	0.266(1)
	$100\times$ U_{iso} / Å^2	1.3(1)	1.39(9)	0.9(1)
Sb1 (8h / 4g)	$(x,\ y,\ 0)$	0.1781(3), 0.1665(2)	0.1777(2), 0.1663(2)	0.6756(7), 0.3338(5)
	$100\times$ U_{iso} / Å^2	1.49(5)	1.45(5)	1.0(2)
Sb2 (4h)	$(x,\ y,\ \frac{1}{2})$	-	-	0.3322(7), 0.3207(6)
	$100\times$ U_{iso} / Å^2	-	-	2.2(2)
$O1_{eq}$ (8h / 4g)	$(x,\ y,\ 0)$	0.089(1), 0.634(1)	0.095(1), 0.640(1)	0.579(2), 0.895(2)
	$100\times$ U_{iso} / Å^2	0.9(2)	1.2(2)	-0.5(2)
$O1_{eq}$ (4h)	$(x,\ y,\ \frac{1}{2})$	-	-	0.826(2), 0.400(2)
	$100\times$ U_{iso} / Å^2	-	-	-0.5(2)
$O2_{ax}$ (8g / 8i)	$(x,\ y,\ \frac{1}{4})$ / $(x,\ y,\ z)$	0.6882(7), 0.1882(7)	0.6839(7), 0.1839(7)	0.303(2), 0.821(2), 0.256(4)
	$100\times$ U_{iso} / Å^2	0.9(2)	1.2(2)	-0.5(2)
χ^2, No. of parameters		2.696, 34	2.086, 38	2.377, 43
R_{wp}, R_p		0.0285, 0.0197	0.0251, 0.0183	0.0268, 0.0189
$(00l)$ Preferred Orientation		0.885(2)	0.904(2)	0.877(2)
stec		-10.4(4)	-	-6.6(4)
ptec		0	1.2(2)	0
GP		0	114(9)	0
η		-	1	-
$S400$		-	0.110(6)	-
$S220$		-	-0.028(3)	-
$S202$		-	0.060(3)	-

Table 6.6 – XRPD-refined values for $Mn_{0.6}Co_{0.4}Sb_2O_4$.

		$P4_2/mbc$ model		*Pbam* model
		Profile #2	Profile #4	Profile #2
a / Å		8.6170(1)	8.6160(2)	8.6120(2)
b / Å		-	-	8.6221(2)
c / Å		5.96649(7)	5.9658(1)	5.96655(7)
Mn / Co (4d / 4f)	$(0,\ \frac{1}{2},\ \frac{1}{4})$ / $(0,\ \frac{1}{2},\ z)$	-	-	0.241(2)
	$100\times$ U_{iso} / Å^2	1.7(1)	1.7(1)	1.4(1)
Sb1 (8h / 4g)	$(x,\ y,\ 0)$	0.1781(3), 0.1670(2)	0.1782(2), 0.1665(2)	0.6764(7), 0.3326(7)
	$100\times$ U_{iso} / Å^2	1.47(5)	1.36(5)	2.1(2)
Sb2 (4h)	$(x,\ y,\ \frac{1}{2})$	-	-	0.3322(7), 0.3217(7)
	$100\times$ U_{iso} / Å^2	-	-	1.0(2)
$O1_{eq}$ (8h / 4g)	$(x,\ y,\ 0)$	0.082(1), 0.632(1)	0.088(1), 0.636(1)	0.602(2), 0.832(2)
	$100\times$ U_{iso} / Å^2	-0.3(2)	0.4(2)	-2.0(2)
$O1_{eq}$ (4h)	$(x,\ y,\ \frac{1}{2})$	-	-	0.896(2), 0.438(3)
	$100\times$ U_{iso} / Å^2	-	-	-2.0(2)
$O2_{ax}$ (8g / 8i)	$(x,\ y,\ \frac{1}{4})$ / $(x,\ y,\ z)$	0.6919(7), 0.1919(7)	0.6883(7), 0.1882(7)	0.324(2), 0.794(2), 0.248(4)
	$100\times$ U_{iso} / Å^2	-0.3(2)	0.4(2)	-2.0(2)
χ^2, No. of parameters		4.075, 33	3.263, 37	3.697, 43
R_{wp}, R_p		0.0356, 0.0237	0.0319, 0.0222	0.0339, 0.0233
$(00l)$ Preferred Orientation		0.825(2)	0.843(2)	0.821(2)
stec		-7.1(3)	-	-4.7(4)
ptec		0	0.3(2)	0
GP		0	0	0
η		-	1	-
$S400$		-	0.051(4)	-
$S220$		-	-0.024(2)	-
$S202$		-	0.047(2)	-

Table 6.7 – XRPD-refined values for $Mn_{0.8}Co_{0.2}Sb_2O_4$.

		$P4_2/mbc$ model		*Pbam* model
		Profile #2	Profile #4	Profile #2
a / Å		8.6596(2)	8.6583(4)	8.6500(3)
b / Å		-	-	8.6697(3)
c / Å		5.9803(1)	5.9793(3)	5.9804(1)
Mn / Co (4d / 4f)	$(0,\ \frac{1}{2},\ \frac{1}{4})$ / $(0,\ \frac{1}{2},\ z)$	-	-	0.262(2)
	$100\times$ U_{iso} / Å^2	1.1(1)	1.2(1)	1.0(1)
Sb1 (8h / 4g)	$(x,\ y,\ 0)$	0.1791(3), 0.1675(3)	0.1788(3), 0.1672(2)	0.6749(8), 0.3312(6)
	$100\times$ U_{iso} / Å^2	1.38(6)	1.31(5)	0.8(2)
Sb2 (4h)	$(x,\ y,\ \frac{1}{2})$	-	-	0.3326(8), 0.3181(7)
	$100\times$ U_{iso} / Å^2	-	-	2.2(2)
$O1_{eq}$ (8h / 4g)	$(x,\ y,\ 0)$	0.089(1), 0.641(1)	0.097(1), 0.644(1)	0.579(3), 0.892(2)
	$100\times$ U_{iso} / Å^2	1.0(2)	1.2(2)	-1.1(3)
$O1_{eq}$ (4h)	$(x,\ y,\ \frac{1}{2})$	-	-	0.817(2), 0.397(2)
	$100\times$ U_{iso} / Å^2	-	-	-1.1(3)
$O2_{ax}$ (8g / 8i)	$(x,\ y,\ \frac{1}{4})$ / $(x,\ y,\ z)$	0.6915(8), 0.1915(8)	0.6847(7), 0.1847(7)	0.321(2), 0.800(2), 0.262(4)
	$100\times$ U_{iso} / Å^2	1.0(2)	1.2(2)	-1.1(3)
χ^2, No. of parameters		2.404, 34	1.787, 38	2.187, 43
R_{wp}, R_p		0.0275, 0.0192	0.0237, 0.0176	0.0262, 0.0189
$(00l)$ Preferred Orientation		0.864(2)	0.884(2)	0.861(2)
stec		-16.7(6)	-	-10.5(7)
ptec		0	3.3(2)	0
GP		0	0	0
η		-	0.80(2)	-
$S400$		-	0.355(9)	-
$S220$		-	-0.071(8)	-
$S202$		-	0.152(9)	-

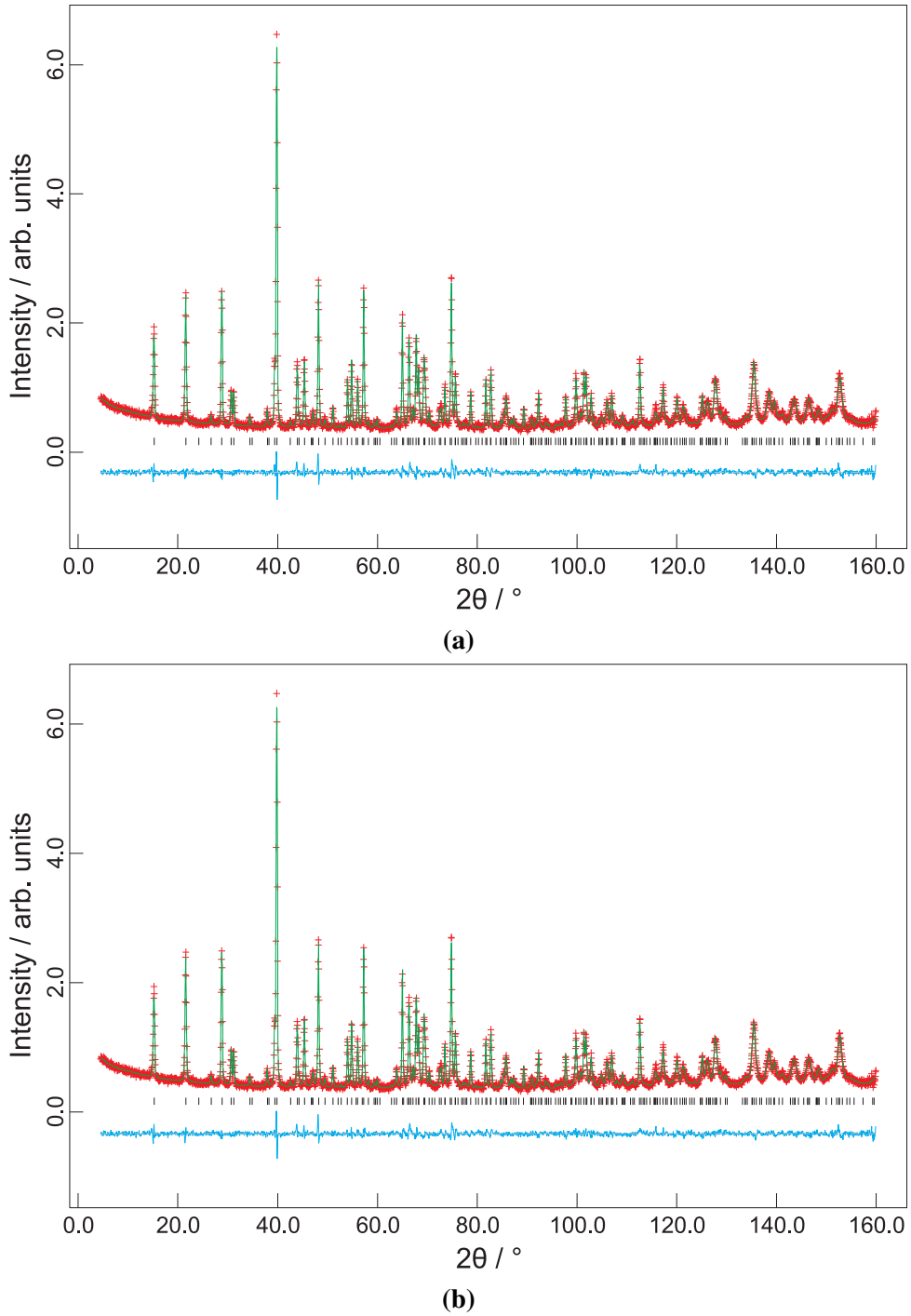

Figure 6.3 – Graphical refinements for $Mn_{0.2}Co_{0.8}Sb_2O_4$ using (a) profile function #2 and (b) profile function #4.

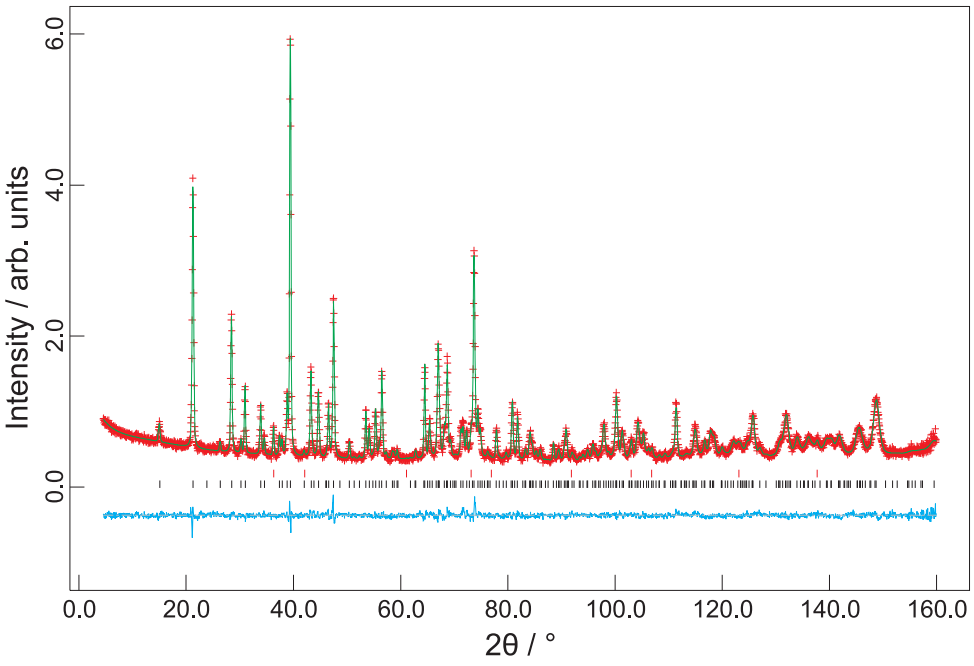

Figure 6.4 – Graphical refinement of $Mn_{0.8}Co_{0.2}Sb_2O_4$ showing MnO impurity peaks (red tickmarks).

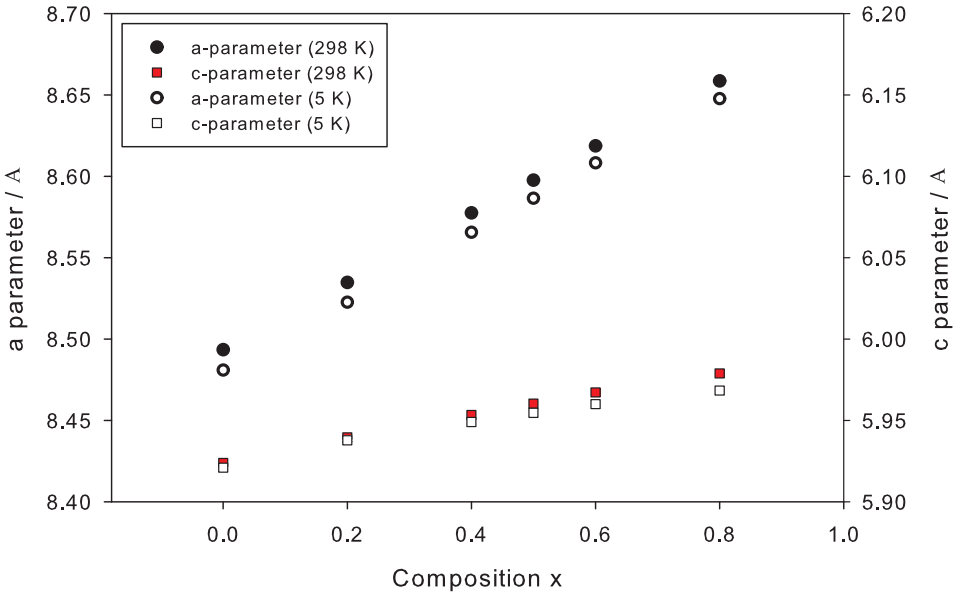

Figure 6.5 – Plot of unit cell parameters *a* and *c vs. x* for $Mn_xCo_{1-x}Sb_2O_4$.

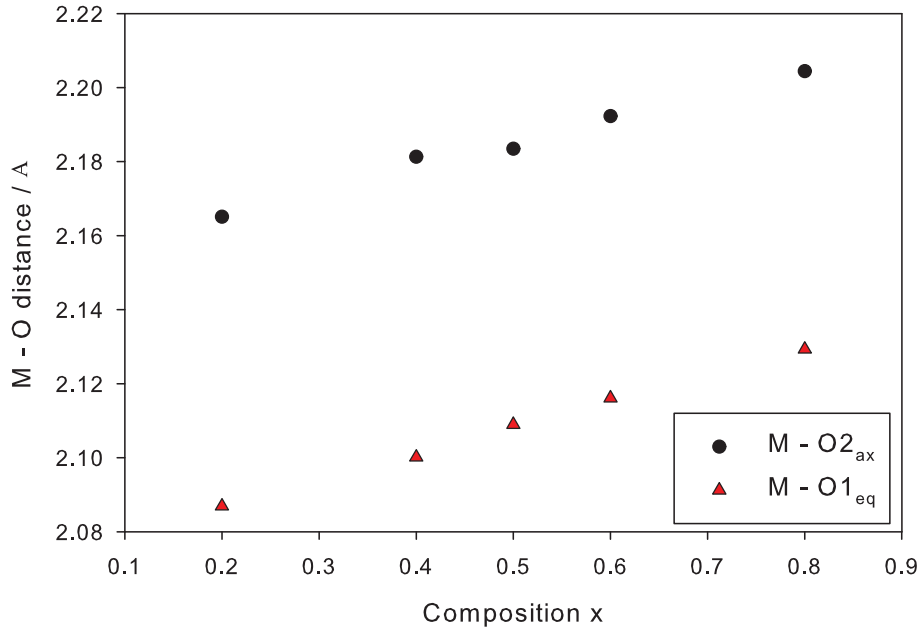

Figure 6.6 – M−O_{ax} and M−O_{eq} bond lengths *vs.* x for $Mn_xCo_{1-x}Sb_2O_4$.

tortions of 0.0170, 0.0155 and 0.0158 for $x = 0.4,\ 0.5$ and 0.6). This deviation is matched by changes in the Sb−O bond lengths across the composition range (figure 6.8), as well as a clear deviation of the bond angles around Sb (figure 6.9). This explains why the M−O bonds can show a deviation for $x = 0.5$, yet the unit cell parameters increase linearly. The changes are consistent with the different bonding around antimony seen for the two end-members, in order to accommodate the larger, less distorted octahedral environment of the Mn cation. The data suggest that for $x \geq 0.5$, the larger Mn^{2+} ion starts to dominate, changing from a $CoSb_2O_4$-like structure with Mn-doping to a $MnSb_2O_4$-like structure with Co-doping. The BVS for M (obtained as a weighted average of Mn and Co R_0 values) shows a very slight increase with x, with a marginally higher value for $x = 0.5$ than the trend.

It is perhaps surprising that the Sb coordination can be so significantly changed by the M cation. The change is most probably related to the size of the structural channel, and the volume associated with each Sb LP; as x increases, the channel becomes larger, allowing the bond angles around Sb to become less distorted. The anomalous parameters seen for $x = 0.5$ could indicate that this is a 'critical' channel volume, possibly related to the equal Mn / Co ratio.

Table 6.8 – Refined unit cell, atomic and statistical parameters for $Mn_xCo_{1-x}Sb_2O_4$ at 300 K.

		$Mn_{0.2}Co_{0.8}Sb_2O_4$	$Mn_{0.4}Co_{0.6}Sb_2O_4$	$Mn_{0.5}Co_{0.5}Sb_2O_4$	$Mn_{0.6}Co_{0.4}Sb_2O_4$	$Mn_{0.8}Co_{0.2}Sb_2O_4$
a / Å		8.5348(1)	8.5775(2)	8.5976(1)	8.6187(1)	8.6585(2)
c / Å		5.93956(9)	5.9534(1)	5.9602(1)	5.96719(8)	5.9788(1)
Mn / Co (4d)	$100 \times U_{iso}$ / Å^2	0.9(3)	0.8 (fixed)	0.5(4)	0.8(2)	0.6(1)
	Mn Occupancy	0.211(5)	0.426(4)	0.510(5)	0.608(5)	0.795(5)
Sb (8h)	x	0.1758(2)	0.1773(2)	0.1778(2)	0.1782(2)	0.1790(2)
	y	0.1649(2)	0.1651(2)	0.1655(2)	0.1664(2)	0.1664(2)
	$100 \times U_{iso}$ / Å^2	0.80(3)	0.92(4)	1.06(3)	1.00(3)	0.84(4)
$O1_{eq}$ (8h)	x	0.0987(2)	0.0981(2)	0.0989(2)	0.0994(2)	0.0994(2)
	y	0.6406(2)	0.6422(2)	0.6427(2)	0.6429(2)	0.6442(2)
	$100 \times U_{iso}$ / Å^2	0.93(3)	1.02(4)	1.17(3)	1.11(3)	1.03(4)
$O2_{ax}$ (8g)	x	0.6794(1)	0.6798(1)	0.6796(1)	0.6799(1)	0.6800(1)
	$100 \times U_{iso}$ / Å^2	1.34(3)	1.36(3)	1.52(3)	1.49(3)	1.38(3)
χ^2		1.981	2.145	4.153	2.242	1.705
No. of Parameters		49	39	39	44	45
R_{wp}, R_p		0.0467, 0.0374	0.0411, 0.0336	0.0446, 0.0361	0.0489, 0.0384	0.0430, 0.0349

Table 6.9 – Selected bond distances and angles for $Mn_xCo_{1-x}Sb_2O_4$ at 300 K.

	$Mn_{0.2}Co_{0.8}Sb_2O_4$	$Mn_{0.4}Co_{0.6}Sb_2O_4$	$Mn_{0.5}Co_{0.5}Sb_2O_4$	$Mn_{0.6}Co_{0.4}Sb_2O_4$	$Mn_{0.8}Co_{0.2}Sb_2O_4$
$M-O1_{eq}$ / Å	2.08691(3)	2.10015(3)	2.10895(3)	2.11610(2)	2.12929(3)
$M-O2_{ax}$ / Å	2.16509(3)	2.18130(4)	2.18349(3)	2.19231(3)	2.20443(4)
Octahedral Distortion Index	0.0164	0.0170	0.0155	0.0158	0.0155
Octahedral Volume / $Å^3$	12.38	12.62	12.74	12.88	13.11
Quadratic Elongation	1.0108	1.0118	1.0114	1.0112	1.0117
Octahedral Twist / °	19.87	20.80	20.54	20.35	20.81
$Sb-O1_{eq}$ / Å	1.93539(3)	1.93679(5)	1.92945(4)	1.92686(3)	1.92834(5)
$Sb-O2_{ax}$ / Å	1.99297(3)	1.99641(4)	1.99857(3)	1.99549(2)	2.00046(3)
$\angle M-O1_{eq}-M$ / °	90.72	90.26	89.91	89.65	89.17
$\angle M-O2_{ax}-Sb$ / °	117.437	117.614	117.772	117.683	117.821

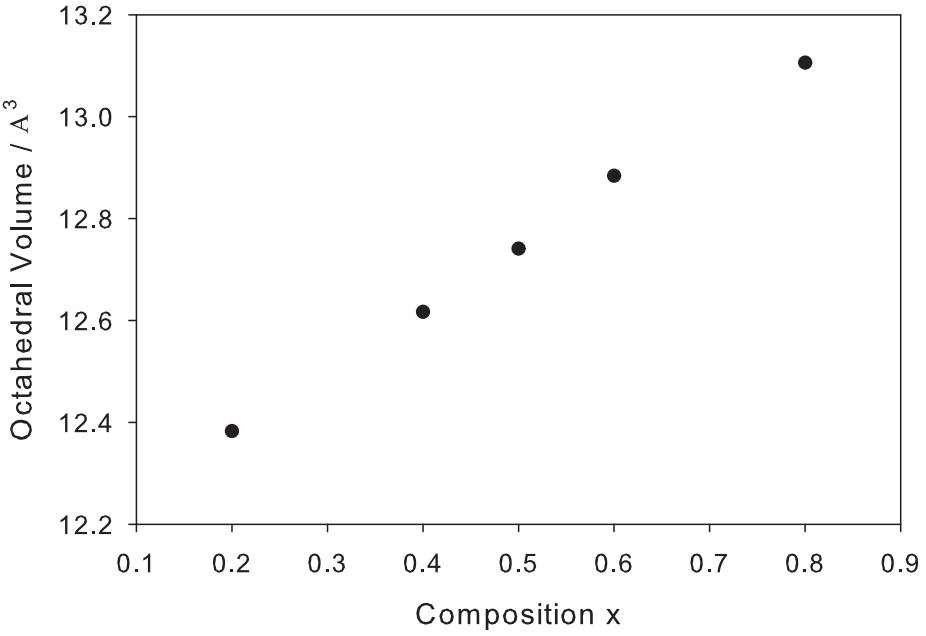

Figure 6.7 – Octahedral volume *vs. x* for $Mn_xCo_{1-x}Sb_2O_4$.

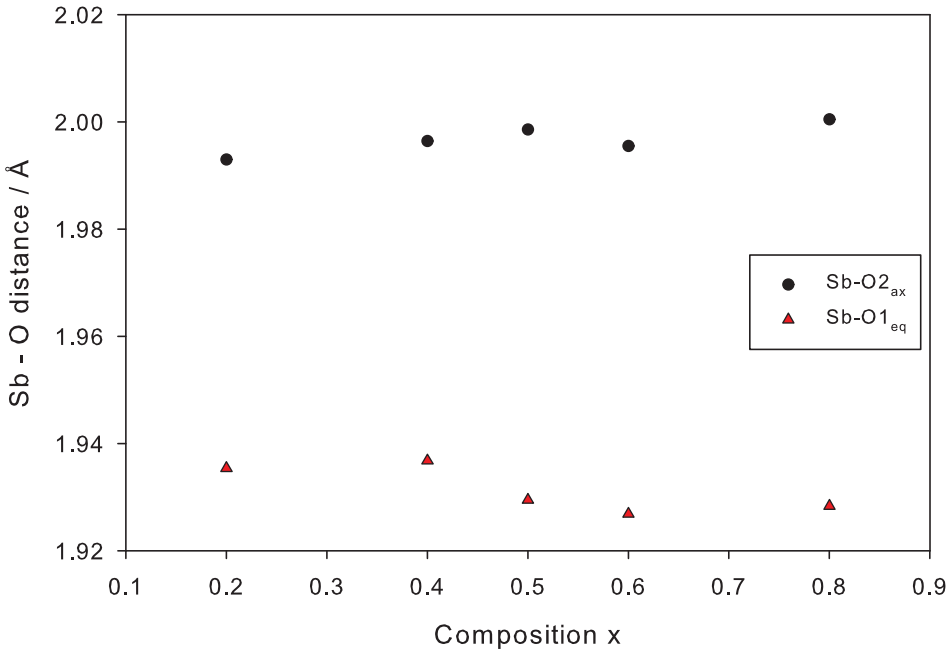

Figure 6.8 – Sb−O bond lengths *vs. x* for $Mn_xCo_{1-x}Sb_2O_4$.

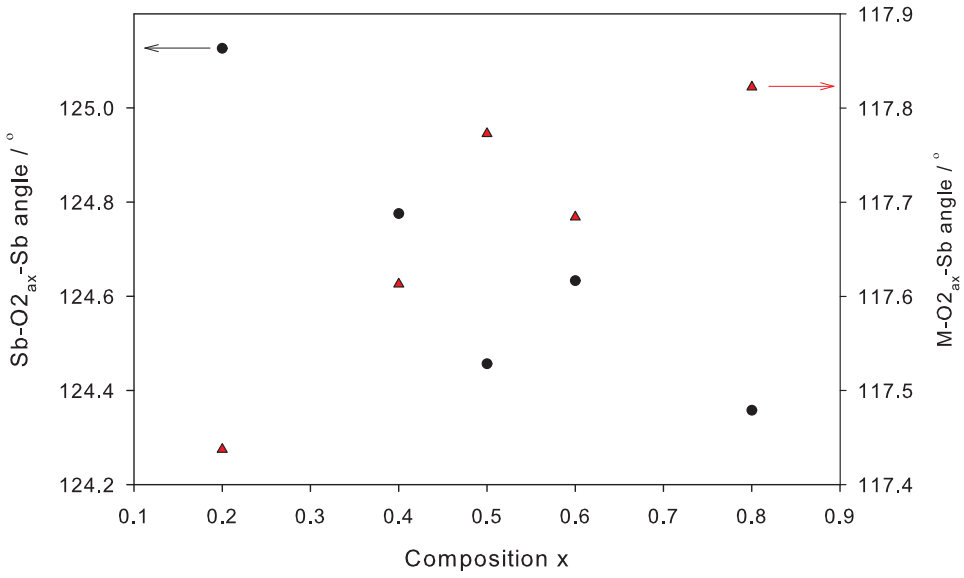

Figure 6.9 – Angles around Sb *vs.* x for $Mn_xCo_{1-x}Sb_2O_4$.

From the values in table 6.8 it can be seen that the O2 (axial) position generally has a large isotropic temperature factor. This is consistent with disorder due to the local coordination requirements around either Mn or Co. A refinement using anisotropic temperature parameters for both oxygen positions in $Mn_{0.5}Co_{0.5}Sb_2O_4$ resulted in a reduction in χ^2 (3.798, 48 variables) and the temperature factors given in table 6.10. These are shown as ellipsoids in figure 6.10. From the graphical representation it can be seen that the $O2_{ax}$ displacement occurs predominantly in the *ab* plane, slightly off perpendicular to the plane of its bonds. The $O1_{eq}$ displacements are less anisotropic, occurring as a slightly oblate spheroid aligned along the [110] direction. These displacements reflect the slightly different octahedral twist angles observed in the end-members, as well as the slightly greater Co−O bond-angle variance (σ^2 = 31.5° *cf.* 35.1° for Mn and Co, respectively) occurring due to the preferred octahedral distortion for Co^{2+} (d^7) *cf.* Mn^{2+} (d^5).

6.3.3 Analysis by NPD on Cooling

NPD data were collected at 40 K, 60 K, 70 K and 80 K for $Mn_{0.2}Co_{0.8}Sb_2O_4$, in addition to data at 5 K for all values of x. In this section structural changes on cooling will be discussed;

Table 6.10 – Anisotropic temperature factors for oxygen positions in $Mn_{0.5}Co_{0.5}Sb_2O_4$.

Parameter	100 × Value / Å^3	
	$O1_{eq}$	$O2_{ax}$
U_{11}	1.19(9)	1.81(5)
U_{22}	1.14(10)	1.81(5)
U_{33}	1.22(7)	1.11(7)
U_{12}	-0.21(6)	-1.06(7)
U_{13}	0	-0.27(5)
U_{23}	0	0.27(5)

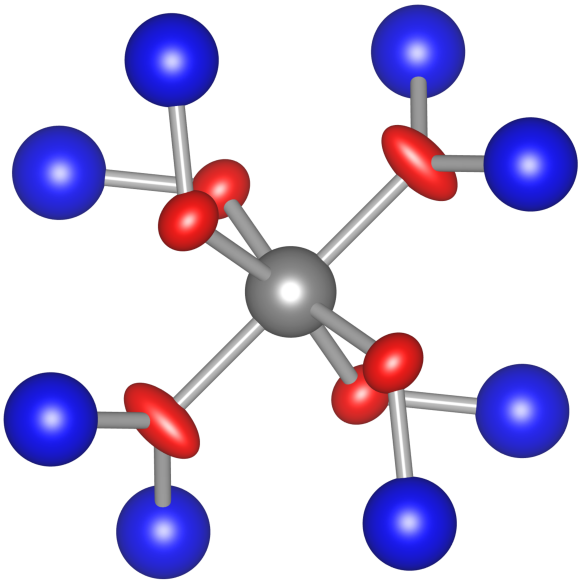

Figure 6.10 – Anisotropic oxygen positions shown for $Mn_{0.5}Co_{0.5}Sb_2O_4$. Mn / Co - grey sphere, Sb - blue spheres, O - red ellipsoids.

section 6.4.2 will deal with magnetic behaviour and structure. All datasets taken within the He cryostat show additional broad peaks in the diffraction patterns at *ca.* 40° and 45° 2θ, due to incorrect background subtraction. Because of the overlap of these peaks with major structural and magnetic reflections these regions were not excluded, but the resulting fits are more error-prone as a result.

The magnetic contribution ($T_N \simeq 122$ K) from the MnO impurity for $x = 0.8$ was modelled using a single (nuclear and magnetic) phase, of monoclinic symmetry $(C2/c)$. Ionic positions were Mn $(0,\ 0,\ 0)$ and O $(0,\ \frac{1}{2},\ \frac{3}{4})$, with Mn moments allowed to refine along a. Additionally, the $x = 0.2$ datasets showed a very weak reflection at $\simeq 18.5°$ 2θ. This could be attributed to the magnetic (001) (monoclinic unit cell) peak of MnO. No nuclear MnO peaks were observed because of the low scattering compared to the strong magnetic scattering of Mn^{2+}.

Structural Change in $Mn_{0.2}Co_{0.8}Sb_2O_4$

On cooling, the volume of $Mn_{0.2}Co_{0.8}Sb_2O_4$ decreases as expected (figure 6.11). The a parameter reflects this change, but the c-axis shows a small increase below 80 K (figure 6.12). Although significant compared to the error for each point (σ is less than the symbol width) the increase corresponds to a 0.01 % change, and so is not very influential.

The most interesting change on cooling occurs for the Mn / Co position, as seen by observing temperature factors (figure 6.13). Using isotropic parameters (fixed to be equal for Mn and Co) the thermal displacement decreases as expected down to 60 K, but then increases slightly at 40 K. At 5 K, the same model proved unstable and unphysical, with a $100 \times U_{iso}$ value greater than the GSAS limit of 80 Å^2. The Mn fractional occupancy also dropped to -0.49(5). These parameters are strongly correlated to the magnetic scattering (occurring for both 5 K and 40 K datasets, see section 6.4.2) but this is reflected in the large error values obtained. Although these errors are often of a similar magnitude as the value itself, trends can still be discussed. The presence of peaks only due to magnetic structure in the pattern does help to accurately separate the nuclear and magnetic contributions, reducing the inherent error. While a ferromagnetic component would coincide entirely with nuclear peaks (and could therefore be

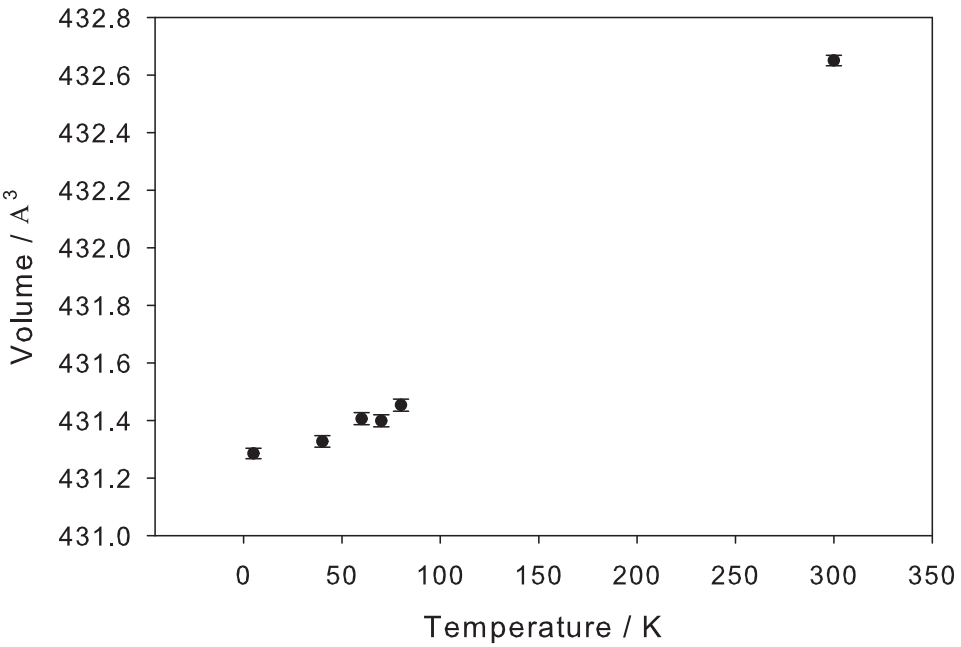

Figure 6.11 – Graph of unit cell volume *vs.* temperature for $Mn_{0.2}Co_{0.8}Sb_2O_4$.

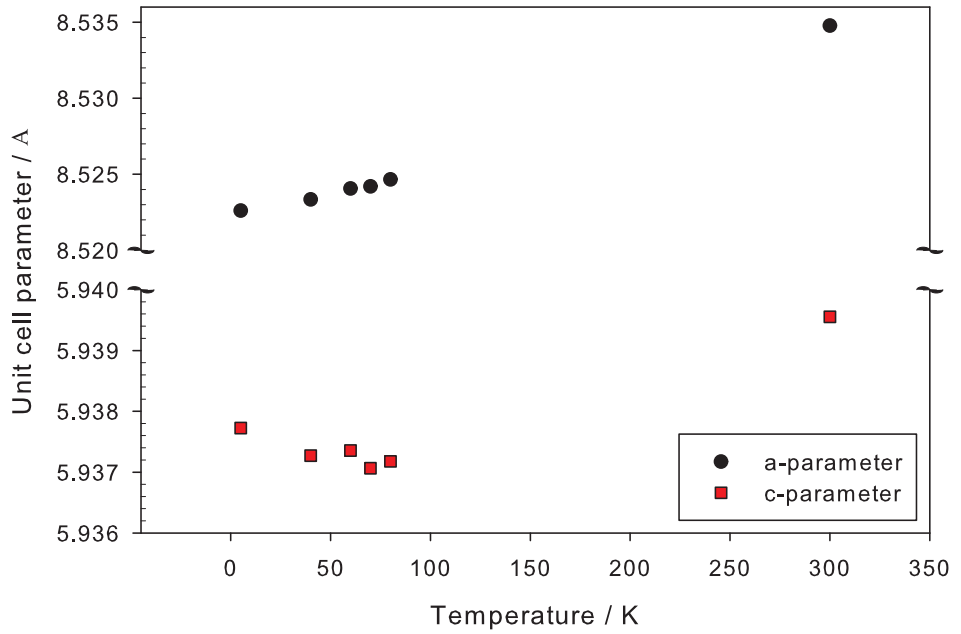

Figure 6.12 – Graph of unit cell parameters *a* and *c vs.* temperature for $Mn_{0.2}Co_{0.8}Sb_2O_4$.

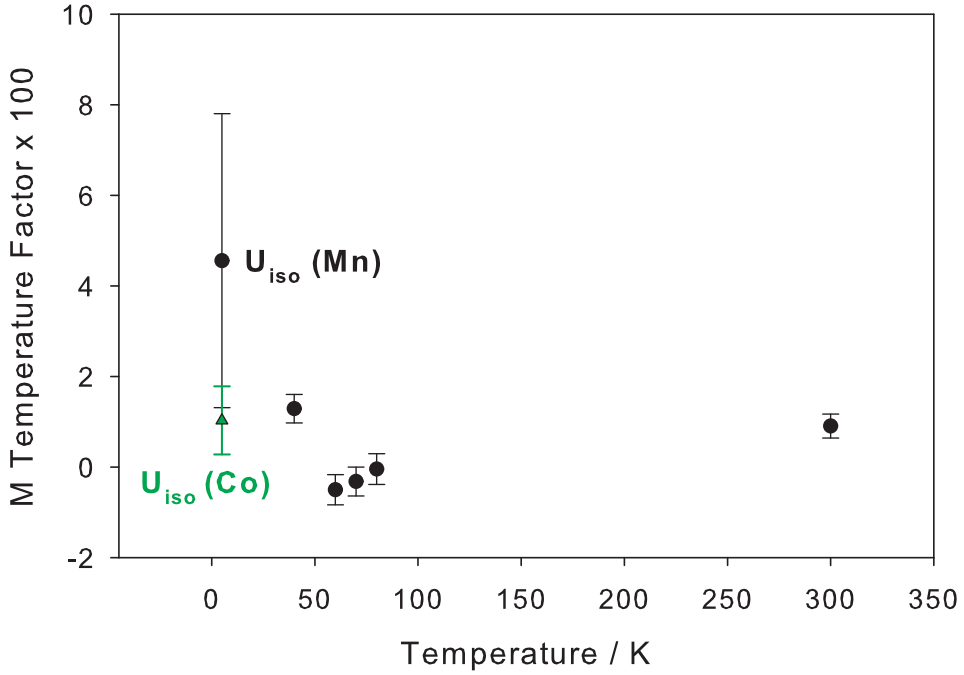

Figure 6.13 – Graph of M cation displacement parameter(s) *vs.* temperature for $Mn_{0.2}Co_{0.8}Sb_2O_4$.

strongly correlated to temperature parameters) no evidence of a significant ferromagnetic signal has been seen from DC susceptibility measurements (section 6.4.1).

Removing the U_{iso} constraint for Mn / Co resulted in the values seen in figure 6.13; a large Mn U_{iso} (4.6 ± 3.2 Å^2) and a more reasonable value for Co (1.0 ± 0.8 Å^2). Alternatively, using anisotropic parameters (constrained to be equal for Mn and Co) gave values of U_{11} = -0.7(4), U_{33} = 0.1(5) and U_{12} = 0.7(5). These two responses indicate that the reflections strongly dependent on the M site (particularly $(hh0)$) are more intense than expected, and the model is trying to increase $\mathbf{F}_{hkl}$ to compensate (see (2.3) and (2.4) for mathematical basis). The overall effect is to increase the average scattering from the site, either by decreasing the effectiveness of Mn scattering relative to Co (higher Mn U) or by maximising the combined positive scattering (negative U). Because of the more normal U_{iso} values obtained at higher temperatures, the effect is not due to changes in the sample environment or crystal morphology (*i.e.* preferred orientation effects). Additionally, the low temperature would prohibit significant ionic diffusion of other (heavily scattering) atoms onto the M site. For these reasons, the thermal parameters obtained indicate a displacement of the (negatively scattering) Mn ions away from the 4d position, or a

greater localisation of Co onto the site.

Because the different scattering lengths for Mn and Co should be separable by NPD, a number of models were tested to deduce the nature of the atomic motion. Models involving both isotropic and anisotropic temperature factors for both Mn and Co as well as 'splitting' the crystallographic site were tested. This involved moving the atom(s) on to lower symmetry sites, and reducing the fractional occupancy accordingly (often the occupancy was then fixed to the $x = 0.2$ value). The sites tested were:

8f $(0,\ \frac{1}{2},\ z)$: Giving freedom of movement along z,

8g $(x,\ x+\frac{1}{2},\ \frac{1}{4})$: This site allows motion along the $[110]$ or $[\bar{1}10]$ directions depending on initial position, corresponding to movement along the $M-O_{ax}$ direction ($8g_{ax}$) or perpendicular to it, in the *ab* plane ($8g_{eq}$),

16i $(x,\ y,\ z)$: This general position allows absolute directional freedom (*i.e.* $(x,\ y,\ z)$).

In all cases, the thermal parameters of the magnetic phase were fixed at $100 \times U_{iso} = 1$ Å^2 and the positions were left as 4d, to avoid correlations. These parameters have less impact than the nuclear phase parameters, due to the diffuse nature of magnetic scattering involved.

A model involving separate anisotropic temperature factors for Mn and Co gave the temperature factors given in table 6.11, consistent with a reduction of the negative Mn scattering, particularly in the *ab* plane. This model refined the Mn occupancy to 0.245(9) however, slightly higher than that expected (and possibly counteracting the effect of U). Fixing the occupancy to 0.2 gave negative U_{11} and U_{12} values. These two different responses seem to conflict; in the first $\mathbf{F}_{hkl}$ is effectively increased by a combination of U and occupancy, while in the second case it is decreased by the combination of U, with calculated values due to the M cations of $\mathbf{F}_{110} \simeq 0.6(\cos\delta_j + i\sin\delta_j)$ and $-11.7(\cos\delta_j + i\sin\delta_j)$, respectively. The χ^2 values for the two models (4.555 and 4.594) could indicate that the increase in $\mathbf{F}_{hkl}$ is more favourable, consistent with the isotropic results.

A slightly better refinement could be achieved using anisotropic temperature factors for Mn, and an isotropic parameter for Co (table 6.12). Whilst giving a better fit, the negative U

Table 6.11 – Separate anisotropic temperature factors for Mn and Co in $Mn_{0.2}Co_{0.8}Sb_2O_4$.

Parameter	100 × U / Å^2			
	Refined Occ.		Fixed Occ.	
	Mn	Co	Mn	Co
U_{11}	7(4)	0.8(7)	-5(2)	-2(1)
U_{33}	4(4)	1(1)	1(3)	1(2)
U_{12}	10(3)	2.8(8)	-2(2)	-1(1)
χ^2	4.555		4.594	

Table 6.12 – Anisotropic temperature factor for Mn with isotropic Co in $Mn_{0.2}Co_{0.8}Sb_2O_4$.

Parameter	100 × U / Å^3, refined occupancy	100 × U / Å^3, fixed occupancy
Co U_{iso}	-5.6(7)	0(1)
Mn U_{11}	-7.7(7)	-2(3)
Mn U_{33}	-7.7(7)	-2(3)
Mn U_{12}	-0.2(1)	-0.8(8)
χ^2	4.541	4.598

parameters are obviously unphysical. The more negative U of Mn *vs.* Co could indicate an incomplete displacement of the Mn away from the site, such that the total scattering factor is less than if all Mn cations were displaced.

Moving Co to lower-symmetry positions (while leaving Mn on 4d) resulted in unstable refinements, except for the 16i position. In this case, the temperature factors for Mn and Co were both negative (-2(3) and -2(1), respectively) and the Co position was (0.019(4), 0.502(2), 0.230(5)). More stable refinements were obtained when moving the Mn cation off-site, mainly to the $8g_{ax}$ and 16i positions. Again, these models resulted in negative U_{iso} values (particularly for Mn) suggesting incomplete displacement of the Mn cation. Refined parameters are given in table 6.13. The most significant results are seen for the Mn 16i position, where the refined

Table 6.13 – Refined off-site Mn positions with isotropic displacement.

Parameter	100 × U / Å^3	
	Mn 8g$_{ax}$	Mn 16i
Mn U$_{iso}$	-1(5)	-4(2)
Co U$_{iso}$	0(2)	-1(1)
x	0.510(6)	0.504(3)
y	0.010(6)	0.021(5)
z	$\frac{1}{4}$	0.229(5)
χ^2	4.597	4.598

positions show the Mn cation occupying positions closer to the octahedral edges (figure 6.14).

Models involving moving both atoms off of the 4d position were also tested (with U$_{iso}$ values constrained to be equal); these gave stable refinements for the 8f, 8g$_{eq}$ and 16i sites, but with large positive thermal parameters (corresponding to an effective reduction of the scattering intensity). This indicates that there must be some scattering occurring from the 4d site.

To investigate if any atomic displacements were occurring concertedly, a model of lower symmetry ($Pmc2_1$) was tested with the axis transformation

$$\begin{pmatrix} 0 & 0 & -1 \\ 0 & 1 & 0 \\ 1 & 0 & 0 \end{pmatrix}$$

which places M on a general (4c) site. This nuclear model was also compatible with the observed magnetic structure, and so could be refined as a single phase. With a single (position- and U-constrained) M site, the cations refined to a position satisfying two shorter bonds, effectively moving towards an octahedral edge (table 6.14). Splitting the Mn and Co positions (while still constraining U) gave an Mn position similar to the single site (*i.e.* towards an octahedral edge) while the Co position moved more towards a face (three shorter bonds). While consistent

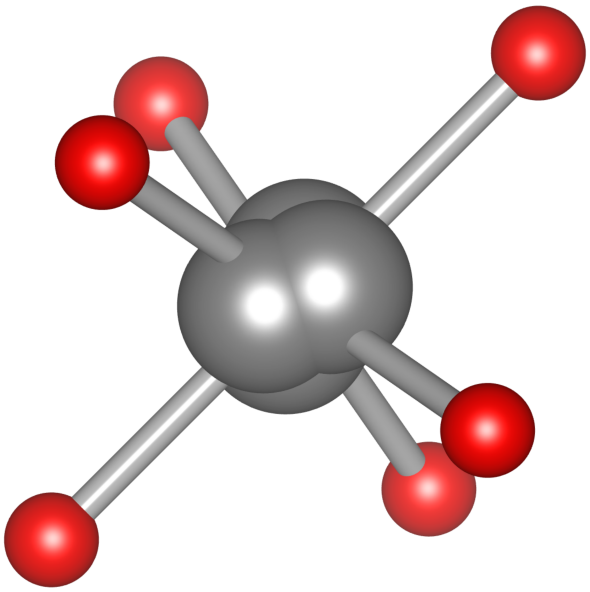

Figure 6.14 – Movement of Mn cations toward octahedral edges in 16i position, viewed along [001].

with the distortion observed for the Mn 16i position, this model gave much higher polyhedral distortion than that of $P4_2/mbc$ (0.050 *cf.* 0.014) in addition to a poorer fit. Given the higher number of variable parameters for the orthorhombic model, the increase in χ^2 shows that the $Pmc2_1$ model does not give a better description of the crystal structure.

From the data presented here, it is clear that on cooling below 40 K a change in structure occurs in $Mn_{0.2}Co_{0.8}Sb_2O_4$ around the M cation site, apparently due to an atomic displacement away from the high-symmetry site. The net result seems to be an overall increase in scattering intensity from the 4d site. From the NPD data, it is unclear what the exact displacement is due to the correlation with magnetic structure and relatively low total scattering length for the Mn / Co ratio. Refined data would suggest that at least some of the Mn cations are shifted towards the octahedral edges, with more distortion occurring in the *ab* plane than along *c*.

The cause of any distortions is most likely due to the presence of the much larger Mn^{2+} in the lattice of $CoSb_2O_4$, which would distort nearby [CoO_6] octahedra. This distortion would complicate the diffraction data, and may give the impression of a long-range atomic displacement (particularly given changes in oxygen positions). At higher temperatures these distortions will be counteracted by atomic vibrations, but as the temperature decreases, the atomic shifts

Table 6.14 – M−O bondlengths for an orthorhombic $Pmc2_1$ model.

	Single M site	Split M site	
		Mn	Co
M−O1a_{eq}	2.26617(3)	2.35523(3)	2.28273(3)
M−O1b_{eq}	2.12176(3)	2.48494(3)	2.26904(3)
M−O1c_{eq}	1.86719(2)	1.81428(3)	1.87347(3)
M−O1d_{eq}	2.10798(3)	1.78583(3)	1.95230(3)
M−O2a_{ax}	2.27349(4)	2.35523(3)	2.28937(4)
M−O2b_{ax}	2.04724(4)	2.48494(3)	2.03268(4)
$100 \times U_{iso}$ / Å^3	-2.7(3)	-0.3(5)	
χ^2	4.99	5.114	

occur. This can be seen both in the refined $H400$ strain parameter and the octahedral chain 'twist' (figures 6.15 and 6.16, respectively). The strain parameter shows an increase to a maximum at 60 K, followed by a sudden drop at lower temperatures. This shows that the atomic displacement occurs to relieve strain at low temperatures. The octahedral twist angle shows a similar effect on cooling, increasing up to a maximum before sharply dropping. The maximum here occurs at 40 K however, so does not fully correlate with the strain parameter. Given the large errors associated with the $H400$ term however, it is reasonable that the strain and octahedral twist reflect each other. This might indicate that the the strain occurs as a 'buckling' of the octahedral chains, which is relieved on cooling by apparent distortion of the M site.

The studies on the 40 K data presented above involved a constrained U_{iso} value for both Mn and Co, which gave rise to a large displacement value (1.3 Å^2). Models were also tested with separate isotropic and anisotropic U values for Mn and Co. These showed similar behaviour to the 5 K data; higher U values for Mn *cf.* Co (table 6.15).

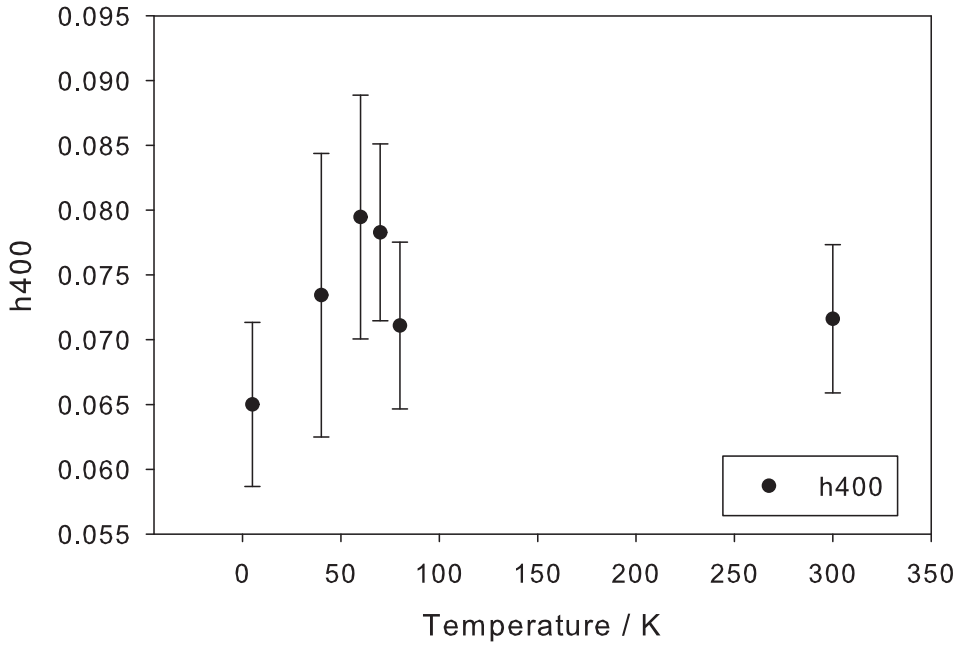

Figure 6.15 – Stephens' *H*400 strain parameter *vs.* temperature in $Mn_{0.2}Co_{0.8}Sb_2O_4$.

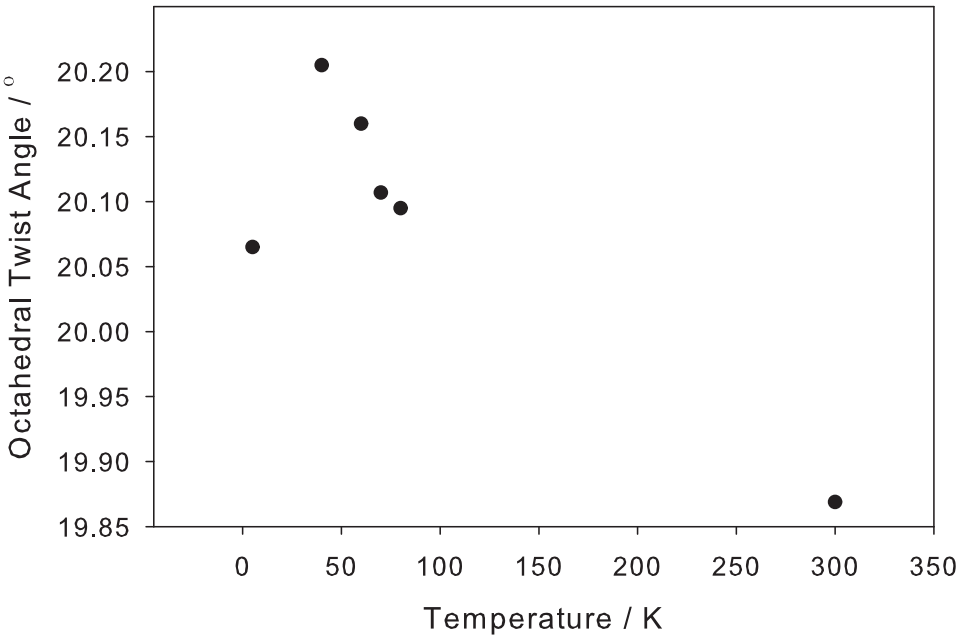

Figure 6.16 – Octahedral twist angle *vs.* temperature in $Mn_{0.2}Co_{0.8}Sb_2O_4$.

Table 6.15 – Temperature factors for Mn and Co at 40 K.

Parameter	U_{aniso}		U_{iso}	
	Mn	Co	Mn	Co
$100 \times U_{iso}$ / Å^3			3(5)	1(1)
$100 \times U_{11}$ / Å^3	8(4)	1.9(8)		
$100 \times U_{33}$ / Å^3	-2(4)	0(2)		
$100 \times U_{12}$ / Å^3	-6(5)	-1(1)		
Mn Occupancy	0.230(9)		0.223(9)	
χ^2	2.998		3.001	

Changes on cooling across the $Mn_xCo_{1-x}Sb_2O_4$ series

The trends seen on varying x in the cooled samples are very similar to those observed at room temperature, *i.e.* the increasing Mn content causes increased octahedral volume, which is reflected in the unit cell parameters (see figure 6.5). The difference here is that lowering the temperature reduces the M−O bond lengths, and thus the octahedral volumes (tables 6.17 and 6.9). Additionally, the octahedral distortion is greatly reduced on cooling, which may be connected with the development of long range magnetic ordering. Unexpectedly, however, the Sb−O bonds actually show a (very slight) lengthening on cooling for many of the compositions studied. This could be connected with the decrease in quadratic elongation on cooling; the slightly less elongated [MO_6] octahedra stretch the Sb−O bonds, despite the overall contraction in volume. The distance between nearest-neighbouring Sb ions across the 'channel' within the structure (approximately along the [110] direction) decreases with temperature as expected, given the change in cell parameters. The ratio of this Sb−Sb distance to the diagonal (110) M−M distance (effectively a measure of the channel size) remains approximately constant with temperature, suggesting that total change in volume occurs equally within the bonds and 'open-space' regions. Another trend to observe is that the octahedral twist angle increases for all samples on cooling; as discussed above, this is possibly a method to accommodate the

contraction in volume. Additionally, the twisting generally increases with x across the series, reflecting the values for the end members.

From the refined unit cell parameters (table 6.16) it is interesting to note that the Sb position shows negative temperature parameters for all samples, whereas they were more normal at 300 K. This may be due to correlations with the magnetic reflections, or possibly due to the additional cryostat peaks for these measurements. They may also indicate that the structural distortion observed in $Mn_{0.2}Co_{0.8}Sb_2O_4$ occurs similarly in the other samples, although this is not necessarily observed in the M site temperature factors (although these values are quite erroneous). Further measurements at intermediate temperatures would be required to fully determine any structural deviations.

6.4 Magnetic Characterisation

6.4.1 Magnetic Susceptibility

Figures 6.17–6.21 show molar and inverse susceptibility for $0.2 \leq x \leq 0.8$ under both FC and ZFC conditions, with an applied field of 500 Oe. In all samples, a complex behaviour is observed. $Mn_{0.2}Co_{0.8}Sb_2O_4$ shows the most significant splitting of FC and ZFC measurements, while the smallest response is seen for $Mn_{0.8}Co_{0.2}Sb_2O_4$.

Susceptibility of $Mn_{0.2}Co_{0.8}Sb_2O_4$

The $x = 0.2$ sample shows a number of magnetic features on heating, seen as divergence between FC and ZFC measurements. The highest temperature transition occurs at $\simeq$ 78 K, as a very slight splitting of the two measurements. The divergence between FC and ZFC increases below this temperature, until another, more significant separation occurs at $\simeq$ 60 K. These two values are very similar to the Néel temperatures of $MnSb_2O_4$ and $CoSb_2O_4$ ($T_N \simeq 55$ K or 79 K, respectively [1,2]) indicating that Mn and Co cations are ordering separately. Although this might suggest that the sample is a phase-separated mixture of $MnSb_2O_4$ and $CoSb_2O_4$ rather than a solid solution, there is no evidence of this from both XRPD and NPD data, where the dif-

Table 6.16 – Refined unit cell, atomic and statistical parameters for $Mn_xCo_{1-x}Sb_2O_4$ at 5 K.

		$Mn_{0.2}Co_{0.8}Sb_2O_4$	$Mn_{0.4}Co_{0.6}Sb_2O_4$	$Mn_{0.5}Co_{0.5}Sb_2O_4$	$Mn_{0.6}Co_{0.4}Sb_2O_4$	$Mn_{0.8}Co_{0.2}Sb_2O_4$
a / Å		8.5226(1)	8.5655(2)	8.5865(1)	8.6082(1)	8.6477(2)
c / Å		5.9377(1)	5.9490(1)	5.9546(1)	5.9601(1)	5.9684(1)
Mn / Co (4d)	$100 \times U_{iso}$ / Å^2	Split U_{aniso} (see text)	1.3 (fixed)	-0.4(3)	1.6(2)	0.2(1)
	Mn Occupancy	0.245(9)	0.444(5)	0.519(5)	0.671(7)	0.822(7)
Sb (8h)	x	0.1757(2)	0.1776(2)	0.1777(2)	0.1779(2)	0.1793(2)
	y	0.1646(2)	0.1650(2)	0.1658(2)	0.1657(2)	0.1665(2)
	$100 \times U_{iso}$ / Å^2	0.00(4)	-0.16(4)	-0.11(3)	-0.04(4)	-0.12(4)
$O1_{eq}$ (8h)	x	0.0984(2)	0.0978(2)	0.0986(2)	0.0985(2)	0.0988(2)
	y	0.6407(2)	0.6424(2)	0.6432(2)	0.6440(2)	0.6451(2)
	$100 \times U_{iso}$ / Å^2	0.22(4)	0.19(4)	0.25(3)	0.23(3)	0.18(4)
$O2_{ax}$ (8g)	x	0.6785(1)	0.6786(1)	0.6790(1)	0.6791(1)	0.6796(1)
	$100 \times U_{iso}$ / Å^2	0.25(3)	0.18(3)	0.21(3)	0.24(3)	0.25(3)
χ^2		4.555	2.73	2.683	3.455	2.509
No. of Parameters		48	44	44	44	53
R_{wp}, R_p		0.0611, 0.0434	0.0544, 0.0414	0.0546, 0.0410	0.0622, 0.0458	0.0530, 0.0397

Table 6.17 – Selected bond distances and angles for $Mn_xCo_{1-x}Sb_2O_4$ at 5 K.

	$Mn_{0.2}Co_{0.8}Sb_2O_4$	$Mn_{0.4}Co_{0.6}Sb_2O_4$	$Mn_{0.5}Co_{0.5}Sb_2O_4$	$Mn_{0.6}Co_{0.4}Sb_2O_4$	$Mn_{0.8}Co_{0.2}Sb_2O_4$
$M-O1_{eq}$ / Å	2.08420(2)	2.09798(4)	2.10815(2)	2.11542(2)	2.12836(3)
$M-O2_{ax}$ / Å	2.15086(3)	2.16315(5)	2.17373(4)	2.18075(3)	2.19631(5)
Octahedral Distortion Index	0.01407	0.01367	0.01367	0.01359	0.01405
Octahedral Volume / $Å^3$	12.27	12.48	12.67	12.79	13.03
Quadratic Elongation	1.0108	1.0118	1.0116	1.0120	1.0124
Octahedral Twist / °	20.06	21.06	20.86	21.27	21.50
$Sb-O1_{eq}$ / Å	1.93629(3)	1.93384(5)	1.93004(3)	1.93379(3)	1.92777(4)
$Sb-O2_{ax}$ / Å	1.99806(2)	2.00177(3)	1.99822(2)	2.00115(2)	1.99957(3)
$\angle$ $M-O1_{eq}-M$ / °	90.83	90.29	89.84	89.56	89.02
$\angle$ $M-O2_{ax}-Sb$ / °	117.704	118.053	117.892	117.927	118.028

ferent unit cell parameters would give split peaks. Both of the transitions are consistent with the formation of a canted AFM structure, due to the divergence of FC and ZFC. The apparent magnitude of the two transitions could indicate that the phase orders predominantly at 60 K, but a small amount orders at higher temperature, presumably due to Co interactions. The slight up-turn in both FC and ZFC susceptibilities at low temperature (< 10 K) is characteristic of a paramagnetic response dominating at low temperature, potentially due to impurity phases or localised paramagnetic regions.

The inverse susceptibility (figure 6.17b) shows that the sample displays Curie-Weiss behaviour above 80 K. Least-squares fitting of this paramagnetic region gave a paramagnetic moment of $5.654(1)\ \mu_B$, and a Weiss constant $\theta = -30.61(2)$ K. This moment is consistent with high-spin Mn and Co, but is considerably higher than the spin-only value computed using the average number of unpaired electrons per M cation ($n = (5\times0.2+3\times0.8),\ \mu_{eff} = 4.28\mu_B$). This is due to the presence of a large orbital moment contribution from Co^{2+}, as seen for $CoSb_2O_4$.[2] The negative value of θ demonstrates that the dominant inter-atomic exchange interaction is antiferromagnetic in the paramagnetic region. This value is much more positive than that observed for $MnSb_2O_4$ ($\theta = -190\pm20\ K$[1]) although is less than that seen for $CoSb_2O_4$ ($\theta = 3.3\pm1\ K$). It is surprisingly close to the weighted average of the two (-35.4 K) suggesting an average of the coupling interactions.

Susceptibility of $Mn_{0.4}Co_{0.6}Sb_2O_4$

$Mn_{0.4}Co_{0.6}Sb_2O_4$ shows similar susceptibility behaviour to $Mn_{0.2}Co_{0.8}Sb_2O_4$, exhibiting a deviation between FC and ZFC measurements at $\simeq 79$ K, followed by a more pronounced transition at lower temperature (figure 6.18). In this sample, however, the 79 K transition is more gradual, indicating a less well-defined ordering temperature. This would be consistent with smaller Co-rich regions, where the ordering is more disrupted by Mn occupation. The temperature at which the main transition occurs is difficult to determine due to the separation of FC and ZFC measurements, but is approximately 45 K. Again, the transition shows divergence of FC and ZFC measurements, consistent with spin canting. Another change in both FC and ZFC

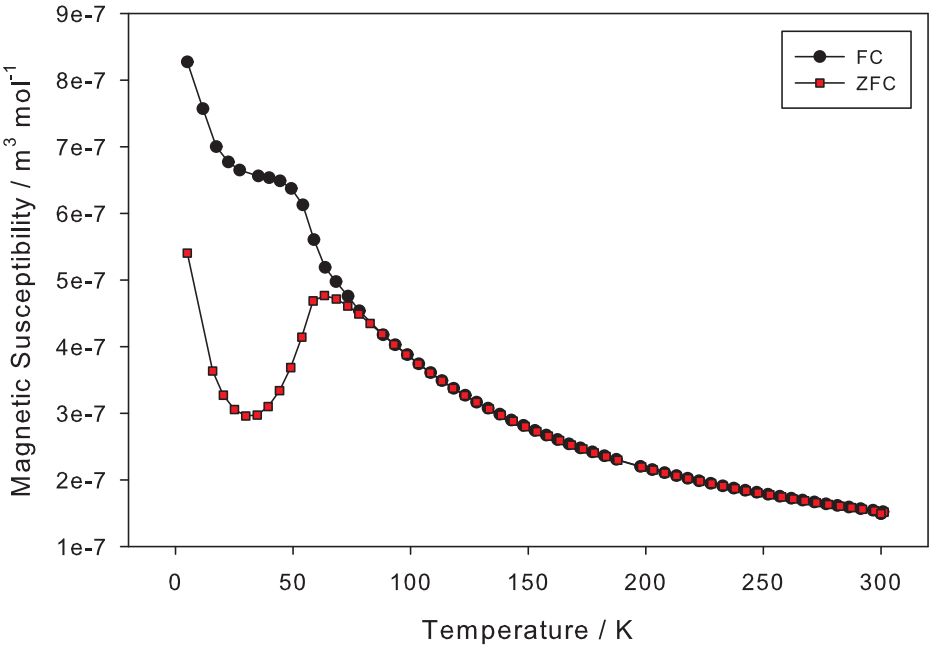

(a)

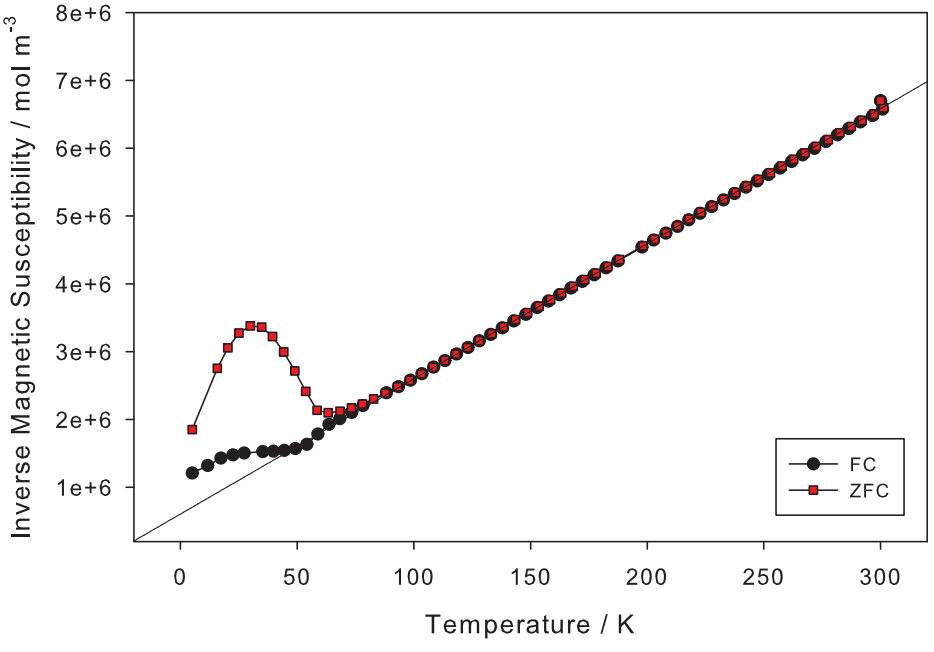

(b)

Figure 6.17 – (a) DC susceptibility and (b) inverse susceptibility measurements for $Mn_{0.2}Co_{0.8}Sb_2O_4$. FC - black circles, ZFC - red squares.

measurements occurs at 22 K, the cause of which is unclear. The inverse magnetic susceptibility shows non-Curie-Weiss behaviour above the magnetic transitions, preventing calculation of a paramagnetic moment.

Susceptibility of $Mn_{0.5}Co_{0.5}Sb_2O_4$

For $x = 0.5$, a strong and sharp magnetic divergence is seen at 27 K, much lower than either transition temperature for $MnSb_2O_4$ or $CoSb_2O_4$. It is also possible to observe a very slight divergence of FC and ZFC at higher temperature, however, starting at 75 K (figure 6.19). The inverse susceptibility plot is not entirely linear, particularly below $\simeq 120$ K. While this hampers calculation of a paramagnetic moment, it is consistent with the results seen for $CoSb_2O_4$, where the change in slope is attributed to a change in dominant exchange interaction.[2] Fitting to the paramagnetic region above 120 K gave $\mu = 5.900(3)\,\mu_B$ and $\theta = -72.68(2)$ K. Again, this value is higher than $\mu_{eff} = 4.89\,\mu_B$ due to orbital contributions.

Susceptibility of $Mn_{0.6}Co_{0.4}Sb_2O_4$

This sample shows a small deviation between FC and ZFC measurements at 22 K, and a second small transition at slightly lower temperature (17 K). There also seems to be a very slight divergence of the two data sets below $\simeq 40$ K. The inverse susceptibility (figure 6.20b) shows slightly non-linear behaviour above the transition(s), although it is unclear whether it shows linear behaviour above $\simeq 120$ K, as for $x = 0.5$. A linear fit of $T > 120$ K resulted in a paramagnetic moment of $6.672(2)\,\mu_B$ and a Weiss constant $\theta = -126.485(7)$ K.

Susceptibility of $Mn_{0.8}Co_{0.2}Sb_2O_4$

$Mn_{0.8}Co_{0.2}Sb_2O_4$ shows very little response from magnetic susceptibility measurements, although a slight divergence of FC and ZFC measurements can be seen starting at $\simeq 69$ K. Additionally, a weak 'kink' can be seen in both measurements at 22 K, although this could lie within error. More useful information can be obtained from the inverse susceptibility (figure 6.21b) where the plot clearly shows a deviation from the paramagnetic response at 70 K. It is important to note that this downturn is normally seen for a ferromagnetic-type response as the susceptibil-

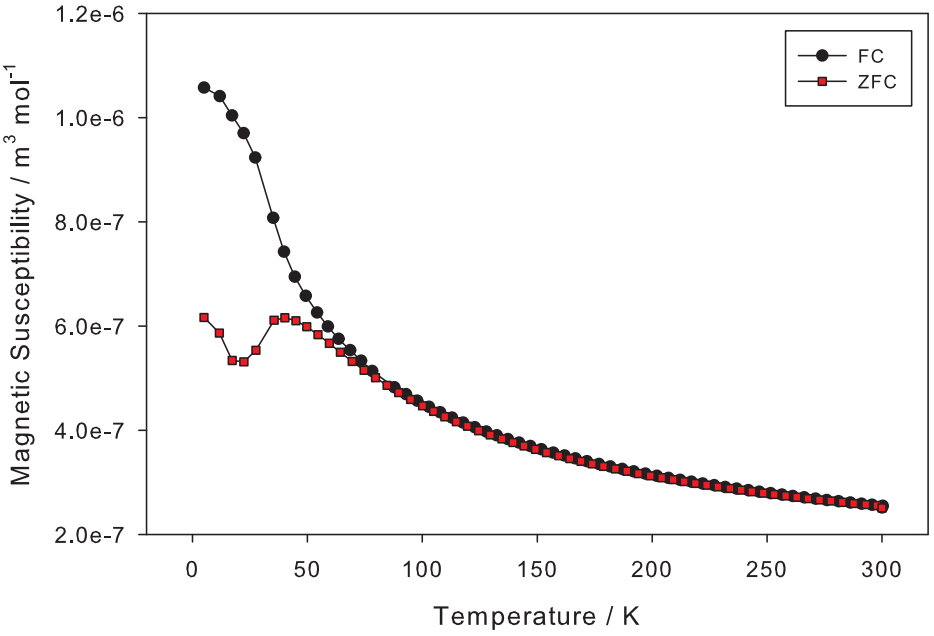

(a)

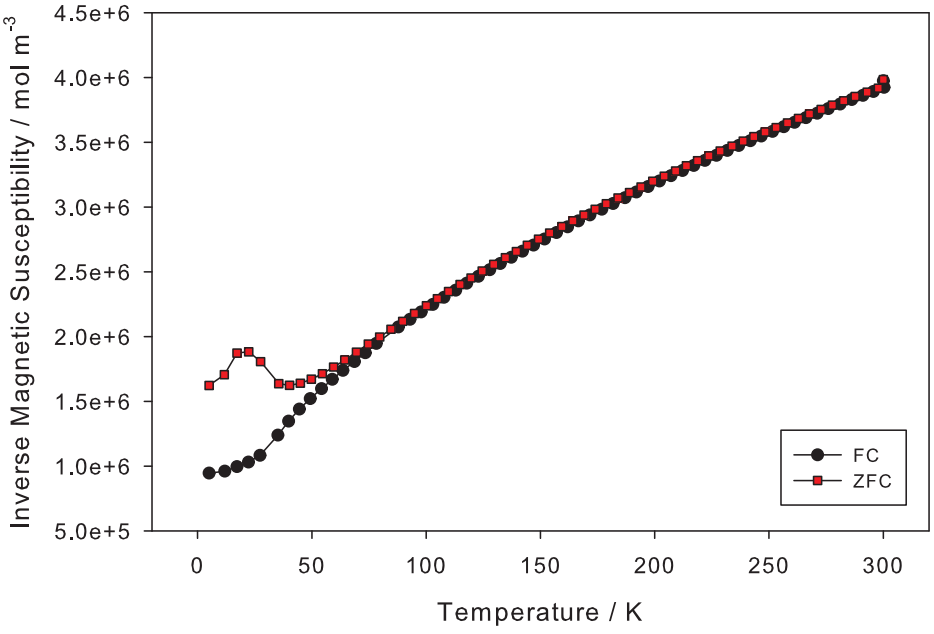

(b)

Figure 6.18 – (a) DC susceptibility and (b) inverse susceptibility measurements for $Mn_{0.4}Co_{0.6}Sb_2O_4$. FC - black circles, ZFC - red squares.

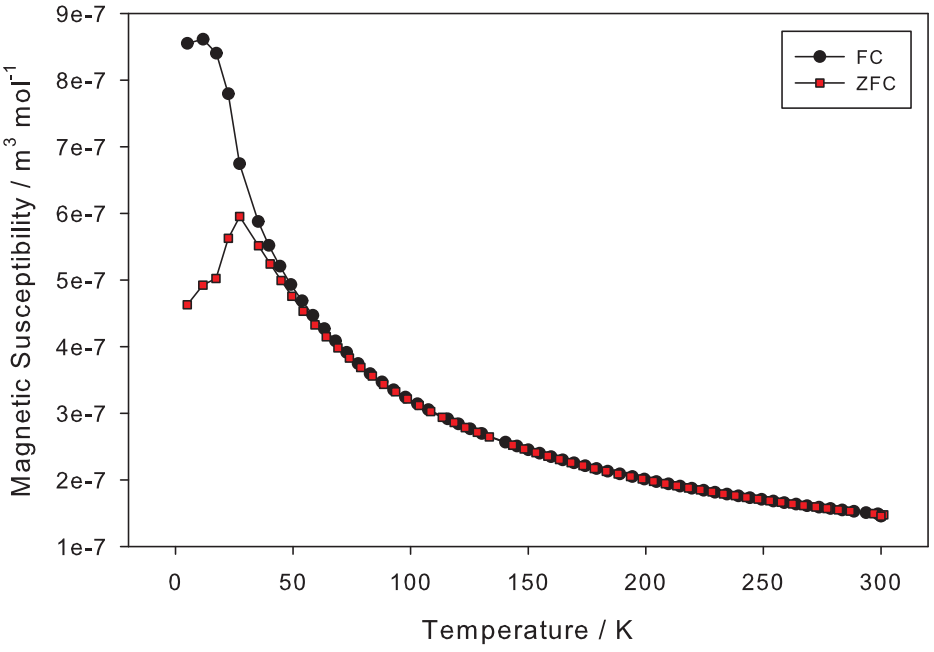

(a)

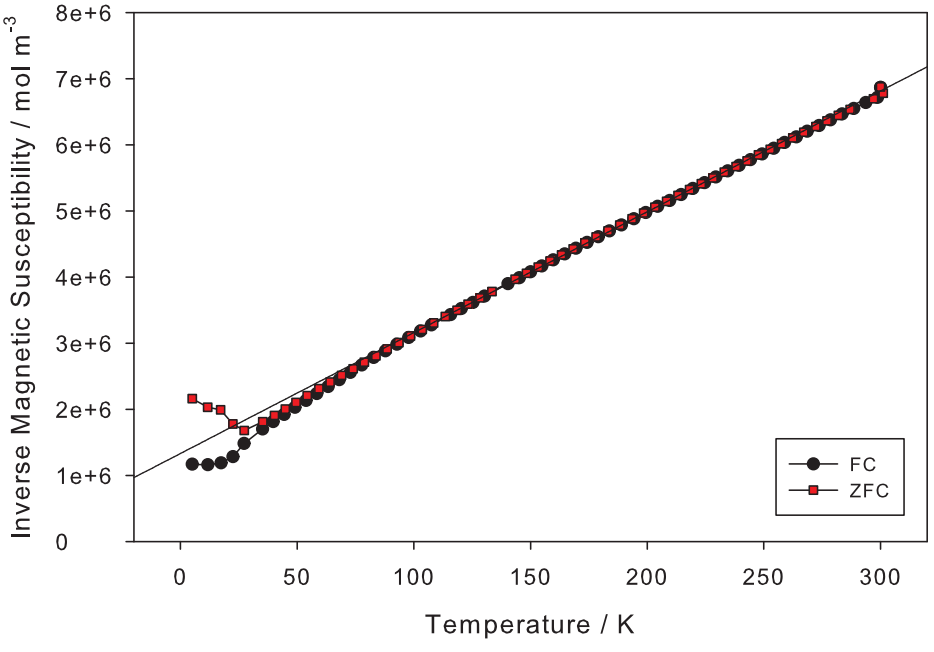

(b)

Figure 6.19 – (a) DC susceptibility and (b) inverse susceptibility measurements for $Mn_{0.5}Co_{0.5}Sb_2O_4$. FC - black circles, ZFC - red squares.

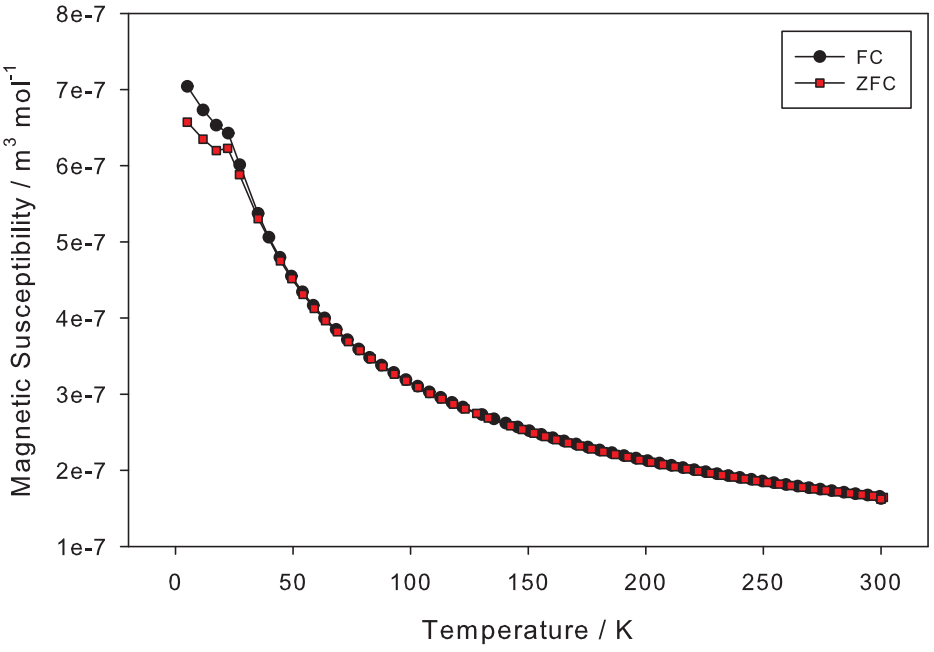

(a)

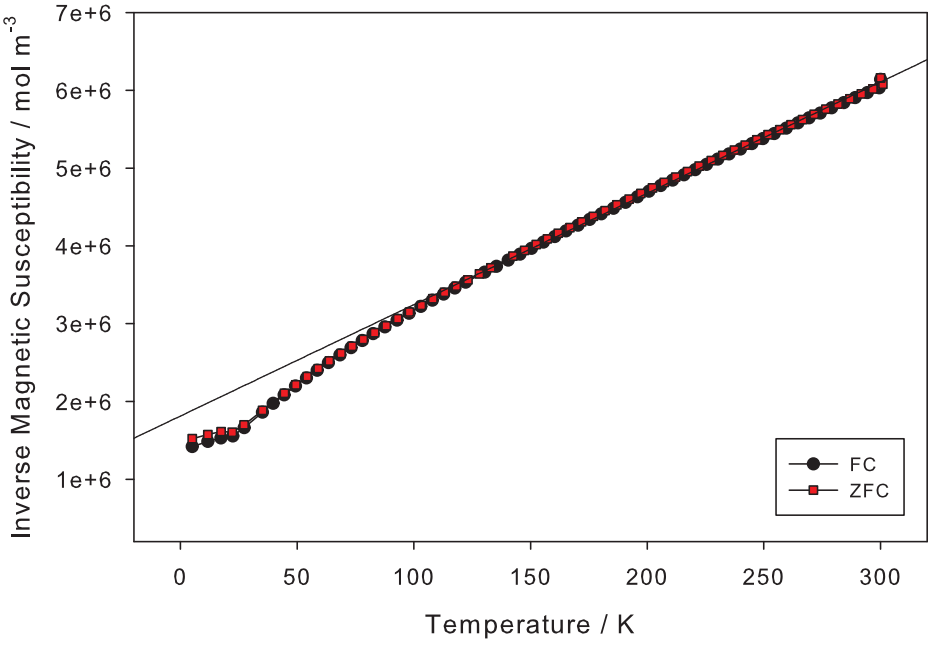

(b)

Figure 6.20 – (a) DC susceptibility and (b) inverse susceptibility measurements for $Mn_{0.6}Co_{0.4}Sb_2O_4$. FC - black circles, ZFC - red squares.

Table 6.18 – Summary of Susceptibility Data for $Mn_xCo_{1-x}Sb_2O_4$.

x	Primary AFM Transition Temperature / K	μ_{eff} / μ_B	θ / K	μ_{SO} / μ_B	Expected θ from literature / K
0.2	60	5.654(1)	-30.61(2)	4.28	-35
0.4	45	-	-	4.69	-74
0.5	27	5.900(3)	-72.68(2)	4.89	-93
0.6	22	6.672(2)	-126.485(7)	5.10	-113
0.8	22	6.164(1)	-154.443(4)	5.51	-151

ity increases below T_c. From a linear fit to the paramagnetic region, however, the Weiss constant is found to be strongly negative ($\theta = -154.443(4)$ K) showing a dominant AFM exchange interaction. The paramagnetic moment from the fit was $6.164(1)\,\mu_B$, only slightly higher than the value observed for $MnSb_2O_4$ ($6.02\mu_B$ [1]).

Comparison of Magnetic Susceptibilities

Table 6.18 summarises the data given in the previous sections. It is obvious both from the values given and visual inspection of the susceptibility plots that increasing x causes a decrease in both the main ordering temperature, and also the extent of canting between the FC and ZFC measurements. This is consistent with the higher ordering temperature of $CoSb_2O_4$ *cf.* $MnSb_2O_4$; decreasing the amount of Co within the structure reduces the strength of the overall magnetic ordering. Interestingly, however, θ decreases with x, indicating stronger AFM exchange interactions. This would suggest that although the dominant interaction at high temperature is increasingly AFM, the interactions are more complex at low temperature, potentially introducing some magnetic frustration. This is presumably due to competing exchange interactions which are fundamentally different for the series end-members, particularly the J_1 (intra-chain) coupling between nearest M neighbours which is positive for C-type $CoSb_2O_4$ and negative for A-type $MnSb_2O_4$.

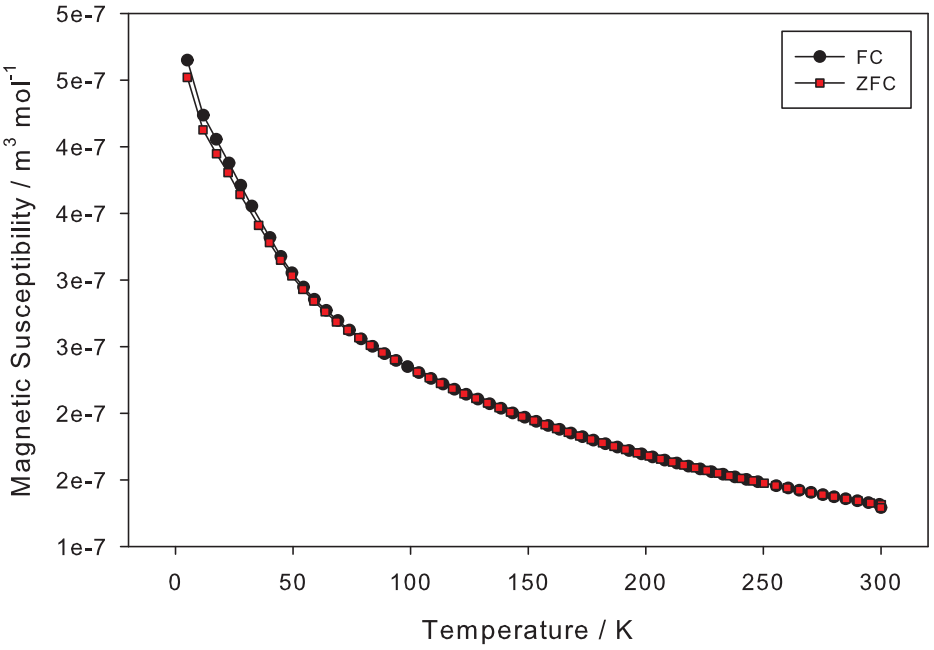

(a)

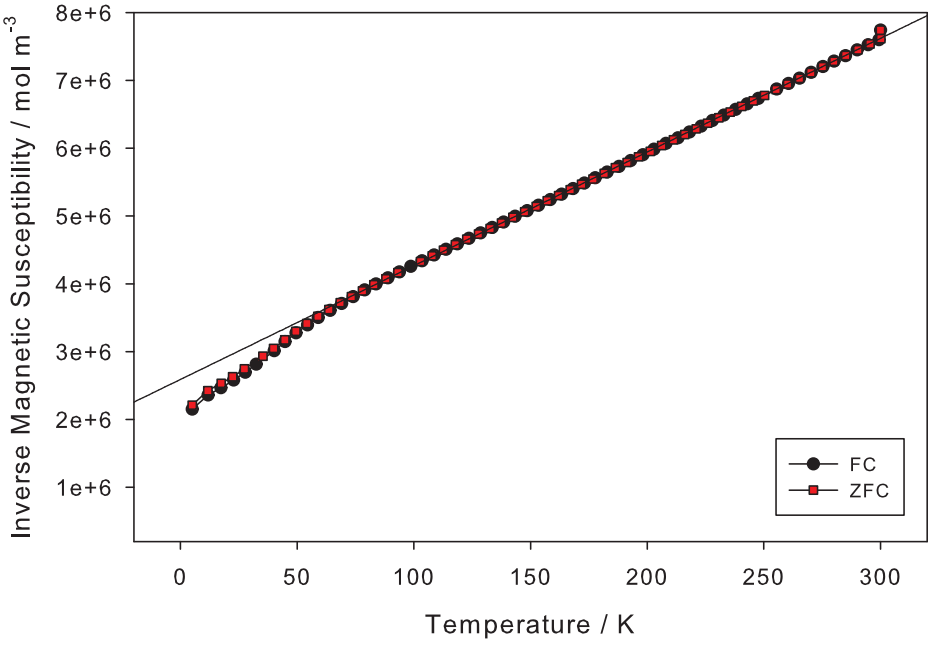

(b)

Figure 6.21 – (a) DC susceptibility and (b) inverse susceptibility measurements for $Mn_{0.8}Co_{0.2}Sb_2O_4$. FC - black circles, ZFC - red squares.

In all samples, there is evidence of a magnetic transition at $\simeq 70$ K. This is consistent with the Néel temperature of $CoSb_2O_4$, and is presumably connected with the presence of cobalt within the structure. This occurs as a down-turn in the inverse susceptibility, and would indicate some form of ferromagnetic component to the susceptibility. This could be related to the positive value of θ for $CoSb_2O_4$, which shows that in the paramagnetic region the dominant coupling interaction is FM. This could represent some FM order occurring along the octahedral chains at this temperature, before long-range AFM order occurs at lower temperature.

6.4.2 Magnetic Structure by Neutron Diffraction

Although magnetic susceptibility would indicate weaker magnetic ordering for larger values of x, NPD patterns for all samples showed development of additional magnetic reflections on cooling, which could be indexed within the nuclear unit cell, $k = (0,\ 0,\ 0)$. For $Mn_{0.2}Co_{0.8}Sb_2O_4$ these reflections were obvious at 60 K (figure 6.22a), although there is limited evidence for a tiny peak at 70 K (figure 6.22b), consistent with the susceptibility data.

The additional reflections for all samples could be indexed either as an A_x model (as for $MnSb_2O_4$) or as C_z (seen in $CoSb_2O_4$) or as a mixture of the two modes. In all cases the magnetic model was applied in $P1$ symmetry, with appropriate constraints to limit the atomic moments to the desired directions, while maintaining equal moments for each atom. Scattering factors[14] for both Mn^{2+} and Co^{2+} were tested for all models, and found to give identical magnetic moments within error; the Co^{2+} parameters gave better fits, and were therefore used throughout. Isotropic displacement parameters were used for the magnetic phase, constrained to be equal to the nuclear phase (or fixed for $x = 0.2$).

Refined magnetic moments are given in table 6.19 and shown graphically in figure 6.23. It is obvious that in all cases, the total moment per magnetic ion is less than that expected for the average number of unpaired electrons. This would suggest incomplete magnetic ordering, even at 5 K. In addition, the total moment decreases with x until an increase for $x = 0.8$, disagreeing with the increase in the number of unpaired electrons. This would imply that disorder is most severe for $x = 0.6$, but decreases significantly for $x = 0.8$. The drop in moment for $0.4 < x < 0.6$

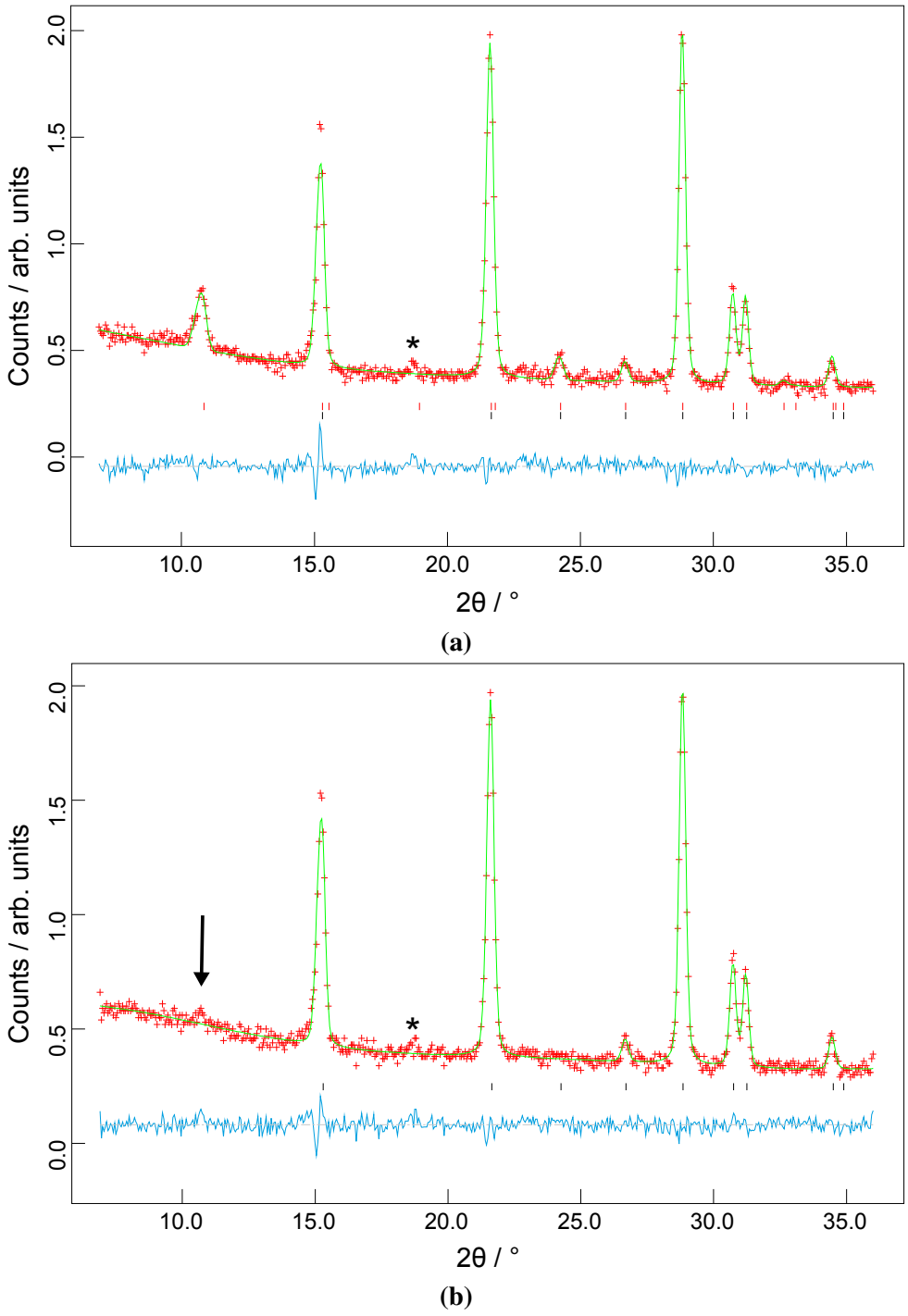

Figure 6.22 – Evidence of additional magnetic reflections in $Mn_{0.2}Co_{0.8}Sb_2O_4$ at (a) 60 K and (b) 70 K. Additional peak (*) corresponds to MnO magnetic (001) reflection.

Table 6.19 – Refined magnetic moments from NPD (5 K) and predicted magnetic moment per cation for $Mn_xCo_{1-x}Sb_2O_4$.

x	$\lvert M_{A_x} \rvert / \mu_B$	$\lvert M_{C_z} \rvert / \mu_B$	$\lvert M_{Tot} \rvert / \mu_B$	Theoretical Moment / μ_B
0.2	0	3.31(2)	3.31(2)	3.4
0.4	1.48(4)	2.37(2)	2.80(4)	3.8
0.5	2.00(4)	1.68(3)	2.61(5)	4.0
0.6	2.30(6)	0.66(6)	2.39(6)	4.2
0.8	3.19(4)	0	3.19(4)	4.6

is probably due to the greater mixing of Mn and Co within the structure for these compounds, resulting in more disruption of the exchange interactions.

The combination of A_x and C_z components of the total moment behave approximately linearly between $x = 0.2$ and $x = 0.8$. From these data, the crossover point (*i.e.* 50 % A_x and 50 % C_z) occurs at $x \simeq 0.45$, which is consistent with Co dominating the ordering direction.

From representational analysis, the refined model of a combined A_xC_z magnetic mode (corresponding to moments at an angle $0° < \beta < 90°$ to the *ab* plane) is incompatible with a single IR, and instead must be described by a combination of Γ_5 and Γ_{10} (see appendix B.1). This is incompatible with a single, second-order phase transition, where a single IR becomes critical during the transition.[15] Combining this result with the susceptibility data suggests that the magnetic order does occur as a second-order transition, but as (at least) a two-step transition. The result observed is also similar to that seen in $Co_xFe_{1-x}Sb_2O_4$, which also displays a change from A_x to C_z-type ordering on increasing x.[2] It is interesting to note that in this work the transition from C- to A-type occurs at a similar rate with x as in $Co_xFe_{1-x}Sb_2O_4$; this would suggest that M occupation is more influential in the observed ordering than the strength of magnetic coupling between M cations ($MnSb_2O_4$ shows a stronger coupling than $FeSb_2O_4$, demonstrated by a higher Néel temperature).

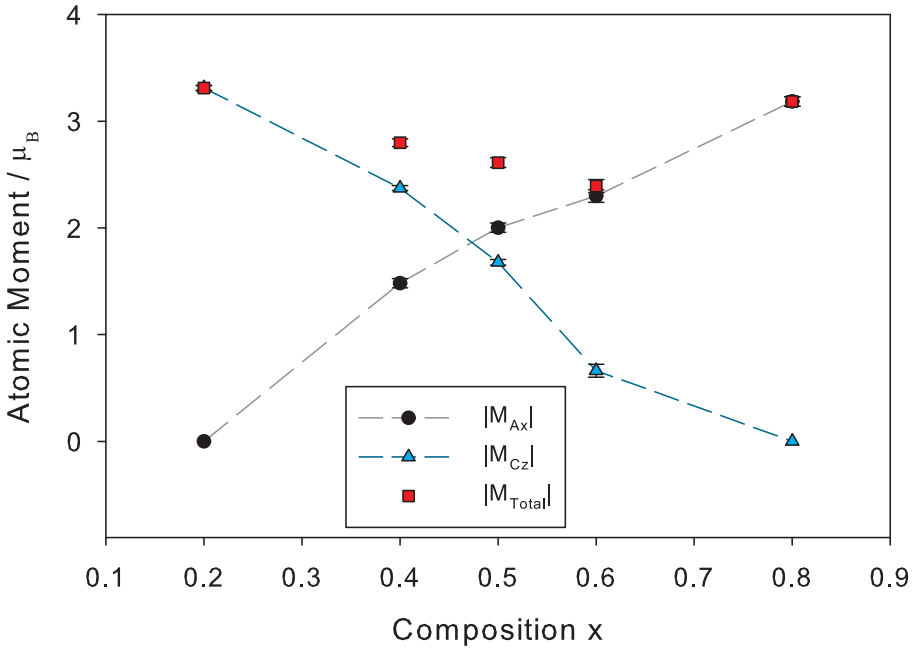

Figure 6.23 – Refined magnetic moments from NPD (5 K) for $Mn_xCo_{1-x}Sb_2O_4$.

6.5 Thermal Gravimetric Analysis

TGA was performed on $Mn_{0.5}Co_{0.5}Sb_2O_4$ in flowing O_2 gas, at a rate of 10 °C min^{-1} up to 1100 °C. The results are shown in figure 6.24. Over the full heating range, the sample gains 8.66 %, corresponding to an addition of two O atoms per formula unit. This is consistent with forming an MSb_2O_6-like phase, as seen for $CoSb_2O_4$.[2] The transition in $Mn_{0.5}Co_{0.5}Sb_2O_4$ occurs slightly higher in temperature than $CoSb_2O_4$, however, over the range 600–800 °C, compared with 550–650 °C. In addition, this transition exhibits a 'shoulder' at 670 °C, indicating two separate oxidation reactions occurring. This could be due to different oxidation temperatures for the Mn and Co cations, however a similar effect has been seen in $Co_xFe_{1-x}Sb_2O_4$, which is attributed to oxygen uptake within the MSb_2O_4 structure, without a full structure change to MSb_2O_6.[9] Further work would be required to determine the exact nature of the oxygen uptake within this series.

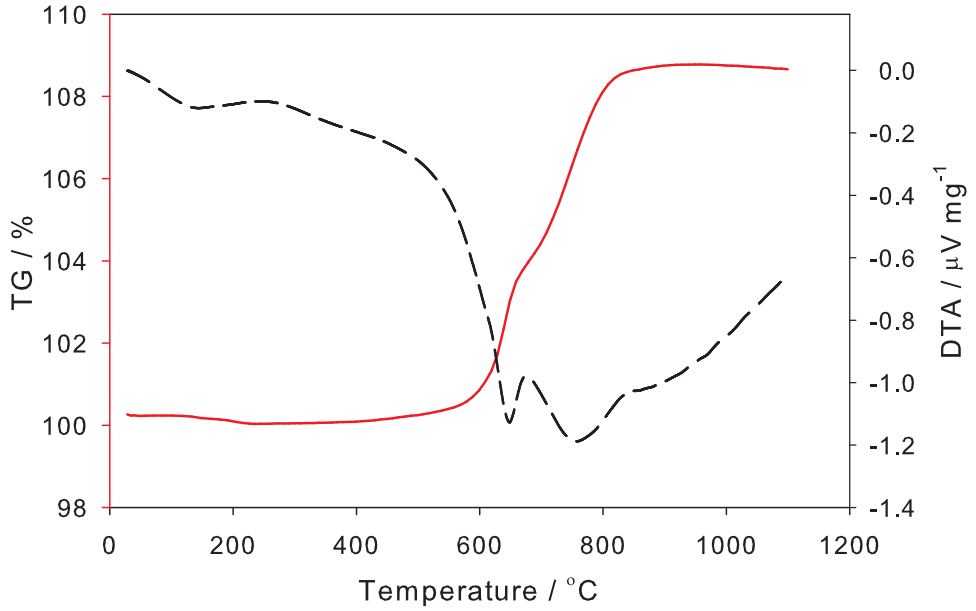

Figure 6.24 – TG (solid red) and DTA (dashed black) curves for $Mn_{0.5}Co_{0.5}Sb_2O_4$ in O_2 gas.

6.6 Conclusions

In this chapter, a range of $Mn_xCo_{1-x}Sb_2O_4$ compositions have been shown to form in the Schafarzikite ($P4_2/mbc$) structure, with lattice parameters increasing with x due to the increasing M cation size. Changes in atomic structure are seen with x, particularly in the antimony coordination. For $x = 0.5$ slightly anomalous structural behaviour has been observed, attributed to the need to accommodate Sb LPs within the structure.

On cooling, $Mn_{0.2}Co_{0.8}Sb_2O_4$ shows a structural transition below *ca.* 40 K, potentially connected with the development of long-range magnetic order. The exact nature of this transition remains undetermined from NPD, however the results suggest a change in the magnetic M cation site. This may be attributed to the different sized cations adopting different coordination environments, but the results observed could be due to local structural distortions due to the proximity of different sized Mn and Co cations, not seen clearly through bulk structure methods. Further work (such as local structure techniques or single-crystal diffraction) would be required to determine the exact nature of the transition.

Magnetically, the compounds show a reduction in susceptibility behaviour with increasing

x, yet all order magnetically from NPD. These results show a gradual change from C_z to A_x magnetic structure with x, rotating the magnetic moments into the *ab*-plane. The magnetic transitions occur as multiple steps, suggesting different ordering temperatures for regions of different stoichiometry. All diffraction data demonstrate a single-phase compound, however. The presence of small amounts of Co^{2+} does not generate an A_z-like structure, despite the presumably small anisotropy (due to SOC) for Mn^{2+}. This result is very similar to that seen for $Co_xFe_{1-x}Sb_2O_4$, which also shows a change in magnetic groundstate and orientation with x.

Thermal analysis of $Mn_{0.5}Co_{0.5}Sb_2O_4$ in O_2 shows oxidation to an MSb_2O_6-like phase/ phases, but with an earlier oxidation at 670 °C. This behaviour is similar to that seen in $FeSb_2O_4$ and $Co_xFe_{1-x}Sb_2O_4$, but further characterisation is required.

References

[1] H. Fjellvåg and A. Kjekshus, *Acta Chemica Scandinavica Series A-Physical and Inorganic Chemistry*, 1985, **39**, 389–395.

[2] B. P. de Laune and C. Greaves, *Journal of Solid State Chemistry*, 2012, **187**, 225–230.

[3] R. D. Shannon, *Acta Crystallographica Section A*, 1976, **32**, 751–767.

[4] J. R. Gavarri, G. Calvarin and B. Chardon, *Journal of Solid State Chemistry*, 1983, **47**, 132–142.

[5] J. R. Gavarri and A. W. Hewat, *Journal of Solid State Chemistry*, 1983, **49**, 14–19.

[6] H. Abe, K. Yoshii and H. Kitazawa, *Physica status solidi (a)*, 2002, **189**, 429–432.

[7] A. M. Abakumov, M. G. Rozova, E. V. Antipov, J. Hadermann, G. V. Tendeloo, M. V. Lobanov, M. Greenblatt, M. Croft, E. V. Tsiper, A. Llobet, K. A. Lokshin and Y. Zhao, *Chemistry of Materials*, 2005, **17**, 1123–1134.

[8] M. J. Whitaker, R. D. Bayliss, F. J. Berry and C. Greaves, *Journal of Materials Chemistry*, 2011, **21**, 14523–14529.

[9] B. P. de Laune, *Low Dimensional Sytructures of some Mixed Metal Oxides Containing Antimony: Synthesis and Characterisation*, PhD thesis, School of Chemistry, The University of Birmingham, 2013.

[10] B. Y. Brach, N. V. Chezhina and Y. V. Shapoval, *Inorganic Materials*, 1989, **25**, 601.

[11] A. C. Larson and R. B. von Dreele, *Los Alamos National Laboratory Report*, 1994, **LAUR 86-748**, 1.

[12] B. H. Toby, *Journal of Applied Crystallography*, 2001, **34**, 210–213.

[13] V. F. Sears, *Neutron News*, 1992, **3**, 26–37.

[14] P. J. Brown, in *International Tables for Crystallography,Volume C: Mathematical, Physical and Chemical Tables*, E. Prince (Ed.), Springer, 2004, ch. 4.4.5, pp. 454–460.

[15] J. Rossat-Mignod, in *Neutron Scattering Part C (Methods of Experimental Physics Volume 23, Part C)*, K. Sköld and D. L. Price (Ed.), Academic Press, 1987, ch. 19, pp. 69–157.

Chapter 7
Magnetic and Structural Characterisation of Versiliaite ($Fe_{12}Sb_{12}O_{32}S_2$) and Apuanite ($Fe_{20}Sb_{16}O_{48}S_4$)

7.1 Background

Versiliaite ($Fe_{12}Sb_{12}O_{32}S_2$) and Apuanite ($Fe_{20}Sb_{16}O_{48}S_4$) are related to Schafarzikite as described in section 1.3. The structures have been reported from single crystal x-ray diffraction (SCXRD) analysis of mineral samples, and are summarised in table 7.1. These mineral samples show some non-stoichiometry from the idealised chemical formula, primarily in the sulfur and tetrahedral Fe content. This has been attributed by transmission electron microscopy (TEM) to stacking faults along the (001) direction, caused by the formation of sulfur-depleted regions within the samples.[1] Some stacking faults have also been observed in the $[110]$ direction, but to a much lesser extent.

No physical properties of Apuanite or Versiliaite have been reported, except for a description of Mössbauer spectra of mineral samples.[4] In both cases two signals (corresponding to Fe^{2+} and Fe^{3+}) were observed, in a ratio similar to the ideal composition (1:2.12 and 1:3.35 for Versiliaite and Apuanite, respectively).

Table 7.1 – Mineral data previously reported for Versiliaite and Apuanite.

	Versiliaite	Apuanite
Composition*	$[Fe^{2+}_{4.65}Zn_{1.04}Fe^{3+}_{2.43}][Fe^{3+}_{2.90}Sb^{3+}_{11.76}As^{3+}_{1.34}]O_{32}S_{1.33}$	$[Fe^{2+}_{4.15}Zn_{0.32}Fe^{3+}_{7.40}][Fe^{3+}_{6.87}Sb^{3+}_{15.64}As^{3+}_{1.49}]O_{48}S_{3.57}$
Ideal Formula	$[Fe^{2+}_{4}Fe^{3+}_{4}][Fe^{3+}_{4}Sb_{12}]O_{32}S_{2}$	$[Fe^{2+}_{4}Fe^{3+}_{8}][Fe^{3+}_{8}Sb_{16}]O_{48}S_{4}$
Spacegroup	*Pbam*	$P4_2/mbc$
$a^{\dagger}$ / Å	8.492(5)	8.372(5)
$b^{\dagger}$ / Å	8.326(5)	-
$c^{\dagger}$ / Å	11.938(7)	17.97(1)

* Taken from [2].

† Taken from [3].

7.2 Synthesis and Experimental

Versiliaite ($Fe_{12}Sb_{12}O_{32}S_2$) and Apuanite ($Fe_{20}Sb_{16}O_{48}S_4$) were synthesised by a solid state reaction method within sealed and evacuated quartz tubes. Samples were synthesised from stoichiometric amounts of Fe_2O_3 (> 99 %, Aldrich), Fe metal (> 99.99 %, Aldrich), Sb_2O_3 (> 99 %, Aldrich) and Sb_2S_3 (99.995 %, Aldrich). It was found to be necessary to heat and cool reaction mixtures at relatively slow rates, in order to ensure successful reaction while minimising Sb_2O_3 and Sb_2S_3 volatility. Slightly different heating regimes were used for each sample, with re-grinding between firings where necessary:

Versiliaite A

$$\text{RT} \xrightarrow{10\ ^\circ\text{C min}^{-1}} \underset{\text{(Dwell 48 Hr)}}{520\ ^\circ\text{C}} \xrightarrow{\text{Furnace Cooling}} \text{RT}$$

$$\text{RT} \xrightarrow{10\ ^\circ\text{C min}^{-1}} \underset{\text{(48 Hr)}}{520\ ^\circ\text{C}} \xrightarrow{0.1\ ^\circ\text{C min}^{-1}} \underset{\text{(12 Hr)}}{600\ ^\circ\text{C}} \xrightarrow{\text{Furnace Cooling}} \text{RT}$$

Apuanite

$$\text{RT} \xrightarrow{10\ ^\circ\text{C min}^{-1}} 400\ ^\circ\text{C} \xrightarrow{0.1\ ^\circ\text{C min}^{-1}} \underset{\text{(Dwell 216 Hr)}}{520\ ^\circ\text{C}} \xrightarrow{0.1\ ^\circ\text{C min}^{-1}} 400\ ^\circ\text{C} \xrightarrow{\text{Furnace Cooling}} \text{RT}$$

In addition to the Versiliaite sample described above (Versiliaite "A") a second sample (Versiliaite "B") was prepared and provided by Ryan Bayliss.[5] This was produced through a slightly different synthetic procedure, starting from $FeSb_2O_4$ (synthesised from $FeSbO_4$ and Sb metal in an evacuated ampoule) and stoichiometric amounts of Fe_2O_3 and Sb_2S_3. This sample was heated at 530 °C for 1 month. In all cases reagents were dried prior to use, either at 150 °C under dynamic vacuum (10^{-6} mbar) for Sb_2O_3 and Sb_2S_3 or at 350 °C in air. The resulting products were black or dark brown in colour.

Phase purity was checked using XRPD (D8 and D2 instruments). NPD data for the provided Versiliaite sample were collected at both the PSI, Zurich (HRPT beamline) and the ILL (beamline D2B) at a range of temperatures. The synthesised Versiliaite sample was studied at RT and 5 K on the D2B diffractometer. Apuanite was initially investigated with the D2B diffractometer

at RT and 4 K, and then further studied using the GEM at ISIS over a range of temperatures.

Both XRPD and NPD data were refined using GSAS and EXPGUI.[6,7] The diffraction background was modelled using a shifted Chebyschev polynomial (GSAS type 1) with between 10 and 25 terms, while peak shapes were modelled using either a pseudo-Voigt function (CW data) or a convolution of pseudo-Voigt and Ikeda-Carpenter functions (TOF data). Anisotropic peak broadening was observed for high-resolution data (XRPD, HRPT and D2B) and was modelled using Stephen's parameters (GSAS profile type 4). Preferred orientation (MD function) was included where significant, particularly for XRPD data. Due to the relatively low scattering of O *cf.* Fe and Sb for XRPD data, it was also necessary to constrain the isotropic displacement parameters of O to be equal to avoid (unphysical) negative values.

7.3 Structural Characterisation at Room Temperature

7.3.1 Versiliaite

X-ray diffraction data

Refinement of XRPD data for both Versiliaite samples proceeded from the model of Mellini *et al.*[3] Both samples were found to contain a small Fe_3O_4 (magnetite) impurity of *ca.* 1.5 *wt%* by refinement; this was modelled as an additional (cubic, $Fd3m$) phase. The two Versiliaite samples showed slightly different diffraction patterns, particularly at low scattering angle. The most significant difference was in the (001) peak, highlighted in figure 7.1. This peak results from the ordering of sulfur and tetrahedrally-coordinated iron along the c-axis direction, and is indicative of the degree of superstructure along the c-axis, compared to $FeSb_2O_4$. The lack of a (001) peak for Versiliaite A would suggest that the Fe−S−Fe cross-channel links are relatively disordered along the $[001]$ direction. This disorder could be explained through the formation of sulfur-depleted (*i.e.* $FeSb_2O_4$-like) regions within the Versiliaite sample, disrupting the long-range ordering. This has been extensively observed in mineral samples of this type.[1] Formation of these S-depleted regions could only occur through loss of S during synthesis, or

a corresponding formation of sulfur-rich (Apuanite-like) regions. It is difficult to quantify any

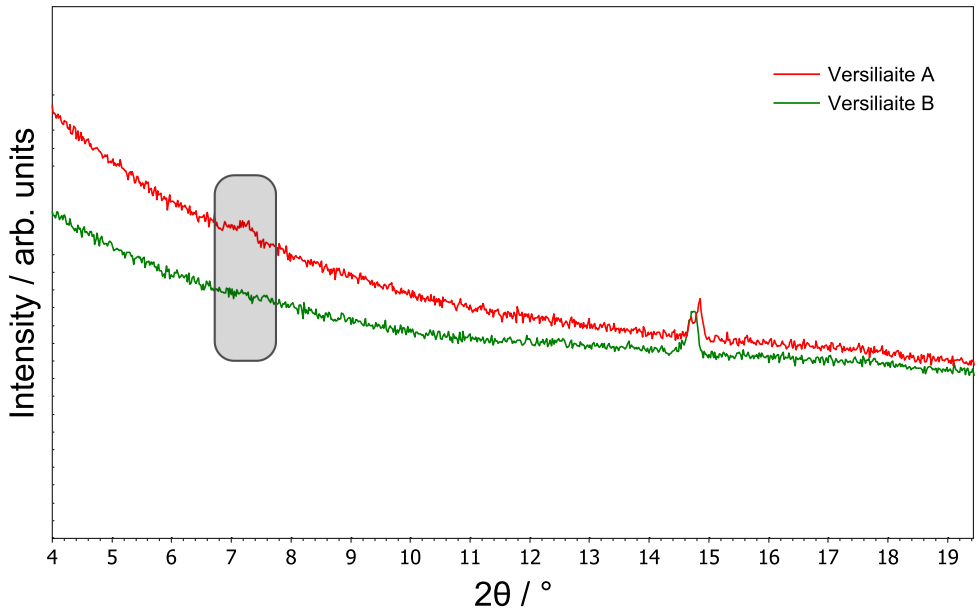

Figure 7.1 – Comparison of low-angle region for Versiliaite A and B samples; (001) peak is highlighted.

potential sulfur-loss during synthesis, although there was significant evidence during repeated syntheses that an amorphous Sb-containing phase (determined from x-ray fluorescence (XRF) spectroscopy) could form on the surface of the quartz-glass tubes used for reactions; it was unclear whether this could be derived from volatile Sb_2S_3. This effect was minimised as much as possible by the reported reaction conditions, however. Repeating the reaction conditions used to prepare sample B proved unsuccessful in forming a sufficiently pure phase, and showed a similar reduction in (001) peak intensity; the cause of this lack of reproducibility is unclear, but could be related to slightly different sample preparation (*e.g.* grinding) technique. While XRF spectroscopy could in theory be used to investigate the sulfur content of the samples, this technique would be hampered by the weak X-ray scattering of S *cf.* Sb; full investigation using this technique was beyond the scope of this project.

The different crystal systems of Versiliaite (orthorhombic) *vs.* Apuanite or Schafarzikite (tetragonal) mean that formation of tetragonal regions during synthesis should cause a reduction in the overall a/b ratio compared to a purely orthorhombic system, as observed through diffraction methods. Examining the lattice parameters of Versiliaite samples A and B confirms

Table 7.2 – Refined lattice parameters for Versiliaite A and B from XRPD, and previously published single-crystal results.[3]

	A		B	Lit.
	Versiliaite-model	Schafarzikite-model		
a / Å	8.4473(6)	8.4482(6)	8.4434(4)	8.492(5)
b / Å	8.3885(5)	8.3885(5)	8.2934(4)	8.326(5)
c / Å	11.9523(4)	5.9763(2)	11.9458(5)	11.938(7)
		[11.9526(4)]		
χ^2, No. of parameters	2.064, 70	2.018, 58	1.662, 69	
R_{wp}, R_p	0.0234, 0.0174	0.0232, 0.0171	0.0209, 0.0153	
$\frac{a}{b}$	1.0070	1.0071	1.0181	1.0199

Table 7.3 – Refined occupancy values for $FeSb_2O_4$-like Versiliaite (A) model.

	Fe−S−Fe Occupancy
$z = 0$	0.33(4)
$z = \frac{1}{2}$	0.17(4)

the formation of regions of different composition in sample A consistent with the reduction in 001 peak intensity, with an a/b ratio much lower than for sample B (table 7.2). Comparing a/b for both samples to previously published SCXRD results[3] would suggest that even sample B shows some reduction in orthorhombic splitting, however.

In addition to the Versiliaite model, the 'disordered' sample (A) could also be refined on a $FeSb_2O_4$-like unit cell ($c \simeq 6$ Å) with all Sb sites described by a mixture of Fe and Sb, with appropriate constraints to maintain correct stoichiometry. Correspondingly, S-sites were added at $z = 0$ and $\frac{1}{2}$, with occupancies constrained to match that of the corresponding tetrahedral Fe, in effect refining the Fe−S−Fe link occupancies. The resulting structure is shown in figure 7.2, while the refined occupancies are given in table 7.3. Graphical refinements are shown in appendix C.2.1. The occupancy values would suggest that approximately one

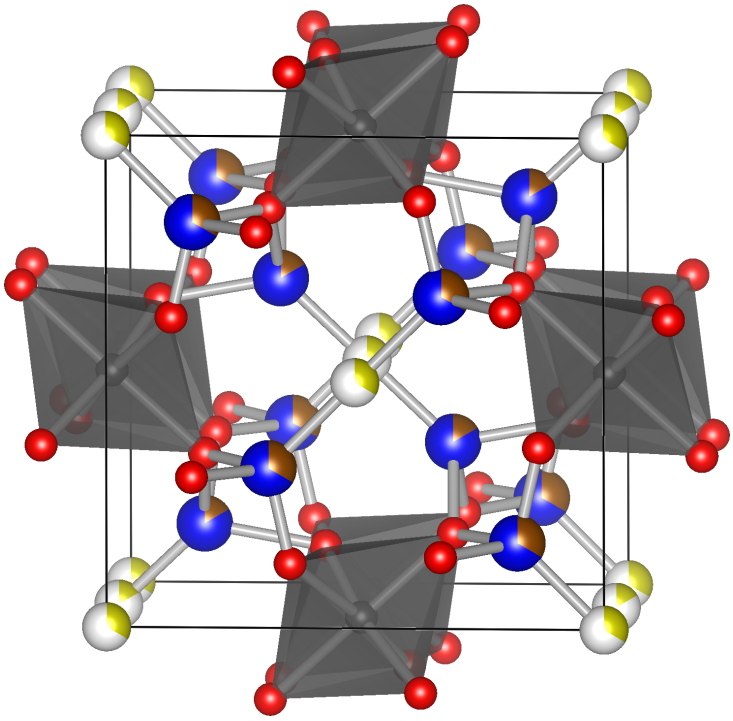

Figure 7.2 – $FeSb_2O_4$-like Versiliaite (A) model, viewed approximately along [001]. Octahedral (chain) Fe - grey polyhedra, tetrahedral Fe - brown spheres, Sb - blue spheres, S - yellow spheres, O - red spheres. Segmented sphere colouring denotes site occupancy (white S colouring indicates no occupancy).

third of all Fe−S−Fe linkages occur perpendicular to that expected for ideal Versiliaite for sample A. From a simplified description of the sample in terms of a mixture of Versiliaite, Apuanite and Schafarzikite, however, this would correspond to 2/3 of all sulfur links occurring as Apuanite! While this could be consistent with the intended stoichiometry (forming Versiliaite:Apuanite:Schafarzikite in the ratio 1:1:4) there is no evidence of any Apuanite-like ordering from diffraction, which should exhibit a (002) peak at $d \simeq 9$ Å. The evidence suggests that the sulfur links are instead distributed over a range of length-scales, with a distribution of approximately one third aligned along [110] and two thirds along $[\bar{1}10]$. The model used also does not account for long-range order of these links, which may introduce error into the refined occupancies.

Neutron Diffraction Data

RT data for both Versiliaite samples were collected and refined starting from the XRPD-refined models. Neutron wavelengths were refined from joint XRPD/NPD refinements, and were then

fixed for further analysis. Visual inspection of the HI data for sample A revealed that the (001) peak at $\simeq 7.5°$ 2θ is present, although quite broad. This could be caused by short-range Versiliaite-like order, with these small regions separated by disordered regions. Refinement using the Schafarzikite-like model as for XRPD data gave a significantly worse fit ($\chi^2 = 9.840$ *cf.* 3.034) than the Versiliaite model, however, indicating that inclusion of the superstructure is important, at least for NPD data. This is consistent with the larger scattering length of Fe (9.45 fm) *cf.* Sb (5.57 fm) for neutrons,[8] compared to the opposite relation for X-rays; the scattering from the Fe−S−Fe links will be much greater for NPD than XRPD. For this reason, the

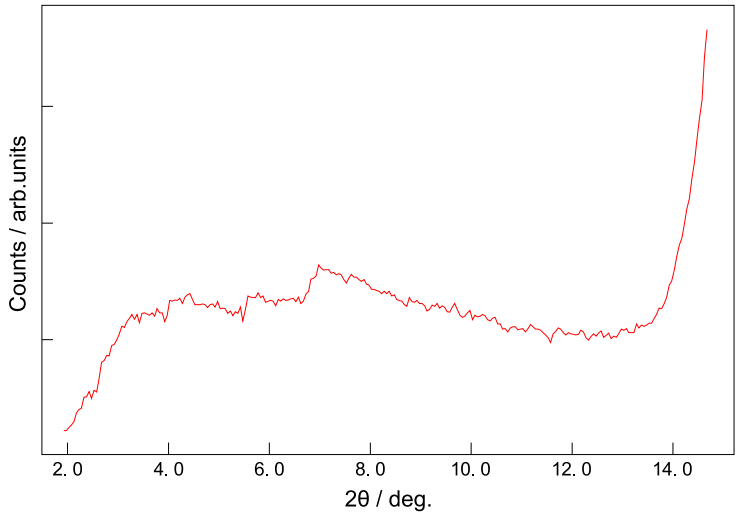

Figure 7.3 – View of low-angle HR NPD data for Versiliaite A, showing broad (001) reflection.

Versiliaite-like model was used for the majority of refinements, both to model the superstructure and for ease of comparison between samples. It was necessary to incorporate anisotropic peak broadening due to the high-resolution of the instruments used, as was seen in the XRPD data. In all cases, the most significant Stephen's parameters were the $H400$ and $H040$ terms, consistent with strain in the a and b parameters within the sample.

The refined parameters for both A and B samples in the Versiliaite model are given in table 7.4, while selected bond lengths are given in table 7.5; graphical displays of the refinements can be found in appendix C.2.2. From these results it is clear that there are considerable differences between the two samples, while sample B bears closest resemblance to the previously reported mineral data. Inspection of the tabulated bond lengths reveals that in sample A, the tetrahedral

Table 7.4 – Refined atomic positions, displacement parameters and refinement statistics for Versiliaite samples, NPD data.

		Sample A	Sample B
a / Å		8.4311(7)	8.4460(4)
b / Å		8.3789(6)	8.3155(3)
c / Å		11.9607(3)	11.9281(3)
Fe1 (4g)	$(x, y, 0)$	0.327(1), 0.324(1)	0.3115(7), 0.3204(6)
	$100 \times U_{iso}$ / Å^2	4.9(2)	1.6(1)
Fe2 (4f)	$(0, \frac{1}{2}, z)$	0.3743(7)	0.3766(5)
	$100 \times U_{iso}$ / Å^2	0.4(1)	0.9(1)
Fe3 (4f)	$(0, \frac{1}{2}, z)$	0.1242(8)	0.1261(6)
	$100 \times U_{iso}$ / Å^2	1.3(2)	0.5(1)
Sb1 (8i)	(x, y, z)	0.1707(7), 0.1717(6), 0.2558(6)	0.1706(5), 0.1677(5), 0.2472(6)
	$100 \times U_{iso}$ / Å^2	0.5(1)	0.85(8)
Sb2 (4h)	$(x, y, \frac{1}{2})$	0.315(1), 0.3201(9)	0.330(1), 0.3267(9)
	$100 \times U_{iso}$ / Å^2	-1.2(1)	0.2(2)
S (2a)	$100 \times U_{iso}$ / Å^2	2.7(5)	2.4(5)
O1 (4h)	$(x, y, \frac{1}{2})$	0.384(2), 0.110(1)	0.3591(9), 0.094(1)
	$100 \times U_{iso}$ / Å^2	1.7(3)	1.2(2)
O2 (8i)	(x, y, z)	0.4015(7), 0.1357(6), 0.2528(8)	0.4015(5), 0.1358(4), 0.2482(7)
	$100 \times U_{iso}$ / Å^2	0.7(1)	1.08(8)
O3 (8i)	(x, y, z)	0.316(1), 0.841(1), 0.3731(7)	0.3254(7), 0.8189(7), 0.3775(5)
	$100 \times U_{iso}$ / Å^2	1.9(2)	1.4(1)
O4 (8i)	(x, y, z)	0.172(1), 0.3180(9), 0.1300(6)	0.1880(6), 0.3419(7), 0.1330(4)
	$100 \times U_{iso}$ / Å^2	1.3(2)	0.5(1)
O5 (4g)	$(x, y, 0)$	0.638(2), 0.904(2)	0.614(1), 0.886(1)
	$100 \times U_{iso}$ / Å^2	2.9(4)	1.1(2)
χ^2, No. of parameters		3.034, 72	2.986, 77
R_{wp}, R_p		0.0420, 0.0328	0.0448, 0.0339

Table 7.5 – Selected bond lengths and structural parameters from Versiliaite (NPD data).

		Sample A	Sample B	Mineral Data[3]
Fe1	Fe1−S / Å	2.0744(1)	2.18286(7)	2.216(4)
	Fe1−O4 (×2) / Å	2.03022(8)	1.90710(5)	1.94(1)
	Fe1−O5 / Å	1.9328(1)	1.82661(7)	1.90(2)
Fe2	Fe2−O1 (×2) / Å	2.01635(6)	2.04869(5)	2.07(1)
	Fe2−O2 (×2) / Å	2.02409(6)	2.07674(5)	2.11(1)
	Fe2−O3 (×2) / Å	2.0477(1)	2.10763(7)	2.13(1)
	Average Fe2−O / Å	2.0294	2.0777	2.1063
	Octahedral Volume / Å^3	11.0637	11.7449	12.2676
	Quadratic Elongation	1.0049	1.0122	1.0106
	Bond Angle Variance / deg.^{2}	17.0096	42.7196	36.7939
Fe3	Fe3−O2 (×2) / Å	2.08515(6)	2.02173(5)	2.01(1)
	Fe3−O4 (×2) / Å	2.1072(1)	2.06307(7)	2.05(1)
	Fe3−O5 (×2) / Å	2.04964(7)	2.02165(5)	1.96(1)
	Average Fe3−O / Å	2.0807	2.0355	2.01
	Octahedral Volume / Å^3	11.8044	11.1655	10.6799
	Quadratic Elongation	1.0117	1.0048	1.0068
	Bond Angle Variance / deg.^{2}	40.786	16.5095	22.4555
Sb1 ($z \simeq \frac{1}{4}$)	Sb−Sb distance / Å	4.0699(3)	4.0106(1)	4.023(3)
	Sb1−O2 / Å	1.9693(2)	1.9680(1)	1.96(1)
	Sb1−O3 / Å	1.99751(8)	1.99934(5)	2.01(1)
	Sb1−O4 / Å	1.94139(7)	1.99379(6)	1.96(1)
	Average Sb−O / Å	1.9694	1.9870	1.98
Sb2 ($z = \frac{1}{2}$)	Sb−Sb distance / Å	4.3344(3)	4.0720(1)	4.045(3)
	Sb2−O1 / Å	1.8510(1)	1.94854(8)	1.94(2)
	Sb2−O3 (×2) / Å	1.88518(7)	1.96408(6)	1.97(1)
	Average Sb−O / Å	1.8738	1.9589	1.96

Fe1 site shows a much smaller deviation of the bond lengths, with a bond distortion index of 0.083 *cf.* 0.232 and 0.217 for sample B and the mineral, respectively. In addition, the average bond length for the site (2.016 Å) is larger than that of sample B (1.956 Å). These two effects are consistent with a mixture of Sb and Fe on this site; the larger Sb^{3+} (4-coordinate ionic radius[9] of 0.76 Å* compared to 0.49 Å for $^{IV}Fe^{3+}$) will give rise to larger M−O bond lengths, but will also tend to occupy a more symmetrical position. Another result of this substitution of Fe/Sb onto the same site is that the Sb sites both show slightly shorter average bond lengths compared to sample B and the mineral data; this is particularly pronounced for the Sb2 site. This is also reflected by an increased Sb−Sb distance across the structural 'channel' in sample A; this occurs as a result of the site coordination being more tetrahedral rather than trigonal pyramidal due to the presence of Fe, and results from an increase in the O−Sb−O bond angles.

Examining the octahedral (Fe2 and Fe3) sites variations are again seen between the different samples. For the Fe2 site (nominally Fe^{2+} according to local charge balance arguments[3]) sample A shows greatly contracted Fe−O bond lengths compared to sample B and the mineral data, as well as significantly less quadratic elongation and bond angle variance within the octahedra. For Fe3 this situation is reversed; longer bond lengths and greater octahedral distortion are seen in sample A. This effect would suggest that in sample A, the nominally Fe^{2+} position (Fe2) is actually closer to Fe^{3+}, while Fe3 is more like Fe^{2+}; this is confirmed by analysis of the BVS (table 7.6) which shows that Fe2 shows a 3+ valence state in sample A, compared to 2+ in sample B and the mineral sample. Fe3 shows the opposite behaviour. The bond-valence estimates are not as close to the ideal valence as the values obtained from the mineral data however; this could indicate that Fe^{2+} and Fe^{3+} are not fully ordered within the structure, as would be expected by changes in charge ordering around the disordered Fe−S−Fe linkages. Alternatively, the effect could also occur due to delocalisation of charges within the chains; this will be discussed further in section 7.4.1.

The cause of the different octahedral coordination environments in samples A and B is unclear; the values obtained for sample B match well with the single-crystal mineral charac-

*Radius tabulated for square-planar geometry only

Table 7.6 – Calculated BVS for Fe sites within Versiliaite (NPD data). Suggested valences are shown in bold.

	Valence (Determines R_0)[†]	Sample A	Sample B	Mineral Data[3]
Fe1	2+	2.614	2.875	2.572
	3+	**2.809**	**3.086**	**2.761**
Fe2	2+	2.702	**2.375**	**2.199**
	3+	**2.891**	2.541	2.352
Fe3	2+	**2.356**	2.66	2.883
	3+	2.521	**2.846**	**3.085**

[†] R_0 used: 1.734 ($Fe^{2+}-O^{2-}$); 1.759 ($Fe^{3+}-O^{2-}$); 2.120 ($Fe^{2+}-S^{2-}$); 2.149 ($Fe^{3+}-S^{2-}$).[10]

terisation, while the results for sample A would suggest that the charge ordering is reversed, with Fe^{2+} within the chains localised adjacent to the Fe−S−Fe linked layers. A refinement of Versiliaite A with variable S occupancy (with fixed tetrahedral Fe occupation) gave a reduced χ^2 (2.997, R_{wp} = 0.0418) however, with an S occupancy of 0.74(4) and structural parameters slightly closer to those of sample B (tables 7.7 and 7.8). For this reason, a fully disordered model (similar to the Schafarzikite-like model used for XRPD refinement, but with a doubled *c*-parameter) was also tested. Within this model, each Sb site was co-occupied by Fe, with a corresponding S site within the 'channel'. Refinement of the occupations across the three sites whilst maintaining overall stoichiometry was achieved within GSAS by a constraint linking Tet1 to both Tet2 and Tet3 (equally proportioned), and additional 'dummy' atoms at sites Tet2 and Tet3, constrained to pivot occupancy around 0. Tabulated occupancies are a combination of these multiple sites. This model gave an improved fit ($\chi^2 = 2.706$, figure 7.4), but also significantly changed the atomic structure from the ordered model.

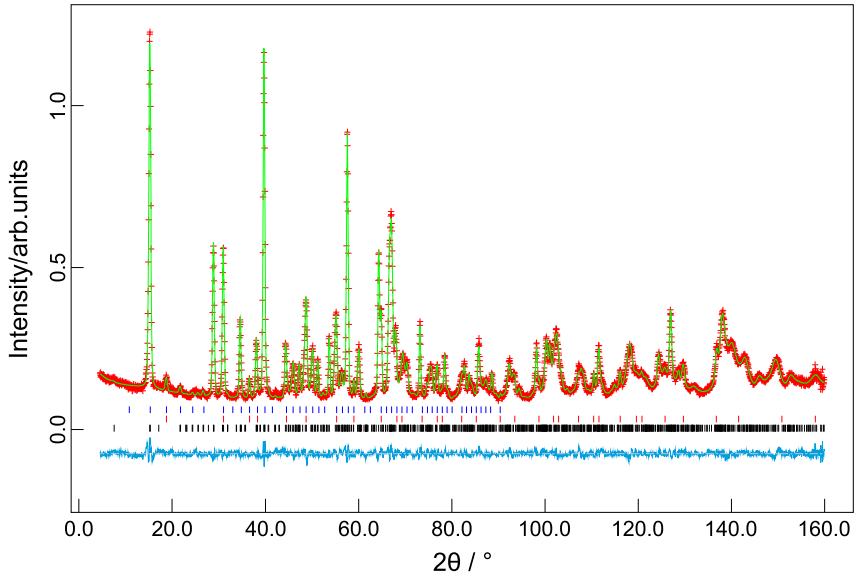

Figure 7.4 – Graphical refinement of Versiliaite A using fully disordered ($c \simeq 12$ Å) model from NPD data. Red and blue tickmarks denote Fe_3O_4 impurity (nuclear and magnetic peaks).

The resulting bond lengths from this disordered model are much closer to the ordered model of sample B, both in the tetrahedral and octahedral sites. In addition, the bond-valences for the Fe-containing sites are closer to the expected charge distribution, although the Fe2 site shows no clear definition of Fe^{2+} or Fe^{3+}. This effect may be due to the incomplete modelling of the

Table 7.7 – Refined atomic positions and parameters for Versiliaite A with refined S occupancies (NPD data).

		Refined S Occupancy	Fully Disordered ($c \simeq 12$ Å) Model
a / Å		8.4308(7)	8.4305(7)
b / Å		8.3790(6)	8.3786(6)
c / Å		11.9606(3)	11.9600(3)
Tet1(Sb/Fe) (4g)	$(x, y, 0)$	0.327(1), 0.325(1)	0.317(1), 0.3198(9)
	$100 \times U_{iso}$ / Å^2	4.8(2)	0.6(2)
	Fe Occupancy	1	0.53(4)
Fe2 (4f)	$(0, \frac{1}{2}, z)$	0.3739(7)	0.3784(8)
	$100 \times U_{iso}$ / Å^2	0.4(1)	1.3(2)
Fe3 (4f)	$(0, \frac{1}{2}, z)$	0.1237(8)	0.1267(7)
	$100 \times U_{iso}$ / Å^2	1.3(2)	0.4(1)
Tet2(Sb/Fe) (8i)	(x, y, z)	0.1708(7), 0.1716(6), 0.2562(5)	0.1698(6), 0.1700(6), 0.2448(6)
	$100 \times U_{iso}$ / Å^2	0.4(1)	1.0(2)
	Fe Occupancy	0	0.10(2)
Tet3(Sb/Fe) (4h)	$(x, y, \frac{1}{2})$	0.314(1), 0.3192(9)	0.324(2), 0.321(1)
	$100 \times U_{iso}$ / Å^2	-1.1(1)	2.4(3)
	Fe Occupancy	0	0.27(5)
S (2a) $(0, 0, 0)$	$100 \times U_{iso}$[†]/ Å^2	0.7(7)	2.2(5)
	Occupancy	0.74(4)	0.53(4)
S2 (4e) $(0, 0, \frac{1}{4})$	Occupancy	-	0.10(2)
S2 (2b) $(0, 0, \frac{1}{2})$	Occupancy	-	0.27(5)
O1 (4h)	$(x, y, \frac{1}{2})$	0.385(2), 0.110(1)	0.362(2), 0.093(2)
	$100 \times U_{iso}$ / Å^2	1.8(3)	2.2(3)
O2 (8i)	(x, y, z)	0.4014(7), 0.1356(6), 0.2522(8)	0.4005(7), 0.1350(6), 0.2507(8)
	$100 \times U_{iso}$ / Å^2	0.6(1)	0.9(1)
O3 (8i)	(x, y, z)	0.316(1), 0.840(1), 0.3724(7)	0.329(1), 0.8168(9), 0.3757(7)
	$100 \times U_{iso}$ / Å^2	1.8(2)	1.3(1)
O4 (8i)	(x, y, z)	0.172(1), 0.318(1), 0.1296(7)	0.186(1), 0.3415(9), 0.1310(6)
	$100 \times U_{iso}$ / Å^2	1.5(2)	1.7(2)
O5 (4g)	$(x, y, 0)$	0.638(2), 0.904(2)	0.615(2), 0.887(1)
	$100 \times U_{iso}$ / Å^2	3.0(4)	2.0(3)
χ^2, No. of parameters		2.997, 73	2.706, 74
R_{wp}, R_p		0.0418, 0.0328	0.0397, 0.0314

[†] Due to the relatively low scattering of S, thermal parameters were constrained equal amongst all sulfur sites.

Table 7.8 – Selected bond lengths for Versilaite A from models with refined S occupancies (NPD data).

			Refined S Occupancy	Fully Disordered ($c \simeq 12$ Å) Model
Tet1 (4g)	Fe1−S / Å		2.0652(1)	2.1617(1)
	Fe1−O4 (×2) / Å		2.03202(8)	1.92480(7)
	Fe1−O5 / Å		1.9366(1)	1.8275(1)
	BVS	Fe^{2+} R_0	2.632	2.864
		Fe^{3+} R_0	2.829	3.075
Tet2 (8i)	$\frac{1}{2}\times$ Sb−Sb distance / Å		2.0349(2)	2.0203(1)
	Sb1−O2 / Å		1.9680(2)	1.9675(2)
	Sb1−O3 / Å		1.98416(8)	1.99067(7)
	Sb1−O4 / Å		1.94706(7)	1.98438(8)
	Average Sb−O / Å		1.9664	1.9809
Tet3 (4h)	$\frac{1}{2}\times$ Sb−Sb distance / Å		2.1776(2)	2.1110(1)
	Sb2−O1 / Å		1.8510(1)	1.9322(1)
	Sb2−O3 (×2) / Å		1.88666(7)	1.96966(8)
	Average Sb−O / Å		1.8748	1.9572
Fe2	Fe2−O1 (×2) / Å		2.01660(6)	2.02123(7)
	Fe2−O2 (×2) / Å		2.02504(6)	2.07765(6)
	Fe2−O3 (×2) / Å		2.0529(1)	2.1050(1)
	Average Fe2−O / Å		2.0315	2.0680
	Octahedral Volume / $Å^3$		11.0945	11.5939
	Quadratic Elongation		1.0051	1.0116
	Bond Angle Variance / $deg.^2$		17.757	39.6351
	BVS	Fe^{2+} R_0	2.687	2.444
		Fe^{3+} R_0	2.875	2.615
Fe3	Fe3−O2 (×2) / Å		2.08473(6)	2.04519(6)
	Fe3−O4 (×2) / Å		2.1066(1)	2.0528(1)
	Fe3−O5 (×2) / Å		2.05058(7)	2.03195(6)
	Average Fe3−O / Å		2.0806	2.0433
	Octahedral Volume / $Å^3$		11.8076	11.2933
	Quadratic Elongation		1.0115	1.0048
	Bond Angle Variance / $deg.^2$		40.0421	17.0449
	BVS	Fe^{2+} R_0	2.356	2.602
		Fe^{3+} R_0	2.520	2.783

disorder, however. Examining the Fe−S−Fe link occupancies, this model would suggest that 53 % of the sulfur occurs in the ideal Versiliaite site. Of the rest, 27 % occurs in a parallel direction ($z = \frac{1}{2}$) while 20 % occurs perpendicular to the expected links. This is lower than the estimate from XRPD results, but the difference could be related to the high correlation of occupation factors with thermal displacement parameters, particularly for XRPD results.

7.3.2 Apuanite

X-ray diffraction data

XRPD data for the synthetic Apuanite sample were initially refined on the model of Mellini *et al.*[3] During the refinement a number of weak reflections were noticed which did not correspond to the model; these were determined as a mixture of magnetite (Fe_3O_4) and haematite (α-Fe_2O_3) impurities in low concentration (1.55(4) *wt%* and 2.23(6) *wt%*, respectively). These were included as additional impurity phases in this and later refinements. The refined parameters are compared with the previously reported mineral data in table 7.9. The refined data show some anomalies, particularly the temperature factors for Fe1, Sb, S and all O. The large negative value for Fe1 and the large positive value for Sb could indicate mixing of iron and antimony on the tetrahedral sites, as seen for the Versiliaite samples. This may also be related to the large U_{iso} seen for S; disordered Fe−S−Fe links would effectively reduce the S occupancy, which may appear in the model as a large thermal displacement. The low x-ray scattering of S *cf.* Sb and Fe increase the error in this value, however.

Neutron Powder Diffraction

RT neutron diffraction data from both D2B and GEM were refined starting from the model produced from XRPD; refinement was hampered by the need to model nuclear and magnetic structures for both impurity phases. The refined parameters are given in table 7.10, while selected bond lengths are given in table 7.11. Although the two datasets largely agree with each other, the GEM data generally show lower displacement parameters. The cause of this difference is unclear, apart from a potentially small contribution due to different sample temperatures

Table 7.9 – Refined atomic positions and displacement parameters for Apuanite (XRPD data).

		Synthetic Sample	Mineral Data[3]
a / Å		8.3692(1)	8.372(5)
c / Å		17.9409(2)	17.97(1)
Fe1 (8h)	$(x, y, 0)$	0.328(2), 0.326(2)	0.3098(3), 0.3179(3)
	$100 \times U_{iso}$ / Å^2	-5.9(2)	1.55
Fe2 (4d)	$100 \times U_{iso}$ / Å^2	2.2(6)	1.01
Fe3 (8f)	$(0, \frac{1}{2}, z)$	0.0817(7)	0.0829(1)
	$100 \times U_{iso}$ / Å^2	1.6(3)	0.90
Sb (16i)	(x, y, z)	0.1716(6), 0.1719(6), 0.1645(2)	0.1677(1), 0.1706(1), 0.1638(1)
	$100 \times U_{iso}$ / Å^2	4.2(1)	0.66
S (4a)	$100 \times U_{iso}$ / Å^2	5.9(7)	1.72
O1 (16i)	(x, y, z)	0.917(2), 0.365(2), 0.156(1)	0.9013(8), 0.3624(8), 0.1628(4)
	$100 \times U_{iso}$ / Å^2	-1.0(3)	0.66
O2 (8h)	$(x, y, 0)$	0.891(4), 0.356(4)	0.893(1), 0.392(1)
	$100 \times U_{iso}$ / Å^2	-1.0(3)	0.96
O3 (16i)	(x, y, z)	0.802(2), 0.677(2), 0.0666(8)	0.8147(9), 0.6574(9), 0.0899(4)
	$100 \times U_{iso}$ / Å^2	-1.0(3)	0.90
O4 (8g)	$(x, y, \frac{1}{4})$	0.837(3), 0.663(3)	0.8221(8), 0.6779
	$100 \times U_{iso}$ / Å^2	-1.0(3)	1.14

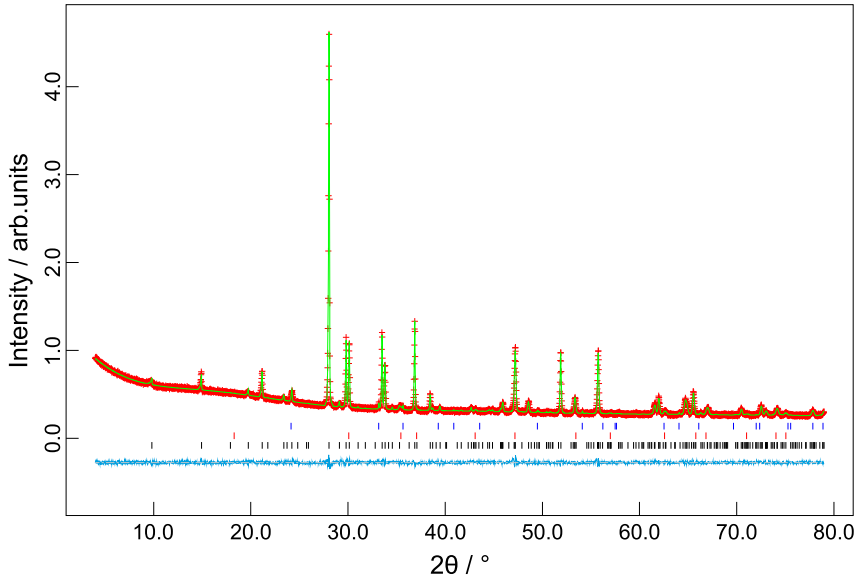

Figure 7.5 – Graphical refinement of Apuanite from XRPD data. Tickmarks: Black; Apuanite, Red; Fe_3O_4, Blue; $\alpha-Fe_2O_3$.

at the two facilities. More significant is probably the treatment of peak shape in the two refinements; for GEM data, anisotropic broadening was not included, due to the greater instrumental broadening. One noticeable feature of both refinements is the large U_{iso} for S; a refinement with anisotropic temperature factors for S showed the largest displacement in a plane approximately perpendicular to the Fe−S−Fe bonds. This could either be due to local displacement away from a linear Fe−S−Fe link, or a large bending mode of the linkage at room temperature; further investigation of this could be achieved with optical spectroscopy (*e.g.* Raman).

Inspection of the bond angles and lengths for the different data sets show largely good agreement between the two RT refinements, and also with the mineral data. The most significant deviations between refinements are observed for Fe3; the cause of these is probably due to peak shape, as mentioned above. Comparing the BVSs between the synthetic and mineral data would support the charge-ordering conclusions made by Mellini *et al.* that the Fe1 and Fe3 sites contain Fe^{3+}, while Fe2 is divalent.

Table 7.10 – Refined atomic positions and displacement parameters for Apuanite (NPD data).

		D2B data	GEM data
a / Å		8.3853(1)	8.3825(3)
c / Å		17.9829(2)	17.9787(7)
Fe1 (8h)	$(x, y, 0)$	0.3135(5), 0.3188(5)	0.3129(5), 0.3194(5)
	$100 \times U_{iso}$ / Å^2	1.74(9)	1.08(8)
Fe2 (4d)	$100 \times U_{iso}$ / Å^2	1.0(1)	1.0(1)
Fe3 (8f)	$(0, \frac{1}{2}, z)$	0.0828(2)	0.0838(2)
	$100 \times U_{iso}$ / Å^2	0.67(6)	0.22(4)
Sb (16i)	(x, y, z)	0.1713(4), 0.1718(4), 0.1664(3)	0.1696(4), 0.1703(5), 0.1652(3)
	$100 \times U_{iso}$ / Å^2	0.96(7)	0.67(6)
S (4a)	$100 \times U_{iso}$ / Å^2	3.4(3)	4.5(4)
O1 (16i)	(x, y, z)	0.9031(4), 0.3627(4), 0.1662(3)	0.9023(4), 0.3639(4), 0.1653(3)
	$100 \times U_{iso}$ / Å^2	1.32(7)	0.71(6)
O2 (8h)	$(x, y, 0)$	0.8851(7), 0.3883(7)	0.8884(8), 0.3893(8)
	$100 \times U_{iso}$ / Å^2	1.3(1)	1.1(1)
O3 (16i)	(x, y, z)	0.8127(4), 0.6587(4), 0.0887(2)	0.8147(4), 0.6566(4), 0.0889(2)
	$100 \times U_{iso}$ / Å^2	1.56(9)	0.88(8)
O4 (8g)	$(x, y, \frac{1}{4})$	0.8227(6), 0.6773(6)	0.8214(5), 0.6786(5)
	$100 \times U_{iso}$ / Å^2	0.8(1)	0.41(8)
χ^2, No. of parameters		3.279, 68	1.858, 70
R_{wp}, R_p		0.0423, 0.0339	0.0431, 0.0369

Table 7.11 – Selected bond lengths and angles for Apuanite from NPD and literature data.

			D2B	GEM	Mineral Data[3]
Fe1	Fe1−S / Å		2.18047(3)	2.17999(7)	2.204(3)
	Fe1−O2 / Å		1.83722(3)	1.86011(7)	1.89(1)
	Fe1−O3 (×2) / Å		1.92308(2)	1.93369(6)	1.934(8)
	BVS	Fe^{2+} R_0	2.806	2.727	2.623
		Fe^{3+} R_0	3.012	2.928	2.816
Fe2	Fe2−O1 (×4) / Å		2.06307(2)	2.07202(6)	2.113(8)
	Fe2−O4 (×2) / Å		2.10299(3)	2.11713(6)	2.106(8)
	Average Fe2−O / Å		2.0764	2.0871	2.111
	Octahedral Volume / $Å^3$		11.7337	11.9201	12.3148
	Quadratic Elongation		1.0115	1.0113	1.0123
	Bond Angle Variance / $deg.^2$		40.4226	39.4093	43.6371
	BVS	Fe^{2+} R_0	2.381	2.314	2.166
		Fe^{3+} R_0	2.548	2.476	2.317
	Fe2−Fe3 distance / Å		3.00721(5)	2.9888(1)	3.003(3)
	∠ Fe2−O1−Fe3 / °		93.727(1)	93.6(2)	93.2(2)
Fe3	Fe3−O1 (×2) / Å		2.05795(2)	2.02960(6)	2.018(8)
	Fe3−O2 (×2) / Å		2.00542(2)	2.00086(6)	1.960(8)
	Fe3−O3 (×2) / Å		2.06144(2)	2.03583(6)	2.039(8)
	Average Fe3−O / Å		2.0416	2.0221	2.0059
	Octahedral Volume / $Å^3$		11.243	10.9267	10.6557
	Quadratic Elongation		1.0063	1.0060	1.0069
	Bond Angle Variance / $deg.^2$		21.9179	21.3227	23.696
	BVS	Fe^{2+} R_0	2.619	2.757	2.889
		Fe^{3+} R_0	2.802	2.949	3.091
	Fe3−Fe3 distance / Å		2.97703(5)	3.0119(1)	2.980(4)
	∠ Fe3−O2−Fe3 / °		95.846(1)	97.6(3)	98.9(3)
Sb	Sb1−O1 / Å		1.96545(3)	1.97134(8)	1.975(7)
	Sb1−O3 / Å		1.99736(2)	2.00114(6)	1.965(8)
	Sb1−O4 / Å		1.96584(2)	1.98308(6)	2.004(6)
	Average Sb−O / Å		1.9762	1.9852	1.9813
	Bond length distortion index		0.00713	0.00536	0.00768

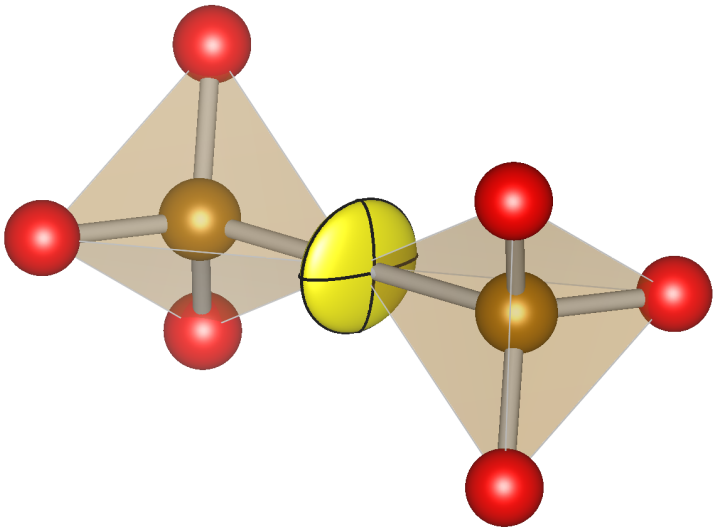

Figure 7.6 – View of Apuanite approximately along [100] showing anisotropic sulfur displacement perpendicular to the Fe−S−Fe linkages.

7.4 Mössbauer Spectroscopy

7.4.1 Versiliaite

Due to the slightly anomalous BVSs calculated for the two Versiliaite samples, as well as the high Fe2 valence seen in Apuanite, Mössbauer spectroscopy was used to investigate the oxidation states and coordination within the synthetic samples. Graphical plots of the results at 298 K are shown in figures 7.7 (Versiliaite A), 7.8 (Versiliaite B) and 7.10 (Apuanite). All data were collected and interpreted by Prof. Frank J. Berry.

The fitted parameters for each of the Versiliaite samples are given in table 7.12; also shown are parameters obtained from a mineral sample in a previous work.[5] The values obtained for sample A agree quite closely with those expected: $^{IV}Fe^{3+}$, $^{VI}Fe^{3+}$ and $^{VI}Fe^{2+}$ in approximately equal amounts (ideally 33.3% each). The best fit to the data was found with two Fe^{2+} sites, however, which is inconsistent with the ideal Versiliaite model which should show just one site. The isomer shifts of the two sites are almost identical (both indicating octahedral coordination) although there is a significant difference in the quadrupole splitting. The origin of this difference could be attributed to the disorder of the Fe−S−Fe links within this sample (as evidenced from diffraction experiments) and the resulting $Fe^{2+}\cdots Fe^{3+}$ distribution along the octahedral chains.

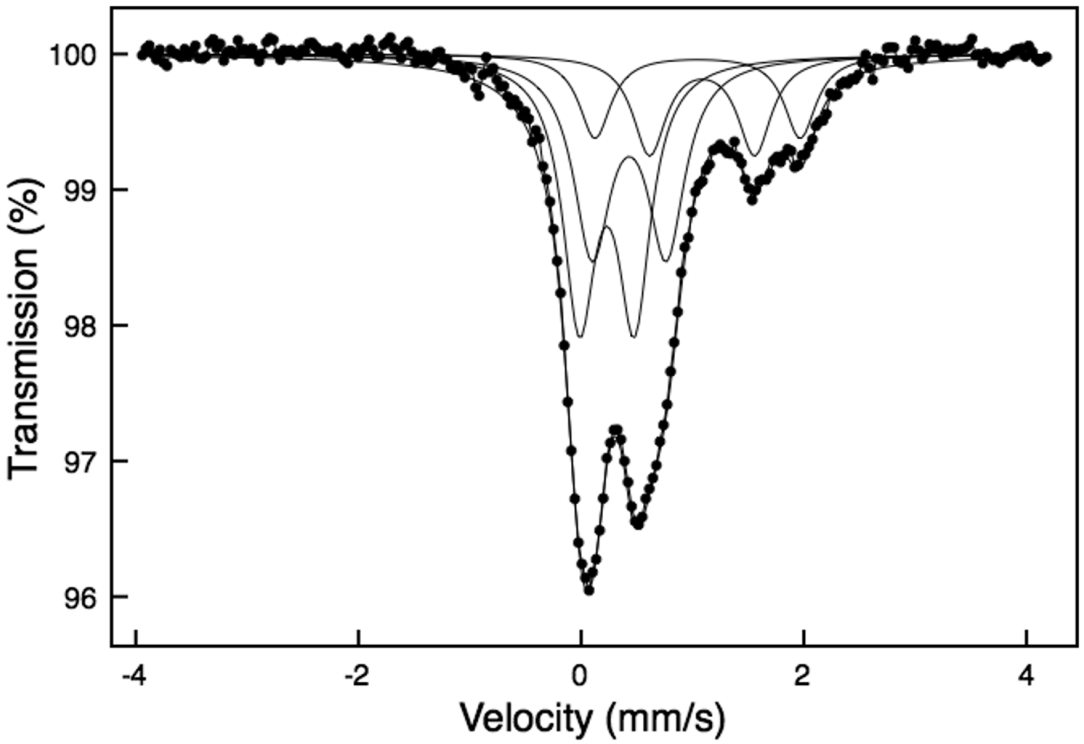

Figure 7.7 – Mössbauer spectrum of Versiliaite A at 298 K showing collected data (black dots) and fit lines (black).

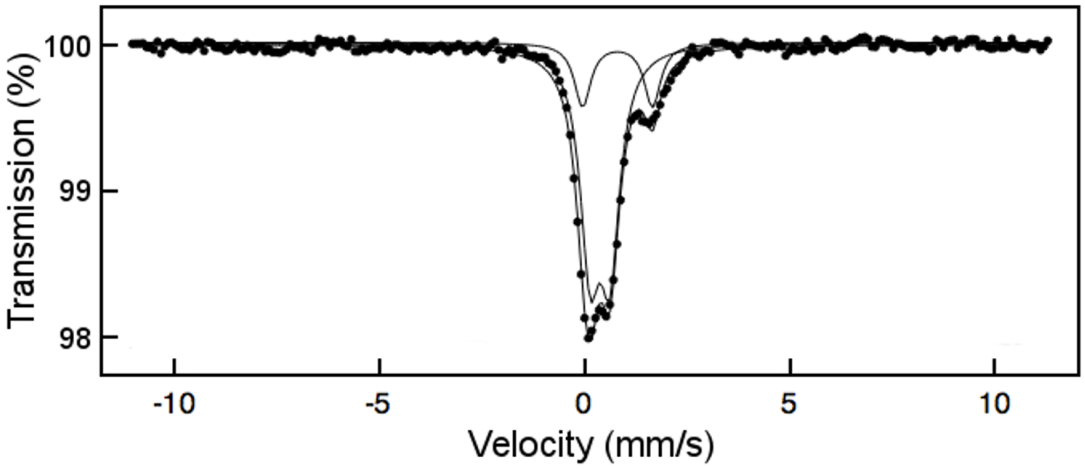

Figure 7.8 – Mössbauer spectrum of Versiliaite B at 298 K (scan 1) showing collected data (black dots) and fit lines (black).

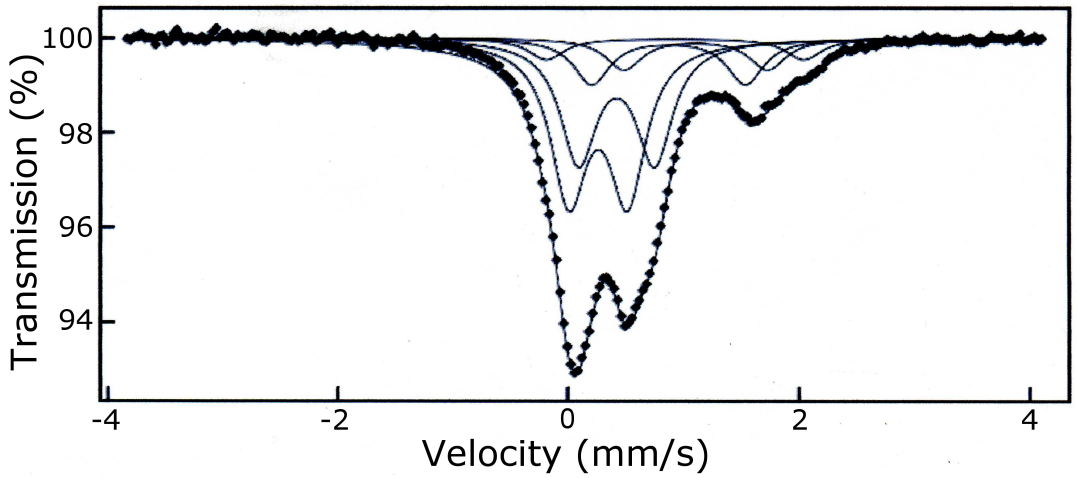

Figure 7.9 – Mössbauer spectrum of Versiliaite B at 298 K (scan 2) showing collected data (black dots) and fit lines (black).

In ideal Versiliaite, all Fe^{2+} sites will be neighboured by one Fe^{2+} and one Fe^{3+}, giving rise to a strongly asymmetric electric field. In a disordered model, however, regions will occur where the Fe^{2+} nearest-neighbours are either all Fe^{2+} (as in $FeSb_2O_4$) or all Fe^{3+}; this will give a much more symmetrical electric field, and would be expected to produce a different quadrupole splitting. A similar effect has previously been observed in Schafarzikite-based structures; $FeSb_2O_4$ shows $\delta = 1.08$ mm s^{-1} and $\Delta = 2.11$ mm s^{-1}, while $FeSb_{1.5}Pb_{0.5}O_4$ gives $\delta = 1.01$ mm s^{-1} and $\Delta = 1.74$ mm s^{-1}, a reduced quadrupole splitting.[4,11] In the latter case, approximately 50% of the Fe occurs as Fe^{3+}, but without any observed charge order; as such, the fitted quadrupole splitting is likely to be due to a mixture of symmetric (*i.e.* $Fe^{3+}\cdots Fe^{2+}\cdots Fe^{3+}$) and asymmetric ($Fe^{2+}\cdots Fe^{2+}\cdots Fe^{3+}$) environments. A completely asymmetric site would be expected to show an even smaller Δ. The data show no evidence of a $Fe^{2.5+}$ species, meaning that the anomalies seen in the diffraction data cannot be attributed to charge delocalisation.

Sample B shows a more complicated Mössbauer behaviour, perhaps surprisingly given the relatively straightforward diffraction data. A measurement over a wide velocity range (figure 7.8) was fitted to two doublets, attributed to Fe^{3+} and Fe^{2+} respectively. The values of Δ agree well with the mineral sample data collected over the same velocity range, however δ for Fe^{3+} is higher than expected. More surprisingly, the ratio of Fe^{2+}:Fe^{3+} is 21%:79%, significantly different to the expected 33%:66%. A scan over a narrower velocity range (figure 7.9) enables two

Table 7.12 – Fitted parameters for Versilaite samples from 298 K Mössbauer data.

Sample	Site	δ / mm s^{-1}	Δ / mm s^{-1}	H / T	Area / %	Assignment
A	1	0.23	0.5	-	39	$^{IV}Fe^{3+}$
	2	0.43	0.67	-	33	$^{VI}Fe^{3+}$
	3	1.05	1.84	-	13	$^{VI}Fe^{2+}$
	4	1.09	0.94	-	15	$^{VI}Fe^{2+}$
B	1	0.38	0.49	-	79	Fe^{3+}
	2	0.80	1.7	-	21	Fe^{2+}
B (scan 2)	1	0.27	0.51	-	41	$^{IV}Fe^{3+}$
	2	0.42	0.66	-	32	$^{VI}Fe^{3+}$
	3	1.11	1.24	-	8	Fe^{2+}
	4	0.87	1.33	-	12	Fe^{2+}
	5	0.93	2.23	-	6	Fe^{2+}
Mineral[5]	1	0.25	0.51	-	68	Fe^{3+}
	2	0.85	1.5	-	32	Fe^{2+}

Fe^{3+} sites to be determined, with parameters very similar to those seen in sample A. The relative areas of the two signals are not equal however, with a suggestion of more tetrahedral iron; the cause of this difference is unclear. Unlike sample A, however, this narrower velocity scan was best fit using three Fe^{2+} sites. The values of δ for these sites are consistent with octahedral coordination, however a range of quadrupole splittings are seen. The data could be explained with a similar argument to sample A, but with more significant differences in the local electric field around the different Fe^{2+} sites; the additional signal compared with sample A could correspond to the differentiation between the symmetrical $Fe^{2+}\cdots Fe^{2+}\cdots Fe^{2+}$ and $Fe^{3+}\cdots Fe^{2+}\cdots Fe^{3+}$ environments.

7.4.2 Apuanite

Fitted parameters for Apuanite are shown in table 7.13 for both synthetic and mineral samples. The fit for the synthetic sample involved four sites, one of which was assigned to the α-Fe_2O_3 impurity. Of the remaining sites, one was attributed to Fe^{2+}, and two to Fe^{3+}. Examining the peak areas, the ratio of Fe^{2+}:$^{IV}Fe^{3+}$:$^{VI}Fe^{3+}$ was 23%:30%:47%. Comparing this to the expected ratio (20%:40%:40%) the relative proportions of tetrahedral and octahedral Fe^{3+} do not agree with the Apuanite model. The cause of this discrepancy is undetermined, but if the signal attributed to α-Fe_2O_3 is included in the calculations, the ratio becomes 20%:39%:41%. While this would better agree with the expected values, this would predict that $\frac{1}{3}$ of the octahedral Fe^{3+} is magnetically ordered at room temperature. This has not been observed through other techniques (section 7.5.1) but does provide an interesting avenue of further investigation.

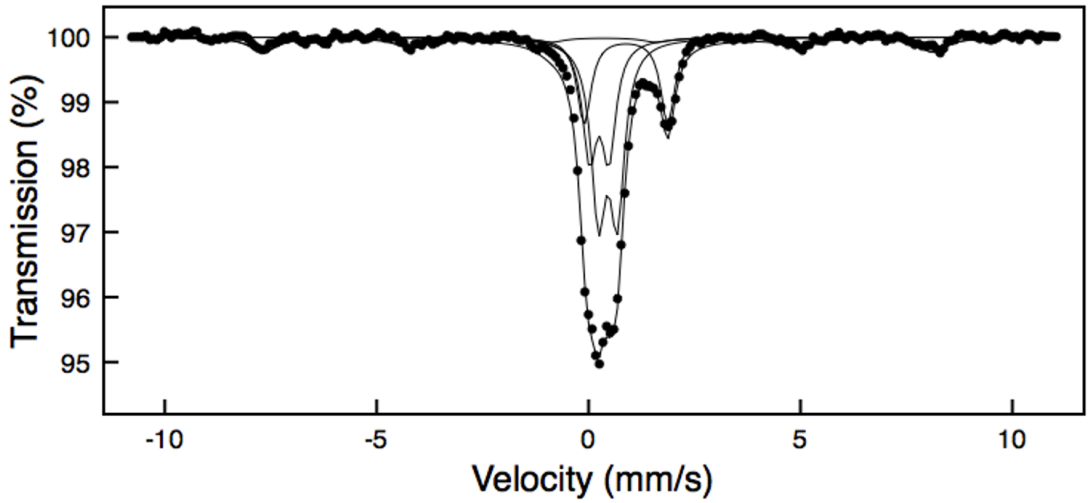

Figure 7.10 – Mössbauer spectrum of Apuanite at 298 K showing collected data (black dots) and fit lines (black).

Table 7.13 – Fitted parameters for Apuanite samples from 298 K Mössbauer data.

Sample	Site	δ / mm s^{-1}	Δ / mm s^{-1}	H / T	Area / %	Assignment
Synthetic	1	0.88	1.97	-	20	Fe^{2+}
	2	0.25	0.45	-	26	$^{IV}Fe^{3+}$
	3	0.45	0.44	-	41	$^{VI}Fe^{3+}$
	4	0.29	-0.13	49.0	13	α-Fe_2O_3
Mineral[5]	1	0.99	2.03	-	23	Fe^{2+}
	2	0.32	0.47	-	77	Fe^{3+}

7.5 Magnetic Characterisation

7.5.1 Magnetic Susceptibility Measurements

Versiliaite

Magnetic susceptibility data for Versiliaite samples A and B are shown in figures 7.11 and 7.12, respectively. Analysis of the data is hampered by the presence of the charge-ordering (Verwey) transition[12] in Fe_3O_4 at 123 K, which dominates any other (AFM) transitions present. A slight change in slope of the ZFC data can be seen in both samples at *ca.* 50 K, however; the down-turn suggests a weak AFM transition, but is very broad. Figures 7.13 and 7.14 show the susceptibility of a mineral Versiliaite sample, collected by R. Bayliss.[5] These data show a similar broad transition to the synthetic samples, but at a slightly higher temperature ($\simeq$ 60 K). The mineral sample also shows a slight up-turn in susceptibility at 16 K not seen in the synthetic samples; this may indicate a paramagnetic impurity. Additionally, the inverse susceptibility shows a deviation from linearity at *ca.* 170 K; while this could indicate non Curie-Weiss behaviour, neutron diffraction results (section 7.5.3) would suggest the onset of magnetic ordering around this temperature.

A fit of the paramagnetic region ($>$ 170 K) for the mineral sample to the Curie-Weiss law reveals a paramagnetic moment of 5.69 μ_B per Fe atom. This is slightly higher than the the-

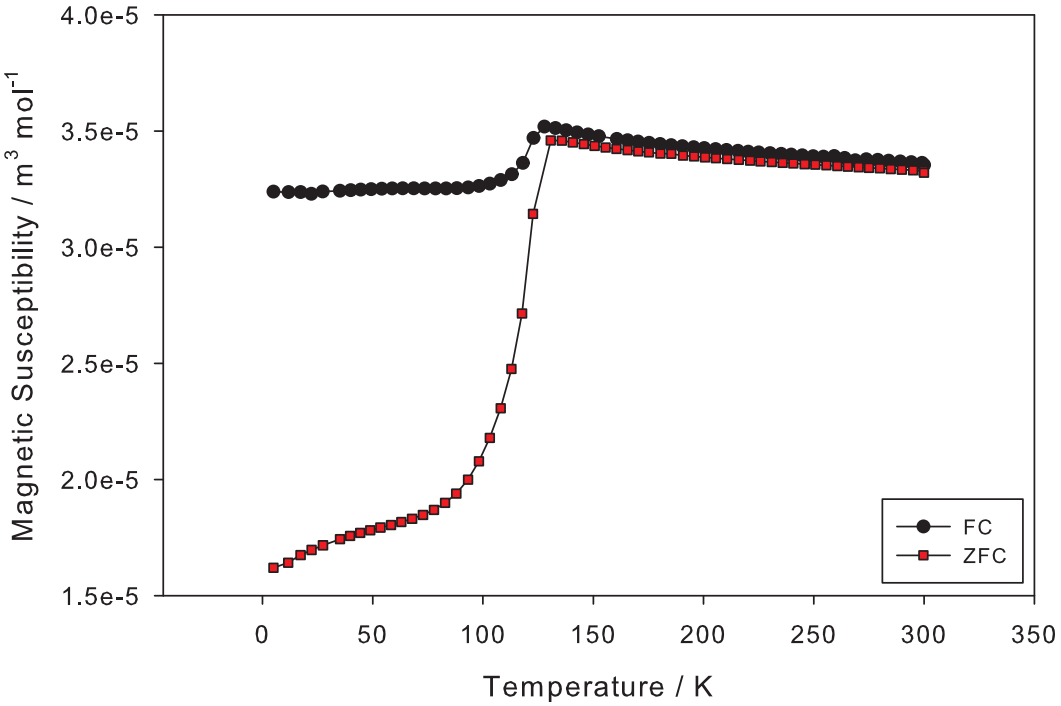

Figure 7.11 – Magnetic susceptibility *vs.* temperature for Versiliaite A. FC - Black circles, ZFC - red squares.

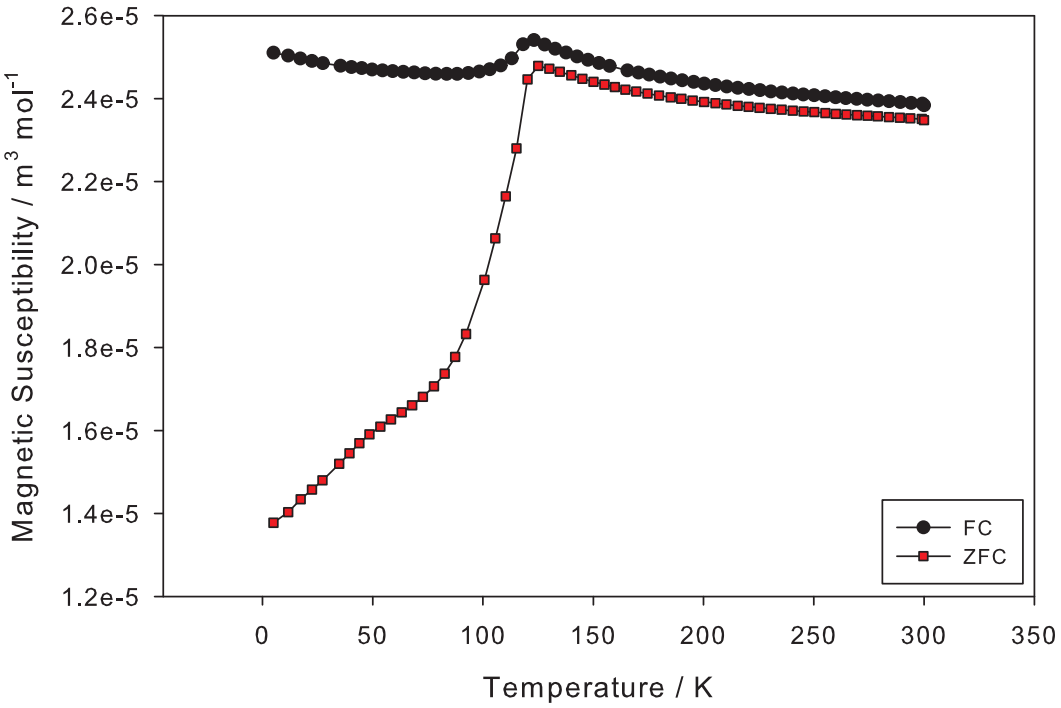

Figure 7.12 – Magnetic susceptibility *vs.* temperature for Versiliaite B. FC - Black circles, ZFC - red squares.

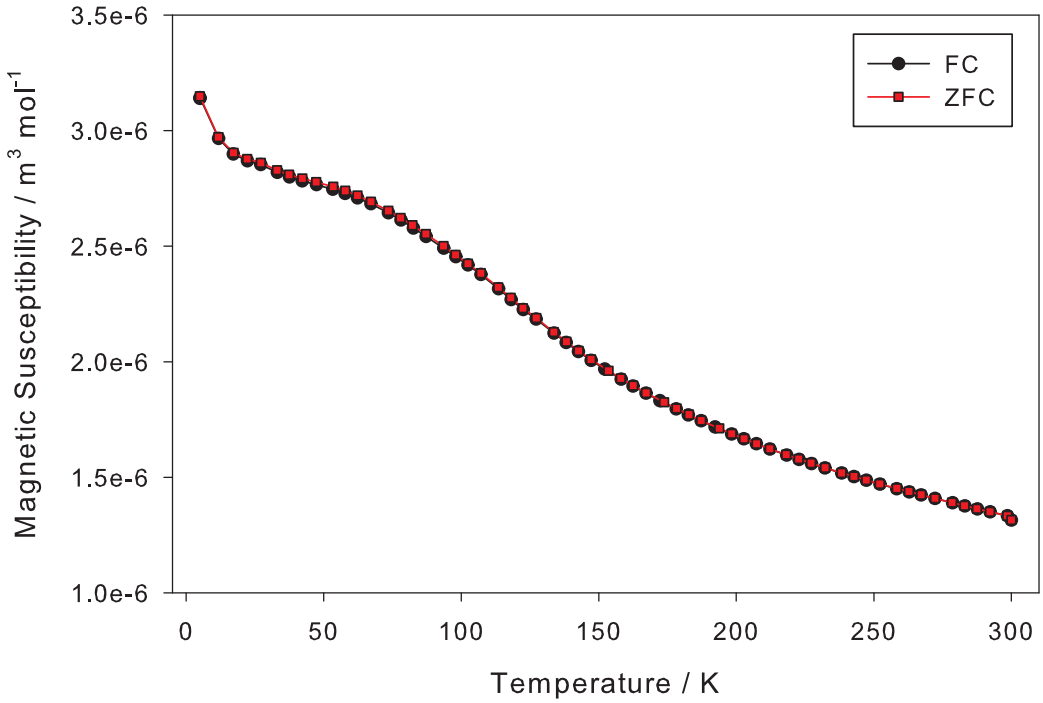

Figure 7.13 – Magnetic susceptibility *vs.* temperature for mineral Versiliaite. FC - Black circles, ZFC - red squares.

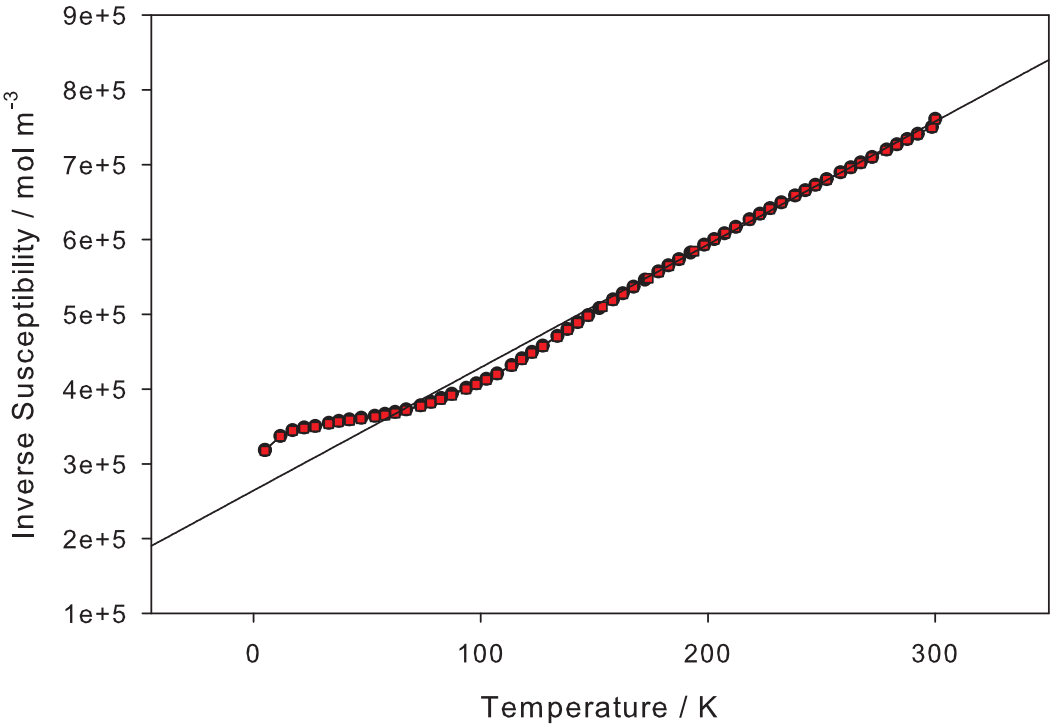

Figure 7.14 – Inverse magnetic susceptibility *vs.* temperature for mineral Versiliaite. FC - Black circles, ZFC - red squares, Curie-Weiss fit - black line.

oretical (spin-only) moment of 5.58 μ_B (calculated as a weighted average of Fe^{2+} and Fe^{3+} values) but lies within error, given the limited number of data points used for the fit. The value of the Weiss constant (θ) is obtained as -160 K, indicating a dominant (and quite strong) AFM exchange interaction.

Apuanite

The magnetic susceptibility data for Apuanite are shown in figure 7.15, while mineral data (collected by R. Bayliss) are shown in figures 7.16 and 7.17. Like the synthetic Versiliaite samples analysis is hampered by the Verwey transition of Fe_3O_4, but a slight downturn in ZFC susceptibility is seen at *ca.* 45 K. The mineral sample shows a very broad transition in the inverse susceptibility at approximately 80 K, but also shows a more well-defined (weakly AFM) transition at 190 K. From a Curie-Weiss fit above this temperature, the paramagnetic moment is determined as 5.13 μ_B. This is quite a lot lower than the weighted average spin-only value of 5.71 μ_B, but could be due to the presence of non-magnetic impurities in the mineral sample. The Weiss constant obtained from these data is $\theta = -217$ K, suggesting a stronger AFM interaction within Apuanite than Versiliaite, consistent with the greater number of Fe−S−Fe links between octahedral chains.

7.5.2 Magnetic Structure from Neutron Diffraction

Versiliaite

Neutron diffraction data for Versiliaite B were collected at 1.5 K on the HRPT powder diffractometer at PSI. On cooling additional magnetic reflections were observed, in particular at $d \simeq 12$ Å and 5.3 Å (figure 7.18 shows the difference plot between 298 K and 1.5 K). Indexing suggested a magnetic model commensurate with the nuclear unit cell, with these two main peaks corresponding to the magnetic (001) and (111), respectively. A wide range of magnetic models were tested, but the best fit was obtained for a model with octahedral moments aligned in a 'double-layer' AFM arrangement, oriented along the y direction. The tetrahedral Fe moments proved difficult to fit, but the best result was obtained for the moments aligned along x,

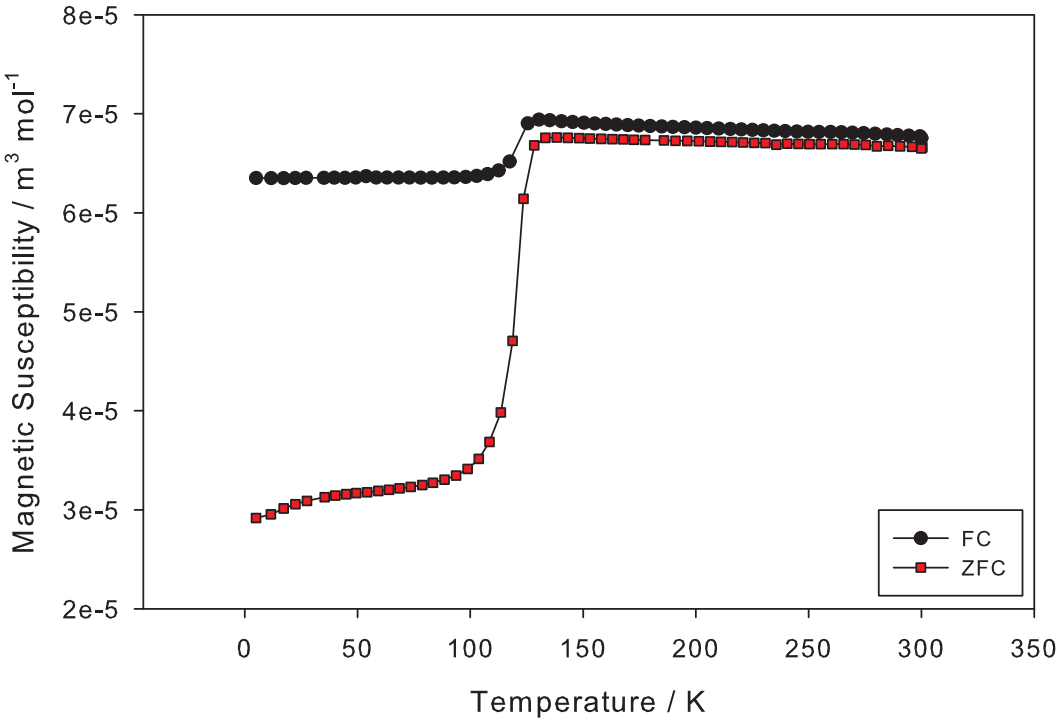

Figure 7.15 – Magnetic susceptibility *vs.* temperature for synthetic Apuanite. FC - Black circles, ZFC - red squares.

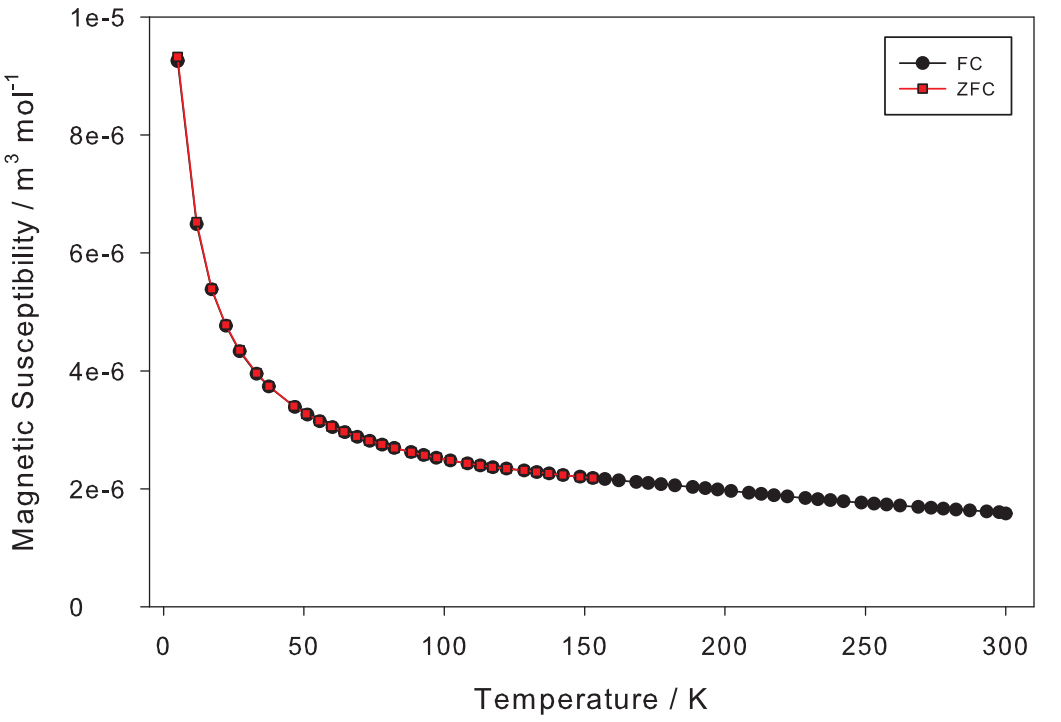

Figure 7.16 – Magnetic susceptibility *vs.* temperature for mineral Apuanite. FC - Black circles, ZFC - red squares.

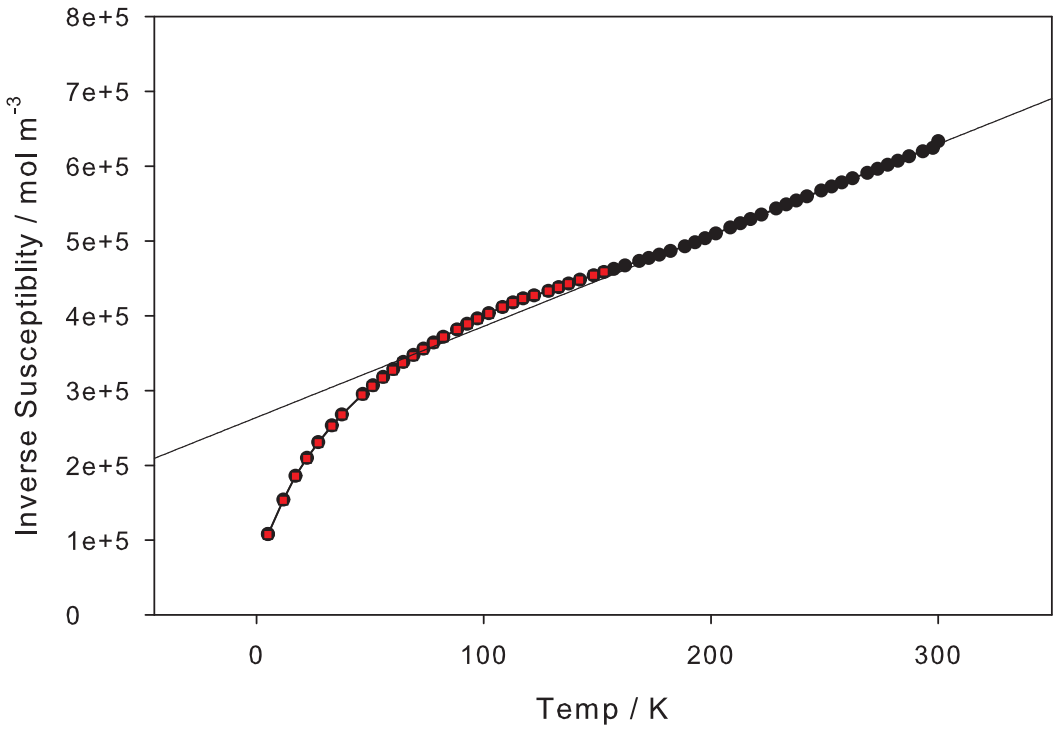

Figure 7.17 – Inverse magnetic susceptibility *vs.* temperature for mineral Apuanite. FC - Black circles, ZFC - red squares, Curie-Weiss fit - black line.

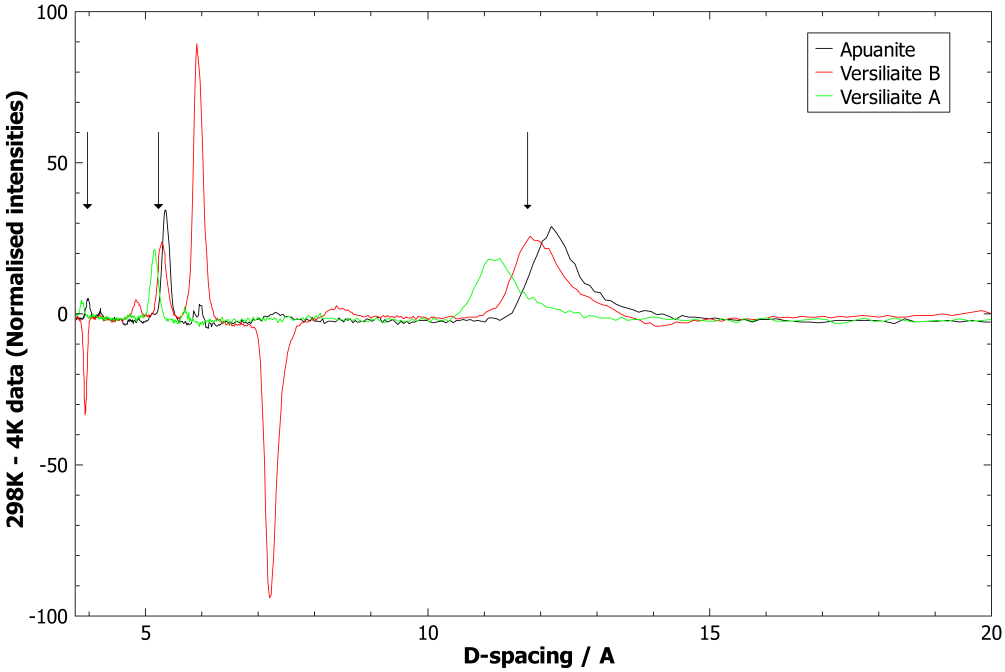

Figure 7.18 – Difference between RT and 4 K (1.5 K for Versiliaite B) NPD data showing development of magnetic reflections on cooling (black arrows). Additional peaks for Versiliaite B are due to different instrumental broadening between RT and 1.5 K datasets. 1.5 K Versiliaite B data have been corrected for the significant (0.6° 2θ) zero-point error.

perpendicular to the octahedral chain sites (figure 7.19). Notably, the $^{IV}Fe^{3+}$ sites bridged by S were arranged parallel to each other within this model; this is inconsistent with a dominant 180° superexchange interaction mediated by the sulfur link, which would predict AFM alignment.

The resulting refinement proved reasonably unstable, and was also a relatively poor fit ($\chi^2 =$ 14.39, R_{wp}=0.0733), particularly with regard to magnetic peaks intensities. Following NPD measurements on the synthetic Apuanite sample (section 7.5.2) it was discovered that the two samples both show magnetic peaks at approximately similar d-spacings (figure 7.18). While these peaks can be indexed on the nuclear unit cell for Versiliaite, they cannot for Apuanite, instead requiring a $k = (\frac{1}{2}, \frac{1}{2}, 0)$ magnetic propagation vector. For this reason, an alternative $k = (\frac{1}{2}, \frac{1}{2}, 0)$ model was investigated for Versiliaite.

Within the magnetic supercell, a number of ordering models were tested. Models based on the A- and C- type structures seen in Schafarzikite (parallel *ab* layers and parallel chains aligned

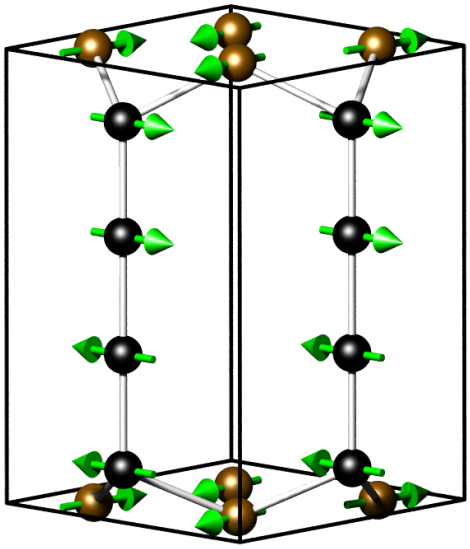

Figure 7.19 – Initially suggested magnetic structure for Versilaite B from NPD, viewed approximately along [110]. Octahedral Fe - black spheres; tetrahedral Fe - brown spheres.

AFM, respectively) proved inconsistent with the observed data. The best fit was achieved with a model in which the moments within a given octahedral chain were aligned parallel to one another (as in C-type), although here the spins were oriented within the *ab* plane. Adjacent chains are aligned ferromagnetically along the nuclear [110] direction, and antiferromagnetically along the perpendicular direction. The orientation of the tetrahedral iron moments were less easily resolved from the powder diffraction data; careful testing revealed that the moments are also aligned within the *ab* plane, and Fe−S−Fe are aligned antiparallel, as expected from a simple superexchange argument. In order to be consistent with the observed $(\frac{1}{2}, \frac{1}{2}, 0)$ propagation vector the ^{IV}Fe sites linked by oxygen on opposite sides of an octahedral chain (*i.e.* ^{IV}Fe1−O_{eq}−Fe3−O_{eq}−^{IV}Fe1 or ^{IV}Fe1−O_{ax}−Fe3−O_{ax}−^{IV}Fe1) must be aligned parallel to one another. This is also consistent with a superexchange argument, where each of the Fe−O−Fe interactions is AFM. The resulting refinement gives adjacent Fe−S−Fe links aligned at approximately 90° to each other (this was constrained for the final fit). The resulting magnetic model is shown in figure 7.20, and the graphical refinement is given in figure 7.21. Note that in this model the chain sites (Fe2 and Fe3) were constrained to have equal moments, but with different magnetic form factors (Fe^{2+} and Fe^{3+}, respectively), while the Fe1 sites were constrained to remain perpendicular to each other. Using the same Fe^{3+} form factors for all magnetic ions

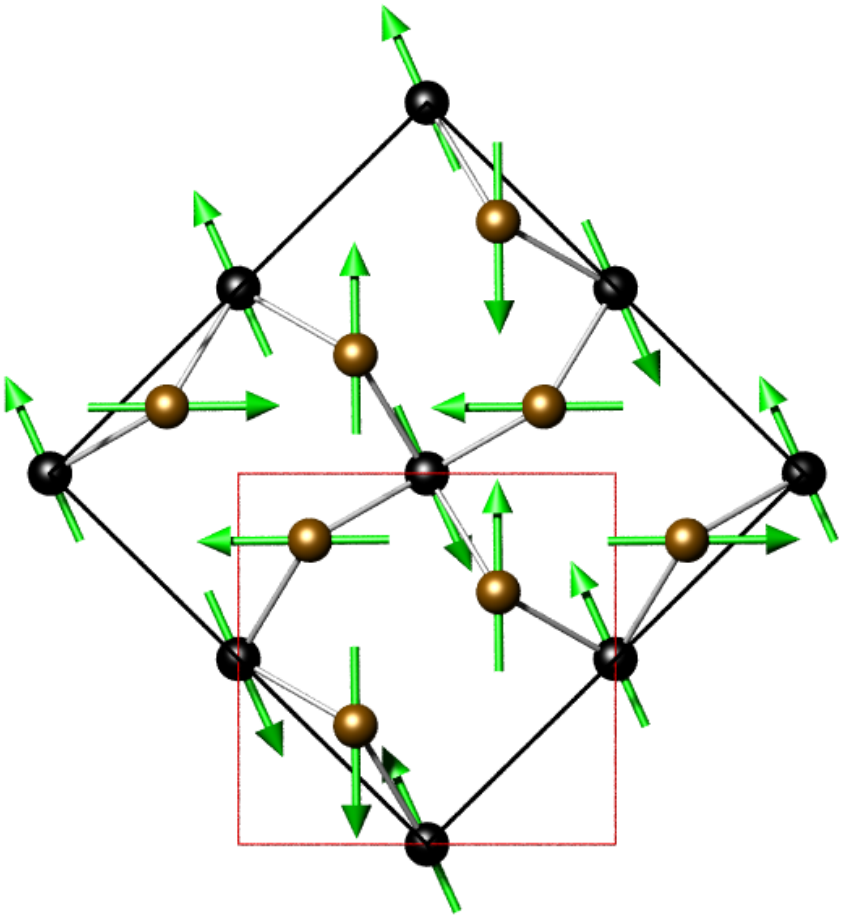

Figure 7.20 – Final magnetic model for Versiliaite B, viewed along [001] direction, showing relationship between nuclear (red) and magnetic (black) unit cells. Black sphere - octahedral Fe; brown sphere - tetrahedral Fe.

gave identical moments within error, but a fit of slightly worse quality. A model without the Fe2/Fe3 constraint mentioned resulted in a slight angle between the two moments, but no significant change in their relative magnitudes. Relaxing the perpendicular Fe1 constraint was also investigated, but resulted in a less stable refinement and significantly different moments on different ^{IV}Fe sites. The refined results for all three models are given in table 7.14.

This magnetic model reflects the competing magnetic interactions occurring within the material, showing signs of frustrated interactions within the *ab* planes, particularly from the Fe−S−Fe linkages. Using a representational analysis approach the structure can be described by a single co-representation, formed by a combination of Γ_2 and Γ_8 irreducible representations under the application of time-reversal symmetry (appendix B.1). Although this could

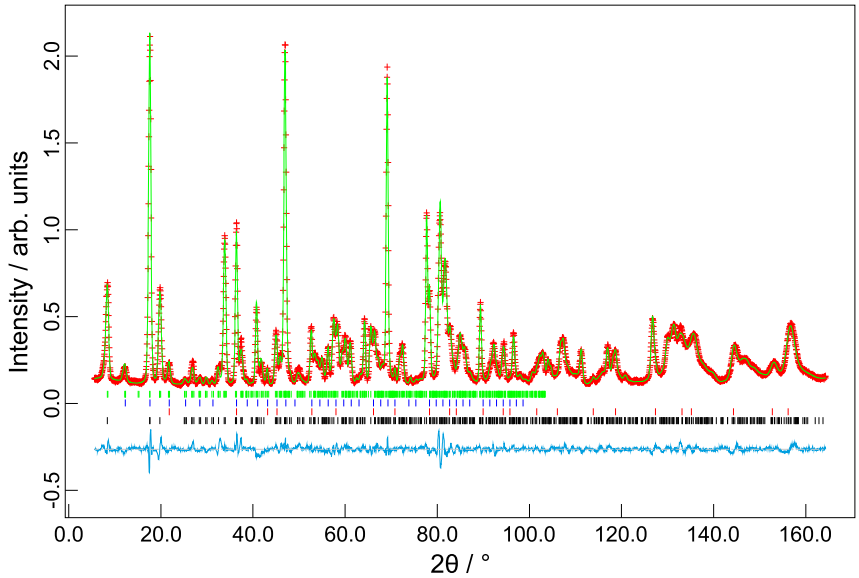

Figure 7.21 – Graphical refinement of Versiliaite B at 1.5 K. Green ticks - magnetic phase; red and blue ticks - Fe_3O_4 impurity.

Table 7.14 – Refined magnetic parameters for Versiliaite B (1.5 K).

		Model		
Applied	Fe2/Fe3 constrained	✓	×	×
constraints	Fe1 constrained	✓	✓	×
Fe1a $(x,\ y,\ 0)$	Mx, My / μ_B	2.8(1), 2.68(9)	2.8(1), 2.9(1)	0.6(6), 2.4(4)
	M_{abs} / μ_B	3.89(7)	3.99(7)	2.5(3)
Fe1b $(\bar{y},\ \bar{x}+\frac{1}{2},\ 0)$	Mx, My / μ_B	2.68(9), -2.8(1)	2.9(1), -2.8(1)	2.7(3), -3.7(1)
	M_{abs} / μ_B	3.89(7)	3.99(7)	4.5(2)
Fe2a $(0,\ 0,\ z)$	Mx, My / μ_B	1.25(3), 3.35(4)	1.4(1), 3.3(1)	1.6(2), 3.2(1)
	M_{abs} / μ_B	3.57(4)	3.6(2)	3.6(2)
Fe2b $(\frac{1}{2},\ \frac{1}{2},\ z)$	Mx, My / μ_B	-1.25(3), -3.35(4)	-1.4(1), -3.3(1)	-1.6(2), -3.2(1)
	M_{abs} / μ_B	3.57(4)	3.6(2)	3.6(2)
Fe3a $(0,\ 0,\ z)$	Mx, My / μ_B	1.25(3), 3.35(4)	1.0(1), 3.4(1)	1.1(1), 3.0(1)
	M_{abs} / μ_B	3.57(4)	3.5(2)	3.1(2)
Fe3b $(\frac{1}{2},\ \frac{1}{2},\ z)$	Mx, My / μ_B	-1.25(3), -3.35(4)	-1.0(1), -3.4(1)	-1.1(1), -3.0(1)
	M_{abs} / μ_B	3.57(4)	3.5(2)	3.1(2)
χ^2, no. of parameters		7.064, 88	7.040, 90	6.810, 91
R_{wp}, R_p		0.0517, 0.0389	0.0516, 0.0389	0.0507, 0.0382

be consistent with a single (second order) magnetic transition, this is not clear from magnetic susceptibility data.

The *ab* planes can be described as a lattice of distorted pentagons, for which the interaction along each edge is ideally AFM (figure 7.22a). Not all of these interactions can be fully satisfied, but the strength of the Fe−S−Fe AFM coupling (red line) dominates, and therefore aligns at 180°. Maximising the remaining interactions results in a 90° angle between the adjacent Fe−S−Fe links, with an intermediate angle formed by the chain cations. An alternative

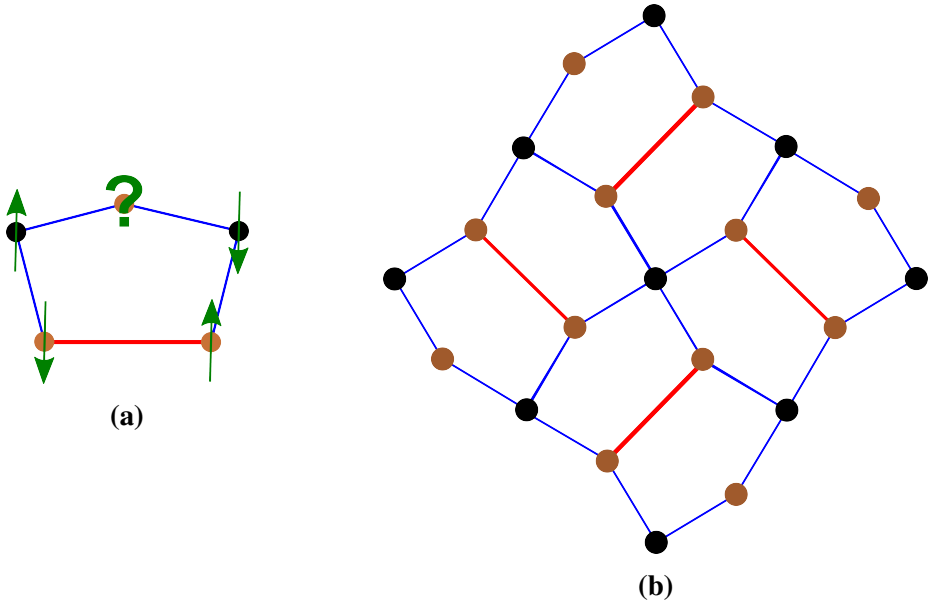

Figure 7.22 – Pentagon schematic for Versiliaite magnetic structure: (a) Frustration within pentagon motif; (b) Array formed by distorted pentagons. Brown circles - tetrahedral Fe; black circles - octahedral Fe.

description of the magnetic structure is based around an array of corner-sharing rectangles, with octahedral chains centred in each quadrilateral (figure 7.23). Within each rectangle, Fe on opposite corners are aligned parallel, while adjacent corners are aligned at 90° to one another. From this description it is easier to see the JT distortions of the octahedra, which should lead to different strength interactions along the Fe3−O_{eq}−Fe1 and Fe3−O_{ax}−Fe1 pathways. Examining the bond angles (128.3700(9)° and 117.055(1)°, respectively) and ignoring variation in bond lengths, this would suggest a stronger AFM interaction mediated through the equatorial oxygen, which is exactly what is observed. The strength of this interaction might be expected

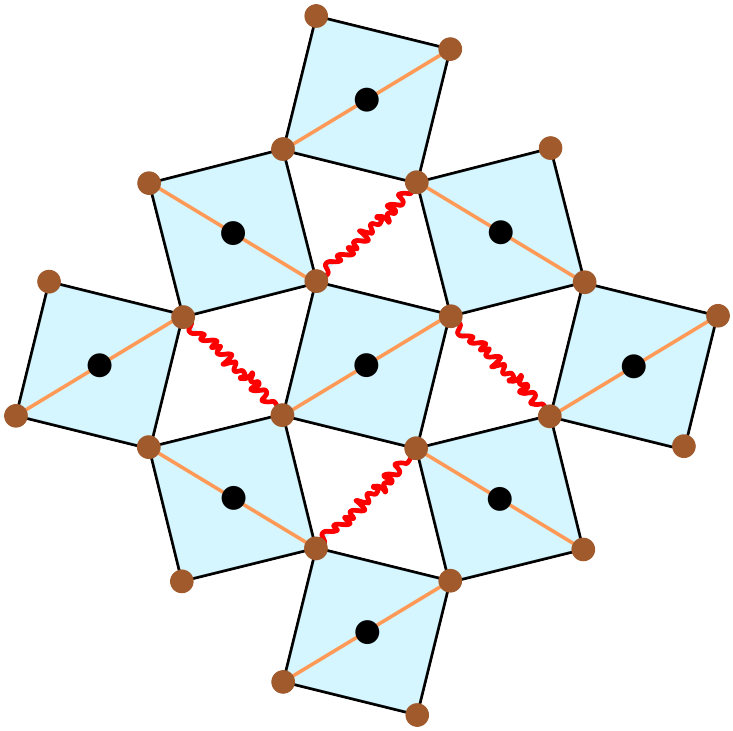

Figure 7.23 – Corner-sharing quadrilateral schematic of Versiliaite magnetic structure, showing Fe−S−Fe links (red wavy lines) and octahedral Jahn-Teller distortion axis (orange lines).

to modulate the magnetic structure in both [110] and [$\bar{1}$10] nuclear directions (as in figure 7.24) although this effect has not been observed from the diffraction data. This order would be expected to give rise to a significant magnetic (110) or (1$\bar{1}$0) peak however (at *ca.* 12° 2θ) which although weakly observed, is modelled mainly as the Fe_3O_4 (001) peak. It is possible that such a modulation does exist, but is being incorrectly fitted as an impurity peak. Alternatively, the observed structure might be a real effect; the slightly orthorhombic nuclear structure combined with spin-orbit coupling effects from the octahedral Fe^{2+} might make the different spin alignment along [110] and [$\bar{1}$10] favourable.

The FM alignment of magnetic moments within the edge-sharing octahedral chains is in stark contrast to the AFM chains observed in Schafarzikite, and is due to the presence of mixed valent iron (the same effect is also seen for $FeSb_{2-x}Pb_xO_4$ [13]). Overall FM chains are difficult to rationalise, however; exchange between Fe^{2+} (d^6) and Fe^{3+} (d^5) would give a FM coupling, while direct d^6-d^6 and d^5-d^5 interactions would be expected to be AFM. Within the chains there are nominally equal numbers of AFM and FM interactions, giving no obvious preference.

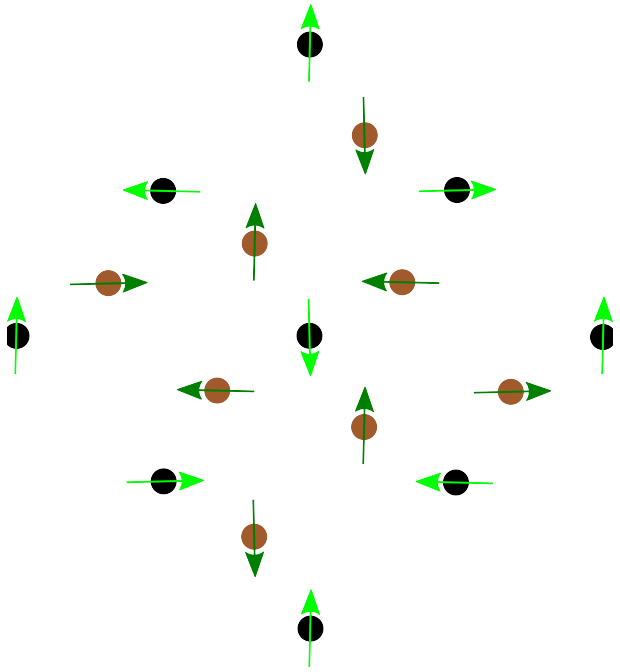

Figure 7.24 – Suggested Versiliaite magnetic structure, modulated along both nuclear [110] and [1$\bar{1}$0], not observed from powder diffraction.

Examining the Fe−Fe distances on cooling (table 7.15) reveals that only the Fe3−Fe3 distance decreases on cooling, while the others increase in length. This would be expected to increase the Fe3−Fe3 direct exchange while decreasing the FM Fe2−Fe3 exchange, in obvious contrast to the observed behaviour. BVS estimates for the cations also produce an interesting result; on cooling the Fe2 valence increases, while that of Fe3 stays roughly constant. Although the absolute values are less reliable at low temperatures (R_0 values are tabulated for RT, therefore thermal contraction should result in higher valences on cooling) this suggests that Fe2 shows a greater bonding requirement *cf.* Fe3. Combined with the changes in Fe−Fe distances on cooling, this might suggest delocalisation of charge between Fe2 and Fe3, although these data are far from conclusive. This could provide an explanation for the observed FM chains; if the extra t_{2g} electrons were delocalised, this could produce a FM state via a double-exchange mechanism between adjacent Fe orbitals. The equal magnetic moments seen for the unconstrained model might also support this, although the value is lower than that expected even for ideal Fe^{2+}. Further measurements (such as low temperature Mössbauer spectroscopy and conductivity measurements) would be needed to draw any definite conclusions.

Table 7.15 – Fe−Fe octahedral chain distances.

Distance / Å	RT	1.5 K
Fe3−Fe3	3.00857(9)	2.95249(7)
Fe2−Fe3	2.98777(9)	3.00648(8)
Fe2−Fe2	2.94397(9)	2.97383(8)
Mean	2.9801	2.9776

Table 7.16 – BVSs for octahedral Fe ions.

	Valence	RT	1.5 K
Fe2	2+	2.375	2.415
	3+	2.541	2.848
Fe3	2+	2.660	2.662
	3+	2.846	2.848

Apuanite

As mentioned in section 7.5.2, the magnetic diffraction peaks observed on cooling Apuanite could not be indexed on the nuclear unit cell, instead requiring a $(\frac{1}{2}, \frac{1}{2}, 0)$ propagation vector. Within the magnetic supercell a range of models were tested, however analysis was hampered by a limit within GSAS to the number of magnetic parameters which could be fixed during refinement. The best-fitting model closely resembles that seen for Versiliaite; FM octahedral chains (aligned in the *ab* plane) coupled FM along one magnetic unit cell axis, and AFM in the perpendicular direction (figure 7.25). From powder diffraction it is not possible to determine the orientation of the moments within the *ab* plane due to the tetragonal nuclear symmetry, but it was not possible to constrain them due to the limit within GSAS. Refinement of the orientation was achieved by fixing the orientation of the Fe−S−Fe links along the nuclear axes, similar to the refined moments seen in Versiliaite. The best model for the tetrahedral sites showed AFM alignment within a given Fe−S−Fe pair with a 90° angle between adjacent pairs, as in

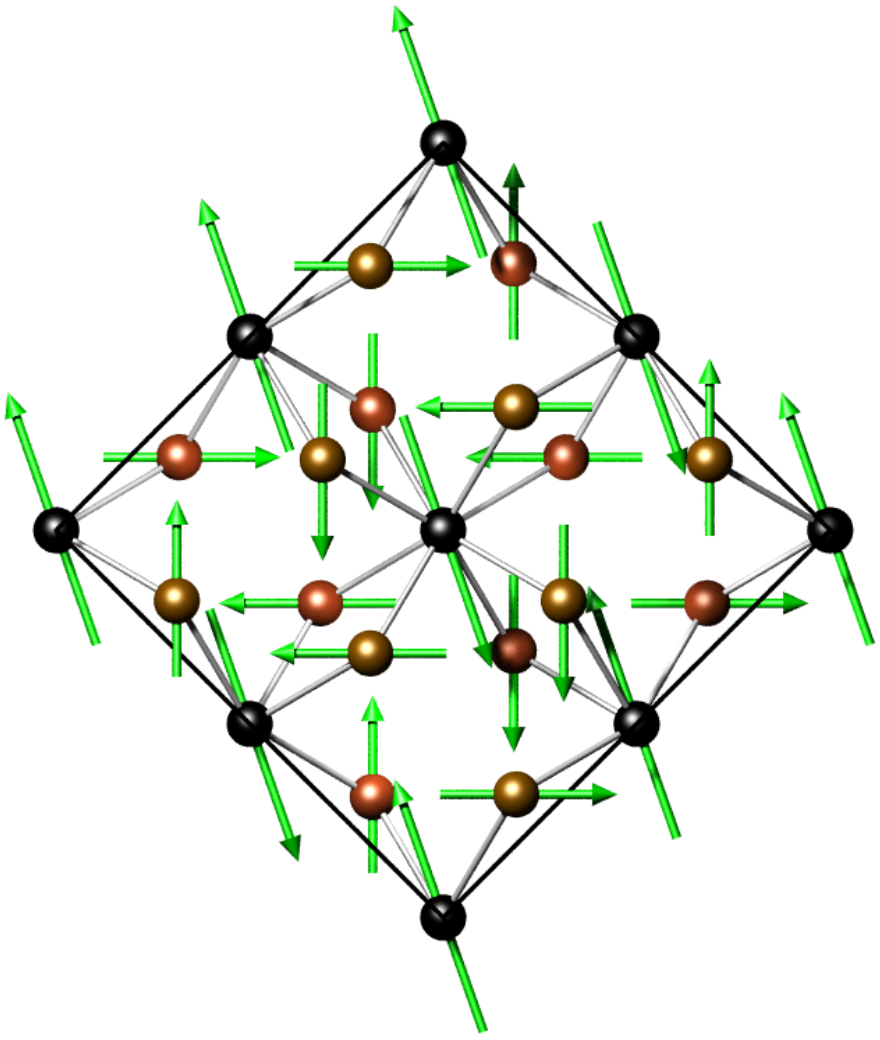

Figure 7.25 – Refined Apuanite magnetic structure viewed along [001]. Red-brown and yellow-brown spheres denote tetrahedral Fe at $z = \frac{1}{2}$ and $z = 0$ respectively.

Versiliaite. In Apuanite, however, the additional Fe−S−Fe containing layer at $z = \frac{1}{2}$ was found to be oriented at 90° to the $z = 0$ layer, in such a way that any two tetrahedral sites bound (via oxygen) to the same two chains exhibit parallel alignment (figure 7.26).

The refined moments and statistical parameters are given in table 7.17, while a graphical plot of the refinement is given in appendix C.3.1. This model can be described by a single IR (appendix B.1) in which all moments are constrained to lie within the *ab* plane. The arguments regarding the observed ordering are very similar to Versiliaite, except that in Apuanite there are a greater number of Fe−S−Fe linkages increasing the coupling between octahedral chains. Although the structure shown exhibits a distinct difference between magnetic [100] and [010]

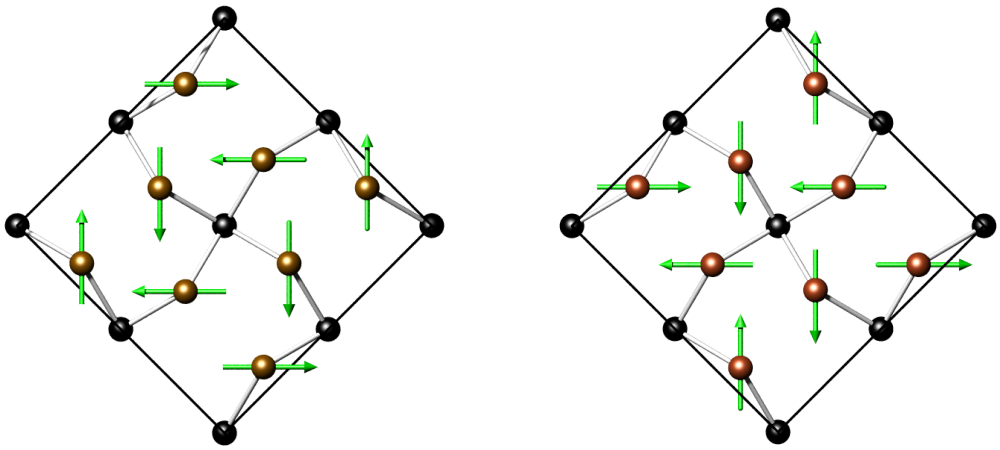

(a) (b)

Figure 7.26 – Refined arrangement of tetrahedral Fe moments at (a) $z = 0$ and (b) $z = \frac{1}{2}$.

directions, this is inconsistent with the tetragonal nuclear symmetry, which shows no significant orthorhombic splitting on cooling. In fact, the true structure is likely to be highly dependent on the local crystal structure (*i.e.* disordered regions) and could adopt a number of orientations within the *ab* plane. A structure modulated in both directions (as suggested for Versiliaite, figure 7.24) may actually be present, but not determinable from powder diffraction data. This sort of structure would also be consistent with the symmetry imposed by the Γ_{10} irreducible representation.

As in Versiliaite, the chain sites show identical magnetic moments when unconstrained. Comparing the Fe−Fe distances and BVS (table 7.18) shows a different behaviour, however; here the distances and BVS all decrease similarly between the two sites, showing no signs of changing charge distribution. It is important to note, however, that the standard deviations of the unconstrained moments encompass the expected values for Fe^{2+} and Fe^{3+}, so the moments may actually be different. The FM order observed along the octahedral chains is consistent with double exchange between Fe^{2+} and Fe^{3+}, but is inconsistent with the Fe3−Fe3 (d^5−d^5) interaction. Given the small change in this distance on cooling, however, it could be argued that the smaller orbital size of Fe3 *cf.* Fe2 effectively prevents this direct overlap, instead favouring a 90° (FM) super-exchange *via* oxygen.

Table 7.17 – Refined magnetic moments for Apuanite with constrained and unconstrained Fe2/Fe3 moments.

		Constrained	Unconstrained
Fe1a $(x,\ y,\ 0)$	Mx, My / μ_B	1.70(3), 1.70(3)	1.87(5), 1.87(5)
	M_{abs} / μ_B	2.41(5)	2.65(7)
Fe1b $(\bar{y}+\frac{1}{2},\ \bar{x},\ 0)$	Mx, My / μ_B	1.70(3), -1.70(3)	1.87(5), -1.87(5)
	M_{abs} / μ_B	2.41(5)	2.65(7)
Fe1c $(x,\ y,\ \frac{1}{2})$	Mx, My / μ_B	-1.70(3), 1.70(3)	-1.87(5), 1.87(5)
	M_{abs} / μ_B	2.41(5)	2.65(7)
Fe1d $(\bar{x},\bar{y},\frac{1}{2})$	Mx, My / μ_B	1.70(3), 1.70(3)	1.87(5), 1.87(5)
	M_{abs} / μ_B	2.41(5)	2.65(7)
Fe2a $(0,\ \frac{1}{2},\ \frac{1}{4})$	Mx, My / μ_B	3.94(2), 1.88(3)	4.2(4), 2.4(5)
	M_{abs} / μ_B	4.36(3)	4.8(6)
Fe2b $(\frac{1}{2},\ 0,\frac{1}{4})$	Mx, My / μ_B	-3.94(2), -1.88(3)	-4.2(4), -2.4(5)
	M_{abs} / μ_B	4.36(3)	4.8(6)
Fe3a $(0,\ \frac{1}{2},\ z)$	Mx, My / μ_B	3.94(2), 1.88(3)	3.9(2), 1.6(2)
	M_{abs} / μ_B	4.36(3)	4.2(2)
Fe3b $(\frac{1}{2},\ 0,z)$	Mx, My / μ_B	-3.94(2), -1.88(3)	-3.9(2), -1.6(2)
	M_{abs} / μ_B	4.36(3)	4.2(2)
χ^2, no. of parameters		4.771, 74	4.494, 84
R_{wp}, R_p		0.0290, 0.0317	0.0280, 0.0310

Table 7.18 – Fe−Fe distances and BVS for Apuanite at RT and 4 K.

		RT	4 K
Fe3−Fe3 / Å		3.0119(1)	2.9987(1)
Fe2−Fe3 / Å		2.9888(1)	2.9867(1)
Mean / Å		3.0004	2.9927
Fe2 BVS	2+	2.314	2.279
	3+	2.476	2.438
Fe3 BVS	2+	2.757	2.733
	3+	2.949	2.924

7.5.3 Magnetic Changes on Cooling

Versiliaite

NPD data were collected for Versiliaite B at a number of intermediate temperatures (150 K, 50 K and 20 K) on the D2B diffractometer, ILL in addition to the 1.5 K data. These data (figure 7.27) show that weak magnetic reflections are observed at 150 K, particularly the nuclear (201) peak ($d \simeq 5.5$ Å). This temperature is slightly lower than the deviation seen in magnetic susceptibility data for the mineral sample, suggesting that magnetic order occurs at *ca.* 170 K. Refinement of the magnetic moments over this full temperature range shows a gradual decrease in moment for both Fe sites, as expected (figure 7.28). The refined moments are lower than expected at 20 K, but are consistent with the trend given the large errors involved.

Apuanite

Variable temperature NPD data were collected for Apuanite on the GEM diffractometer at 210 K, 170 K, 150 K, 130 K, 120 K, 100 K, 80 K and 40 K, in addition to 5 K. Inspection of the data (figure 7.29) suggest that short-range magnetic order is present up to 210 K, as evidenced by the small broad peak at $d \simeq 5.5$ Å. The variation of the magnetic moments with temperature is shown in figure 7.30. The values obtained from fitting the Brillouin function

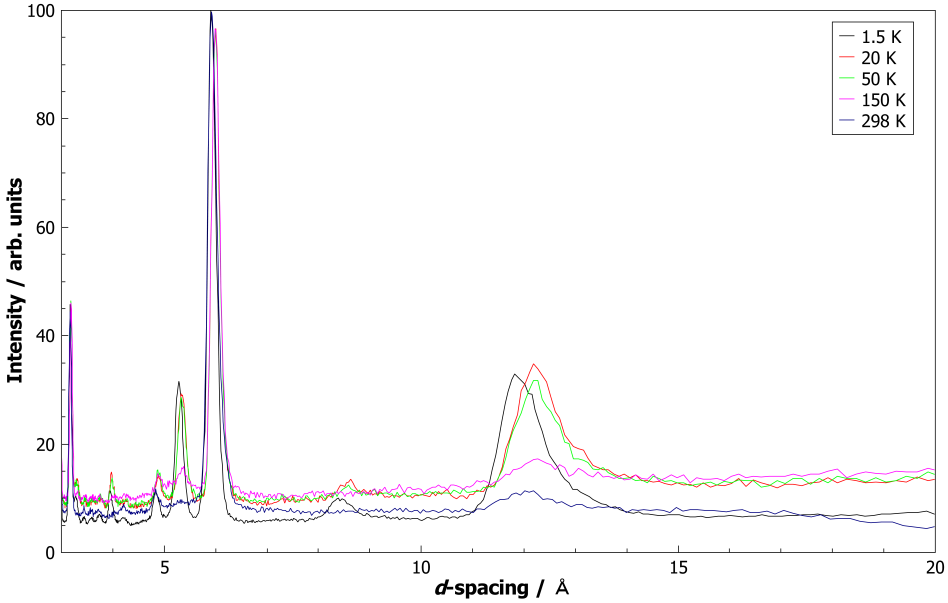

Figure 7.27 – Plot of variable-temperature NPD data for Versiliaite B, showing development of magnetic reflections on cooling. 1.5 K data have been corrected for a significant zero-point error.

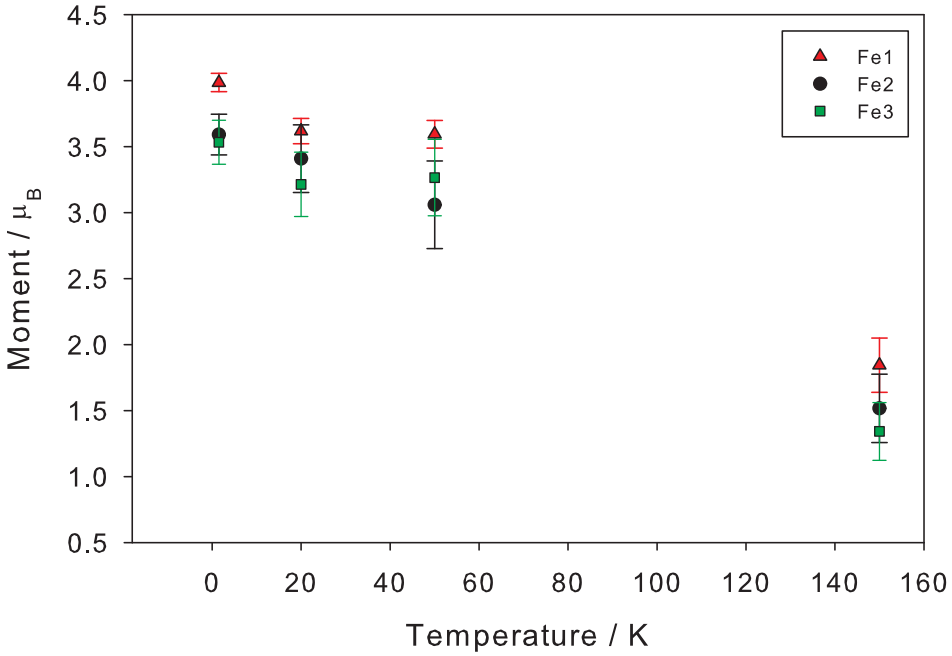

Figure 7.28 – Plot of refined magnetic moment *vs.* temperature for Versiliaite B.

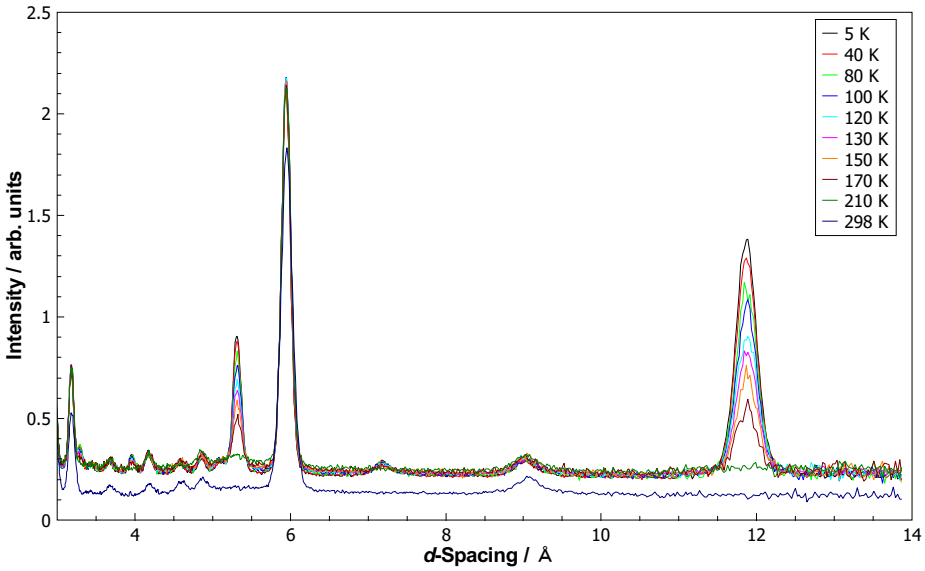

Figure 7.29 – Variable temperature NPD data for Apuanite, showing development of magnetic reflections on cooling.

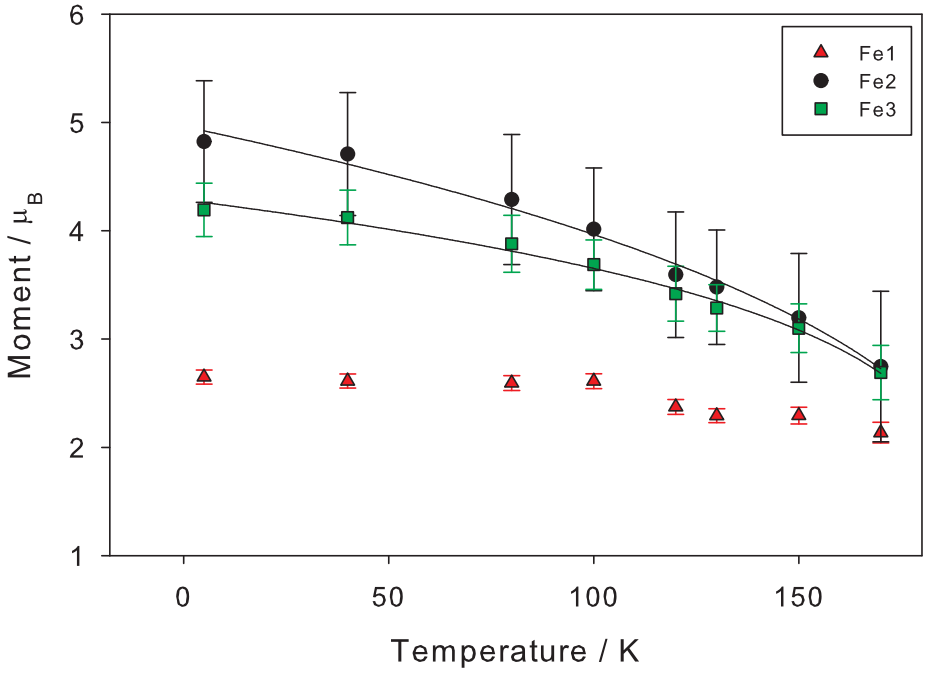

Figure 7.30 – Refined magnetic moments for Apuanite, with associated Brillouin function fit (black lines).

Table 7.19 – Fitted parameters to the Brillouin function for Apuanite magnetic moments.

Parameter	Value (error estimate from regression)	
	Fe2	Fe3
M_0/μ_B	4.96(8)	4.29(5)
T_c / K	200(14)	193(8)
β	0.33(6)	0.22(3)

(5.1) to these data are shown in table 7.19. These values are not significantly different for the two octahedral sites, as expected given the large errors for the magnetic moments. The fitted parameters suggest a magnetic ordering temperature for Fe2/Fe3 of *ca*. 200 K, similar to the Weiss constant (−217 K) obtained from susceptibility data. Interestingly, the fitted data suggest a smaller M_0 for Fe3 than Fe2, which should nominally be d^5 and d^6, respectively. Given the underestimated errors from this regression fit, however, this is not significant. The values of β obtained are consistent with a 3D ordered structure.

The variation of the Fe1 moments shows anomalous behaviour; above 100 K they decrease as expected (although at a much slower rate than Fe2/Fe3), but below this temperature they remain constant, at a much lower moment (2.6 μ_B) than that expected for HS d^5. This could be indicative of frustration causing disordered moments (not modelled from diffraction) or could suggest an incorrect magnetic model for these sites.

7.6 Structural Changes on Cooling

7.6.1 Versiliaite

The refined atomic parameters over the full temperature range are given in table 7.20. The refined lattice parameters are shown graphically in figure 7.31. The refined *b* parameter decreases with temperature, while the *a* parameter shows a slight increase on cooling, such that the orthorhombic separation increases at lower temperatures. The value of *b* observed at 1.5 K

is slightly anomalous, however, increasing to more than the RT value. This is attributable to the different instrument (and therefore neutron wavelength) used for this measurement, which could not be refined against XRPD data. The *c*-axis shows a similar increase at this temperature. Interestingly, the largest *c* parameter (and also volume) is observed at 150 K, not RT, suggesting negative thermal expansion in this region. This may be attributable to differences in instrument profile (and resulting correlations with lattice parameters) for the RT dataset, however, and would require further study.

Examining the bond lengths on cooling, the 50 K (and to some extent the 20 K) data show either a maximum or minimum for many of the parameters, for instance the average bond length or bond distortion index around Fe1 (figures 7.32 and 7.33), the average Fe2−O bond length (7.34) or the Fe3 quadratic elongation (7.35). While 50 K is most significant for Fe1, Fe2 and Fe3 show the most significant changes in behaviour at 20 K for many parameters (such as average Fe3−O bond length, figure 7.36). These effects would suggest a slight structural change below 20–50 K, probably connected with the deviations seen in magnetic susceptibility at approximately this temperature. For Fe1, the tetrahedral site becomes larger but with a greater deviation between bondlengths, but also shows an smaller angular distortion on cooling. The Fe1−S bond shows a significant increase in length during this distortion. Fe2 shows a sudden decrease in Fe−O bond length below 50 K, while the bond length distortion, quadratic elongation and angular variance also decrease at low temperature, but with a maximum at 20 K. Fe3 shows effectively the opposite behaviour; the octahedral volume increases rapidly below 20 K, while the quadratic elongation and bond angle variance decrease below this temperature. Given the small number of temperatures studied and the potential errors due to different instrumental profiles, it is difficult to draw any firm conclusions from these behaviours.

7.6.2 Apuanite

The *a* and *c* parameters of Apuanite both contract on cooling, giving an overall reduction in unit cell volume (figure 7.37). Examining the individual bond lengths and angles, many of these parameters show quite large deviations around the general (often almost linear) trend. One recur-

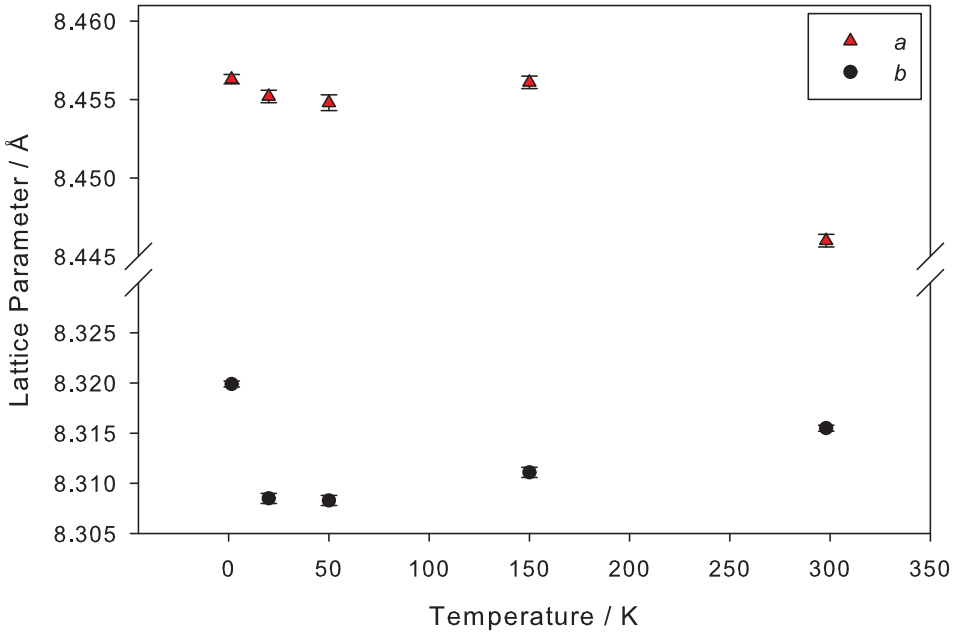

(a)

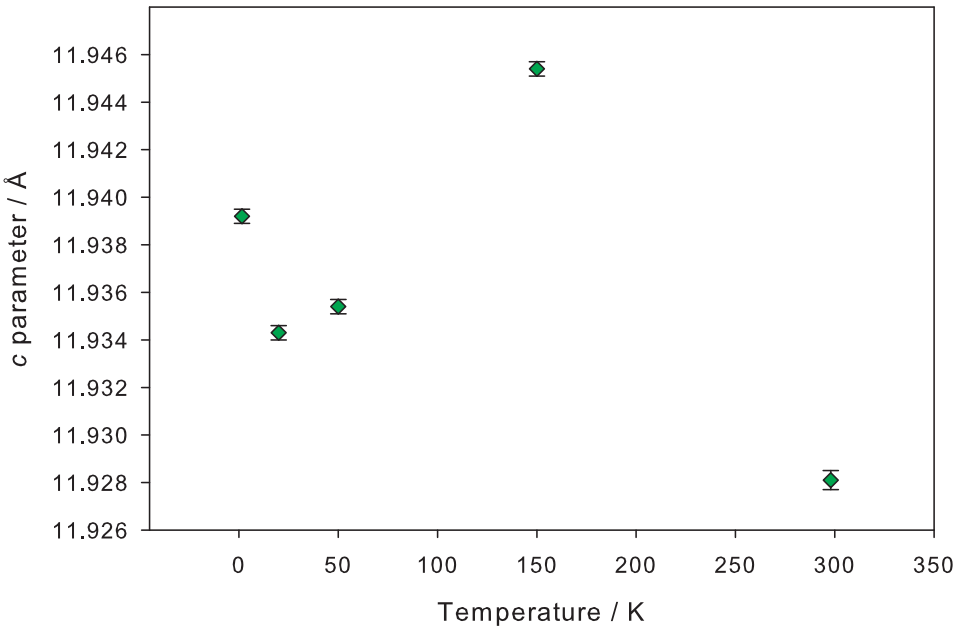

(b)

Figure 7.31 – Variation of (a) *a* and *b* parameters and (b) *c* parameter with temperature in Versiliaite B.

Table 7.20 – Refined unit cell and atomic parameters for Versiliaite B at variable temperatures.

		RT	150 K	50 K	20 K	1.5 K
a / Å		8.4460(4)	8.4561(4)	8.4548(5)	8.4552(4)	8.4563(3)
b / Å		8.3155(3)	8.3111(5)	8.3083(5)	8.3085(5)	8.3199(3)
c / Å		11.9281(4)	11.9454(3)	11.9354(3)	11.9343(3)	11.9392(3)
Volume / Å^3		837.74(7)	839.52(8)	838.41(8)	838.39(8)	839.98(6)
Fe1 (4g)	*x*	0.3115(7)	0.3112(8)	0.3103(8)	0.3102(8)	0.3113(6)
	y	0.3204(6)	0.3225(8)	0.3204(8)	0.3208(7)	0.3174(7)
	$100 \times U_{iso}$ / Å^2	1.6(1)	0.9(1)	0.6(1)	0.4(1)	1.2(1)
Fe2 (4f)	*z*	0.3766(5)	0.3799(6)	0.3778(7)	0.3789(6)	0.3755(6)
	$100 \times U_{iso}$ / Å^2	0.9(1)	0.8(1)	0.9(2)	0.8(1)	0.4(1)
Fe3 (4f)	*z*	0.1261(6)	0.1282(7)	0.1280(7)	0.1293(7)	0.1237(7)
	$100 \times U_{iso}$ / Å^2	0.5(1)	-0.1(1)	-0.3(1)	-0.4(1)	0.5(1)
Sb1 (8i)	*x*	0.1705(5)	0.1691(6)	0.1689(6)	0.1681(6)	0.1694(5)
	y	0.1677(5)	0.1658(6)	0.1659(6)	0.1663(6)	0.1670(4)
	z	0.2472(6)	0.2460(6)	0.2450(7)	0.2456(7)	0.2455(6)
	$100 \times U_{iso}$ / Å^2	0.85(8)	0.8(1)	0.4(1)	0.5(1)	0.18(8)
Sb2 (4h)	*x*	0.330(1)	0.331(1)	0.332(1)	0.333(1)	0.334(1)
	y	0.3267(9)	0.327(1)	0.330(1)	0.329(1)	0.332(1)
	$100 \times U_{iso}$ / Å^2	0.2(2)	0.4(3)	0.7(3)	0.8(3)	1.4(2)
S (2a)	$100 \times U_{iso}$ / Å^2	2.4(5)	4.3(8)	2.9(7)	3.4(7)	0.6(4)
O1 (4h)	*x*	0.3591(9)	0.359(1)	0.359(1)	0.360(1)	0.3597(9)
	y	0.094(1)	0.093(1)	0.092(1)	0.091(1)	0.095(1)
	$100 \times U_{iso}$ / Å^2	1.2(2)	0.8(2)	0.7(2)	0.7(2)	1.3(2)
O2 (8i)	*x*	0.4015(5)	0.4015(5)	0.4012(5)	0.4009(5)	0.3995(4)
	y	0.1358(4)	0.1360(5)	0.1363(5)	0.1359(5)	0.1358(4)
	z	0.2482(7)	0.2476(7)	0.2470(8)	0.2464(7)	0.2483(7)
	$100 \times U_{iso}$ / Å^2	1.08(8)	0.4(1)	0.2(1)	0.1(1)	0.9(1)
O3 (8i)	*x*	0.3254(7)	0.3265(9)	0.3264(9)	0.3262(8)	0.3292(6)
	y	0.8189(7)	0.820(1)	0.8183(9)	0.8186(9)	0.8198(7)
	z	0.3775(5)	0.3769(7)	0.3763(7)	0.3762(7)	0.3764(5)
	$100 \times U_{iso}$ / Å^2	1.4(1)	1.7(2)	1.4(2)	1.3(2)	1.0(1)
O4 (8i)	*x*	0.1880(6)	0.1824(8)	0.1821(8)	0.1812(8)	0.1868(6)
	y	0.3419(7)	0.339(1)	0.3412(9)	0.3407(9)	0.3426(7)
	z	0.1330(4)	0.1306(6)	0.1303(7)	0.1303(6)	0.1320(5)
	$100 \times U_{iso}$ / Å^2	0.5(1)	0.7(2)	0.6(2)	0.6(2)	0.9(2)
O5 (4g)	*x*	0.614(1)	0.611(1)	0.613(1)	0.613(1)	0.612(1)
	y	0.886(1)	0.880(1)	0.878(1)	0.878(1)	0.884(1)
	$100 \times U_{iso}$ / Å^2	1.1(2)	0.8(3)	1.0(3)	1.0(3)	0.7(3)

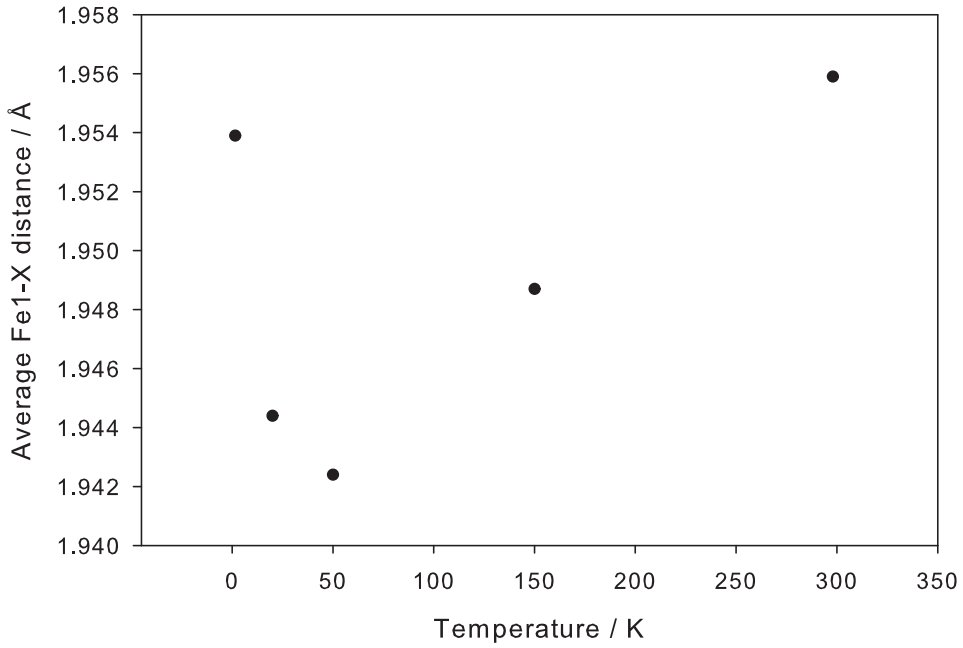

Figure 7.32 – Variation of average Fe1−X (X = S or O) bond length on cooling in Versiliaite B.

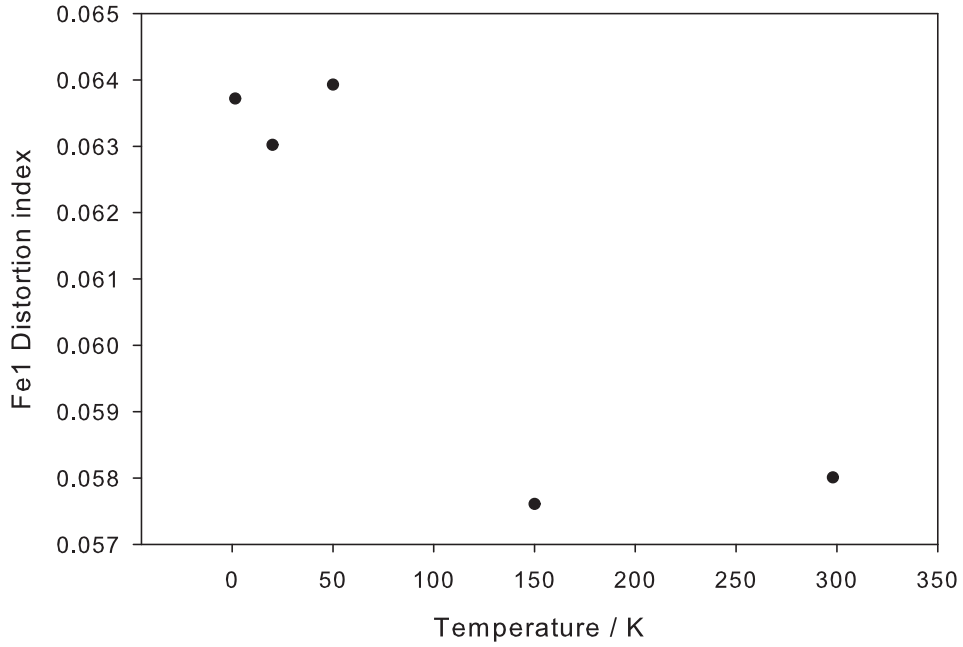

Figure 7.33 – Variation of Fe1 bond distortion index with temperature in Versiliaite B.

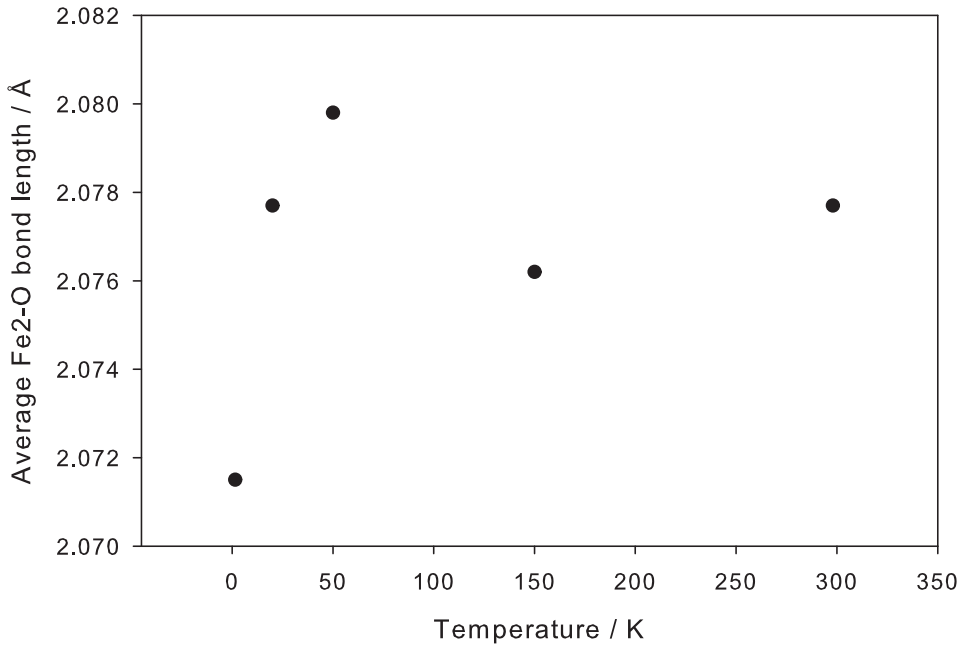

Figure 7.34 – Variation of average Fe2−O bond length with temperature in Versiliaite B.

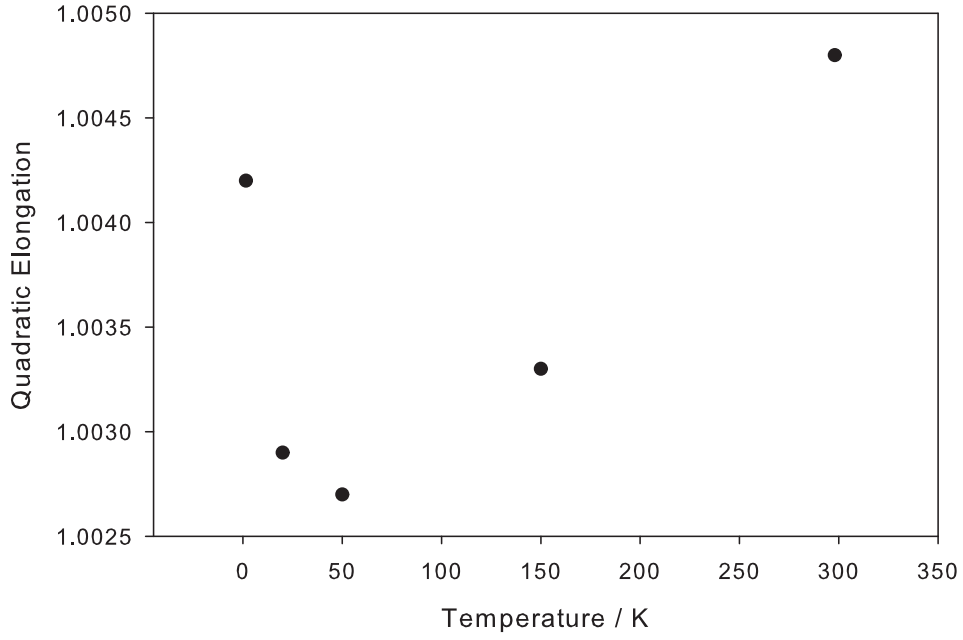

Figure 7.35 – Variation of Fe3 quadratic elongation with temperature in Versiliaite B.

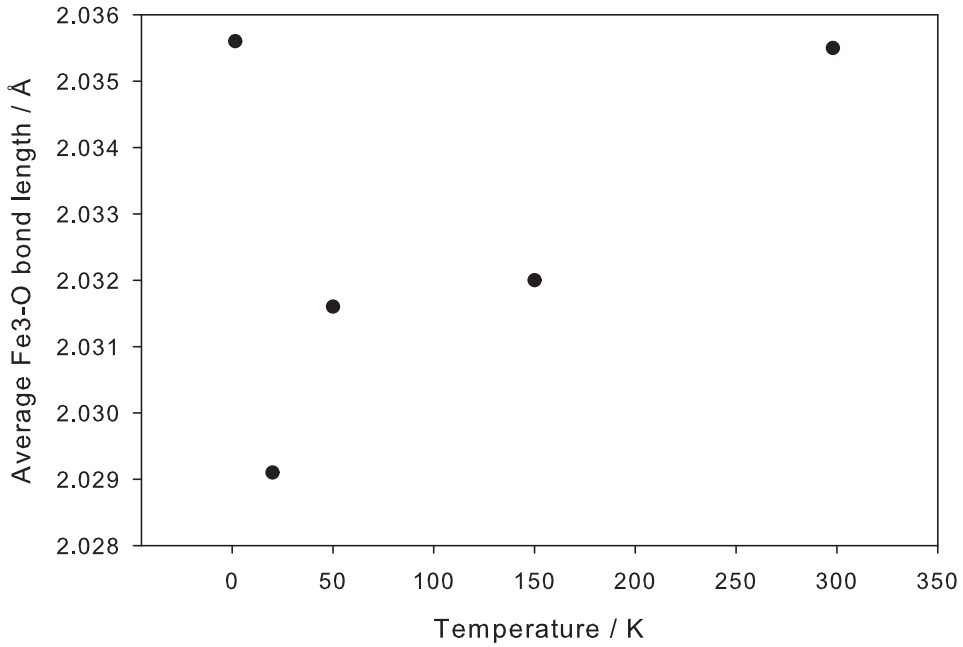

Figure 7.36 – Variation of average Fe3−O bond length with temperature in Versiliaite B.

ring feature of many of the studied parameters, however, is a step below 210 K, particularly in the Fe−O bond lengths for Fe1 and Fe3 (figures 7.38 and 7.40) and the corresponding distortion indices (7.39 and 7.41). This could suggest a structural change similar to that seen in Versiliaite, but at a higher temperature, again corresponding to a small deviation in the magnetic susceptibility measurements. The angular distortion around Fe1 and Fe3 shows no obvious trend with temperature, showing quite a wide scattering of points. Fe2, however, shows a gradual increase in bond angle variance on cooling, matched almost exactly by an increase in quadratic elongation (figure 7.43). This is accompanied by an almost linear decrease in distortion index on cooling such that as the sample is cooled, Fe2 becomes more angularly- and JT- distorted, but with less deviation between the Fe2−O bond lengths.

7.7 Thermal Analysis

Thermal analysis up to 1100 °C was performed on samples of Versiliaite A and B under flowing O_2 and N_2, and for Apuanite under O_2 only. Under N_2 (figure 7.44) Versiliaite B lost a significant proportion of its mass above *ca.* 600 °C, resulting in a residual mass of 41.5 % after

Table 7.21 – Refined unit cell and atomic parameters for Apuanite at variable temperatures.

		RT	210 K	170 K	150 K	130 K	120 K	100 K	80 K	40 K	5 K
a / Å		8.3825(3)	8.3821(4)	8.3817(4)	8.3816(4)	8.3816(3)	8.3811(4)	8.3814(4)	8.3812(4)	8.3804(3)	8.3806(3)
c / Å		17.9787(7)	17.9678(9)	17.9601(9)	17.9569(9)	17.9550(8)	17.9521(9)	17.9500(9)	17.9476(9)	17.9444(8)	17.9440(8)
Volume / Å^3		1263.3(1)	1262.4(2)	1261.8(2)	1261.5(2)	1261.4(1)	1261.0(2)	1261.0(2)	1260.7(2)	1260.2(1)	1260.3(1)
Fe1 (8h)	*x*	0.3129(5)	0.3141(6)	0.3114(6)	0.3115(5)	0.3117(4)	0.3123(5)	0.3122(5)	0.3117(5)	0.3115(5)	0.3113(5)
	y	0.3194(5)	0.3188(6)	0.3192(5)	0.3194(5)	0.3188(4)	0.3179(5)	0.3184(5)	0.3176(5)	0.3179(5)	0.3178(5)
	$100 \times U_{iso}$ / Å^2	1.08(8)	0.75(7)	0.55(7)	0.55(6)	0.48(5)	0.52(6)	0.40(6)	0.44(6)	0.32(5)	0.31(5)
Fe2 (4d)	$100 \times U_{iso}$ / Å^2	1.0(1)	0.7(1)	0.7(1)	0.5(1)	0.57(9)	0.44(9)	0.39(9)	0.41(9)	0.34(8)	0.33(8)
Fe3 (8f)	*z*	0.0838(2)	0.0840(3)	0.0835(3)	0.0839(3)	0.0837(3)	0.0836(3)	0.0837(3)	0.0835(3)	0.0836(3)	0.0836(3)
	$100 \times U_{iso}$ / Å^2	0.22(4)	0.14(5)	0.05(5)	0.04(4)	0.03(4)	0.04(4)	0.00(4)	0.01(4)	-0.03(4)	-0.03(4)
Sb (16i)	*x*	0.1696(4)	0.1696(5)	0.1698(6)	0.1689(5)	0.1693(5)	0.1687(5)	0.1688(5)	0.1686(5)	0.1686(5)	0.1686(5)
	y	0.1703(5)	0.1704(6)	0.1688(6)	0.1702(5)	0.1693(5)	0.1703(5)	0.1691(5)	0.1701(5)	0.1692(5)	0.1695(5)
	z	0.1652(3)	0.1643(3)	0.1653(4)	0.1649(3)	0.1651(3)	0.1649(3)	0.1649(4)	0.1647(3)	0.1652(3)	0.1651(3)
	$100 \times U_{iso}$ / Å^2	0.67(6)	0.50(7)	0.40(6)	0.37(6)	0.39(5)	0.34(6)	0.38(6)	0.27(5)	0.28(5)	0.29(5)
S (2a)	$100 \times U_{iso}$ / Å^2	4.5(4)	4.3(5)	3.0(5)	2.0(3)	2.5(3)	3.0(4)	2.3(4)	1.6(3)	1.8(3)	1.6(3)
O1 (16i)	*x*	0.9023(4)	0.9023(5)	0.9024(5)	0.9030(4)	0.9032(4)	0.9031(4)	0.9034(4)	0.9029(5)	0.9028(4)	0.9031(4)
	y	0.3639(4)	0.3636(4)	0.3609(4)	0.3615(4)	0.3612(4)	0.3614(4)	0.3609(4)	0.3611(4)	0.3609(4)	0.3605(4)
	z	0.1653(3)	0.1646(4)	0.1653(4)	0.1649(4)	0.1652(3)	0.1650(4)	0.1654(4)	0.1648(4)	0.1652(3)	0.1649(3)
	$100 \times U_{iso}$ / Å^2	0.71(6)	0.53(6)	0.37(6)	0.44(6)	0.44(5)	0.42(6)	0.36(5)	0.28(5)	0.35(5)	0.34(5)
O2 (8h)	*x*	0.8884(8)	0.8900(9)	0.8901(9)	0.8896(8)	0.8887(7)	0.8883(8)	0.8883(8)	0.8895(8)	0.8883(7)	0.8886(7)
	y	0.3893(8)	0.3874(8)	0.3874(9)	0.3875(8)	0.3874(7)	0.3876(8)	0.3882(8)	0.3864(8)	0.3876(7)	0.3872(7)
	$100 \times U_{iso}$ / Å^2	1.1(1)	0.8(1)	0.6(1)	0.5(1)	0.44(8)	0.6(1)	0.42(9)	0.6(1)	0.42(8)	0.40(8)
O3 (16i)	*x*	0.8147(4)	0.8157(5)	0.8145(5)	0.8145(5)	0.8149(4)	0.8149(5)	0.8151(5)	0.8153(5)	0.8153(4)	0.8152(4)
	y	0.6566(4)	0.6568(5)	0.6570(5)	0.6563(4)	0.6568(4)	0.6573(5)	0.6575(5)	0.6575(5)	0.6574(4)	0.6571(4)
	z	0.0889(2)	0.0881(3)	0.0877(3)	0.0877(3)	0.0878(2)	0.0877(3)	0.0880(3)	0.0878(3)	0.0876(3)	0.0876(3)
	$100 \times U_{iso}$ / Å^2	0.88(8)	0.67(8)	0.49(8)	0.54(7)	0.50(6)	0.51(7)	0.52(8)	0.46(7)	0.44(6)	0.44(6)
O4 (8g)	*x*	0.8214(5)	0.8214(6)	0.8219(6)	0.8223(5)	0.8223(5)	0.8224(5)	0.8228(5)	0.8226(6)	0.8226(5)	0.8227(5)
	$100 \times U_{iso}$ / Å^2	0.41(8)	0.4(1)	0.19(9)	0.21(8)	0.18(7)	0.17(8)	0.16(8)	0.25(9)	0.07(7)	0.10(7)

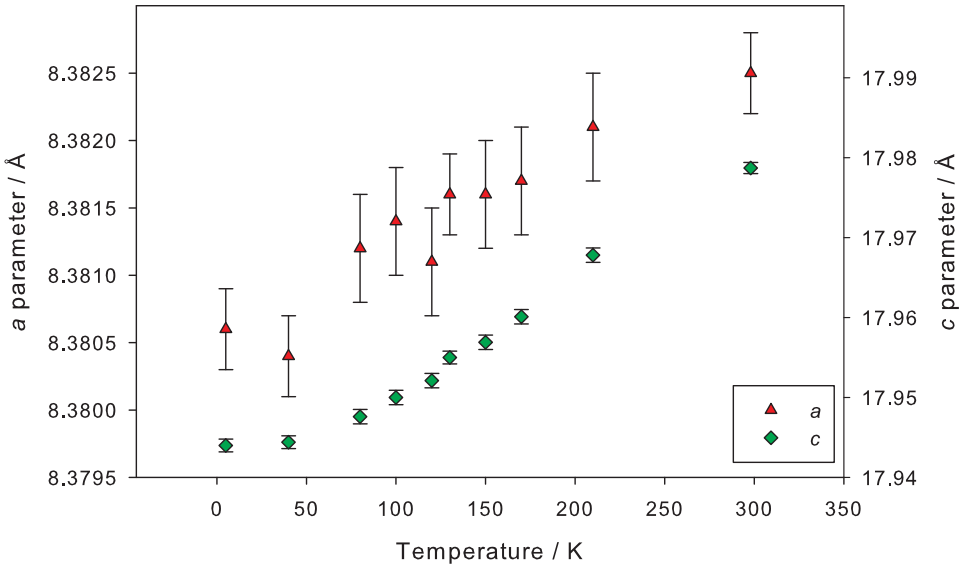

Figure 7.37 – Variation of unit cell parameters with temperature in Apuanite.

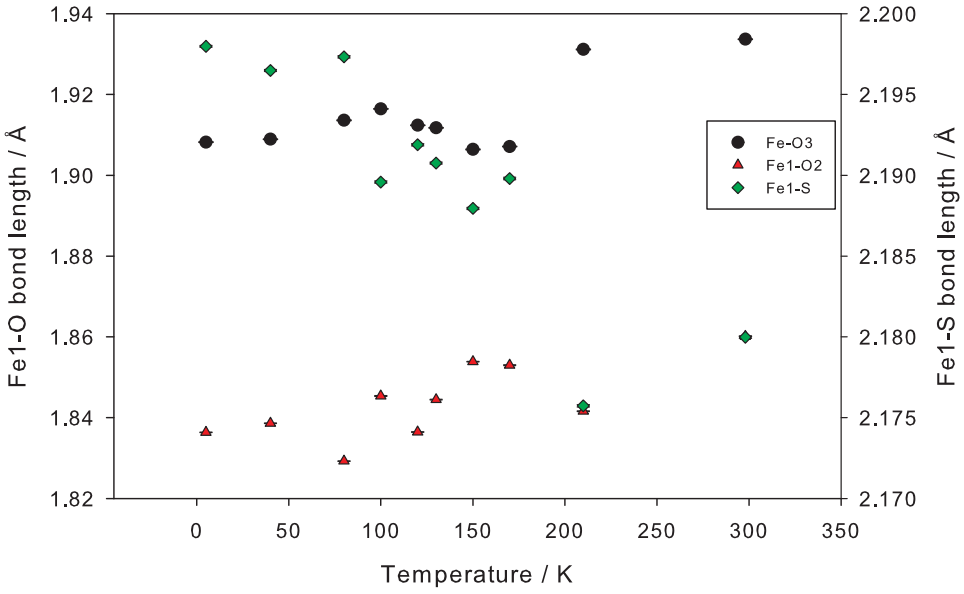

Figure 7.38 – Variation of Fe1−O bond lengths with temperature in Apuanite.

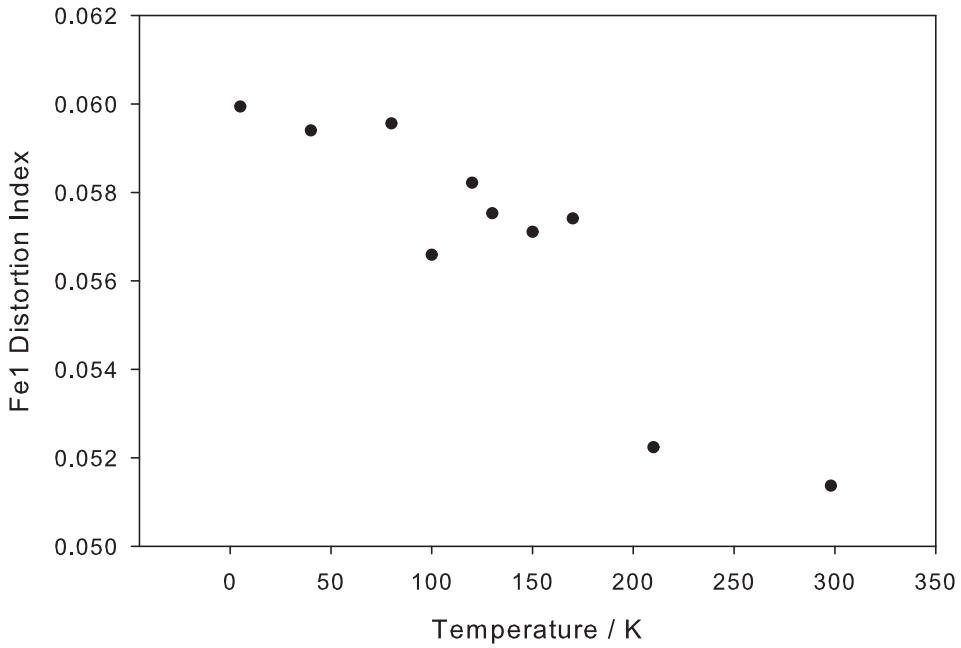

Figure 7.39 – Variation of Fe1 distortion index with temperature in Apuanite.

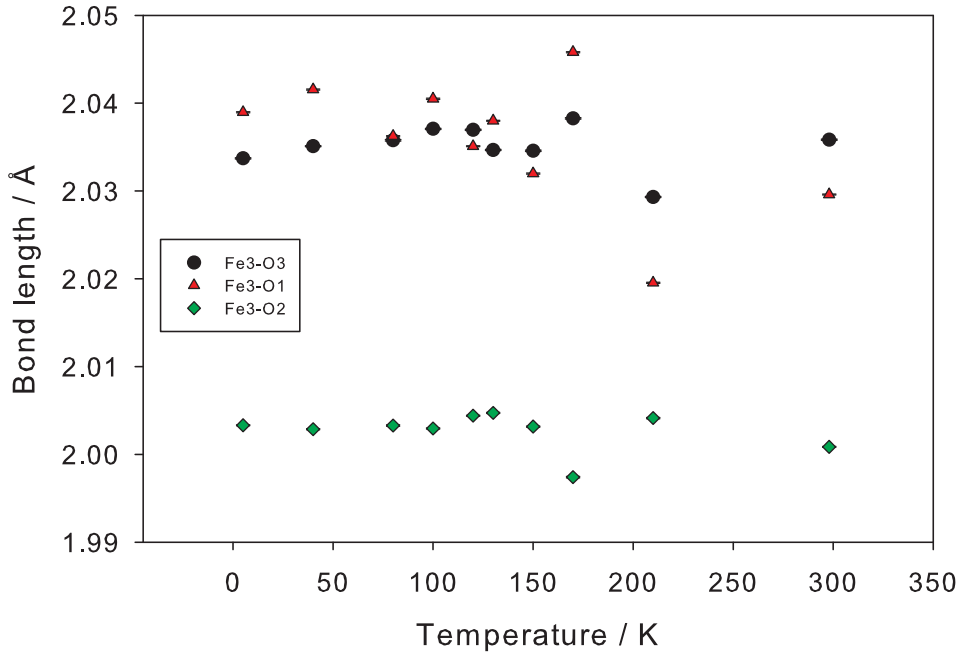

Figure 7.40 – Variation of Fe3−O bond lengths with temperature in Apuanite.

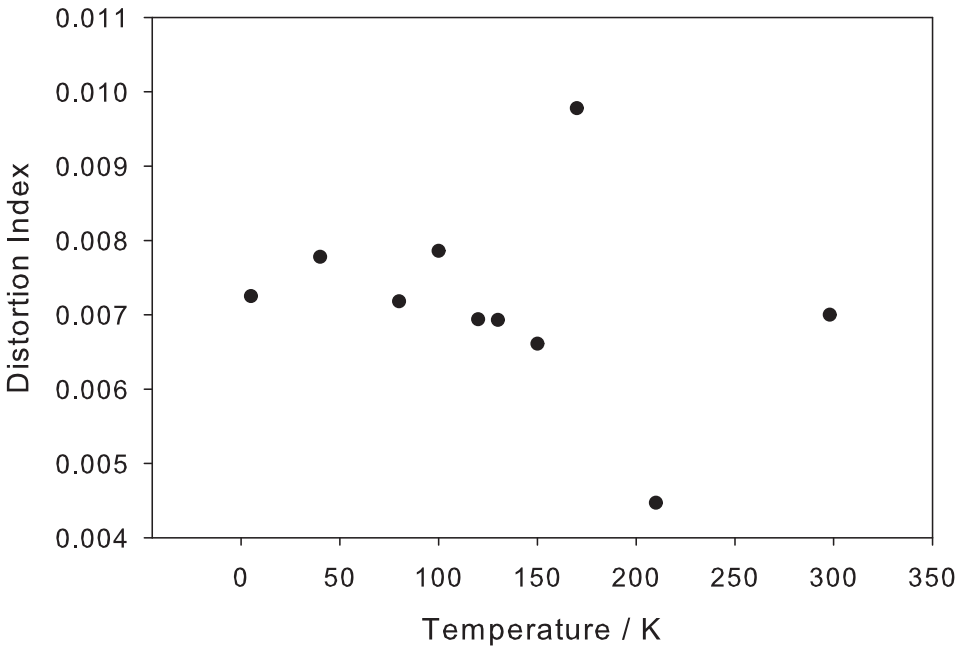

Figure 7.41 – Variation of Fe3 distortion index with temperature in Apuanite.

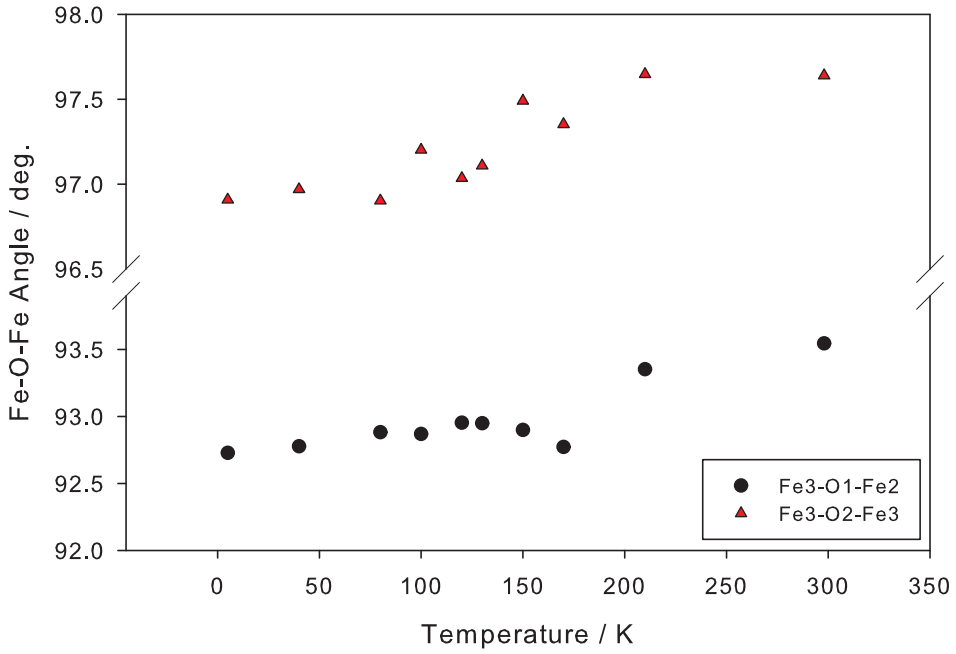

Figure 7.42 – Variation of Fe−O−Fe bond angles with temperature in Apuanite.

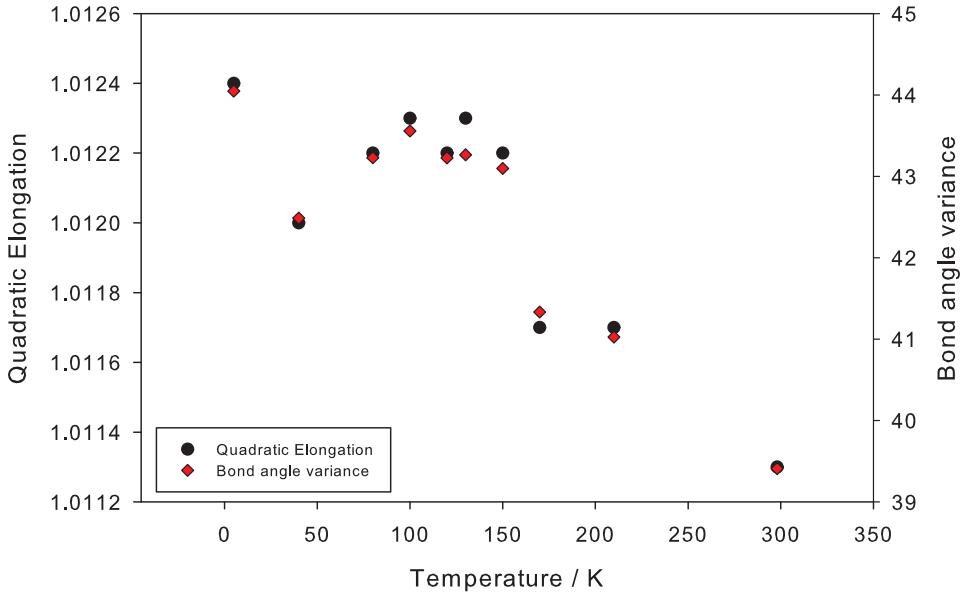

Figure 7.43 – Variation of quadratic elongation and bond angle variance for Fe2 in Apuanite.

cooling. From post-heating XRPD the resulting product was determined as Fe_3O_4, corresponding to a loss of "$Sb_{12}O_{16}S_2$" on heating. Examining the mass change, however, formation of pure Fe_3O_4 would predict a final mass of 34.2 %, lower than observed. This difference might suggest that a small amount of residual antimony remains in the sample, for some reason not observed from XRPD. The corresponding DTA curve shows three small endothermic peaks on heating (the large curve at low temperature is due to an incorrect instrumental correction) accounting for the broad change in mass, indicating that the loss occurs as multiple steps, rather than a single transition.

Under oxygen, the Versiliaite samples show more interesting behaviour; the mass increases to a maximum (109 %) at 680 °C or 620 °C for Versiliaite A and B respectively, before dropping to 106.5 % at higher temperatures. On cooling, the mass then remains almost constant. XRPD of the resulting material found that it had transformed to $FeSbO_4$, suggesting an ideal mass change of +7.1 %. This value is similar to that observed, any slight deviations being attributed to non-stoichiometry in the final product. The presence of multiple peaks in the DTA signal (particularly for sample B) would support the necessary sulfur-loss and oxidation steps required to give the final $FeSbO_4$; the maximum mass corresponding to small DTA peaks at $\simeq$ 620 °C

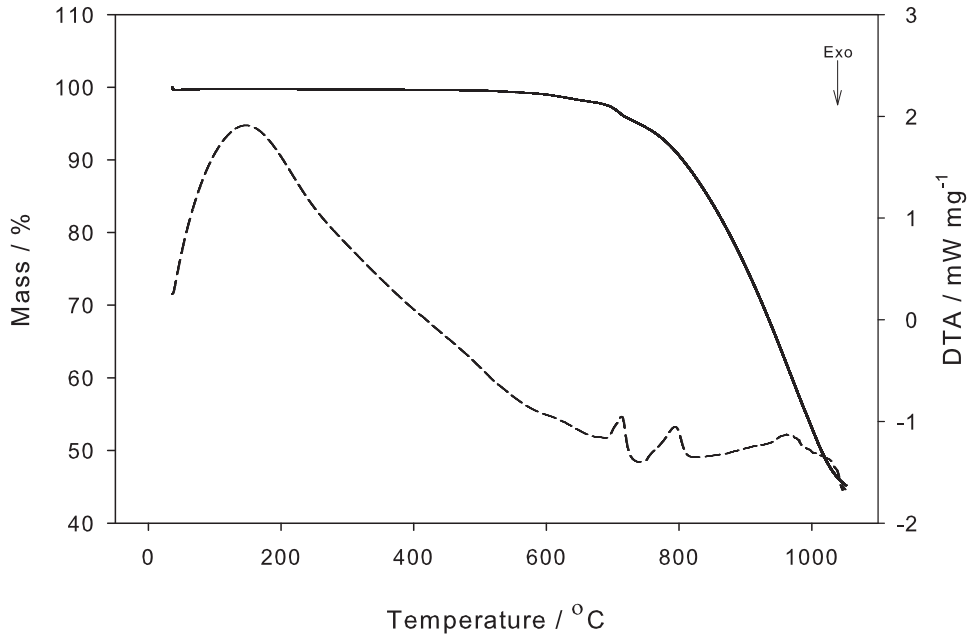

Figure 7.44 – TGA of Versiliaite B on heating in N_2 atmosphere, showing TG (solid line) and DTA (dashed line).

would suggest that oxidation occurs before sulfur loss. The cause of the different mass changes and curve shapes for the two samples is unclear, however, it could be related to different particle morphologies, or the different degrees of structural disorder.

Interestingly, both Versiliaite samples show a shoulder to the main peak, approximately in the 400–500 °C temperature range. This is similar to behaviour observed in $FeSb_2O_4$ and related compounds [13,14] where the structures show uptake of oxygen into the structural channels, without a significant change in crystal structure. For this reason, a second sample of Versiliaite B was heated under oxygen to 415°C and maintained for 15 minutes, before cooling. The XRPD pattern of this substance is shown in figure 7.46; many of the peak positions have obviously shifted to lower 2θ (indicating an expansion of the unit cell, particularly in the *ab* plane) but the main structural character is maintained. The peaks do show a significant increase in broadening however, preventing a full indexing of the structure. An attempt to anneal a larger sample in oxygen resulted in a similarly broad diffraction pattern; further work would be required to investigate if this oxygen uptake can result in a highly crystalline phase suitable for further analysis.

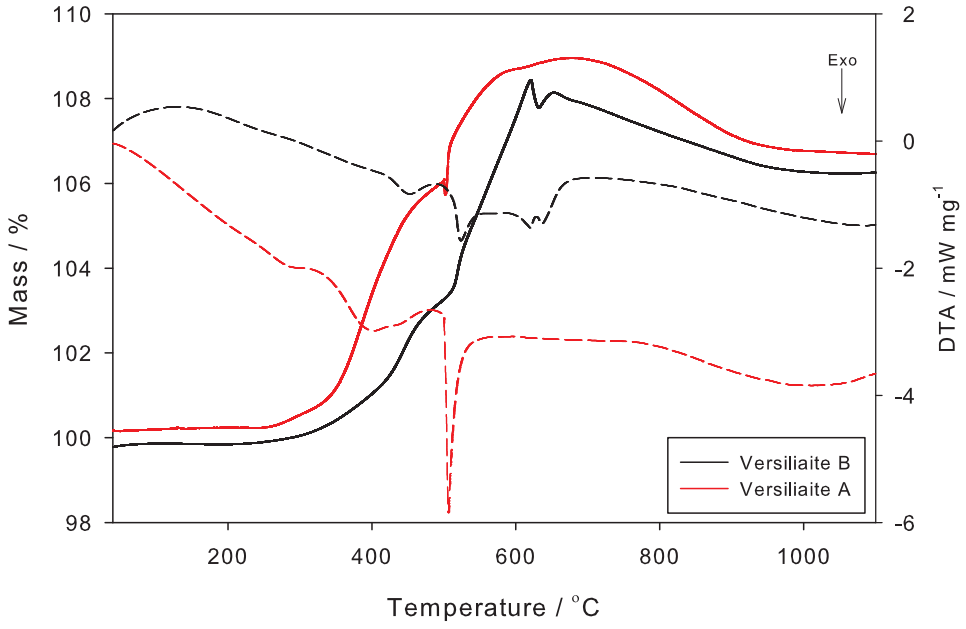

Figure 7.45 – TGA of Versiliaite on heating in O_2 atmosphere, showing TG (solid lines) and DTA (dashed lines) response.

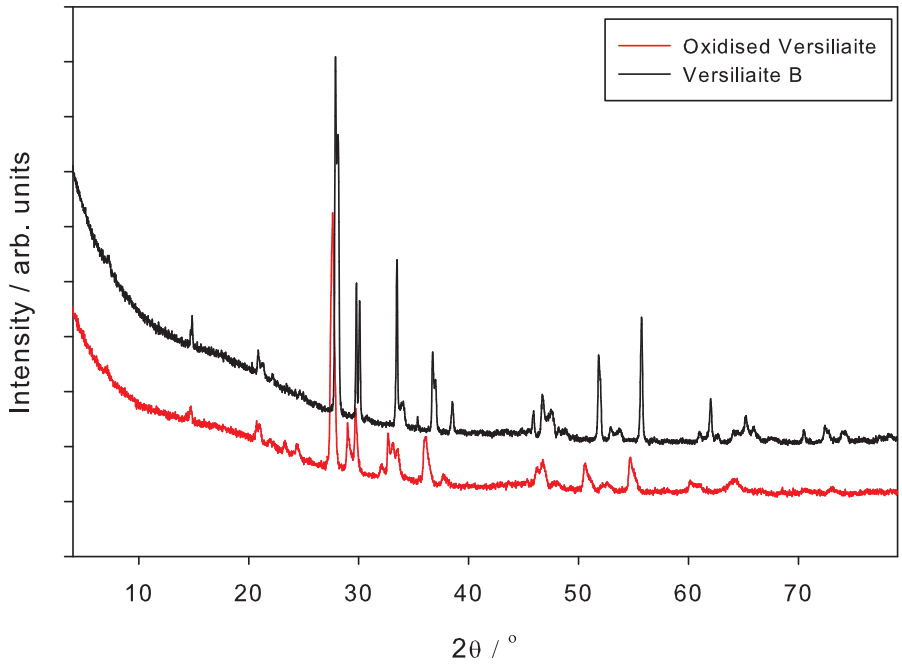

Figure 7.46 – XRPD patterns of Versiliaite B before (black) and after (red) TGA heating to 415°C in O_2.

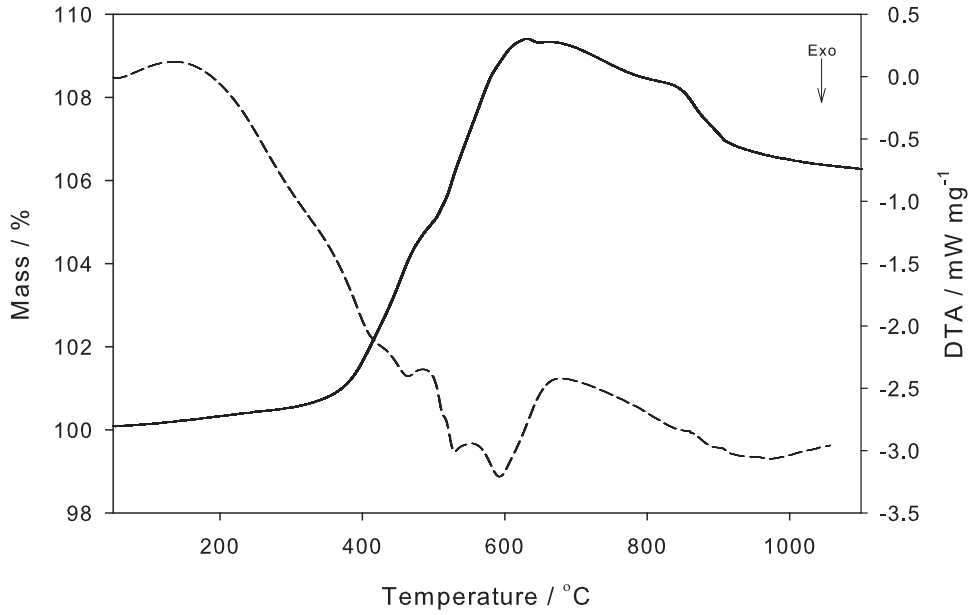

Figure 7.47 – TGA of Apuanite on heating in O_2 atmosphere, showing TG (solid lines) and DTA (dashed lines).

Investigation of the behaviour of Apuanite under heating in O_2 revealed a similar behaviour to Versiliaite (figure 7.47). In Apuanite, however, a mass-loss step is observed at 800 °C, not seen as clearly in the Versiliaite samples (although mass losses do occur). In addition, the DTA signal shows two exothermic peaks between 500 and 600 °C, while Versiliaite only shows one. The mass changes in this region look very similar, however. From XRPD, Apuanite forms predominantly $FeSbO_4$ after heating, as seen for Versiliaite, but with a small proportion of Fe_2O_3. This is consistent with the excess of Fe relative to Sb in Apuanite, which is oxidised to Fe^{3+}. This additional oxidation step explains the additional DTA peak.

7.8 Impedance Spectroscopy

Samples for impedance spectroscopy were prepared by pressing pellets of 8 mm diameter of powdered sample, and then heating (in evacuated quartz ampoules) at 500 °C. It proved impossible to create a sintered pellet of Apuanite (the pellets broke up significantly upon heating) however a suitable pellet was obtained for Versiliaite A. This pellet had a density of 74 % of the theoretical maximum, and a thickness of 1.255 mm. Impedance spectra were collected at

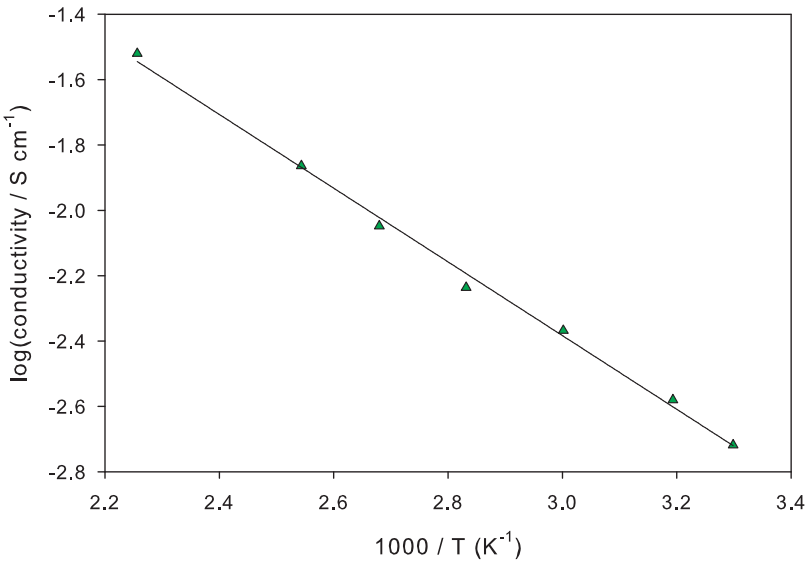

Figure 7.48 – Total conductivity data for Versiliaite A.

a range of temperatures between 170 °C and 30 °C, the maximum temperature was chosen to avoid any possible decomposition of the material. The spectra obtained showed a single semi-circle, preventing separation of bulk and grain boundary contributions to the conductivity; for this reason total conductivity values are reported. The variation of conductivity with temperature is shown in figure 7.48, as well as the linear fit to an Arrhenius relationship (2.13). From this fit, the thermal activation energy E_a is obtained as 21.6 kJ mol^{-1}, giving a thermal band gap e_g of 0.448 eV.

7.9 Conclusions

In this chapter, successful synthesis of Versiliaite ($Fe_{12}Sb_{12}O_{32}S_2$) and Apuanite ($Fe_{20}Sb_{16}O_{48}S_4$) phases have been reported, with structures similar to previous mineral data. Structural differences are observed between different samples; these can largely be attributed to the formation of sulfur-depleted or sulfur-rich regions within the material, giving rise to a range of properties. From NPD diffraction results, approximately 20 % of Fe−S−Fe links in the Versiliaite 'A' sample occur perpendicular to the idealised nuclear structure. BVS estimates suggest a charge-ordering of Fe cations as seen for the mineral sample (Fe1, Fe3 = 3+, Fe2 = 2+) although this is

highly correlated with the refined Fe−S−Fe occupancy. For Apuanite, the sulfur atoms exhibit a large anisotropic thermal displacment (perpendicular to the Fe−S−Fe link) at RT, but it is unclear whether this is a static or dynamic effect.

Mössbauer spectroscopy revealed distinct Fe^{3+} and Fe^{2+} environments in Versiliaite and Apuanite, negating a possible charge-delocalised structure. In both Versiliaite samples, multiple Fe^{2+} sites are observed, rationalised due to the possible arrangements of Fe^{3+} and Fe^{2+} within the disordered structures. Versiliaite B shows an exaggerated proportion of tetrahedral Fe^{3+}, the cause of which is unclear. Apuanite shows the iron sites expected for the ideal model, but with an excess of $^{VI}Fe^{3+}$; if the peaks assigned to an $\alpha-Fe_2O_3$ impurity are included, the ratio is closer to the model.

On cooling, Versiliaite and Apuanite both show magnetic ordering below *ca.* 170 K and 190 K, respectively. NPD revealed a common $k = (\frac{1}{2}, \frac{1}{2}, 0)$ magnetic propagation vector, and a magnetic structure described by FM-aligned octahedral chains, oriented in the *ab* plane. Data suggest a FM alignment between adjacent chains in the $[110]$ (nuclear) direction and AFM alignment in the $[\bar{1}10]$ direction in both Versiliaite and Apuanite, however, a modulated structure along both directions is not ruled out. The tetrahedral Fe sites show a frustrated 90° interaction, with individual Fe−S−Fe links aligned strongly AFM. The observed magnetic arrangement may give rise to an itinerant double-exchange mechanism along the octahedral chains, however further techniques are required to determine this. The magnetic transitions observed show related nuclear geometry changes, particularly for the Fe1 site.

Thermal analysis reveals oxidation to $FeSbO_4$ in both Apuanite and Versiliaite between 600 °C and 700 °C, but with an additional Fe_2O_3 product in Apuanite (corresponding to greater Fe content). All samples show an increase in mass before the main transition, while largely retaining the parent structure; this could indicate uptake of oxygen into the structure as seen for $FeSb_2O_4$,[13] however crystallinity is reduced. Impedance spectroscopy for Versiliaite find a relatively small bandgap semiconductor ($e_g = 0.45$ eV).

References

[1] M. Mellini, *American Mineralogist*, 1981, **66**, 1073–1079.

[2] S. M. Marcello Mellini and P. Orlandi, *American Mineralogist*, 1979, **64**, 1230–1234.

[3] M. Mellini and S. Merlino, *American Mineralogist*, 1979, **64**, 1235–1242.

[4] R. Bayliss, F. J. Berry, A. Bowden, C. Greaves and M. F. Thomas, *Journal of Physics: Conference Series*, 2010, **217**, 012049.

[5] R. Bayliss, *MRes Thesis*, MSc thesis, University of Birmingham, Chemistry, 2008.

[6] A. C. Larson and R. B. von Dreele, *Los Alamos National Laboratory Report*, 1994, **LAUR 86-748**, 1.

[7] B. H. Toby, *Journal of Applied Crystallography*, 2001, **34**, 210–213.

[8] V. F. Sears, *Neutron News*, 1992, **3**, 26–37.

[9] R. D. Shannon, *Acta Crystallographica Section A*, 1976, **32**, 751–767.

[10] I. D. Brown and D. Altermatt, *Acta Crystallographica Section B Structural Crystallography and Crystal Chemistry*, 1985, **41**, 244–247.

[11] M. J. Whitaker, R. D. Bayliss, F. J. Berry and C. Greaves, *Journal of Materials Chemistry*, 2011, **21**, 14523–14529.

[12] E. J. W. Verwey, *Nature*, 1939, **144**, 327–328.

[13] M. J. Whitaker, *Synthesis and Characterisation of Chemically Modified Schafarzikite and Pyrochlore minerals*, PhD thesis, School of Chemistry, The University of Birmingham, 2013.

[14] B. P. de Laune, *Low Dimensional Sytructures of some Mixed Metal Oxides Containing Antimony: Synthesis and Characterisation*, PhD thesis, School of Chemistry, The University of Birmingham, 2013.

CHAPTER 8
CONCLUSIONS AND FURTHER WORK

The work presented and discussed here concerns both chemical and theoretical study of functional materials related to Schafarzikite ($FeSb_2O_4$). A wide range of MX_2O_4 compositions have been studied using DFT calculations, particularly with regards to magnetic properties, and behaviour at high pressure. $CuAs_2O_4$ has been synthesised and magnetically characterised for the first time, as have a range of $Mn_xCo_{1-x}Sb_2O_4$ compositions. Finally, Versiliaite ($Fe_{12}Sb_{12}O_{32}S_2$) and Apuanite ($Fe_{20}Sb_{16}O_{48}S_4$) phases have been successfully synthesised for the first time, and characterised magnetically at a range of temperatures.

8.1 MX_2O_4 Density Functional Theory

Chapter 4 reported the DFT study of magnetism in a range of MSb_2O_4 compounds using the PBE functional and planewave/pseudopotential methods. The results agree quite closely with experimental data, although DFT predicts an incorrect (C-type) magnetic groundstate for $FeSb_2O_4$ (actually A-type). An extension to this work would be investigation of the need for SOC and non-collinear magnetism, as well as investigation of other exchange-correlation functionals, including hybrid functional methods. First principles calculation of a Hubbard U parameter for this system would also be desirable, for use in future studies.

The results also showed potential for changes in magnetic groundstate for $MnSb_2O_4$ and $NiSb_2O_4$ under applied pressure; this could prove an interesting experimental study, given the structural changes already known to occur in $FeSb_2O_4$ and Pb_3O_4 due to the effect of the anti-

mony lone-pairs.[1,2]

Calculating magnetic (Heisenberg) coupling parameters between cation sites reveal that generally the J_1 (intra-chain) interaction is strongest, as expected. The J_2 (intra-plane, inter-chain) and J_3 (inter-plane, inter-chain) couplings were found to be non-negligible, however, with J_3 generally larger. This has been attributed to competition between different J_2 pathways. The computed coupling constants are characteristic of the magnetic groundstate. An extension to this study could involve calculation of non-isotropic coupling parameters, and also comparison of the results with experimental measurement of the exchange interactions, such as with inelastic neutron scattering.

8.2 $CuAs_2O_4$

Chapter 5 reported the prediction of ferromagnetic ordering and subsequent synthesis and magnetic characterisation of $CuAs_2O_4$. This compound is the first example of a FM Schafarzikite-like structure, ordering at 8 K. Investigation of the magnetic behaviour found an ordered moment (from NPD) of 0.96(4) μ_B, with an ordering exponent $\beta = 0.13(5)$, characteristic of a low-dimensional system.

Further investigation of the theoretical prediction found anomalously large magnetic moments connected with the default pseudopotential employed; changing the atomic description resulted in a change of magnetic groundstate (to G-type). Attempts to include a Hubbard U parameter with the new pseudopotential proved unsuccessful. Further work could involve thorough testing of the pseudopotential used, or even adopting the LAPW approach. The magnetic groundstate change should be investigated for the cause of the variation.

Although some effort was applied to synthesising a mixed-valent copper variant, this proved unsuccessful. Success in this approach could lead to very interesting low-dimensional properties, and is therefore an exciting avenue of exploration.

8.3 $Mn_xCo_{1-x}Sb_2O_4$

In this chapter, the solid solution $Mn_xCo_{1-x}Sb_2O_4$ was successfully synthesised and characterised for a wide range of x. The lattice parameters are found to change almost linearly with x, although the atomic structure shows less even variation, particularly for Sb. This is attributed to a fundamental change from $CoSb_2O_4$-like to $MnSb_2O_4$-like across the range due to a critical unit cell size occurring at $x = 0.5$. No evidence is observed for a mixed-phase product, however anisotropic peak strain is observed due to formation of Co- and Mn-rich regions.

On cooling, $Mn_{0.2}Co_{0.8}Sb_2O_4$ shows anomalous behaviour of the M cation below *ca.* 40 K, suggesting a change in octahedral coordination. The structural distortions do not occur in a concerted fashion, however, it has not been possible to fully rationalise the nature of the transition. Further work (particularly local structure methods) could help to elucidate the cause of the observed anomaly.

Magnetically, all compositions show long-range order at 5 K, although the magnetic moments are reduced from ideal values. The magnetic susceptibility data show a reduction in definition with x, but data suggest multiple ordering transitions. NPD show a change from C_z to A_x-type order on increasing x, with a gradual rotation of the atomic spins into the *ab*-plane. Study of further samples over a range of temperatures would help to elucidate the exact nature of the ordering, as would single crystal neutron diffraction.

8.4 Versiliaite and Apuanite

Chapter 7 reported the first successful synthesis and magnetic characterisation of Versiliaite ($Fe_{12}Sb_{12}O_{32}S_2$) and Apuanite ($Fe_{20}Sb_{16}O_{48}S_4$). Samples showed evidence of disorder of the Fe−S−Fe cross-channel links, resulting in slightly anomalous structural data. Similar disorder has been reported as common in mineral samples of this type, however.[3] Although the synthetic procedures used in this work resulted in disordered structures, it is possible that other techniques might allow greater control of exact stoichiometry. Mössbauer spectroscopy of the materials found distinct Fe^{2+} and Fe^{3+} environments, although the ratios of the different environments are

not as expected, particularly for Versiliaite B and Apuanite. The cause of this is undetermined, and is currently undergoing a more complete Mössbauer study.

Magnetically, the compounds both show broad transitions in magnetic susceptiblity measurements, but analysis is hampered by the dominant contribution from a small Fe_3O_4 impurity. NPD data show both compounds to order with a magnetic propagation vector $k = (\frac{1}{2}, \frac{1}{2}, 0)$, described by FM alignment of spins within each octahedral chain, oriented in the *ab* plane. Adjacent chains show a combination of AFM and FM alignment in different directions (giving an overall antiferromagnet) although the exact modulation is difficult to determine from NPD. A single-crystal study would be required to fully determine the magnetic ordering. The tetrahedral Fe sites show strong AFM alignment between Fe−S−Fe groups, with adjacent groups aligned at 90° to one another. These moments are also aligned in the *ab* plane, although show reduced moments to those expected.

Another aspect of this project has been the synthesis of cation-substituted Apuanite and Versiliaite samples, although these are not reported here. A range of compositions have been synthesised to varying degrees of success, but a lot of further work remains to be explored. Given the high flexibility of the Schafarzikite structure to atomic substitution, it is not unreasonable that similar capabilities could exist in these closely related compounds.

References

[1] B. Hinrichsen, R. E. Dinnebier, P. Rajiv, M. Hanfland, A. Grzechnik and M. Jansen, *Journal of Physics: Condensed Matter*, 2006, **18**, S1021–S1037.

[2] R. E. Dinnebier, S. Carlson, M. Hanfland and M. Jansen, *American Mineralogist*, 2003, **88**, 996–1002.

[3] M. Mellini, *American Mineralogist*, 1981, **66**, 1073–1079.

Appendices

APPENDIX A
COMPUTATIONAL APPENDIX

A.1 CASTEP Input Files

The following extracts represent the CASTEP input files generating unusually high Cu^{2+} magnetic moments in $CuAs_2O_4$.

Cell input file

```
%BLOCK lattice_cart
   ANG
      8.23312583252102        -0.219237717656228E-16    0.165147199239304E-16
      0.482209788123090E-15    8.23312583252102         0.165147199239304E-16
      0.337706338849611E-15    0.337706338849611E-15    5.74820259734876
%ENDBLOCK lattice_cart

%BLOCK positions_frac
 O   0.6824132563   0.1824132563   0.2500000000
 O   0.8177023309   0.6822976690   0.7500000000
 O   0.3175867436   0.8175867436   0.2500000000
 O   0.1822976690   0.3177023309   0.7500000000
 O   0.3177023309   0.8177023309   0.7500000000
 O   0.1824132563   0.3175867436   0.2500000000
 O   0.6822976690   0.1822976690   0.7500000000
 O   0.8175867436   0.6824132563   0.2500000000
 O   0.1075255154   0.6265892892  -0.0000135237
 O   0.3734107107   0.1075255154   0.5000135237
 O   0.8924744845   0.3734107107  -0.0000135237
 O   0.6265892892   0.8924744845   0.5000135237
 O   0.6075255154   0.8734107107  -0.0000135237
 O   0.3924744845   0.1265892892  -0.0000135237
 O   0.1265892892   0.6075255154   0.5000135237
 O   0.8734107107   0.3924744845   0.5000135237          (A)     (C)     (G)     (FM)
 Cu  0.0000000000   0.5000000000   0.2500000000   SPIN= -1.00   -1.00   -1.00   1.00
 Cu  0.5000000000   0.0000000000   0.7500000000   SPIN=  1.00    1.00   -1.00   1.00
 Cu  0.0000000000   0.5000000000   0.7500000000   SPIN=  1.00   -1.00    1.00   1.00
 Cu  0.5000000000   0.0000000000   0.2500000000   SPIN= -1.00    1.00    1.00   1.00
 As  0.1802515194   0.1690816200  -0.0000089841
 As  0.8309183799   0.1802515194   0.5000089841
 As  0.8197484805   0.8309183799  -0.0000089841
 As  0.1690816200   0.8197484805   0.5000089841
 As  0.6802515194   0.3309183799  -0.0000089841
 As  0.3197484805   0.6690816200  -0.0000089841
 As  0.6690816200   0.6802515194   0.5000089841
```

```
 As  0.3309183799   0.3197484805   0.5000089841
%ENDBLOCK positions_frac

FIX_COM : false

%BLOCK species_pot
   O       2|1.3|16.537|18.375|20.212|20UU:21UU(qc=7.5)[]
   Cu      3|2|2|1.5|10|11.7|12.8|40U=-0.22U=+0.2:41U=-0.5U=+0.25:32U=-0.36U=+0.075[]
   As      2|1.6|1.6|0.9|6|7.3|9.9|40U=-0.54U=+0.5:41U=-0.195U=+0.25[]
%ENDBLOCK species_pot

kpoint_mp_grid :    3   3   4

supercell_kpoint_mp_grid :    3   3   4

symmetry_generate
```

Parameter input file

```
task = geometryoptimisation

xc_functional = pbe

geom_max_iter = 70

cut_off_energy = 1050 eV

nextra_bands = 60                   <= A
nextra_bands = 35                   <= C, FM
nextra_bands = 50                   <= G

spin_fix = 350                      <= A, C, G
spin_fix = 10 (default)             <= FM

geom_spin_fix = 50                  <= A, G
geom_spin_fix = 20                  <= C
geom_spin_fix = 0 (default)         <= FM

spin = 4.0                          <= FM

fixed_npw = false

max_scf_cycles = 500

fix_occupancy = false
spin_polarised = true

calculate_stress = true

mix_charge_amp = 0.6
mix_spin_amp = 1.5

opt_strategy_bias = +3
page_wvfns = 0
num_dump_cycles = 0
```

A.2 CASTEP Pseudopotential Definitions

For $CuAs_2O_4$ the default, on-the-fly pseudopotential definitions used within CASTEP were:

```
O 2|1.0|1.3|0.7|13|16|18|20:21(qc=7)
Cu 3|2.0|2.0|1.5|11|13|14|40:41:32(qc=6,q0=5)
As 2|1.6|1.6|1.3|7|8|11|40:41
```

all generated within the Perdew, Burke and Ernzerhof (PBE) scheme. The modified definitions (section 5.3.2) used were:

```
O 2|1.3|16.537|18.375|20.212|20UU:21UU(qc=7.5)[]
Cu 3|2|2|1.5|10|11.7|12.8|40U=-0.22U=+0.2:41U=-0.5U=+0.25:32U=-0.36U=+0.075[]
As 2|1.6|1.6|0.9|6|7.3|9.9|40U=-0.54U=+0.5:41U=-0.195U=+0.25[]
```

A.3 Additional Bandstructure Plots

A.3.1 $MnSb_2O_4$

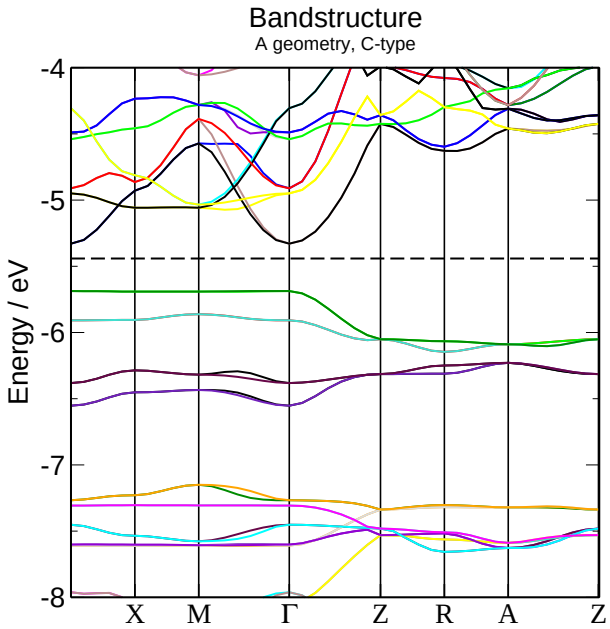

Figure A.1 – Section of bandstructure around E_f in C-type $MnSb_2O_4$.

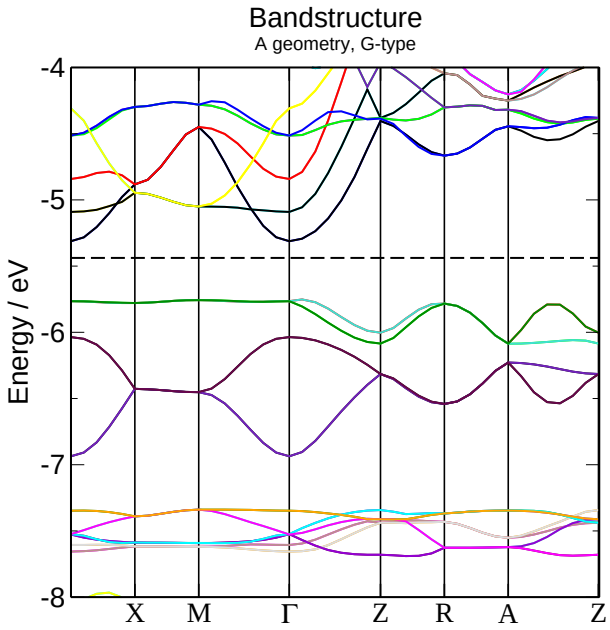

Figure A.2 – Section of bandstructure around E_f in G-type $MnSb_2O_4$.

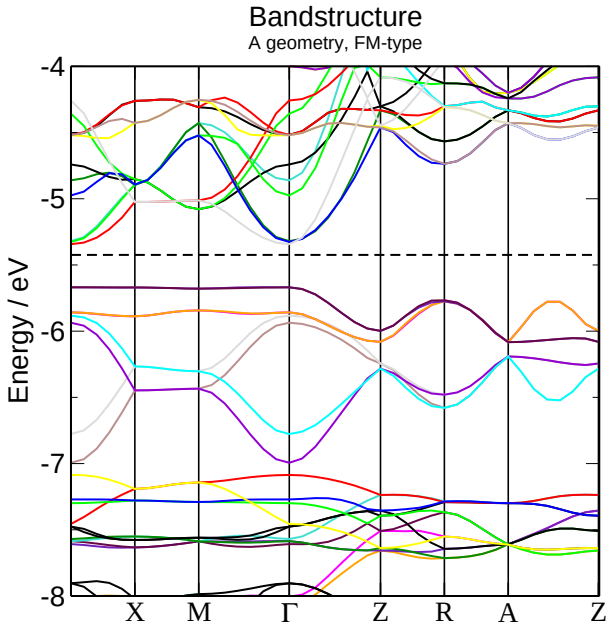

Figure A.3 – Section of bandstructure around E_f in FM-type $MnSb_2O_4$.

APPENDIX B
MAGNETIC ANALYSIS

B.1 Irreducible Representations

The following tables give details of the basis vectors (BVs) for irreducible representations (IRs) that can be used describe magnetic ordering for the compounds reported in this work, to give an indication of the magnetic freedom allowed within a chosen representation. Data were produced using the SARAh software[1] and use the labelling convention of Kovalev.[2]

B.1.1 $FeSb_2O_4$

The decomposition into IRs is based on a $k = (0,0,0)$ magnetic propagation vector, the $P4_2/mbc$ parent (*i.e.* non-magnetic) structure and the magnetic ion at the 4*d* Wyckoff position. Atom positions are 1: (0, 0.5, 0.25), 2:(0.5, 0, 0.75), 3: (0, 0.5, 0.75), 4: (0.5, 0, 0.25).

Table B.1 – IR decomposition for Schafarzikite ($P4_2/mbc$) with $k = (0, 0, 0)$.

IR	Basis Vector	Atom	BV components		
			$m_{\|a}$	$m_{\|b}$	$m_{\|c}$
Γ_3	ψ_1	1	0	0	4
		2	0	0	4
		3	0	0	4
		4	0	0	4
Γ_4	ψ_2	1	0	0	4
		2	0	0	4
		3	0	0	-4
		4	0	0	-4

IR	Basis Vector	Atom	BV components		
			$m_{\|a}$	$m_{\|b}$	$m_{\|c}$
Γ_5	ψ_3	1	0	0	4
		2	0	0	-4
		3	0	0	4
		4	0	0	-4
Γ_6	ψ_4	1	0	0	4
		2	0	0	-4
		3	0	0	-4
		4	0	0	4
Γ_9	ψ_5	1	4	0	0
		2	0	0	0
		3	4	0	0
		4	0	0	0
	ψ_6	1	0	4	0
		2	0	0	0
		3	0	4	0
		4	0	0	0
	ψ_7	1	0	0	0
		2	4	0	0
		3	0	0	0
		4	4	0	0
	ψ_8	1	0	0	0
		2	0	-4	0
		3	0	0	0
		4	0	-4	0
Γ_{10}	ψ_9	1	4	0	0
		2	0	0	0
		3	-4	0	0
		4	0	0	0
	ψ_{10}	1	0	4	0
		2	0	0	0
		3	0	-4	0
		4	0	0	0
	ψ_{11}	1	0	0	0
		2	4	0	0
		3	0	0	0
		4	-4	0	0
	ψ_{12}	1	0	0	0
		2	0	-4	0
		3	0	0	0
		4	0	4	0

B.1.2 Versiliaite, $Fe_{12}Sb_{12}O_{32}S_2$

Representational analysis was performed for Versiliaite starting from the room temperature (RT) nuclear (*Pbam*) model, with a $(\frac{1}{2}, \frac{1}{2}, 0)$ propagation vector. Table B.3 gives the basis vector components of the Γ_2 and Γ_8 irreducible representations, which (on application of time-reversal symmetry) can be combined to represent the observed magnetic structure. Atom labels are given in table B.2.

Table B.2 – Atomic labels and coordinates for Versiliaite IRs.

Site	Atom	Coordinates
Fe1	1	(0.3106, 0.3198, 0)
	2	(0.8106, 0.1802, 0)
	3	(0.1894, 0.8198, 0)
	4	(0.6894, 0.6802, 0)
Fe2	1	$(0, \frac{1}{2}, 0.378)$
	2	$(\frac{1}{2}, 0, 0.622)$
	3	$(0, \frac{1}{2}, 0.622)$
	4	$(\frac{1}{2}, 0, 0.378)$
Fe3	1	$(0, \frac{1}{2}, 0.127)$
	2	$(\frac{1}{2}, 0, 0.873)$
	3	$(0, \frac{1}{2}, 0.873)$
	4	$(\frac{1}{2}, 0, 0.127)$

Table B.3 – Selected IRs for Versiliaite (*Pbam*) with $k = (\frac{1}{2}, \frac{1}{2}, 0)$.

Site	IR	Basis Vector	Atom	BV components		
				$m_{\|a}$	$m_{\|b}$	$m_{\|c}$
Fe1	Γ_2	ψ_2	1	4	0	0
			2	0	0	0
			3	0	0	0
			4	-4	0	0
		ψ_3	1	0	4	0
			2	0	0	0
			3	0	0	0
			4	0	-4	0
	Γ_8	ψ_{11}	1	0	0	0
			2	4	0	0
			3	-4	0	0
			4	0	0	0

Site	IR	Basis Vector	Atom	BV components		
				$m_{\|a}$	$m_{\|b}$	$m_{\|c}$
		ψ_{12}	1	0	0	0
			2	0	-4	0
			3	0	4	0
			4	0	0	0
Fe2	Γ_2	ψ_3	1	4	0	0
			2	0	0	0
			3	4	0	0
			4	0	0	0
		ψ_4	1	0	4	0
			2	0	0	0
			3	0	4	0
			4	0	0	0
	Γ_8	ψ_{11}	1	0	0	0
			2	4	0	0
			3	0	0	0
			4	4	0	0
		ψ_{12}	1	0	0	0
			2	0	-4	0
			3	0	0	0
			4	0	-4	0
Fe3	Γ_2	ψ_3	1	4	0	0
			2	0	0	0
			3	4	0	0
			4	0	0	0
		ψ_4	1	0	4	0
			2	0	0	0
			3	0	4	0
			4	0	0	0
	Γ_8	ψ_{11}	1	0	0	0
			2	4	0	0
			3	0	0	0
			4	4	0	0
		ψ_{12}	1	0	0	0
			2	0	-4	0
			3	0	0	0
			4	0	-4	0

B.1.3 Apuanite, $Fe_{20}Sb_{16}O_{48}S_4$

Representational analysis was performed for Apuanite starting from the RT nuclear $(P4_2/mbc)$ model, with a $(\frac{1}{2}, \frac{1}{2}, 0)$ propagation vector. Table B.5 gives the basis vector components of the Γ_{10} irreducible representation, which represents the observed magnetic structure. Atom labels are given in table B.4.

Table B.4 – Atomic labels and coordinates for Apuanite IRs.

Site	Atom	Coordinates
Fe1	1	$(0.314, 0.317, 0)$
	2	$(0.814, 0.183, 0)$
	3	$(0.186, 0.817, 0)$
	4	$(0.686, 0.683, 0)$
	5	$(0.183, 0.186, \frac{1}{2})$
	6	$(0.683, 0.314, \frac{1}{2})$
	7	$(0.317, 0.686, \frac{1}{2})$
	8	$(0.817, 0.814, \frac{1}{2})$
Fe2	1	$(0, \frac{1}{2}, \frac{1}{4})$
	2	$(\frac{1}{2}, 0, \frac{3}{4})$
	3	$(0, \frac{1}{2}, \frac{3}{4})$
	4	$(\frac{1}{2}, 0, \frac{1}{4})$
Fe3	1	$(0, \frac{1}{2}, 0.0816)$
	2	$(\frac{1}{2}, 0, 0.9184)$
	3	$(0, \frac{1}{2}, 0.4184)$
	4	$(\frac{1}{2}, 0, 0.5816)$
	5	$(0, \frac{1}{2}, 0.9184)$
	6	$(\frac{1}{2}, 0, 0.0816)$
	7	$(0, \frac{1}{2}, 0.5816)$
	8	$(\frac{1}{2}, 0, 0.4184)$

Table B.5 – Selected IRs for Apuanite $(P4_2/mbc)$ with $k = (\frac{1}{2}, \frac{1}{2}, 0)$.

Site	IR	Basis Vector	Atom	BV components		
				$m_{\parallel a}$	$m_{\parallel b}$	$m_{\parallel c}$
Fe1	Γ_{10}	ψ_{17}	1	4	0	0
			2	0	0	0
			3	0	0	0
			4	-4	0	0
			5	0	0	0
			6	0	0	0
			7	0	0	0

Site	IR	Basis Vector	Atom	BV components		
				$m_{\|a}$	$m_{\|b}$	$m_{\|c}$
			8	0	0	0
		ψ_{18}	1	0	4	0
			2	0	0	0
			3	0	0	0
			4	0	-4	0
			5	0	0	0
			6	0	0	0
			7	0	0	0
			8	0	0	0
		ψ_{19}	1	0	0	0
			2	0	0	0
			3	0	0	0
			4	0	0	0
			5	0	4	0
			6	0	0	0
			7	0	0	0
			8	0	-4	0
		ψ_{20}	1	0	0	0
			2	0	0	0
			3	0	0	0
			4	0	0	0
			5	4	0	0
			6	0	0	0
			7	0	0	0
			8	-4	0	0
		ψ_{21}	1	0	0	0
			2	0	0	0
			3	0	0	0
			4	0	0	0
			5	0	0	0
			6	0	-4	0
			7	0	4	0
			8	0	0	0
		ψ_{22}	1	0	0	0
			2	0	0	0
			3	0	0	0
			4	0	0	0
			5	0	0	0
			6	4	0	0
			7	-4	0	0
			8	0	0	0
		ψ_{23}	1	0	0	0
			2	4	0	0

Site	IR	Basis Vector	Atom	BV components		
				$m_{\|a}$	$m_{\|b}$	$m_{\|c}$
			3	-4	0	0
			4	0	0	0
			5	0	0	0
			6	0	0	0
			7	0	0	0
			8	0	0	0
		ψ_{24}	1	0	0	0
			2	0	-4	0
			3	0	4	0
			4	0	0	0
			5	0	0	0
			6	0	0	0
			7	0	0	0
			8	0	0	0
Fe2	Γ_{10}	ψ_9	1	4	0	0
			2	0	0	0
			3	4	0	0
			4	0	0	0
		ψ_{10}	1	0	4	0
			2	0	0	0
			3	0	4	0
			4	0	0	0
		ψ_{11}	1	0	0	0
			2	0	-4	0
			3	0	0	0
			4	0	-4	0
		ψ_{12}	1	0	0	0
			2	4	0	0
			3	0	0	0
			4	4	0	0
Fe3	Γ_{10}	ψ_{17}	1	4	0	0
			2	0	0	0
			3	0	0	0
			4	0	0	0
			5	4	0	0
			6	0	0	0
			7	0	0	0
			8	0	0	0
		ψ_{18}	1	0	4	0
			2	0	0	0
			3	0	0	0
			4	0	0	0
			5	0	4	0

Site	IR	Basis Vector	Atom	BV components		
				$m_{\|a}$	$m_{\|b}$	$m_{\|c}$
			6	0	0	0
			7	0	0	0
			8	0	0	0
		ψ_{19}	1	0	0	0
			2	0	0	0
			3	0	4	0
			4	0	0	0
			5	0	0	0
			6	0	0	0
			7	0	4	0
			8	0	0	0
		ψ_{20}	1	0	0	0
			2	0	0	0
			3	4	0	0
			4	0	0	0
			5	0	0	0
			6	0	0	0
			7	4	0	0
			8	0	0	0

References

[1] A. S. Wills, *Physica B: Condensed Matter*, 2000, **276–278**, 680–681.

[2] O. V. Kovalev, *Representations of the Crystallographic Space Groups: Irreducible Representations, Induced Representations and Corepresentations*, Gordon and Breach, 1993.

APPENDIX C
ADDITIONAL REFINEMENT PLOTS

C.1 $Mn_xCo_{1-x}Sb_2O_4$

C.1.1 XRPD Refinements

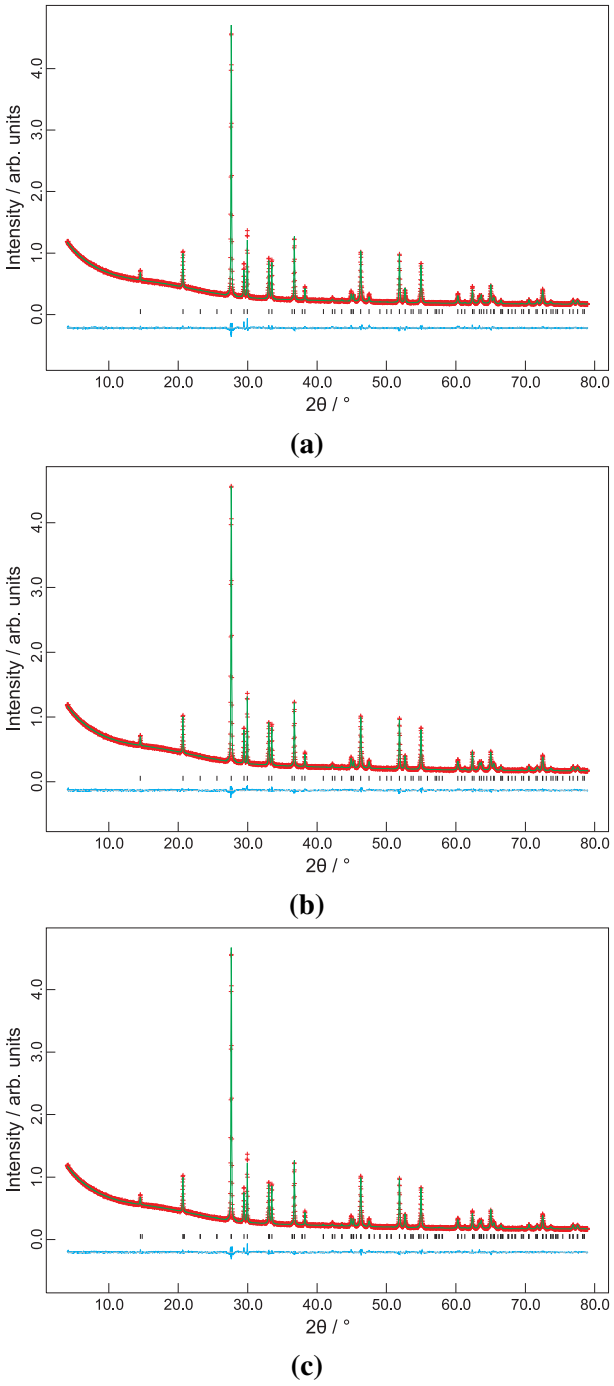

Figure C.1 – Refinement graphs for $Mn_{0.2}Co_{0.8}Sb_2O_4$: (a) Profile function #2; (b) Profile function #4; (c) *Pbam* model (profile #2).

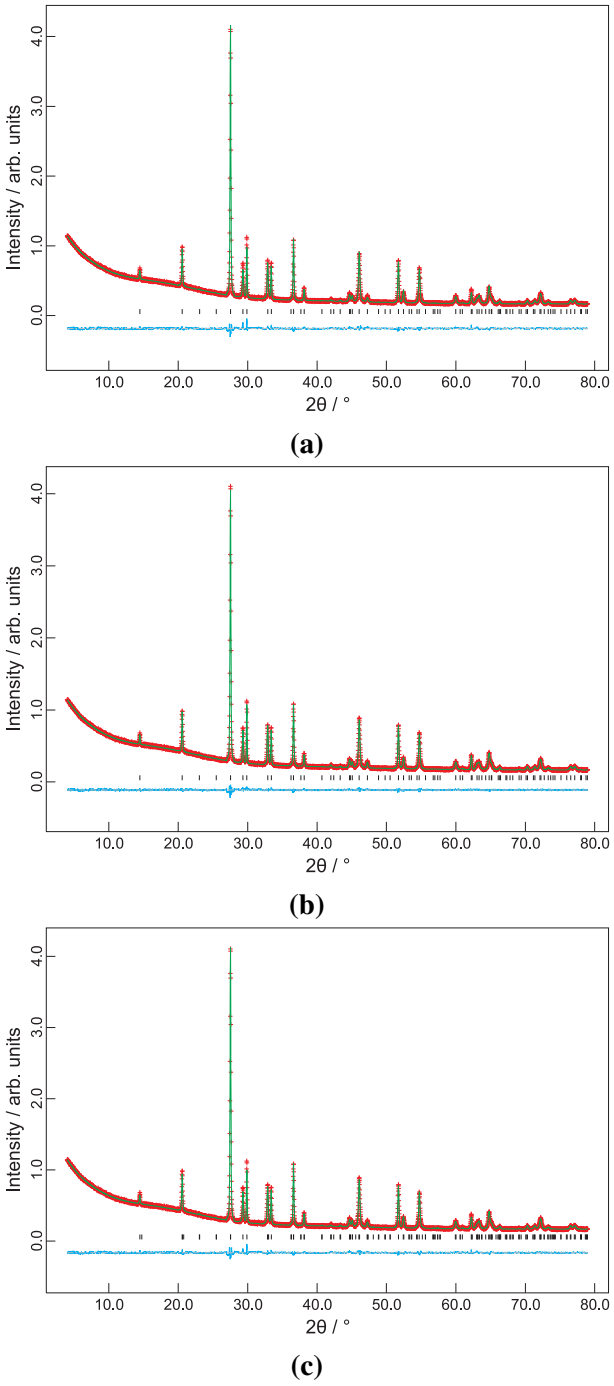

Figure C.2 – Refinement graphs for $Mn_{0.4}Co_{0.6}Sb_2O_4$: (a) Profile function #2; (b) Profile function #4; (c) *Pbam* model (profile #2).

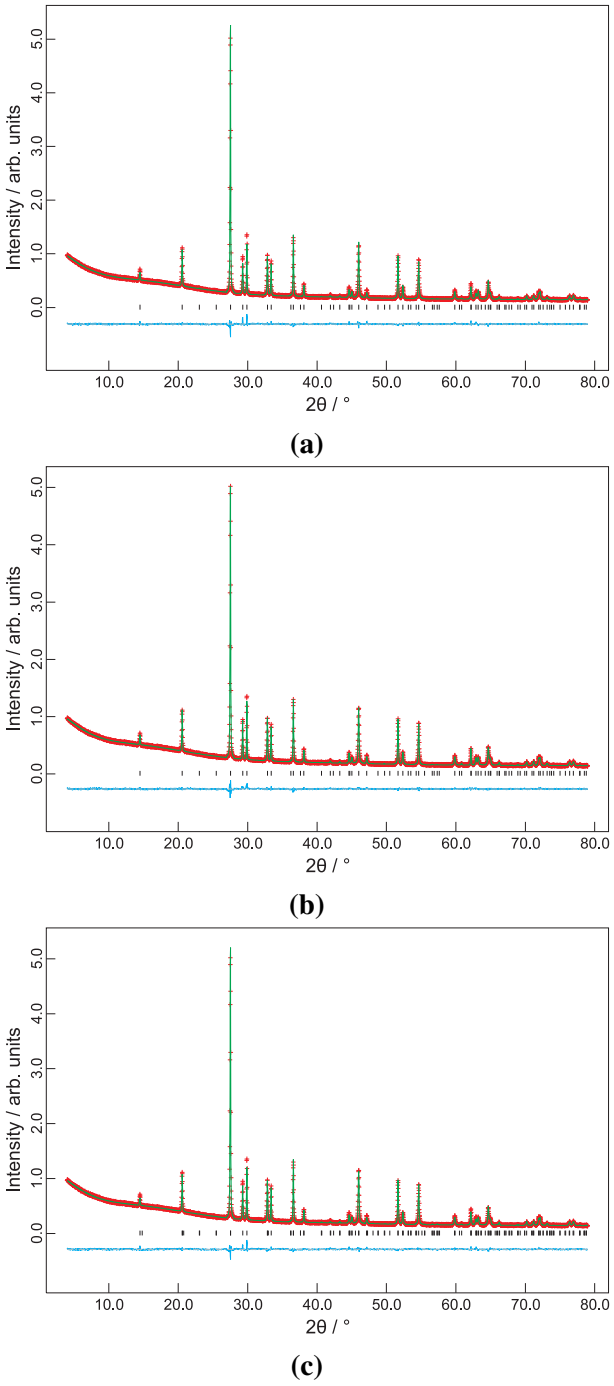

Figure C.3 – Refinement graphs for $Mn_{0.5}Co_{0.5}Sb_2O_4$: (a) Profile function #2; (b) Profile function #4; (c) *Pbam* model (profile #2).

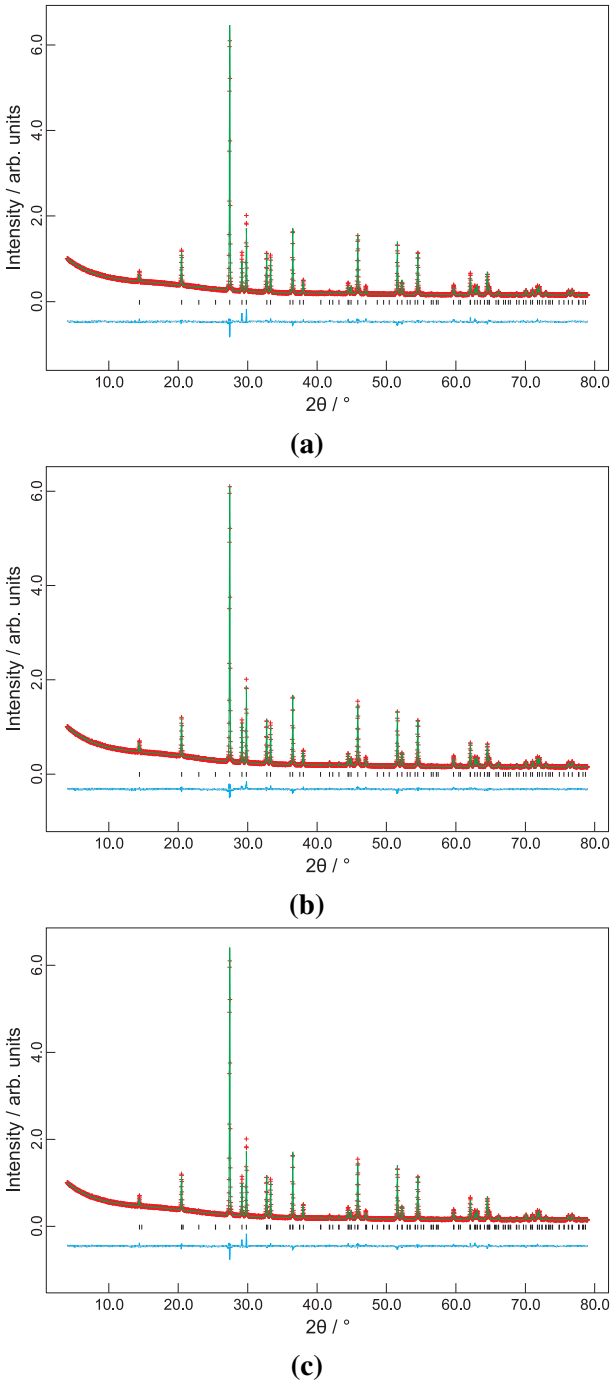

Figure C.4 – Refinement graphs for $Mn_{0.6}Co_{0.4}Sb_2O_4$: (a) Profile function #2; (b) Profile function #4; (c) *Pbam* model (profile #2).

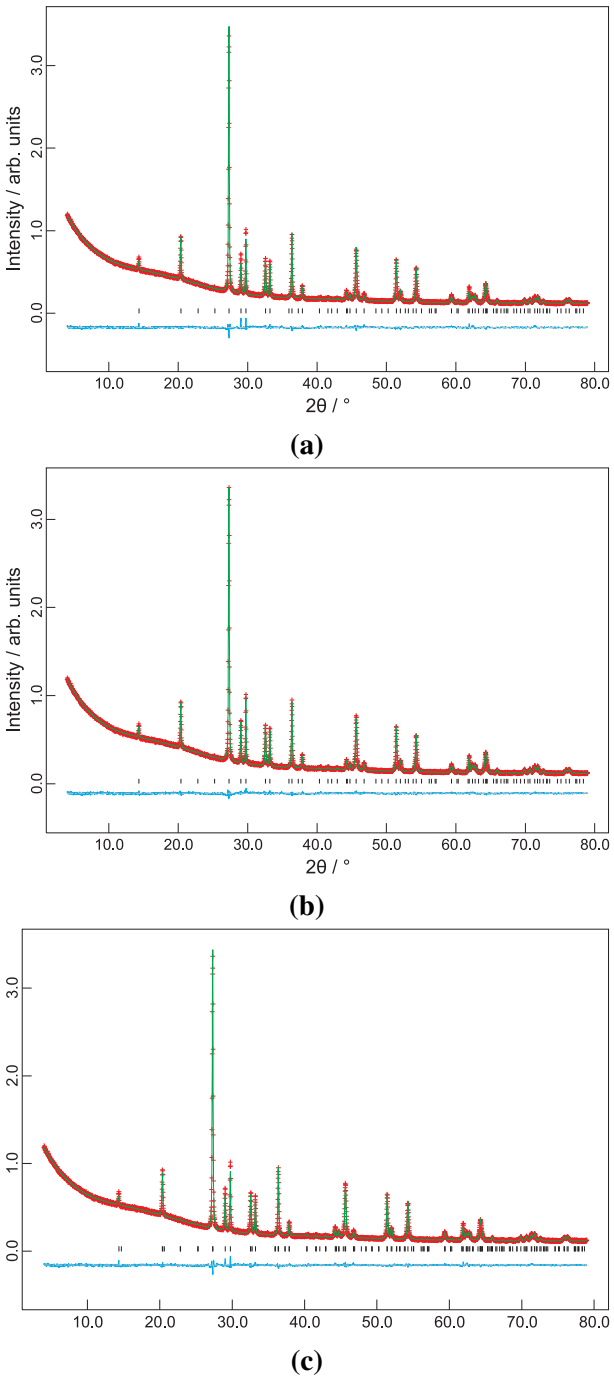

Figure C.5 – Refinement graphs for $Mn_{0.8}Co_{0.2}Sb_2O_4$: (a) Profile function #2; (b) Profile function #4; (c) *Pbam* model (profile #2).

C.1.2 NPD Refinements (300 K)

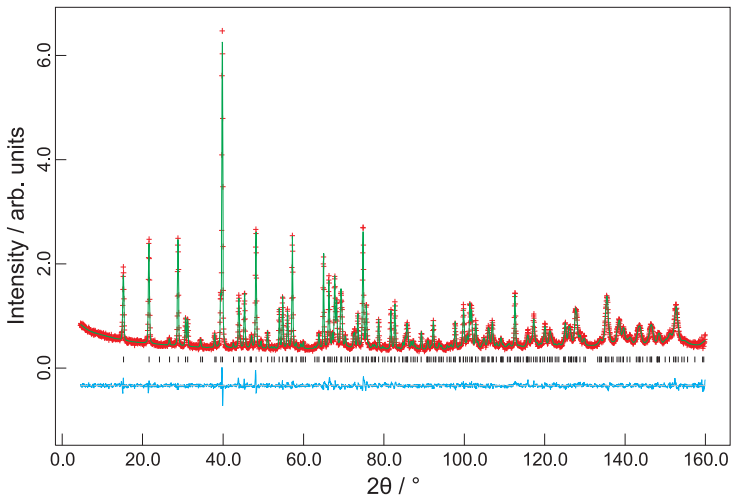

Figure C.6 – Graphical refinement of $Mn_{0.2}Co_{0.8}Sb_2O_4$ (profile #4).

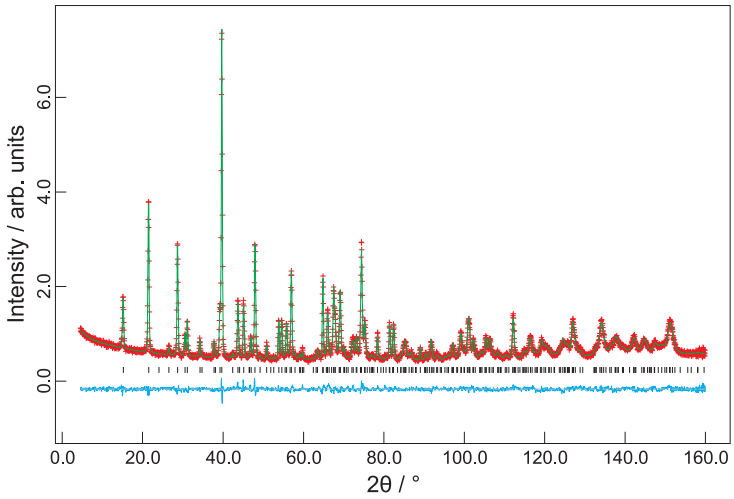

Figure C.7 – Graphical refinement of $Mn_{0.4}Co_{0.6}Sb_2O_4$ (profile #4).

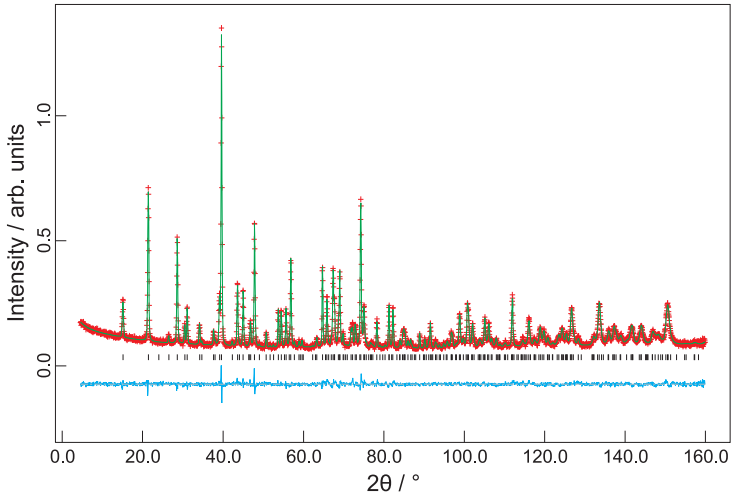

Figure C.8 – Graphical refinement of $Mn_{0.5}Co_{0.5}Sb_2O_4$ (profile #4).

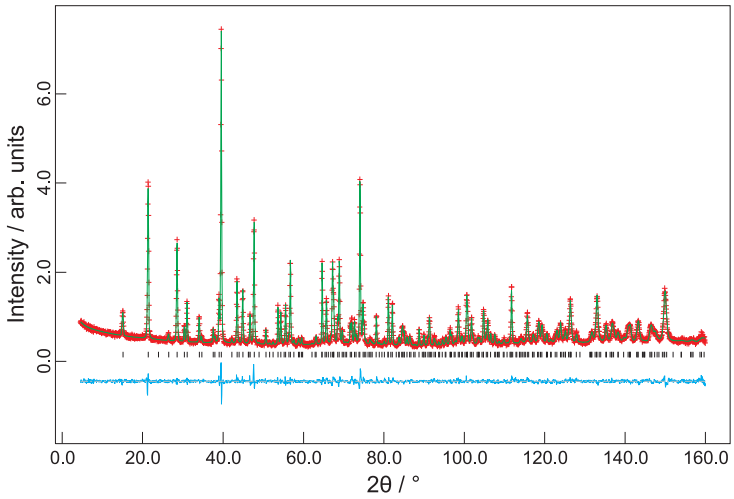

Figure C.9 – Graphical refinement of $Mn_{0.6}Co_{0.4}Sb_2O_4$ (profile #4).

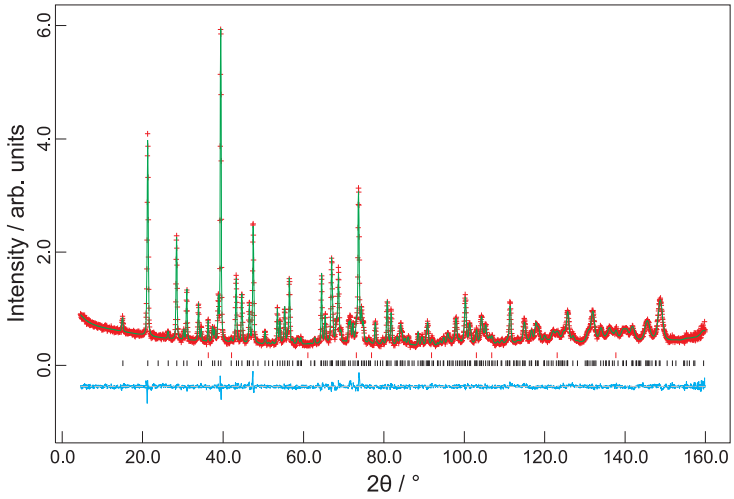

Figure C.10 – Graphical refinement of $Mn_{0.8}Co_{0.2}Sb_2O_4$ (profile #4).

C.2 Versiliaite

C.2.1 XRPD Refinements

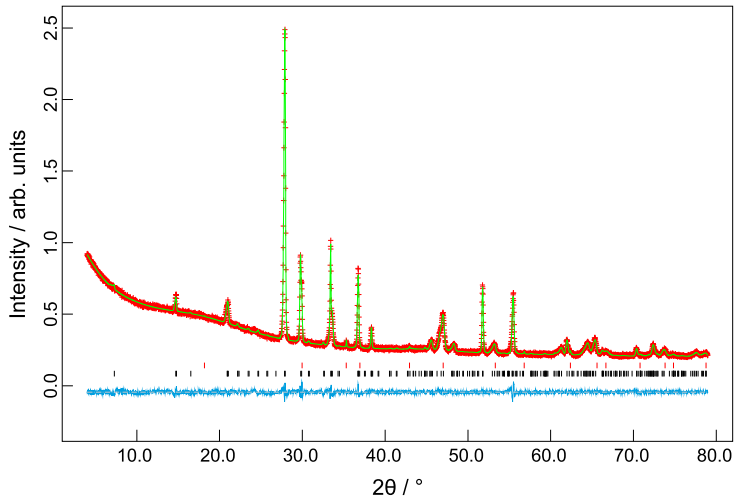

Figure C.11 – Graphical refinement of Versiliaite A using Versiliaite-like model. Black ticks-main phase, red ticks-Fe_3O_4 impurity.

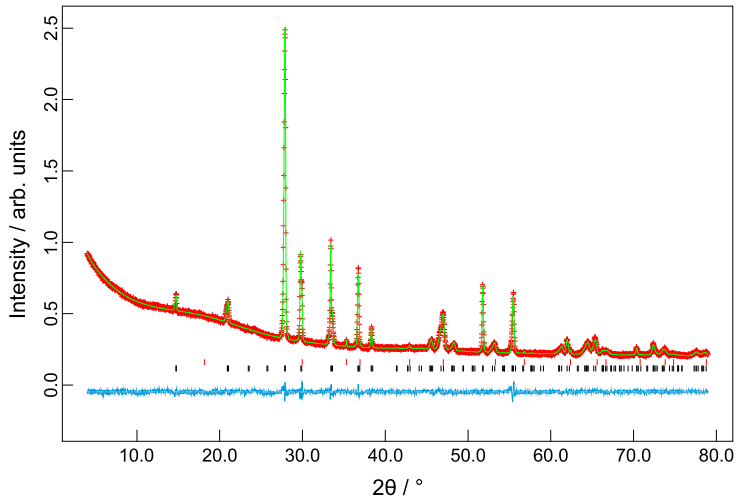

Figure C.12 – Graphical refinement of Versiliaite A using Schafarzikite-like model. Black ticks-main phase, red ticks-Fe_3O_4 impurity.

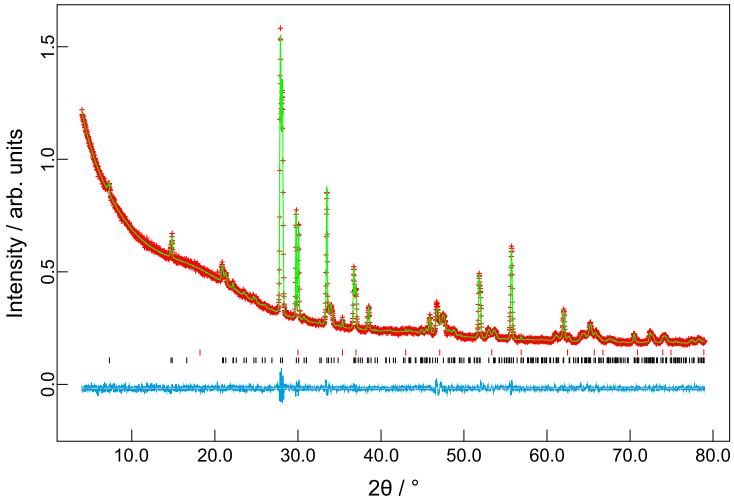

Figure C.13 – Graphical refinement of Versiliaite B using Versiliaite-like model. Black ticks-main phase, red ticks-Fe_3O_4 impurity.

C.2.2 NPD Refinements

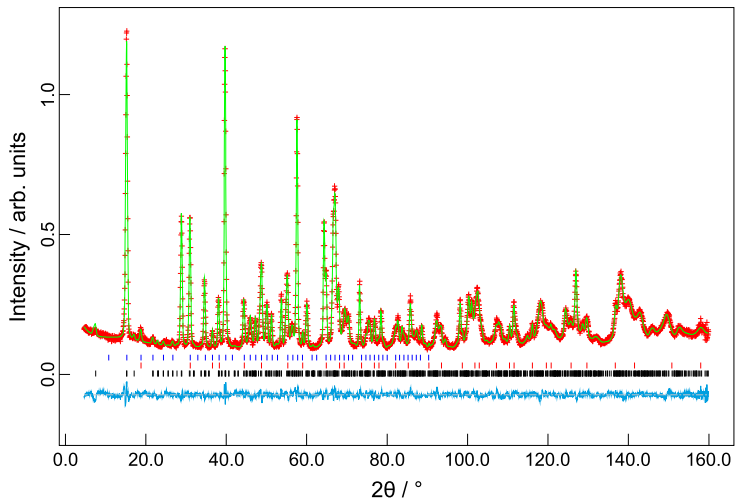

Figure C.14 – Graphical refinement of Versiliaite A from 300 K neutron powder diffraction (NPD) data. Black ticks-main phase, red and blue ticks-Fe_3O_4 impurity.

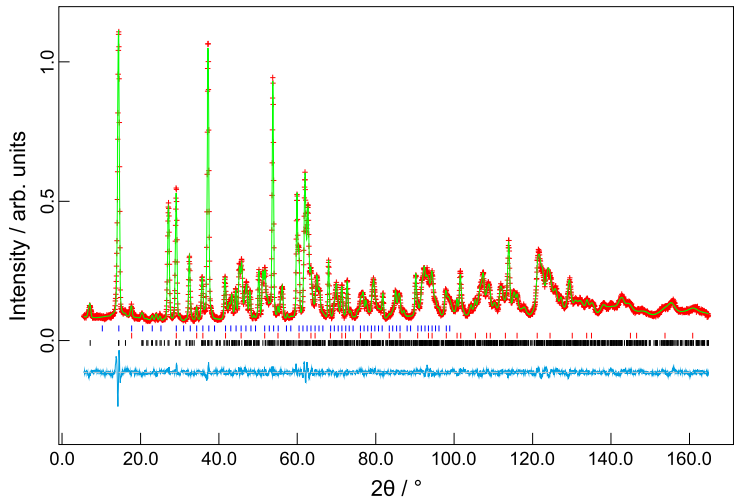

Figure C.15 – Graphical refinement of Versiliaite B from 300 K NPD data. Black ticks-main phase, red and blue ticks-Fe_3O_4 impurity.

C.3 Apuanite

C.3.1 NPD Refinements

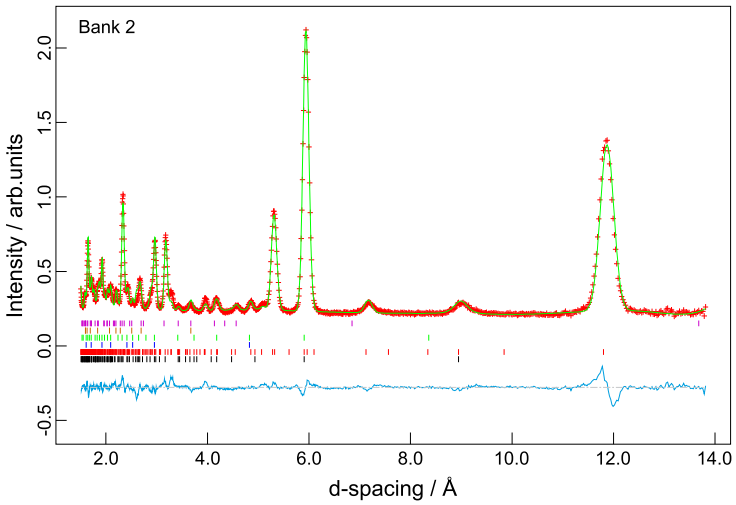

Figure C.16 – Graphical refinement of Apuanite at 5 K from general materials diffractometer (GEM) bank 2. Apuanite-black (nuclear) and red (magnetic) tickmarks, Fe_3O_4-blue (nuclear) and green (magnetic), Fe_2O_3-brown (nuclear) and purple (magnetic) tickmarks.

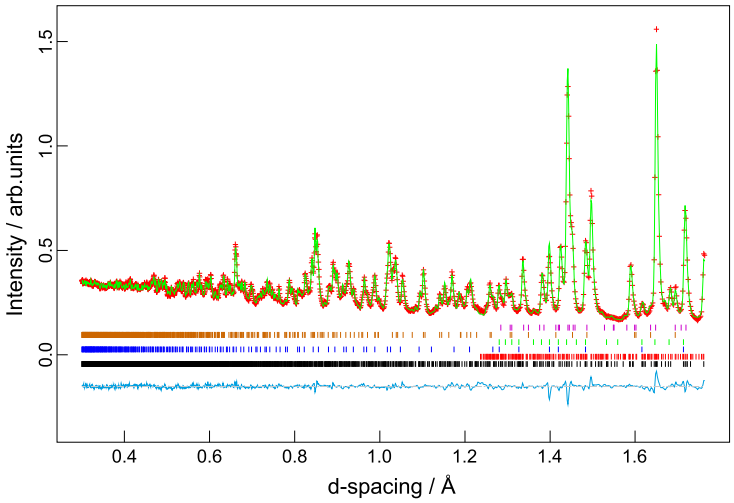

Figure C.17 – Graphical refinement of Apuanite at 5 K from GEM bank 6. Apuanite-black (nuclear) and red (magnetic) tickmarks, Fe_3O_4-blue (nuclear) and green (magnetic), Fe_2O_3-brown (nuclear) and purple (magnetic) tickmarks.